AERODYNAMIC AND MECHANICAL PERFORMANCE OF A HIGH-PRESSURE TURBINE STAGE IN A TRANSIENT WIND TUNNEL

A.G. SHEARD

Keble College
Oxford

A thesis submitted in partial fulfilment of the requirements of the degree of Doctor of Philosophy at the University of Oxford, Trinity Term 1989

Department of Engineering Science
Parks Road
Oxford
OX1 3PJ

AERODYNAMIC AND MECHANICAL PERFORMANCE OF A HIGH-PRESSURE TURBINE STAGE IN A TRANSIENT WIND TUNNEL

Anthony Geoffrey Sheard, Keble College

A thesis submitted in partial fulfilment of the requirements of the degree of Doctor of Philosophy at the University of Oxford, Trinity Term 1989

ABSTRACT

Unsteady three-dimensional flow phenomena have major effects on the aerodynamic performance of, and heat transfer to, gas-turbine blading. Investigation of the mechanisms associated with these phenomena requires an experimental facility that is capable of simulating a gas turbine, but at lower levels of temperature and pressure to allow conventional measurement techniques.

This thesis reports on the design, development and commissioning of a new experimental facility that models these unsteady three-dimensional flow phenomena. The new facility, which consists of a 62%-size, high-pressure gas-turbine stage mounted in a transient wind tunnel, simulates the turbine design point of a full-stage turbine.

The thesis describes the aerodynamic and mechanical design of the new facility, a rigorous stress analysis of the facility's rotating system and the three-stage commissioning of the facility. The thesis concludes with an assessment of the turbine stage performance.

ACKNOWLEDGMENTS

In April 1985, the now late Professor Donald Schultz, OBE,[1] took the present author on a guided tour of the Osney Laboratory which housed the Oxford University Turbo-machinery Group. Professor Schultz's easy confidence, purpose and clarity of vision inspired me to make a formal application to join his research group soon after my visit. During my first year as a research student, Professor Schultz's guidance and constructive criticism gave me confidence to stretch myself to achieve the potential that he apparently recognised, but of which I was largely unaware. There are no words to express my thanks to Professor Schultz for the opportunity he gave me, nor my grief (and that of his friends and colleagues) at his untimely death.

I thank my supervisor, Dr R.W. Ainsworth, for his help and encouragement over the past three years, particularly during the preparation of this thesis. Ms Caroline Broadbridge and Dr A.V. Sheard also warrant special mention for their diligent proofreading of draft copies of all my written work. Dr Ainsworth and myself greatly appreciate the help and guidance of Mr Neville Stimpson in all matters relating to the turbine module's bearing system, in particular its computer modelling. Neville's constant good-humoured advice and technical expertise was invaluable. The help of Dr Martin Rose in running the FINSUP predictions included in this thesis was also invaluable, as were the many technical discussions we had about three-dimensional fluid flow. I am indebted to Martin for finding the time in an already overcrowded schedule to help me.

My co-workers on the 'rotor project', Dr Mark Davies, Dr Patrick Forth, Mrs Mary Hilditch, Mr Mike Izsak, Lt Billy Allan, FLG OFF Tony Dietz and Mr John Slater, were largely responsible for making my time at Oxford so enjoyable through our many stimulating and illuminating technical discussions. During the commissioning phase of the 'rotor project', Mr Kevin Grindrod's technical assistance was invaluable, as was Ms Melanie Rigby and Dr Ashley Johnson's advice and assistance. I also thank Ms Susan Hughes, without whose guidance I would not have been able to write my computer code ('ROTOR') as quickly, or as clearly. My work would have been impossible without the help of the Osney Laboratory workshop staff, with special thanks to Mr Geoff Horton for his help in assembling the 'turbine module' and Mr Ernie Woodward for his morale-boosting encouragement during the project's initial design phase.

Rolls-Royce plc and the Science and Engineering Research Council jointly funded my work under grants GR/D 21189 and GR/E 28062.

---

[1] Professor Donald Lorimer Schultz MA, DPhil, BE Canterbury NZ, OBE, Professor of Mechanical Engineering in the Department of Engineering Science, University of Oxford, Professorial Fellow St Hugh's College and Emeritus Fellow St Catherine's College died on 27 April 1987 in New Zealand. He was 60.

LIST OF CONTENTS

CHAPTER ONE
INTRODUCTION

1.1 BACKGROUND

CHAPTER TWO
THE TURBINE FLOW FIELD

CHAPTER THREE
EXPERIMENTAL ARRANGEMENT

3.1 INTRODUCTION

3.2 DYNAMIC SIMILARITY REQUIREMENTS

3.3 ACHIEVEMENT OF THE B22 TURBINE DESIGN CONDITION

3.4 PREDICTED FACILITY PERFORMANCE

3.5 DATA ACQUISITION SYSTEM

CHAPTER FOUR

AERODYNAMIC AND MECHANICAL DESIGN OF TURBINE MODULE

4.1 THE BEARING SYSTEM

4.2 TURBINE AIR MOTOR

4.3 DEVELOPMENT OF THE ANNULAR GATE VALVE AND INLET DUCT

4.4 THE SECOND THROAT

4.5 TURBINE SPEED AND POWER MEASURMENT

CHAPTER FIVE
STRESS ANALYSIS OF TURBINE DISC AND BLADE

CHAPTER SIX
FACILITY CONSTRUCTION AND COMMISSIONING

CHAPTER SEVEN
TURBINE STAGE PERFORMANCE

LIST OF FIGURES

LIST OF TABLES

NOMENCLATURE

Symbol	**Measure**	**Units**
A	Area	m^2
A_b	Blade inlet annulus area	m^2
A_k	Hot wire ‘no-flow’ voltage	v
A_t	Pump tube area	m^2
a	Speed of sound	m/s
a_c	Acceleration	m/s^2
B	Constant in King’s law	
B_t	Axial load for tandem bearing set	N
B_s	Axial load for single bearing	N
C_1	Tachometer IC capacitor	F
C_2	Tachometer IC capacitor	F
C_f	Ultimate bearing axial load	N
C_l	Total pressure loss coefficient	
C_p	Specific heat capacity	J/kgK
$C_{pr(th)}$	Theoretical diffuser pressure rise coefficient	
$C_{pr(ac)}$	Actual diffuser pressure rise coefficient	
c	Vane mid-height axial chord	m
D_m	Carbon face seal mean diameter	m
d	Diameter	m
d_m	Bearing mean diameter	m
dv	AC voltage	v
E	Young’s modulus	N/m^2
F	Turbine axial load	N
F_a	Bearing axial pre-load	N
F_d	Turbine disc axial pressure load	N
F_f	Force	N/m^2
F_o	AGV ‘o’ ring friction force	N/m^2
F_r	Bearing radial load	N
F_t	Carbon face seal closing force	N
f	Laminar pipe flow friction factor	
f_c	Cut-off frequency	Hz
f_f	Heavy mist lubrication factor	
f_{in}	Tachometer IC input square-wave frequency	Hz
g	Gravitational acceleration	m/s^2
H	Head against which a rolling element bearing pumps	m
H_l	Head loss	m
$H_{Q=0}$	Head against which a rolling element bearing can pump at zero flow rate	m
ΔH_r	Manometer water height, static pressure at a reference point	m
ΔH_{0r}	Manometer water height, total pressure at a reference point	m
ΔH_{0m}	Manometer water height, total pressure at a measurement point	m
H_*	Boundary layer shape factor	
h	Height	m
h_t	Heat-transfer coefficient	W/m^2K
I	Moment of inertia	kgm^2
I_0	Maximum tachometer chip output current	amp
J	Torque	N/m

Symbol	**Measure**	**Units**
J_v	Viscous friction moment	N/m
J_c	Contact friction moment	N/m
J_s	Carbon face seal retarding torqueN/m	
K	Pipe flow minor loss coefficient	
K_i	Tachometer IC output gain constant	
K_l	Bearing pumping ball-bearing correction factor	
k	Gauze pressure drop coefficient	
L_t	Pump tube length	m
l	Length	m
ΔL	Change of length	m
M	Mach number	
M_c	AGV centre section mass	kg
M_f	Turbine mass flow number	ms/K^{½}
M_r	Mass	kg
M_t	ILPT piston mass	kg
$M_{\alpha i}$	Inner bearing race/ball moment	N/m
$M_{\alpha o}$	Outer bearing race/ball moment	N/m
M_x	Moment about the x axis	N/m
M_y	Moment about the y axis	N/m
$\dot{m}$	Mass flow rate	Kg/s
N	Turbine speed	rpm
N_i	Pre-run turbine speed	
N_f	Post-run turbine speed	
Nu	Nusselt number	
n	Rotational speed	rpm
P	Pressure	N/m^2
ΔP	Pressure drop	N/m^2
P_i	Initial ILPT tube pressure	N/m^2
P_l	Frictional power loss	J/s
P_{0r}	Total pressure at a reference point	N/m^2
P_{0m}	Total pressure at a measurement point	N/m^2
P_r	Turbine pressure ratio	
P_w	Turbine power	J/s
p	Constant used in King's law	
Q	Torque	Nm
$Q_{H=0}$	Oil flow rate through a rolling element bearing against zero head1/min	1/min
$\dot{q}$	Oil flow rate through a rolling element bearing	1/min
$\dot{q}_a$	Flow rate	m^3/s
R	Gas constant	m^2/s^{2}K
R_α	Radius of curvature	m
R_c	Labyrinth seal radius	m
R_*	Resistance	ohm
Re	Reynolds number	
$Re_{\delta *}$	Reynolds number coefficient (as defined by Wilson, 1984)	
R_0	Blade mid-height section radius	m
r	Radius	m
S_s	Turbine specific speed	rpm/K^{½}
T	Temperature	K
T_g	Gas temperature	K

Symbol	**Measure**	**Units**
T_i	Initial ILPT tube temperature	K
T_r	Temperature ratio	
T_p	Time period of piston oscillations	s
T_w	Wall temperature	K
ΔT	Temperature change	K
t	Time	s
U	Velocity	m/s
U_f	Free stream velocity	m/s
u	Displacement	m
V	Volume	m^3
V_a	Volume between piston and AGV	m^3
V_b	Volume between reservoir and piston	m^3
ΔV	Volume between AGV and vane throat	m^3
V_0	Tachometer IC output voltage	volt
V_{ri}	Tachometer IC output ripple	volt
V_z	Tachometer IC zener voltage	volt
v	Volts (DC)	volt
v_l	Velocity	m/s
v_r	Velocity at a reference point	
W	Weight	kg
W_f	Turbine specific work number	J/kgK
x	Distance	m
Y_c	Diffuser entry width	m
Z	Number of balls per bearing	
α	Mid-height vane exit angle	degree
α_i	Bearing inner race contact angle	degree
α_0	Bearing outer race contact angle	degree
β	Turbine blade mid-height exit angle	degree
β_{no}	Number of bearings in a set	
δ	Angle between axial direction and stationary frame blade exit gas angle	degree
δ_*	Boundary layer displacement thickness	m
δ^*_c	Boundary layer displacement thickness at diffuser entry	m
δ_{cl}	Labyrinth seal clearance	m
ε	Strain	
γ	Ratio of specific heats	
κ	Carbon face seal coefficient of friction	
λ	Bearing inner race contact angle at which truncation occurs	degree
φ	Angle between the outer race contact and the moment of the outer bearing racer/ball	degree
ψ	Angle between circumferential direction and stationary frame blade exit gas path	degree
ξ	Blade inlet gas angle	
η	Efficiency	
η_b	Turbine blade gas path efficiency	
η_c	Compressor efficiency	
η_t	Turbine efficiency	
ρ	Density	kg/m^3
ρ_w	Density of water	kg/m^3
σ	Stress	N/m^2
τ	Time period of oscillation	s

Symbol	**Measure**	**Units**
τ_{run}	Facility run time	s
τ_t	Facility run time, no tube compression	s
θ	Angle	radians
ν	Kinematic viscosity	mm^2/s
μ	Fluid viscosity	kg/ms
ω	Angular velocity	rads/s
$\dot{\omega}$	Angular acceleration	$rads/s^2$
θ	Boundary layer momentum thickness	

Subscripts

Subscript	**Meaning**
0	Total gas conditions
1	Vane inlet conditions
2	Vane exit conditions
3	Blade relative inlet conditions
4	Blade relative exit conditions
5	Blade exit conditions, stationary frame
a	Axial
b	Beferring to turbine blade
c	Inlet
d	Exit
I	Initial condition
f	Final condition
r	Radial
s	Referring to turbine stage
w	Wall conditions
x	About the X axis
y	About the Y axis
xy	Parameter in the XY plane
p	About the centroid
8	Free stream conditions

Superscripts

Superscript	**Meaning**
*	Throat conditions

CHAPTER ONE

INTRODUCTION

1.1 BACKGROUND

1.1.1 Historical Perspective

The gas turbine made its début as a propulsion system in the early 1940s when, on 15 May 1941, Sir Frank Whittle's W1 engine flew in the Gloucester E.28 aircraft. The gas turbine entered service with the Royal Air Force when the first Meteor was delivered to 616 Squadron on 12 July 1944, fitted with Welland 1 engines. These Whittle-designed, Rolls-Royce-developed successors to the W1 gave the Meteor a maximum air speed of 460 mph in level flight.

The Messerschmitt Me262, which first flew in July 1942 and entered service in July 1944, was fitted with Junkers Jumo 004B engines. The 004B engines had a turbine entry temperature (TET) of 700°C and a thrust-to-weight ratio of 1.25, which gave the Me262 a maximum air speed of 540 mph in level flight.

Since then, engineers have made continuous efforts to increase the performance, reliability and efficiency of aircraft propulsion gas turbines. At the time of writing, state-of-the-art aircraft gas turbines have a TET of approximately 1,370°C and military engines have a thrust-to-weight ratio of more than 7:1. High thrust-to-weight ratios have opened up a radically new flight regime for military aircraft—the ability to climb vertically and accelerate simultaneously.

Jeal (1988) considered the future of military engines and predicted an increase in engine thrust-to-weight ratio to 20:1 in the subsequent two decades, together with stoichiometric burning in the engine combustion can, which would give a theoretical maximum TET of approximately 2,200ºC. Engines might also achieve increased thrust-to-weight ratio and fuel efficiency by increasing the TET (as described below).

1.1.2 Basic principles of improved performance

The efficiency of a gas turbine operating on an ideal air standard Joule cycle, known as the 'Joule cycle efficiency' (Haywood, 1980), is a function of the turbine pressure ratio and the ratio of specific heats of the gas. When engineers consider the irreversible effects, compressor and turbine inefficiencies modify the ideal Joule cycle (see Figure 1.1). For a compressor efficiency (η_c) of 85% and a turbine efficiency (η_t) of 88%, the overall efficiency of the gas turbine progressively increases with increasing TET, resulting in higher TET's giving and overall efficiency closer to that of the Joule cycle efficiency (see Figure1.2).

The materials in modern high-pressure turbines have a melting point of approximately 1,250°C. Because 900°C is the upper limit for metal temperature to achieve reasonable engine life, the turbine requires effective cooling methods as TETs increase above 900°C. Air is 'bled' from the high-pressure compressor to cool the turbine; as TETs increase, the turbine requires more coolant flow. The trend for increasing TETs has resulted in a corresponding increase in the proportion of engine core flow that serves as coolant flow in both in-service and high-temperature demonstrator engines (see Figure 1.3). Rolls-Royce plc is currently developing an engine for the new European Fighter Aircraft, which uses 20% of the engine core flow for high-pressure turbine cooling alone.

Because the coolant flow must compress before it is 'bled off' from the high-pressure compressor, an increase in the mass flow rate of coolant inevitably offsets any gains in cycle efficiency achieved by increasing the TET. However, apart from increasing cycle efficiency, one can associate a second benefit with increasing TET. As TET increases, the specific thrust (defined as thrust per unit mass flow of inlet air) also increases, which allows the size of the compressor inlet to reduce for a given thrust rating. A smaller compressor inlet area leads to a smaller engine, which reduces both weight and skin friction drag, thus ultimately reducing the thrust required of the propulsion system for a given air frame.

The principal reasons for engine manufacturers constantly striving for higher TETs differ between civil aircraft and military aircraft. For civil engines, increasing specific thrust allows for smaller engines of a given thrust rating, which brings a variety of attendant advantages one associates with reduced size. For military engines, increased specific thrust enables the engine's thrust-to-weight ratio to increase, which provides an attendant improvement in aircraft performance.

To understand why increasing TET results in an increase in specific thrust, one must consider the physical basis on which the Joule cycle operates. The lines of constant pressure on the enthalpy–entropy diagram (Figure 1.1) diverge as temperature increases. As a result, the higher the temperature leaving the combustor and entering the turbine, the larger the enthalpy drop across the turbine. This drop is proportional to the net power out of the cycle. For a propulsion system operating on the Joule cycle, this is equivalent to an increase in specific thrust.

1.1.3 Current study

As part of the continuing trend to more efficient gas turbines, engine manufacturers are looking towards the utilisation of fully three-dimensional design techniques in the near future. The development of such three-dimensional design techniques is dependent upon the availability of accurate experimental data the researcher obtained in an environment that simulates the flow features of interest. Such data enable the researcher to understand and then model physical mechanisms that they associate with unsteady three-dimensional and rotating effects. The measured data also provide a test case against which one can validate the three-dimensional design techniques.

This thesis describes the design, development and commissioning of a new turbine test facility in order to examine the flow field of the high-pressure turbine stage. The author's specific areas of responsibility included all aerodynamic and mechanical aspects of the new facility. Upon completion of commissioning trials, the new facility was capable of accurate simulation of the design point of its B22 turbine. Other workers currently use the facility to study the turbine flow field under engine representative conditions.

1.2 SUMMARY OF CHAPTERS

The turbine stage incorporated into the isentropic light piston tunnel (ILPT) is the focus of a major research effort at Oxford. The following is a summary of the thesis chapters which reference specific contributions to this research.

Chapter 2 reviews previous studies of both vane and blade mid-height sections in cascade. The chapter also discusses three-dimensional and unsteady flow phenomena. It concludes with a review of other full-stage, short-duration and transient turbine-test facilities. Chapter 3 describes the ILPT's mode of operation and data-acquisition systems. Chapter 4 presents the detailed design of the ILPT working section containing the turbine stage (or 'turbine module'). Chapter 5 provides the details of a comprehensive stress analysis of the turbine module's rotating system. Chapter 6 describes the construction and assembly of the turbine module and the subsequent three-stage commissioning of the ILPT with the turbine module fitted. Chapter 7 provides an analysis of the accuracy with which the turbine design point simulates the engine condition flow field, followed by an assessment of the success with which the design point flow field was simulated. Chapter 8 presents the conclusions of the thesis.

CHAPTER TWO

TURBINE FLOW FIELD

2.1 CASCADE STUDIES OF B22 TURBINE

Nicholson (1981) first studied the B22 turbine mid-height vane and blade sections in cascade and measured static-pressure and heat-transfer distributions around both vane and blade over a range of conditions. He used Schlieren photographs and holographic interferograms (Oldfield et al., 1986) to gain a qualitative understanding of the blade and vane flow fields. Nicholson (1981) compared blade-passage Mach number contours from absolute holograms with time-marching predictions of the flow field and found them in reasonable agreement. The same author developed a novel technique for measuring blade-profile loss (Oldfield et al., 1981), which he used to measure vane and blade loss at design Mach and Reynolds numbers over a range of gas-to-wall temperature ratios. He concluded from this investigation that aerodynamic loss was not a function of gas-to-wall temperature ratio, which provided a justification for the common practice of measuring losses in isothermal cascades. Nicholson (1981) also measured the loss of the B22 turbine mid-height blade section with 0.2% and 4% inlet turbulence and found that the change from 0.2% to 4% turbulence had a negligible effect on loss.

Nicholson (1981) used unsteady heat transfer traces to identify the state of vane and blade boundary layers. On the vane suction surface, the author observed a laminar boundary layer up to 10% surface length, followed by rapid transition. He judged the pressure surface boundary layer transitional from 20% to 80% surface length, with evidence of a fully laminar boundary layer only over the very early pressure surface and a turbulent boundary layer only over the very late pressure surface. He identified the blade suction and pressure surface boundary layers as laminar over the first 40% of surface length, transitional over the following 30% of surface length and turbulent until the trailing edge. Nicholson (1981) used his deductions about boundary-layer state to illuminate mean heat-transfer results. He associated laminar boundary layers with a low mean heat-transfer rate, transitional boundary layers with a rapidly rising mean heat-transfer rate and turbulent boundary layers with a high mean heat-transfer rate.

Horton (1985) subsequently studied the B22 blade mid-height section over the same range of conditions as Nicholson (1981), with the addition of film cooling. Film cooling at the blade leading edge produced a significant reduction in heat-transfer rates on the suction surface and a slight reduction on the pressure surface. Film cooling of the suction surface was very effective; however, film cooling of the pressure surface actually resulted in an 18% increase in heat-transfer rates immediately downstream of the coolant holes. Horton (1985) concluded that the performance of the cooling geometries was particularly sensitive to curvature.

Horton (1985) also measured the loss associated with film cooling. For a given coolant mass-flow rate, cooling the suction surface produced more loss than cooling the pressure surface. Loss measurements made at other than design gas-to-coolant temperature ratios were sensitive to density ratio, from which Horton (1985) concluded that cooling loss measurements must be made under engine-representative conditions of density ratio.

Doorly (1983) studied the effect of wake passing on the B22 turbine blade mid-height section using a novel ‘wake generator’ that consisted of a rotating disc with radial bars fitted around its circumference (see Figure 2.1). To generate wakes, he spun the bars in front of a linear cascade of blades. Doorly chose the ‘wake generator’ bar diameter to produce a velocity deficit through the wake similar to that produced by a vane. The conditions Doorly (1983) used in a linear cascade, which were similar to those of Nicholson (1981) and Horton (1985), achieved a reasonable simulation of the conditions the B22 turbine blade mid-height section at design conditions encountered (see Figure 2.2).

Doorly's (1983) wake-passing study revealed that the bar-generated wakes had a significant effect on blade heat-transfer rates as they convected through the blade passage. The author observed that the most striking effects of wake passing occurred with a free-stream turbulence level of 0.2%; however, the effects of wake passing on blade heat-transfer rates remained demonstrable with a free-stream turbulence level of 4%. Doorly (1983) concluded that the turbulent wakes convected through the blade passage forced the suction-surface boundary layer to undergo transition from a laminar state to a turbulent state. Once the bar wake convected through the blade passage, the boundary layer immediately reverted to its previous laminar state. The periodic tripping of the blade boundary layer resulted in heat-transfer rates alternating between those associated with a laminar boundary layer and those associated with a turbulent boundary layer. The author concluded that the effect of wake passing caused a significant increase in the level of mean heat transfer around the blade. Rigby (1989) continued Doorly's (1983) work on a different transonic blade profile and was able to quantify the effects of both shock and wake passing on blade mean heat-transfer rates.

Baines et al. (1982) developed a short-duration blow-down facility to conduct large-scale aerodynamic studies of the B22 turbine blade mid-height section in cascade. King (1986) commissioned the blow-down facility and measured Mach number distributions around 100-mm and 300-mm chord cascades and compared them to the Mach number distributions that Nicholson (1981) measured in the isentropic light piston tunnel (ILPT). King (1986) concluded that the large chord results were in good agreement with Nicholson's (1981). King's (1986) large chords allowed for detailed measurements of static pressure around the blade leading-edge. The new leading-edge detail indicated the presence of a sharp deceleration near the suction-surface/leading-edge blend point. King (1986) used Schlieren photography to identify a separation/reattachment bubble at this location.

Dickens (1989) subsequently used King’s (1986) blow-down facility to continue investigation of the B22 turbine blade mid-height section’s aerodynamics. Dickens (1989) studied the aerodynamic losses of a cascade of 100-mm chord blades over a range of conditions. He found loss only a weak function of Reynolds number and turbulence level over the range of tested conditions.

2.2 THREE-DIMENSIONAL FLOW PHENOMINA

Researchers have used linear cascades to provide a wealth of data on the turbine flow field; however, Paulon et al‘s (1975) interesting experimental investigation exposed their limitations. The team investigated supersonic compressor blading in linear cascades and annular cascades and found significant variations between the performance of the same profile in the two cases. The linear cascade suffered from separations, whereas the annular cascade gave good results, which agreed with theoretical pressure distributions. In Paulon et al’s (1975) experimental investigation, the effects of changing from a linear cascade to an annular cascade were significant and suggested that researchers cannot neglect three-dimensional annular cascade flow phenomenon.

One can conveniently divide the three-dimensional flow field of an annular cascade into two classes: (i) the *primary* flow, which one can regard as the irrotational potential flow that arises as a consequence of blade-to-blade passage geometry; and (ii) the *secondary* flow, which is the difference between the actual flow and the primary flow. The secondary flow arises as a consequence of viscous effects—principally the cascade inlet boundary layer. Many researchers have studied secondary flows in linear and annular cascades and there are now several excellent reviews of this work, Sieverding (1985) offering the most comprehensive.

Secondary flows arise in a turbine as a consequence of two main mechanisms. A ‘passage vortex’ arises because of the deflection of the inner and outer annulus surface boundary layers through a cascade due to the pressure gradient within a blade passage. The interaction of the inner and outer annulus surface boundary layers at the cascade inlet with the blade leading edge gives rise to a ‘horseshoe’ vortex.

Klein (1966) studied the mechanism by which a passage vortex forms (see Figure 2.3) and proposed a mechanisem for its development. This mechanisem can best be visualised by considering the flow into a cascade of turbine blades. Assuming certain conditions (an incompressible flow, a thin inlet boundary layer, and no separated flow regions), the static pressure of the free-stream flow will be constant throughout the boundary layer to the annulus surface. Both the free-stream and the boundary layer will be subject to a pressure gradient (dP/dn) due to the presence of the aerofoils, normal to the streamlines. This can be expressed as,

$$\frac{dP}{dn} \propto \rho \frac{U^2}{R_\alpha}$$

where R_α *= the radius of curvature*

U *= the fluid velocity*

The fluid velocity (U) in the boundary layer will be less than that of the free stream (U_f); therefore, the radius of curvature of the boundary layer must be less by a factor of $(U/U_f)^2$. The curvature of the streamlines will be higher at the annulus surface. Boundary layer flow therefore develops a velocity component normal to the free-stream flow from high-to-low pressure regions—that is, from the pressure surface side of the passage to the suction surface side. As the flow approaches the suction surface it is forced up the blade, setting up a circular motion; this is the passage vortex.

Langston et al. (1977) studied the mechanism by which a horseshoe vortex forms (see Figure 2.4). The horseshoe vortex can be visulised as the 'rolling up' of the annulus surface boundary layer in front of the aerofoil leading edge. The flow approaching an aerofoil leading edge separates and passes on both sides of the aerofoil. There is a dividing plane between the two halves of the flow and the streamlines in this plane are stagnation streamlines that come to rest on the surface of the aerofoil. On the annulus surface in which the aerofoil is mounted, there is a boundary layer in which the velocity is less than that in the surrounding free stream. Because one can assume that static pressure is constant through the thin boundary layers, a pressure gradient develops towards the aerofoil–annulus interface when the boundary layer stagnation streamlines come to a rest on the aerofoil surface. Under the influence of the pressure gradient, fluid then flows towards the aerofoil–annulus interface. The fluid deflects away from both the aerofoil and the annulus surface in the opposite direction to the free-stream flow until the axial pressure gradient of the free stream deflects the flow out of the stagnation streamline plane. The fluid dissipates along the suction and pressure surfaces with a vortex motion. The vortices that pass either side of the aerofoil leading edge at the aerofoil–annulus interface constitute the suction and pressure surface legs of the horseshoe vortex.

Ishii and Honami (1985) modelled the flow field in the stagnation streamline plane (see Figure 2.5) and postulated the existence of three secondary vortices (a separation vortex, a counter vortex, and a corner vortex), in addition to the dominant horseshoe vortex. Fluid streamlines actively feed the separation vortex, which is much smaller than the horseshoe vortex and therefore has far less impact on the passage flow field. Ireland (1988) measured its effect on annulus surface heat-transfer rate. Think of the corner vortex and the counter vortex as stagnant regions of fluid that acquire vorticity as a consequence of the shear layers in the flow. In practical terms, the counter and corner vortices are of second-order significance in the turbine flow field compared to the horseshoe vortex.

Goldstein and Spores (1988) studied the three-dimensional flow field that exists in the annulus surface region of a cascade and proposed a model of the flow field that develops as a consequence of the passage vortex and the horseshoe vortex (see Figure 2.6). The pressure surface leg of the horseshoe vortex (‘Vortex 1’) drives across the passage to the low-pressure region on the crown of the suction surface where it combines with the passage vortex (‘Vortex 3’), which has the same sense of rotation. Upon reaching the suction surface, this combined vortex, or ‘pressure–passage vortex’, lifts off the annulus surface and continues downstream along the suction surface side of the passage. The motion of the pressure–passage vortex to the crown of the suction surface forms a separation line across the passage with a new boundary layer forming downstream from it. The same pressure gradient that drives the pressure–passage vortex from the pressure surface to the suction surface also generates a down flow on the pressure surface and an up flow on the suction surface. Chapter 7 discusses this effect and presents a two-colour flow visualisation of the B22 turbine vanes.

The suction surface leg of the horseshoe vortex (‘Vortex 2’) proceeds (from its inception) along the aerofoil–annulus interface until it reaches the annulus-surface boundary-layer separation line (region D). At the separation line, the suction-surface leg of the horseshoe vortex lifts off the annulus surface and continues downstream along the suction surface adjacent to the pressure–passage vortex. Both ‘Vortex 2’ and ‘Vortex 3’ most likely lift off the annulus surface as a consequence of the higher average velocities (and therefore lower pressures) located away from the annulus surface along the suction surface.

Goldstein and Spores (1988) postulated the nature of the separation lines that Langston et al. (1977) previously observed (see Figure 2.7). Ireland et al. (1988) graphically illustrated the accuracy of the model by using a cold heat-transfer cascade coated with liquid crystals to measure heat-transfer coefficients over the entire annulus surface region (see Figure 2.8). Because this method generates complete contours as a matter of course, the contours in Figure 2.8 are not numerically smoothed. This ensures preservation of the contour's subtle features.

Ireland (1989) considered Goldstein and Spores' (1988) model and concluded that Ireland et al's (1988) results were consistent. They attributed the rapid rise of heat-transfer coefficients around the aerofoil leading edge to the horseshoe vortex. They attributed the rapid fall, at approximately 15% suction- and pressure-surface length, to 'lift off' of the suction-surface leg (and migration of the pressure-surface leg) of the horseshoe vortex. Moreover, Ireland (1989) attributed the twin-spiked form of the contours around the aerofoil leading edge to the attachment lines of the horseshoe vortex and the separation vortex. Ireland attributed the increase in the heat-transfer coefficients through the cascade to thinning of the annulus surface boundary layer as a consequence of the accelerating flow through the blade passage. The very high heat-transfer levels in the aerofoil wake region were a consequence of the high turbulence levels in that position.

Gregory-Smith and Graves (1983) studied the quantitative effect of secondary flow development on a cascade exit flow field. They used three- and five-hole probes to study the cascade flow field at ten axial locations—from 14% aerofoil axial chord upstream of the cascade to 28% aerofoil axial chord downstream. They observed the migration of the pressure–passage vortex and its lift off from the annulus surface. Gregory-Smith and Graves (1983) defined a loss coefficient, as,

$$C_1 = \frac{P_{01} - P_{0(local)}}{P_{01} - P_1}$$

in which they measured P_{01} and P_1 at a mid-span reference point in the axial plane 14% aerofoil axial chord upstream of the cascade. Contour plots of loss coefficient clearly demonstrated the development of a three-dimensional flow field in the cascade annulus wall region. The contour plot of loss coefficient from the axial plane 87% axial chord downstream of the cascade leading edge (see Figure 2.9) clearly indicates the presence of: (i) loss cores associated with the suction-surface leg of the horseshoe vortex and (ii) the stronger pressure–passage vortex. The overall effect of secondary flow in the annulus surface region was to produce up to ±10% variation in exit flow angle due to the sense of rotation of the two vortices (see Figure 2.10).

Goldstein and Spores' (1988) model proposed that the suction-surface leg of the horseshoe vortex lifts off the annulus surface, with the pressure–passage vortex displacing it. However, Gregory-Smith and Graves' (1983) measurements suggested that the suction-surface leg of the horseshoe vortex remains in the aerofoil–annulus surface junction. This discrepancy is not entirely unexpected because Goldstein and Spores (1988) emphasised that the relative positions of the two vortices are strongly dependent on cascade geometry and overall conditions. Sieverding (1985) supports this assertion.

Binder (1982) studied the fully three-dimensional vane exit flow field and conducted area traverses of total pressure, yaw angle and slope angle in an annular cascade in a plane that was 60% vane axial chord downstream of vane exit. A region of high loss with a loss coefficient (C_1, defined in a similar manner to Gregory-Smith and Graves' (1983) loss coefficient) of 0.2 characterise wakes. Figure 2.11a shows the location of the inner and outer annulus suction surface legs of the horseshoe vortices (Vortices iii and iv) and the location of the pressure–passage vortex (Vortices i and ii) are consistent with Goldstein and Spores' model (1988). One can observe the inner and outer annulus pressure–passage vortex as 0.32 and 0.15 contours of loss coefficient (regions A and B in Figure 2.11a). The high-loss region A is some distance from the outer annulus, whereas region B is close to the inner annulus. This is a consequence of the vane exit radial-pressure gradient, which builds up in annular cascades due to the deflection of flow from the axial through the vanes.

Figure 2.11b shows the area traverse of slope angle, which clearly illustrates the high radial inclination of the wake and region A under the influence of the radial-pressure gradient. Region B cannot move towards the hub as it is already there.

Because the nominal yaw angle of Binder's (1982) annular cascade was 21°, one can identify the centres of the vortices on the yaw angle area traverse (Figure 2.11c) as design-value contours of yaw, with over- and under-turned flow above and below the vortex (or vice versa, depending on the vortex sense of rotation). One can see the centre of Vortex ii on the yaw angle plot which Binder (1982) explained as being due to the breakdown of the vortex (as a consequence of viscous action) into a non-rotating high-loss region.

Binder (1985a), who measured turbulence levels at the vane exit using a laser-2-focus velocimeter, observed high levels of flow unsteadiness in the wakes and secondary flow loss cores. The same author subsequently investigated the effect of the vane exit flow field on a downstream rotor (see below, Section 2.3).

The secondary flow models and experimental work above clearly demonstrate the three-dimensional nature of the flow field leaving the B22 vanes. The combination of secondary flows and wakes produces a circumferential periodic flow field from vane to vane, which a downstream rotor will pass through. Chapter 7 considers the magnitude of the B22 vane secondary flow on the inner and outer annulus. Section 2.3 considers the effect of vane wakes and secondary flows on the flow field of a downstream rotor as well as the secondary flow mechanisms engineers' associate with a rotating blade passage and the transition from a stationary frame of reference to a rotating frame of reference.

2.3 UNSTEADY FLOW PHENOMENA

An understanding of the unsteady flow phenomena found in a turbine stage is essential for a full appreciation of the requirements of a full-stage experimental facility. Hodson (1984a) found that profile loss from a rotor-blade mid-height section was 50% greater than that of the same section in cascade. He ascribed the difference to the periodic tripping of the blade boundary layer by vane wakes. Hodson's (1984a) work, which was concerned with the development of blade boundary layers under the influence of unsteady flow outside the influence of secondary flows, was therefore essentially two dimensional. Doorly's work (1983, 1985a, 1985b) demonstrated the dramatic effect that vane wakes can have on a blade boundary layer (see Section 2.1) and his observation of the periodic tripping of the blade boundary layer as a consequence of wake passing was consistent with Hodson's (1984a) conclusions.

Hodson (1984b) demonstrated the effect of vane wakes on the blade-passage flow field and used an inviscid blade-to-blade prediction code with a prescribed velocity distribution through the wake, which moved across the computational mesh inlet at blade relative speed. This provided a true picture of the wake-generated unsteadiness by subtracting the steady flow solution from the unsteady flow solution (see Figure 2.12). The effects of the wakes, which were clearly responsible for the unsteady features of the flow field, were quite apparent. Low-entropy contours are drawn at the edge of the wakes to make them more visible. The low velocities in the wake regions cause them to become 'negative jets' when one subtracts the steady-state solution. Letcourt (1965) first mooted this concept. As the wake enters the blade passage it is bowed because the mid-passage convection velocity is much greater than that near the leading-edge stagnation point. This effect is in close agreement with Doorly's reports (1983) (illustrated in Figure 2.1). The action of the wake, as a 'negative jet', results in migration of fluid from the pressure surface to the suction surface of the blade passage. The migration of wakes towards the suction surface results in a migration of fluid towards the pressure surface to replace the migrated wake fluid. The net result of the transport of fluid is the establishment of two vortices (of opposite sign), one of which lies on either side of the wake. Hodson's (1984b) predictions of unsteady pressures on the pressure and suction surfaces were in reasonable agreement with those reported in Hodson (1984a). This suggests that the prediction was a good representation of the actual flow field.

Binder (1985a) used a laser-2-focus velocimeter to measure instantaneous fluctuations in velocity levels in a rotor-blade passage. As wakes convected through the blade passage, the number of random fluctuations in velocity more than doubled from inlet to mid-passage, which the author attributed to the breakdown of large vortices. Binder (1985b) subsequently utilised the laser-2-focus velocity technique to investigate this increase in the number of random velocity fluctuations observed in wake segments passing through a blade passage. The author proposed that the energy of the vortex motion converted into random fluctuating energy during breakdown, thus causing a breakdown of the vane secondary flows cut by the downstream rotor. The vane secondary flow vortices are cut in a similar manner to wakes by a downstream rotor and are similarly distorted as they pass through the blade passage. The rotation of the vortex creates a low-pressure zone at its centre, which fills from the pressure surface due to the higher pressure in that position. The combined filling and distortion of the secondary flow segments result in rapid breakdown, thus causing the observed increase in turbulent energy. Binder et al. (1986) further reported laser-2-focus measurements which confirmed the mechanisms.

Dring and colleagues at the United Technologies Research Centre (Dring & Joslyn, 1981, 1983; Dring et al., 1982) have conducted considerable work on the three-dimensional and unsteady turbine flow field. They performed the work on a 1.52 meter diameter large-scale rotating rig (LSRR), which permitted extensive instrumentation in the stationary and rotating frame at realistic Reynolds numbers, but low Mach numbers. With a typical vane exit

Mach number of 0.2, researchers can use the facility to study only those phenomena that are insensitive to compressible effects.

Dring and Joslyn (1981) utilised the LSRR's capacity to allow detailed measurements in the rotating frame in an investigation of turbine rotor blade flows. The researchers performed flow visualisation on the blade suction and pressure surfaces, which indicated strong radial flows towards the tip on the pressure surface and reduced radial flows towards the hub on the suction surface. These effects were independent of tip clearance, from which Dring and Joslyn (1981) deduced that tip-clearance effects were not responsible for the observed behaviour of the flow.

Dring and Joslyn (1983) subsequently undertook further studies of the mechanisms responsible for radial flows on the blade suction and pressure surfaces. Based on a consideration of blade-passage relative vorticity, the authors postulated the existence of a 'relative eddy' in the blade passage. In essence, because the blade speed is greater at the blade tip than at the hub for a uniform stationary frame inlet flow, there is a smaller blade relative inlet angle at the tip than at the hub. The consequence of this is a net relative velocity vector from the pressure surface to the suction surface at the tip (and vice versa at the hub). This has the effect of establishing a 'relative eddy' as a consequence of the move from stationary to rotating frames of reference.

Dring et al. (1982) and Blair et al. (1989) used the LSRR to study the rotor–stator interaction that occurred as the axial spacing between vane and blade rows changed. Engineers divide the study of rotor–stator interaction into two separate areas: (i) potential flow (inviscid) and (ii) viscous interactions (wakes and secondary flows). Parker and Watson (1972) considered potential flow effects and concluded that they were negligible (with a sensibly non-periodic blade inlet flow field) for a rotor–stator spacing of more than 30%

blade axial chord. Dring et al. (1982) conducted static pressure measurements on both vane and blade with 15% and 65% axial gap and concluded that unsteady pressures were significantly higher (on both vane and blade mid-height sections) at 15% spacing than they were at 65%. Blair et al. (1989) continued Dring et al's work (1982) by measuring blade and vane steady heat-transfer rates at vane and blade mid-height sections for 15% and 65% axial gap. The authors concluded that the rotor-stator spacing did not affect the steady heat-transfer rates which suggested that they were insensitive to the magnitude of unsteady pressure levels.

Parker and Watson (1972), Dring et al. (1982), and Blair et al's (1989) work suggests that, for the 25% blade-chord axial gap at mid-height that is present in the B22 turbine, potential flow effects will be secondary to the viscous interactions of wake and secondary flow cutting.

The study of tip-clearance losses in an unshrouded turbine (such as the B22 turbine) forms a major area of research in its own right. The extent of this work makes it impossible to present a full review here; however, the mechanisms responsible for the formation of a tip-leakage vortex are of immediate relevance to the present study.

Dring and Joslyn (1981) conducted a rotor relative total pressure area traverse through a blade wake (see Figure 2.13), which showed that the loss in the tip-leakage vortex was 50% greater than that in rotor secondary flows, thus highlighting the significance of this loss mechanism. Bindon (1988) also studied tip-clearance losses and made detailed over-tip measurements in a linear cascade of 0.456-m chord blades. The large scale of Bindon's (1988) cascade facilitated detailed measurements in the tip-clearance region from which the author was able to propose a model for tip-leakage flows (see Figure 2.14). Bindon's (1988) static pressure measurements and flow visualisation indicated the presence of two dominant flow features in the tip region: (i) a separation bubble due to the sharp edge between pressure surface and tip and (ii) a leakage jet that ejected flow into the lowest pressure region of the suction surface over the crown. The jet's high velocity drove the flow in the separation bubble towards the leakage jet and the consequent low pressure in that position. Bindon (1988) proposed that the major cause of tip-clearance loss was the entrainment of high-loss fluid from the separation bubble into the leakage jet. The author reasoned that if there were a way to eliminate the separation bubble, this loss would substantially reduce.

Morphis and Bindon (1988) studied the effect of blade edge radius on the separation bubble. Flow-visualisation techniques established that a blade edge radius of 2.5-times the tip-clearance gap eliminated the separation bubble. Moreover, although the separation bubble increased loss, it also caused a blockage, which reduced the effective tip clearance. Eliminating the separation bubble had the consequence of increasing the strength of the leakage jet. Denton and Cumpsty (1987) considered loss mechanisms in turbomachines and concluded that the effects of tip leakage are twofold. First, the force excerted by fluid on the blade reduces which means that less work is done. Second, the leaking flow mixes with the flow that has passed through the blades and thus generates loss. Morphis and Bindon (1988) recognised that elimination of the separation bubble reduces mixing losses because high-loss fluid no longer entrained into the leakage jet; however, the increased flow rate over the tip reduced the work done. Morphis and Bindon (1988) envisaged the next phase of work as quantifying the effect of eliminating the separation bubble. At the time of writing, they had not published the results of this projected work.

The turbine flow field is not only three dimensional, but also unsteady. There are little data in the literature from experimental facilities that are capable of adequately modelling all three-dimensional and unsteady effects under engine-representative conditions. The two facilities that are capable of making measurements in the rotating frame at engine-representative conditions are at MIT (described by Epstein et al., 1984) and at Calspan (described by Dunn et al., 1984).

The MIT facility works on a blow-down principle using a working fluid of Argon and Freon-12, with a run time of approximately 0.3 seconds. Guenette et al. (1988) used this facility to measure mean and unsteady heat-transfer rates at the blade mid-height section. Ashworth et al. (1985) and Rigby (1989) studied the same blade mid-height section using Doorly's (1983) wake generator, which enabled Guenette et al. (1988) to compare steady and unsteady heat-transfer rate measurements obtained in a linear cascade with those in a full-stage turbine. In general, agreement between the results of Guenette et al. (1988) and those of Ashworth et al. (1985) and Rigby (1989) was excellent, with the exception of the last part of the suction surface where full-stage results were 40% lower. Guenette et al. (1988) concluded that rotating, three-dimensional and blade-row interaction effects did not explain the differences between the cascade results and the full-stage results. The authors suggested further work.

Dunn et al's (1984) description of the Calspan facility uses a shock tube to supply air at the required temperature and pressure to simulate engine conditions for a run time of approximately 20 ms. Dunn and Hause (1982) used this facility to investigate the effect of a downstream rotor on vane heat-transfer rates. They conducted a test series with a rotor in place at a Reynolds number of 1.67×10^5, compared with 1.25×10^5 without a rotor; nevertheless, the results were comparable. Dunn and Hause (1982) concluded that the heat-transfer rates on the vane were greater with a rotor than without. Dunn (1984) continued Dunn and Hause's (1982) work on the same turbine—measuring vane heat-transfer rates with and without vane film cooling, and with and without a rotor present. They principally concluded that the presence of a downstream rotor had a disruptive effect on vane cooling, thus reducing its effectiveness.

Dunn (1984) continued his work (1986) and investigated the effect of vane cooling on the downstream rotor. He (1986) concluded that vane coolant flow resulted in an increase in blade leading-edge heat-transfer rate.

In Dunn et al's (1988) study, they identified the periodic tripping of the blade boundary layer by vane wakes, which was consistent with Doorly (1983) and Hodson's (1984a) results. Dunn et al. (1988) also investigated the effect of increasing rotor–stator spacing and demonstrated that the character of the blade unsteady heat transfer became more diffuse with increased spacing.

Hilditch (1989) used the new turbine test facility containing the B22 turbine to measure heat-transfer in the rotating frame. Many instrumentation requirements for the measurement of unsteady heat transfer in the rotating frame are common to the measurement of unsteady pressures. Shelly (1988) describes miniature Kulite pressure transducers and the method to implant them in a turbine blade. These issues are currently part of an ongoing experimental program in the B22 turbine facility to measure blade relative unsteady and steady heat transfer and pressure.

CHAPTER THREE

EXPERIMENTAL ARRANGEMENT

3.1 INTRODUCTION

3.1.1 Advantages of a transient turbine test facility

The launch of a new gas turbine by an engine manufacturer represents the successful conclusion of an intense cycle of design, build, development and redesign. During this process, the testing of 'prototype' or 'demonstrator' engines is a vital step in ensuring ultimate success.

Conventional turbine test facilities have often been built to operate continuously at full-scale engine operating conditions of mass flow, temperature and pressure. Problems with extracting detailed measurements from such a facility become steadily greater as the turbine inlet temperature increases, resulting in the facility’s role becoming one of design validation. Engineers do not require a full scale facility to test engines; rather, they require a less complex facility to obtain the detailed measurements they require for the derivation, development and validation of theoretical design methods.

Engine manufacturers favour the use of advanced computational methods for aero-thermo dynamic design of engine components, as it reduces the time to produce a design and therefore reduces an engine's 'launch cost'. The validation of the prediction codes at correct engine operating conditions requires detailed measurements that would be difficult to make in a full scale, hot, continuous turbine test facility. It is in this area where a transient turbine test facility can be of greatest advantage.

Schultz, et al. (1987) discussed the role of short duration and transient facilities in gas turbine research and concluded that aerodynamic and heat transfer measurements made in these facilities were in excellent agreement with measurements they took in a high pressure, high temperature continuous facility. Schultz, et al. estimated the overall power requirement for short duration facilities at one fortieth of those for a similar continuous facility, substantially reducing overall cost, whilst retaining correct engine parameter simulation (see Section 3.2). The reduced levels of total temperature and total pressure possible in a short duration or transient turbine test facility required to achieve representative turbine conditions (see Section 3.3) allow for required detailed measurements for prediction code validation.

The low operating cost of short duration facilities, combined with their suitability for the derivation, development and validation of theoretical design methods, makes them ideal for use in a university environment. The equivalent continuous facility capital and running cost would be high and beyond the resources of all but the best equipped research group or engine manufacturer.

3.1.2 The O.U.E.L. Isentropic Light Piston Tunnel facility

Jones & Schultz (1970) conceived the Isentropic Light Piston Tunnel (ILPT) as a short duration air supply for a working section containing a cascade of aerofoils. Schultz et al. (1977) describes the particular facility that the author utilised for this thesis. The ILPT concept is of a free piston compressor, in which the working fluid compresses isentropically over a period of approximately one second to the required temperature and pressure, then passes through a working section under steady state conditions for a period of order 0.25 seconds. A high pressure reservoir, (see Figure 3.1), connects via a throat and valve to a pump tube and drives the light piston down the pump tube, compressing the gas in front of it. A fast acting valve (the Annular Gate Valve, or AGV) separates the pump tube and working section and opens once it reaches the required pump tube temperature and pressure. When the AGV opens, test gas conditions remain constant if the volumetric flow rate out of the pump tube equals that flowing into it from the high pressure reservoir. When the ILPT operates under these conditions, it is said to be “matched”.

Total pressure and temperature in the pump tube immediately prior to opening the AGV can be varied vary by changing the initial tube pressure and compression ratio. Engineers fit the working section with an adjustable second throat that allows calibrated changes too be made to the working section exit Mach number. Working section inlet total temperature, pressure and exit Mach number are, therefore, independently variable.

3.1.3 Proposed mode of operation

In the programme of work reported in this thesis, the author's aim was to extend Doorly's work (1983) (see Section 2.1). Doorly (1983) simulated wake passing using a cascade of two-dimensional mid-height blades sections. A cascade is useful for studying wake passing in isolation however a full stage turbine is required to simulate all aspects of the turbine flow field. As the authors aim was to extend Doorly's work, a full stage turbine was mounted in the ILPT's working section (see Figure 3.2). The change in working section from cascade to a full turbine stage was described by Ainsworth et a1. (1988) & (1989). The ILPT was treated by Ainsworth et a1. (1988) & (1989) as a short duration air supply, able to supply air at the required temperature and pressure to achieve representative turbine operating conditions in the working section to which it is connected (see Figure3.3).

The facility's mode of operation consisted of a pre-run set up procedure, facility operation and finally ILPT operation. The pre-run set up procedure commenced by closing the AGV and evacuating the working section and dump tank. The author then set the initial pump tube pressure and high pressure reservoir pressure. The author then accelerated the turbine to a speed of approximately 6,500 rpm using an air motor (see Figure 3.4). The author then cut power to the turbine causing the turbine to decelerate under the action of bearing losses (Point A, Figure 3.4). ILPT operation commenced when it 'fired'. Engineers use the term to describe the automatic sequence of events after pressing the 'fire' button. The valve between high pressure reservoir and the pump tube opens, driving the piston down the pump tube until the gas ahead of the piston reaches the required temperature and pressure. The author then opened the AGV to allow air into the evacuated working section which triggered the ILPT low speed data acquisition system (see Section 3.5.1).

As a compressor or brake was not used to absorb power developed in the turbine, the turbine accelerated until the piston reached the end of the pump tube, and mass flow rate through the working section stopped (point B, Figure3.4). The author chose the initial turbine speed to ensure the turbine passed through its design speed during ILPT run time. As the turbine reached design speed, it triggered a high speed data acquisition system (see Section 3.5) that took data from blade mounted instrumentation for seven milli seconds. During the data acquisition period, the turbine speed changed by less than one percent, therefore the author concluded that change in turbine speed could be neglected during high speed data acquisition.

3.2 DYNAMIC SIMILARITY REQUIREMENTS

3.2.1 Derivation of turbine non-dimensional groups

For the high pressure stage of a gas turbine, full engine operating conditions include a turbine entry temperature of the order of 1,800 K, making the environment through the turbine very hostile and therefore, a difficult one in which to make detailed measurements. Horlock (1966) considered the relevant variable parameters to the performance of an adiabatic axial flow turbine (see Table 3.1) and regarded turbine mass flow rate, efficiency and stagnation temperature drop of gas passing through the turbine as dependent parameters of turbine performance which we can express as functions of the independent variables.

$$\dot{m}, \eta, \Delta T_0 = f\{P_{01}, P_{05}, T_{01}, N, l, R, \gamma, \mu\} \qquad - \quad 3.1$$

According to the Buckingham π Theorem, the number of independent dimensionless groups that one can employ to describe a phenomenon known to involve n variables, is equal to the number n - r, where r is the number of basic dimensions one needs to express the variables dimensionally. The number of independent variables in Equation 3.1 is ten (the

Table 3.1
Variables affecting turbine performance
Subscripts defined Figure 3.5

$\dot{m}$	*Gas mass flow rate*	*kg/s*
η	*Turbine efficiency*	
P_{01}	*Vane inlet total pressure*	*Pa*
P_{05}	*Turbine exit total pressure*	*Pa*
T_{01}	*Vane inlet total temperature*	*K*
ΔT_0	*Total temperature drop of gas passing through the turbine*	*K*
N	*Rotational speed*	*rpm*
l	*Linear dimension*	*m*
μ	*Gas dynamic viscosity*	*kg/ms*
R	*Gas constant*	M^2/s^2K^1
γ	*Specific heat ratio*	

author will demonstrate the dependence of the eleventh, η), the basic dimensions of which are mass, length, time and temperature. The Buckingham π Theorem, therefore, predicts six independent dimensional groups. Applying non dimensional analysis to Equation 3.1 yields,

$$\frac{\dot{m}\sqrt{RT_{01}}}{P_{01}l^2},\eta,\frac{\Delta T_0}{T_{01}} = f\left\{\frac{N\ l}{\sqrt{RT_{01}}},\frac{P_{01}}{P_{05}},\frac{\dot{m}}{\mu\ l},\gamma\right\} \qquad - \quad 3.2$$

One can derive efficiency, η, if $\Delta T_0 / T_{01}$ and P_{01} / P_{05} are known as,

$$\frac{P_{01}}{P_{05}} = \left\{1-\frac{\Delta T}{\eta T_{01}}\right\}^{\frac{\gamma}{\gamma-1}}$$

It is common practice to drop some constants from Equation 3.2, leaving non and 'quasi' non dimensional groups. Engineers also define pressure ratio as upstream total pressure divided by downstream static pressure, as a reliable measurement of downstream static pressure is easier to make than downstream total, therefore Equation 3.2 reduces to,

$$\frac{\dot{m}\sqrt{T}}{P}, \frac{C_p \Delta T}{T} = f\left\{\frac{N}{\sqrt{T}}, P_r, \mathrm{Re}, \gamma\right\} \qquad - \quad 3.3$$

Engineers use the six non and quasi non dimensional groups in Equation 3.3 to define the B22 turbine's 'design point'. They can realistically test a turbine at its design point by matching the six critical non and quasi non dimensional groups regardless of the absolute levels of the turbine inlet temperature and pressure. By matching turbine design point non and quasi non dimensional groups at reduced total temperature and pressure levels, engineers can achieve a realistic simulation of the turbine flow field with an environment through the turbine suitable for making detailed measurements.

3.2.2 The B22 turbine design point

The B22 turbine is a 0.62 scale Rolls-Royce plc model high pressure (H.P.) turbine, with a design point typical of a high bypass ratio civil gas turbine. Table 3.2 defines the turbine operating point, as specified by Rolls-Royce plc. Table 3.3 defines essential ILPT and turbine geometry.

The specification of vane and blade exit Mach numbers is equivalent to specifying a turbine pressure ratio. The specific heat ratio, γ; should be 1.275 (the 'engine' γ) to match that of the hot combustion products encountered in a high pressure turbine. The ratio of specific heats of air near ambient temperature (the 'rig' γ) is 1.4, approximately 11% high. To correctly model engine γ, Epstein et al. (1984) used a mixture of Argon and Freon-12 in a blow down facility containing a full stage turbine. The highly toxic nature of Freon-12, however, makes it an unpopular choice of working fluid.

If one uses air as a working fluid in a turbine test facility, the discrepancy between rig and engine γ will result in the incorrect modelling of the engine static pressure and heat transfer rate (as Nusselt number is a function of Reynolds number).

Table 3.2
The B22 turbine operating point

Reynolds number, Re *(Based on vane exit conditions and mid-height axial chord)*	$\frac{\rho_2 U_2 c}{\mu_2} = 2.7x10^6$	
Vane Mach number, M_2 *(Mid-height isentropic vane exit)*	$\frac{V_2}{a_2} = 0.946$	
Blade Mach number, M_4 *(Mid-height isentropic blade relative exit)*	$\frac{V_4}{a_4} = 0.959$	
Gas to wall temperature ratio, T_r	$\frac{T_1}{T_w} = 1.3$	
Turbine specific speed, S_s	$\frac{N}{\sqrt{T_{01}}} = 435.885$	*rpm/K*$^{1/2}$
Turbine mass flow number, M_f	$\frac{\dot{m}\sqrt{T_{01}}}{P_{01}} = 7.03x10^{-4}$	*m s K*$^{1/2}$
Turbine specific work number, W_f	$\frac{C_p \Delta T_0}{\Delta T_{01}} = 216.3$	*J/kg K*

Table 3.3
Turbine and ILPT geometry

Vane throat area	$A^* = 0.0185322$	m^2
Vane mid-height exit angle	$\alpha = 70$	*deg*
Blade mid-height exit angle	$\beta = -63.13$	*deg*
Vane mid-height axial chord	$c = 0.0312$	*m*
ILPT tube volume	$V_t = 1.604$	m^3

An incorrect static pressure field will have a secondary effect on blade and annulus surface boundary layer growth and transition point. The change in boundary layer growth will affect secondary flow development and the movement of the boundary layer transition point will have a non-linear effect on heat transfer rate. The correct engine γ is crucial to an accurate simulation of the turbine flow field.

The primary objective of the new working section was not, however, a rigorous simulation of every aspect of the turbine flow field, but to provide detailed measurements of the flow field required for the derivation, development and validation of theoretical design methods. The computer codes that constitute an engine manufacturer's theoretical design method are flexible enough to predict the turbine flow field using rig total temperature and pressure levels. Engineers well understand and can accurately predict the variation of γ due to the presence of combustion products. Therefore, engineers can use a theoretical design method to predict the rig flow field and validate against measured rig data. Once they establish that the theoretical design method can accurately predict the rig flow field, engineers use it with confidence to predict the engine flow field.

As a transient turbine test facility can fulfil its primary requirement whilst operating at a γ other than engine γ, the author decided to use air as a working fluid. The advantages the use of air offers over Freon-12 in ease of storage, handling and availability are enormous. Section 7.3.2 considers the error in flow field simulation as a consequence of this decision.

Table 3.2 fully specifies the turbine design point with the exception of γ and with the addition of a gas to wall temperature ratio. The non and quasi non dimensional groups that comprise the turbin design point are independent of temperature ratio. As such the ILPT can be set up to achive design point non and quasi non dimensional groups within the turbine at any temperature ratio (within the facility's operating envelope, see Section 3.4.1). Fitt et a1. (1986) studied the effect of temperature ratio on heat transfer rate and concluded that for constant free stream Reynolds number, heat transfer coefficient was a function of temperature ratio. Hilditch (1989) utilised Fitt's results to correct heat transfer measurements made on the B22 turbine to facilitate direct comparison with the results of other workers (most notably Doorly (1983), Doorly & Oldfield (1985) and Doorly et a1. (1985)). Fitt's correlation is reliable, making engineers' choice of temperature ratio in the B22 design point flexible. The author chose a temperature ratio of 1.3 to give a good compromise between run time and piston oscillations (see Section 3.4.2).

3.3 ACHIEVEMENT OF THE B22 TURBINE DESIGN CONDITION

3.3.1 Philosophy of the experiment

The turbine non and quasi non dimensional groups (see Table 3.2) characterise the turbine design point. The author had to realise these during the ILPT run time to simulate the turbine flow field accurately. To achieve design conditions, the author used design values of the non and quasi non dimensional groups as a starting point from which to calculate required total temperature, pressure, mass flow rate, turbine speed and run time. Once the author established these basic parameters, he found turbine power, acceleration and speed change during ILPT operation. Figure 3.5 illustrates the inter relationship between the design point non and quasi non dimensional groups and the important derived quantities.

Known working section inlet total temperature and pressure allowed the author to calculate initial required pump tube conditions. The prediction of turbine speed change during ILPT operation enabled the author to estimate a suitable pre-run turbine speed in order to achieve turbine design speed during ILPT operation. Therefore, the author calculated all necessary parameters for ILPT operation to establish the suitability of the ILPT as a short duration air supply. Design pressure levels were well within the ILPT's operating range, with an ILPT – working section facility run times of similar length to those of previous workers (see Section 2.1). Predicted ILPT performance (see Section 3.4) indicated that the facility could achieve an acceptable range of conditions in a working section fitted with the B22 turbine using the ILPT as a short duration air supply.

3.3.2 Derivation of facility parameters from the turbine design point

Figure 3.6 denotes the conditions at vane inlet, vane exit, blade inlet and blade exit using subscripts from 1 to 5. We can calculate the total pressure, P_{02}, necessary to achieve design Reynolds number at design temperature ratio using vane exit conditions. Assuming an ambient temperature, T_w, of 288 K and a gas to wall temperature ratio, T_g/T_w of 1.3 gives a gas temperature, T_{02}, of 374 K.

$$\textit{Using} \quad \frac{T_{02}}{T_2} = 1 + \frac{\gamma - 1}{2} M_2{}^2 \quad \textit{gives} \quad T_2 = 317.56\ K$$

$$\textit{Also} \quad M_2 = \frac{U_2}{a_2} = \frac{U_2}{\sqrt{\gamma R T_2}} \quad \textit{gives} \quad U_2 = 377.92\ m/s$$

We can find viscosity, μ, using Sutherlands Law:

$$\mu = \mu_{ref} \left[\frac{T}{T_{ref}} \right]^{1.5} \left[\frac{T_{ref} + 110}{T + 110} \right]$$

Using a reference temperature and viscosity, T_{ref}, and μ_{ref}, of 273 K and 1.7235x10^{-5} Kg/ms respectively, at vane exit static temperature gives a viscosity, μ_2, of 1.9369x10^{-5} Kg/ms. One can determine flow density at vane exit from design Reynolds number, as one can express Reynolds number, Re, as $\rho_2 U_2 c/\mu_2$, therefore one can express density, ρ_2, as $Re\mu_2/U_2c$ giving a density of 4.943 Kg/m^3. One can express vane exit static pressure, P_2, as $\rho_2 R T_2$, giving a vane exit static pressure of 4.505x10^5 Pa. Using the relationship,

$$P_{02} = P_2 \left[1 + \frac{\gamma - 1}{2} M_2{}^2 \right]^{\frac{\gamma}{\gamma - 1}}$$

gives a vane exit total pressure, P_{02} , of 8.02x10^5 Pa. As the author calculated the vane exit conditions using the isentropic mid-height vane exit Mach number, one can assume the vane exit total temperature and pressure to equal vane inlet temperature, T_{01}, and pressure, P_{01}. The ILPT must achieve these conditions of temperature and pressure. One can calculate the initial ILPT piston tube pressure for the required final total temperature and pressure by assuming the initial gas temperature, T_i, is at ambient temperature, 288 K. For isentropic compression of ideal gas,

$$\frac{P_i}{P_{01}} = \left[\frac{T_i}{T_{01}}\right]^{\frac{\gamma}{\gamma-1}}$$

Therefore, the author required an initial tube pressure, P_i, of $3.2\text{x}10^5$ Pa.. One can determine the required turbine mass flow rate through the stage from the design mass flow number,

$$\frac{\dot{m}\sqrt{T_{01}}}{P_{01}} = 7.03x10^{-4} \qquad \therefore \qquad \dot{m} = 7.03x10^{-4}\frac{P_{01}}{\sqrt{T_{01}}}$$

The calculated vane upstream total conditions show that the design mass flow rate, $\dot{m}$, was 29.13 Kg/s. One can calculate the power generated by the turbine at design conditions from the specific work function as,

$$P_w = \dot{m}C_p\Delta T\,, \quad and \quad \frac{C_p\Delta T_0}{T_{01}} = 216.3 \quad therefore \quad P_w = 216.3T_{01}\dot{m}$$

$$\therefore \quad P_w = 2.36x10^6\ W$$

Using Jones' method (1973), one can show facility run time, τ_{run}, as 0.213 s,

$$\tau_{run} = \frac{V_t}{M_f}\frac{1}{R\sqrt{T_i}}\left[\frac{T_i}{T_{01}}\right]^3$$

One can show the turbine design speed as 8,434 rpm from design specific speed,

$$\frac{N}{\sqrt{T_{01}}} = 435.885$$

The turbine speed will change during facility run time as the power generated by the turbine will cause it to accelerate,

$$P_w = Q\omega \quad and \quad Q = I\dot{\omega} \quad therefore \quad \dot{\omega} = \frac{P_w}{\omega I}$$

The author measured the turbine's moment of inertia (see Section 5.4) at 1.64 Kgm^2. To a first order approximation the turbine power remained constant during the facility run time. By assuming constant turbine power, the turbine's angular acceleration, $\dot{\omega}$, was calculated to be 1,630 rad/s^2. Assuming constant turbine power implies constant turbine acceleration. By assuming constant turbine acceleration the turbine speed change during facility run time was calculated to be 3,320 rpm. For an initial turbine speed of 6,500 rpm, design speed occurs in the middle of the facility run time and reaches a final turbine speed of approximately 9,800 rpm as the piston reaches the end of the ILPT. Turbine power will reduce at off design conditions, so the calculated turbine speed rise may be high, and therefore a worst case estimate.

One can now calculate the blade relative conditions at the blade inlet and exit. Static temperature and pressure are conserved in the transition from a stationary to rotating frame of reference, $T_2 = T_3$, and $P_2 = P_3$, in order to find the mid-height blade Mach number M_{b2},

$$M_{b2} = \frac{U_b}{a_3} = \frac{\omega\, r}{\sqrt{\gamma R T_3}} = 0.63$$

Figure 3.7 considers the blade relative Mach number M_3, by examining the blade mid-height velocity triangle,

$$M_3^{\ 2} = M_2^{\ 2} + M_{b2}^{\ 2} - 2M_2 M_{b2} \sin\alpha = (0.415)^2$$

One can calculate the blade inlet relative total temperature and pressure using M_3,

$$P_{03} = P_2\left[1 + \frac{\gamma-1}{2} M_3^{\ 2}\right]^{\frac{\gamma}{\gamma-1}} = 5.072x10^5\, Pa$$

$$T_{03} = T_2\left[1 - \frac{\gamma-1}{2} M_3^{\ 2}\right] = 328.5K$$

Therefore, one can calculate the blade relative temperature ratio,

$$\frac{T_{03}}{T_w} = \frac{328.5}{288} = 1.14$$

Engineers base the rotor relative exit isentropic Mach number M_4 on blade relative inlet total conditions; therefore, one can calculate using M_4 blade relative exit static conditions,

$$T_4 = \frac{T_{03}}{\left[1 + \frac{\gamma-1}{2} M_4^{\ 2}\right]} = 277.5K$$

$$P_4 = \frac{P_{03}}{\left[1 + \frac{\gamma-1}{2} M_4^{\ 2}\right]^{\frac{\gamma}{\gamma-1}}} = 2.81x10^5\, Pa$$

Using the blade relative exit static temperature, one can calculate Mach number at blade exit,

$$M_{b4} = \frac{U_b}{a_4} = \frac{\omega r}{\sqrt{\gamma R T_4}} = 0.675$$

Using the mid-height blade exit angle, β, M4, and Mb4, one can construct an exit velocity triangle for the blade (see Figure3.7), from which one can calculateM5 and ψ,

$$M_5{}^2 = M_4{}^2 + M_{b4} - 2M_4 M_{b4} \sin\beta = (0.47)^2$$

$$\psi = \sin^{-1}\left[\frac{M_4 \cos\beta}{M_5}\right] = 67.25^\circ$$

$$\therefore \quad \delta = -22.75^\circ$$

One can calculate the isentropic blade exit total temperature and pressure using M5, and assuming preservation of static conditions from the rotating to stationary frame of reference, T5 = T4, and P5 = P4, therefore,

$$P_{05} = P_5\left[1 + \frac{\gamma - 1}{2} M_5{}^2\right]^{\frac{\gamma}{\gamma-1}} = 3.27x10^5\, Pa \quad (isentropic)$$

$$T_{05} = T_5\left[1 + \frac{\gamma - 1}{2} M_5{}^2\right] = 289.8K \quad (isentropic)$$

One can also find the exit total temperature using the turbine specific work number,

$$\frac{C_p \Delta T_o}{T_{01}} = 216.3 \qquad \therefore \qquad \Delta T_0 = \frac{216.3 T_{01}}{C_p}$$

$$therefore \quad \Delta T_0 = 80.58K = T_0 - T_{05}$$

$$\therefore \quad T_{05} = 293.8K$$

The discrepancy between the value of T05, calculated from specific work number and isentropic Mach numbers, occurs as a consequence of the assumed blade efficiency in the specific work number. Rolls-Royce plc quote a design turbine stage efficiency of 87% and a design blade efficiency, ηb, of 95%. It was not appropriate to consider turbine loss mechanisms in a first order analysis of the turbine design point; however, one can demonstrate the consistency of specific work number with a blade efficiency of 95%,

$$\frac{C_p \Delta T_0}{T_0} = \frac{C_p [T_{01} - T_{05}]}{T_{01}}$$

where $T_{05} = 289.8\ K$ *(isentropic)*

$$\therefore \quad \frac{C_p \Delta T_0}{T_0} = 227.1\ J/Kg\ K\ (isentropic)$$

$$\frac{C_p \Delta T_0}{T_0} = 216.3\ J/Kg\ K\ (Rolls\text{-}Royce\ quoted)$$

$$\eta_b = \frac{\Delta T_{0(actual)}}{\Delta T_{0(ideal)}} = \frac{216.3}{227.1} = 0.952$$

$$\therefore \quad \eta_b = 95.2\%$$

Table 3.4
ILPT and turbine design condition parameters

Vane exit mid height total temperature,	T_{02}	374.4 *K*
Vane exit mid height static temperature,	T_2	317.56 *K*
Blade relative temperature ratio,	T_r	1.141
Vane exit mid height total pressure,	P_{02}	$8.02x10^5$ *Pa*
Vane exit mid height static pressure,	P_2	$4.505x10^5$ *Pa*
Vane exit mid height gas density,	ρ_2	*4.943 Kg/m³*
Vane exit mid height speed of sound,	U_2	337.92 *m/s*
Initial pump tube pressure,	P_i	$3.2x10^5$ *Pa*
Gas mass flow rate,	$\dot{m}$	29.13 *Kg/s*
Turbine power,	P_w	$2.36x10^6$ *W*
ILPT run time,	τ_{run}	0.2132 *s*
Turbine design speed,	N	8,434 *rpm*
Pre run turbine speed,	N_i	6,500 *rpm*
Post run turbine speed,	N_f	9,800 *rpm*

Rolls-Royce plc defines the turbine stage pressure ratio, P_r, as inlet total pressure divided by exit static,

$$P_r = \frac{P_{01}}{P_5} = 2.854$$

The above calculation of the value of turbine stage pressure ratio matches closely the Rolls-Royce plc supplied value of 2.872. Table 3.4 summarises turbine design conditions.

3.4 PREDICTED FACILITY PERFORMANCE

3.4.1 Facility operating envelope

The turbine design point gas to wall temperature ratio is 1.3; however, the ILPT facility could achieve all non and quasi-non dimensional groups over a range of temperature ratios. In practice, a range of gas to wall temperature ratios from 1.0 to 1.5 was practical (see Figure3.8 and Table 3.5).

Table 3.5
Facility parameters at turbine design condition
for a range of gas to wall temperature ratios

Facility Parameters	*Temperature Ratio (T_g/T_w)*		
	1.0	1.3	1.5
Initial Tube Pressure	$5.73x10^5$ *N/m*^{2}	$3.20x10^5$ *N/m*^{2}	$2.32x10^5$ *N/m*^{2}
Initial Tube Temperature	288 *K*	288 *K*	288 *K*
Final Tube Pressure	$5.73x10^5$ *N/m*^{2}	$8.02x10^5$ *N/m*^{2}	$9.61x10^5$ *N/m*^{2}
Final Tube Temperature	288.0 *K*	374.4 *K*	432.0 *K*
Blade Relative Total Temp.	252.4 *K*	328.5 *K*	379.0 *K*
Blade Relative Temp. Ratio	0.876	1.141	1.316
Run Time	468 *ms*	213 *ms*	139 *ms*
Turbine Output Power	1.48 *MW*	2.36 *MW*	3.04 *MW*
Turbine Speed Change (During a run)	5,214 *rpm*	3,320 *rpm*	2596 *rpm*
Turbine Design Speed	7,397 *rpm*	8,434 *rpm*	9,060 *rpm*

During commissioning of the new facility's rotating system (see Section 6.4.4), the author increased Reynolds number to design value in increments, as low Reynolds numbers result in a smaller turbine speed change (see Table 3.6.).

Table 3.6
Facility parameters at a gas to wall temperature ratio of 1.3 over a range of Reynolds numbers

Facility Parameters	*Reynolds Number*		
	¼ Design	*½ Design*	*Design*
Initial Tube Pressure	$0.80x10^5$ *N/m²*	$1.60x10^5$ *N/m²*	$3.20x10^5$ *N/m²*
Final Tube Pressure	$2.00x10^5$ *N/m²*	$4.01x10^5$ *N/m²*	$8.02x10^5$ *N/m²*
Turbine Output Power	0.59 *MW*	1.18 *MW*	2.36 *MW*
Turbine Speed Change (during a run)	830 *rpm*	1,660 *rpm*	3,320 *rpm*

3.4.2 Piston oscillations

Brooks and Jones (1989) considered the departure of ILPT performance from the ideal. Pressure rises linearly in front of the piston (see Figure3.9) as air from the high pressure reservoir drives the piston down the pump tube. The AGV opens and the working section second throat is set to match the mass flow rate in and out of the working section. When the mass flow rate in, and out, of the working section are matched, the pressure level in front of the piston (and therefore the working section) remains constant. In practice, finite piston mass and AGV downstream volume result in a departure from ideal ILPT performance.

The effect of finite piston mass on ILPT performance is that piston velocity does not respond instantly to any velocity changes determined by the gas volume flow rates into and out of the pump tube. The velocity of a mass-less piston during ILPT operation, Figure3.9, instantly assumes the velocity it requires for matched conditions when the AGV opens. For a finite piston mass a step change in velocity is impossible, leading to oscillations about the matched piston velocity, and therefore oscillations of temperature and pressure.

A second mechanism by which piston oscillations arise is the effect of downstream volume, Figure 3.1, between AGV and working section second throat. When the AGV opens, the downstream volume fills quickly, causing an isentropic expansion of the gas in front of the piston, and therefore a drop in pressure. A mass-less piston would move along the tube to equalise pressure on both sides, however the inertia of a piston with finite mass causes it to overshoot, resulting in oscillations in piston velocity and therefore pressure and temperature.

The pressure drop due to downstream volume occurs as the AGV opens; therefore, the pressure force accelerating the piston due to the downstream volume is a maximum when the AGV opens. Pressure force acting across the piston as a consequence of finite piston mass is a minimum when the AGV opens, resulting in the two mechanisms generating piston oscillations that are 90° out of phase. The resulting piston oscillation is a consequence of the combined effect of the two mechanisms.

Brooks and Jones derived expressions for the time period of pressure oscillations, T_p,

$$T_p = \frac{2\pi}{\gamma^{\frac{1}{2}}} \left\{ \left[\frac{P_i}{P_{01}} \right]^{\frac{1}{\gamma}} \left(1 - \left[\frac{P_i}{P_{01}} \right]^{\frac{1}{\gamma}} \right) \right\}^{\frac{1}{2}} \left[\frac{L_t M_t}{A_t P_{01}} \right]^{\frac{1}{2}} \qquad - \quad 3.4$$

and for the amplitude of pressure oscillations due to finite piston mass,

$$\frac{\Delta P}{P_{01}} = \frac{\gamma}{2\pi} \cdot \frac{T_p}{\tau_{run}} \left\{ \left[\frac{\tau_t}{\tau_{run}} \right]^{\frac{-2}{\gamma+1}} - 1 \right\}$$

and to downstream volume,

$$\frac{\Delta P}{P_{01}} = \frac{\gamma \, \Delta V}{V_a} \left[\frac{\frac{1}{V_a}}{\frac{1}{V_a} - \frac{1}{V_b}} \right]$$

Piston oscillation due to finite piston mass downstream volume are 90° degrees out of phase; therefore, one can express total piston oscillation amplitude as,

$$\frac{\Delta P}{P} = \left\{ \left[\frac{\gamma}{2\pi} \cdot \frac{T_p}{\tau_{run}} \left\{ \left[\frac{\tau_t}{\tau_{run}} \right]^{\frac{-2}{\gamma+1}} - 1 \right\} \right]^2 + \left[\frac{\gamma \, \Delta V}{V_a} \left[\frac{\frac{1}{V_a}}{\frac{1}{V_a} - \frac{1}{V_b}} \right] \right]^2 \right\}^{\frac{1}{2}} \qquad - \quad 3.5$$

Using Equation 3.5, one can calculate the effect of varying piston mass and downstream volume, Figure3.10 and Figure.3.11, clearly showing that piston mass has a secondary effect on amplitude of pressure oscillations compared to downstream volume. One achieves gas to wall temperature ratios greater than 1.0 by compressing the gas in the ILPT pump tube prior to opening the AGV. Gas compression in the pump tube results in a mismatch between required and actual piston velocities at the conclusion of compression. The higher the compression ratio, the greater the velocity mismatch, and therefore for a finite piston mass, the greater the piston oscillations. Using Equation 3.5, one can calculate the effect of varying temperature ratio (see Figure 3.12). The author used an ultraviolet chart recorder (see Section 3.3.2) to monitor facility parameters during ILPT operation, Figure 3.13, which clearly illustrates the piston oscillations.

3.5 DATA ACQUISITION SYSTEM

3.5.1 Computer data acquisition

During each ILPT run, the author recorded pressure and thin film gauge output signals using an on-line mini-computer system based on a Digital PDPl1/34 processor. The PDP11/34 sampled 64 measurement channels by multiplexing them through a 12 bit A/D converter with a conversion rate of 27.8 KHz, giving each channel a sampling rate of 435 Hz. The author recorded the signal from each channel (for 460 ms from the time ILPT operation commenced) on the PDPl1/34's hard disc ready for post run analysis. The author refers to the computer data acquisition system as the "low speed" data acquisition system throughout this thesis. For a full description, refer to Oldfield et a1. (1978).

The author measured the unsteady blade pressure and temperature using a transient recorder sampling at 500 KHz. The transient recorder 3.5 KB memory enabled the author to take 7 ms of data at 500 KHz, during which time thirty five vane wakes influenced one rotor blade (when revolving at design speed). During the 7 ms data acquisition period, turbine speed changed by less than one percent, so the author could neglect turbine speed change.

3.5.2 Ultraviolet chart recorder

The author used a 24 channel SE6008 ultraviolet (U.V.) chart recorder to monitor ILPT and working section performance during ILPT facility operation. He fitted the seven valves separating the high pressure reservoir from the pump tube with position indicator transducers and the output signal displayed on the U.V. recorder. Prior to ILPT facility operation, the author "cycled" the high pressure valves by opening and closing them until the U.V. recorder indicated all valves were opening simultaneously. The effect of one valve opening early reduced the load on the others which then opened very quickly, giving a short pulse of high pressure air which imposed oscillations on the piston's movement.

The output from a linear displacement transducer, which was located on the AGV, displayed on the U.V. recorder during ILPT operation. This provided a record of the AGV opening characteristics. Pump tube pressure, working section temperature and pressure and the transient data recorder trigger, also connected to the U.V. chart recorder to provide required information to determine the quality of ILPT facility run (see Figure3.13).

Thus, we see the feasibility of using the ILPT as a short duration air supply for a new working section containing a B22 turbine. The turbine can achieve its design point over an adequate facility operating envelope, with existing ILPT data acquisition systems suitable for use with the new working section. Chapter 4 presents the detailed design of the new working section.

CHAPTER FOUR

AERODYNAMIC AND MECHANICAL DESIGN OF THE TURBINE MODULE

4.1 THE BEARING SYSTEM

4.1.1 Operating requirements

The Rolls-Royce plc turbine disc and blades in the turbine module came with two matched pairs of split inner race deep groove ball bearings. Rolls-Royce plc originally designed the bearings for use in a Rolls-Royce Olympus marine gas turbine. Bearing specification (supplied by Rolls-Royce plc with the bearings) for normal engine life was 32 kN axial load per bearing, at 12,000 rpm with a 1.5 l/min coolant oil flow per bearing.

The turbine (and therefore the bearings) was subject to an axial thrust load as a consequence of the pressure ratio and momentum change across it. To a first order approximation, one can calculate axial gas load on the turbine from a consideration of the mid-height blade section. The gas load in the axial direction will be the sum of the pressure force and force due to change of momentum through the turbine blades,

$$F = A_b(P_3 - P_4) + \dot{m}(V_4 - V_3)$$

where velocities V_3, and V_4, are in the axial direction, and one defines A_b as the blade inlet annulus area. One can show at turbine design conditions that,

$$F = 14.1\ kN$$

The ILPT mode of operation (see Section 3.1.3) requires evacuation of the working section prior to ILPT facility operation. Pressure on both sides of the turbine disc will be near vacuum prior to a run; however, once a run commences, pressure in the working section will reach design value. The labyrinth seal between inner annulus and the upstream side of the turbine disc, Figure3.2, had the potential to leak as it was run with a 0.125 mm clearance (see Section 6.1). In a worst case, pressure downstream of the disc could remain near to vacuum, whilst the leaking labyrinth seal would pressurise the volume upstream of the turbine disc.

Pressure across the turbine disc would, therefore, result in an axial load on the disc. One can calculate disc load from a consideration of the labyrinth seal, Figure 4.1, and the fill rate of the turbine disc upstream volume. Consider the boundary layer on the seal. One can express the boundary layer Reynolds number as,

$$\mathrm{Re} = \frac{U_{\infty} l \rho}{\mu}$$

Assuming the choking of the seal flow and therefore a Mach number of 1.0,

$$M = 1.0 \qquad \therefore \qquad U_{\infty} = a^{*}$$

Using vane upstream total conditions and a Mach number of 1.0 to calculate conditions in the choked seal, and a seal length of 16 mm,

$$\mathrm{Re} = 1.4x10^{6}$$

Using Shame's (1982) method, one can calculate boundary layer displacement thickness, δ^{*},

for laminar boundary layers $$\frac{\delta^{*}}{x} = 1.73\,\mathrm{Re}^{-0\ 5} \qquad - \quad 4.1$$

for turbulent boundary layers $$\frac{\delta^{*}}{x} = 1.73\,\mathrm{Re}^{-0\ 2} \qquad - \quad 4.2$$

Shames cites a critical Reynolds number for laminar/turbulent boundary layer transition of $3.5\text{x}10^{5}$, indicating the boundary layer undergoes transition after 4 mm and (using Equation 4.1) has a displacement thickness of $12\text{x}10^{-6}$ m when it does (see Figure 4.1). Equation 4.2 predicted a boundary displacement thickness of $12\text{x}10^{-6}$ m using a length of 3.3 mm indicating that the turbulent boundary layer can start 0.7 mm through the labyrinth seal, Figure 4.1. One can, therefore, predict boundary layer displacement thickness, δ^{*}, accurately using Equation 4.2 with a Reynolds number of $1.4\text{x}10^{6}$ and a length of 15.3 mm. At the end of the seal,

$$\delta^{*} = 42x10^{-6}\,m$$

The design seal clearance, δ_{cl}, was $125\text{x}10^{-6}$ m; therefore, one can calculate the effective seal clearance,

$$\delta_{cl} - \delta^* = 83x10^{-6} m$$

$$Seal\ clearance\ area \qquad A^* = 2\pi R_c \left[\delta_{cl} - \delta^*\right]$$

$$Where\ R_c = 0.233\ m,\ the\ labyrinth\ seal\ radius$$

$$\therefore \qquad A^* = 116.0x10^{-6} m^2$$

Now calculate the mass flow rate through the choked seal clearance,

$$\dot{m} = \rho^* a^* A^*$$

One can show that at the B22 turbine design conditions, the mass flow rate through the seal, $\dot{m}$, was 0.194 kg/s. During the 213 ms ILPT run time, one can show total mass that leaks through the seal, M_r, as 0.041 kg. The upstream volume of the disc was 18x10^{-3} m^3, with a disc area of 143x10^{-3} m^2. Disc axial force due to 0.041 kg of leakage flow through the upstream labyrinth seal was 21.8 kN. One can, therefore, calculate total axial force on the turbine over the ILPT's range of temperature ratios (see Table 4.1).

Table 4.1
Bearing loading at turbine design condition for a range of gas to wall temperature ratios

$\frac{T_g}{T_w}$	*Blade inlet static pressure* $x10^5$ *Pa*	*Blade axial force* *kN*	*Disc axial force* *kN*	*Total axial turbine load* *kN*
1.0	*3.22*	*10.10*	*39.50*	*49.60*
1.3	*4.50*	*14.10*	*21.80*	*35.90*
1.5	*5.40*	*16.80*	*16.10*	*32.9*

As temperature ratio increased, mass flow through the labyrinth seal increased due to the increase in working section pressure. Disc axial force fell with increasing temperature ratio; however, as the increased mass flow rate was more than off set by the reduced facility run time (see Table 3.5). The author only applied the axial gas load on the turbine when there was mass flow through the working section, not during spin up and spin down of the turbine. In order to ensure the bearings did not skid (see definition in section 4.1.3), the author required a method of pre-loading the bearings. From a bearing dynamics point of view, the author desired a high pre-load to minimise the probability of skidding; however, he could not exceed a maximum axial load per bearing of 32 kN.

During commissioning trials of the turbine module (see Chapter 6), the author tuned the ILPT to a temperature ratio of 1.0; however, without fitting the turbine disc and therefore, without any axial gas loads on the bearings. A temperature ratio of 1.3 was achived during normal ILPT operation, at which the disc pressure load was 21.8 kN and the axial gas load was 14.1 kN. This resulted in an axial load of 35.9 kN, plus any applied pre-load. The author rated a single bearing to 32 kN axial load, indicating that the turbine required more than one bearing. The International Standard IS0 281 (1977) covers the dynamic capacity of rolling element bearings. IS0 281 defines the capacity of tandem bearings as,

$$B_t = B_s(\beta_{no})^{0\ 7}$$

where B_t = *axial load for bearing set*

B_s = *axial load for a single bearing*

B_{no} = *number of bearings in the set*

For a matched pair of bearings, the number of bearings in a set, β_{no}, is two and for the bearings under consideration, the axial load for a single bearing, B_s, is 32 kN, therefore,

$$B_t = 32x10^3(2)^{0\ 7} = 52\ kN$$

$$\therefore \quad Max.\,pre\text{-}load = (52 - 35.9)\ kN = 16.1\ kN$$

For bearings similar to those with the B22 turbine, the SKF General Catalogue (1981) recommends a maximum pre-load of 10 kN. The 10 kN maximum recommended pre-load was below 16.1 kN; therefore, it was ideal for the bearing design. The author desired a high pre-load as he predicted the turbine to accelerate at 1,600 rad/s^2 during ILPT operation (see Section 3.3.2), with the SKF General Catalogue citing 300 rad/s^2 as the acceleration at which skidding of the bearing (see Section 4.1.3) may occur. The SKF General Catalogue recommends high pre-loads in applications where accelerations are in excess of 300 rad/s^2 to minimise the probability of skidding. However, the author recognised the high pre-load as a source of high power loss in the bearings (power loss is a function of bearing load, speed and coolant viscosity). The author considered paramount minimising the risk of bearing skidding and their consequent failure.

A design constraint on the bearing system was that it should be single sided with bearings upstream of the turbine disc to allow its easy removal and remounting. The author conceived a single sided bearing system, Figure 4.2, that utilised a matched bearing pair to take axial loads and a single 'floating' bearing through which the author applied the 10 kN pre-load.

The author then estimated bearing power loss using the SKF General Catalogue’s (1981) recommendation. The total retarding bearing frictional moment J (N/m), is the sum of J$_v$, due to viscous friction (load independent), and J$_c$, the contact friction (load dependent).

$$J = J_v + J_c$$

$$J_v = 0.1 f_f (vn)^{0.66} {d_m}^3$$

$$J_c = 0.0009 (F_0 / C_f)^{0.55} F_1 d_m$$

where v *= Kinematic viscosity of lubricant, mm^2/s*

n *= Bearing speed, rpm*

d_m *= Mean diameter, m*

$$F_0 = 0.6F_r + 0.5F_a$$

$$F_1 = 3F_a + 0.1F_r$$

F_r = *558 N, Bearing radial load*

F_a = *10 kN, Bearing axial pre-load*

C_f = *78 kN, Max bearing axial load before failure*

f_f = *0.75, For a heavy mist jet lubrication system*

The bearing specification included a recommended coolant oil flow rate of 1.5 l/min per bearing. The author identified Shell Tellus 22 as a suitable low viscosity coolant oil, with a density, ρ, of 900 kg/m^3 and a specific heat capacity, C_p, of 1,700J/kgK. The author assumed that all power dissipated in a bearing was removed by 1.5 1/min of Shell Tellus 22 oil. He calculated bearing power loss assuming an oil inlet temperature of 20°C, using Equations 4.3 and 4.4. The predicted power loss enabled the author to calculate coolant oil temperature rise which, in turn, allowed him to estimate oil viscosity from the manufacturer's data sheets. Once the author knew the oil viscosity, he used Equations 4.3 and 4.4 to find bearing power loss, and he repeated the procedure until he could achieve a converged solution. The result, Table 4.2, was a prediction of bearing power loss for the three bearings in the proposed bearing system.

Oil viscosity was critical to a prediction of bearing power loss, a 10 K change in ambient temperature from 15°C to 25°C causing a change in coolant oil viscosity from 12 mm^2/s to 8 mm^2/s at 6,500 rpm, which in turn resulted in a 1 kW reduction in total bearing power loss. The author assumed ambient temperature at 20°C for all calculations.

The SKF General Catalogue (1981) cites an oil temperature rise of 80 K as the maximum attainable value limited by bearing ball/oil heat transfer rate. Predicted temperature rises (Table 4.2) for each bearing was well below the 80 K maximum at all conditions; therefore, the author considered the proposed bearing system suitable.

In a practical bearing system the oil would not remove all power dissipated in the bearings: the bearing housing would conduct approximately half away as heat (see Section

6.4.3). The author therefore predicted and considered bearing coolant oil temperature rises a worst case estimate.

Table 4.2
Bearing power loss at pre & post ILPT run speeds

Bearing	*Load kN Axial*	*Load kN Radial*	*Contact friction Power loss, kW*		*Viscous friction Power loss, kW*	
			@ 6,500 rpm	*@ 9,800 rpm*	*@ 6,500 rpm*	*@ 9,800 rpm*
1 *Pre load*	*10*	*0.3*	*0.66* *ΔT=30K*	*1.02* *ΔT=43K*	*0.51* *ΔT=30K*	*0.67* *ΔT=43K*
2 *Pair*	*6*	*0.18*	*0.3* *ΔT=24K*	*0.47* *ΔT=36K*	*0.60* *ΔT=24K*	*0.87* *ΔT=36K*
3 *Pair*	*4*	*0.12*	*0.17* *ΔT=23K*	*0.24* *ΔT=32K*	*0.67* *ΔT=23K*	*0.98* *ΔT=32K*

The final bearing system design utilised the single plus twin bearing concept, Figure 4.3, and an oil supply system based on that used by Doorly (1983) (see Section 4.1.6.). The bearing system was designed as a self contained unit that bolted to the centre of the rear Annular Gate Valve (AGV) section (see Section 4.3). Oil supply and drain from the bearing system was via the AGV. Initially, the author conducted the design of the bearing system in parallel to design of the AGV as it placed constraints on the AGV design. The author finalised the bearing system design at an early stage in the project once he decided to use an AGV, as opposed to any other valve type.

4.1.2 Bearing dynamics

The author undertook an analysis of the bearing dynamic performance to ascertain the suitability of the bearings that Rolls-Royce plc supplied for use in the turbine module. Truncation and bearing cage shaft speed ratio (see Section 4.1.3) are the two relevant parameters when considering bearing performance. We can define truncation as the ellipsoid of contact between bearing balls and the bearing raceway overriding the inner raceway shoulder, Figure 4.4, which results in severe frictional bearing heating and the bearings consequent rapid failure.

The author considered the starting point for a dynamic analysis of the bearings which he would incorporate into the turbine module, concluding that the analysis must start with a consideration of the loads to which they would be subjected during ILPT operation. Consider the single floating bearing. The author applied the bearing pre-load to the single bearing, therefore immediately prior to ILPT operation (see Section 3.1.3) the turbine was rotating at 6,500 rpm, with a 10 kN load applied across the bearing. During ILPT operation bearing load remained constant as the bearing outer race floated whilst turbine speed increased to 9,800 rpm.

Now, consider the tandem bearing set. As soon as an ILPT run commenced, the author applied turbine disc and gas loads (see Section 4.1.1) which increased the load on the bearing set from the 10 kN pre-load to 45.9 kN (from 5 kN to ≈23 kN per bearing). The author assumed that bearing load remained constant during ILPT run time, as turbine speed rose from 6,500 rpm to 9,800 rpm. At the end of an ILPT run, gas loads fell to zero; therefore, load on the bearing set returned to the pre-load value of 10 kN. Table 4.3 below summarises bearing speeds and loads during ILPT operation.

The author ran the SKF prediction code BEARCENT with the bearing loads corresponding to pre-run, run start, run end and post run conditions. BEARCENT calculated the bearing inner and outer race contact angles and contact loads from the bearing geometry, applied bearing axial load and rotational speed (from which he calculated centrifugal load).

Table 4.3
Bearing loads during ILPT operation

ILPT run State	*Single floating bearing*		*Bearing from the Tandem set*	
	Bearing load	*Turbine speed*	*Bearing load*	*Turbine speed*
Pre run	*10 kN*	*6,500 rpm*	*5 kN*	*6,500 rpm*
Run start	*10 kN*	*6,500 rpm*	*23 kN*	*6,500 rpm*
Run end	*10 kN*	*9,800 rpm*	*23 kN*	*9,800 rpm*
Post run	*10 kN*	*9,800 rpm*	*5 kN*	*9,800 rpm*

The author then calculated the deformation of the bearing balls and inner and outer races under applied contact loads and then recalculated bearing inner and outer race contact angles and loads for the modified geometry. In this way, BEARCENT iterated until input contact angles matched output contact angles, and the solution could therefore be considered to have converged. Table 4.4 shows tabulations for predicted inner and outer race contact angles and loads for the four run states shown in Table 4.3. To aid interpretation of Table 4.4, Figure 4.5 illustrates the BEARCENT prediction of contact angles and loads for the pre-run loading of the bearing system.

Table 4.4
Bearing contact angles and forces during ILPT operation

ILPT run State	*Single bearing*				*Bearing from the Tandem set*			
	Inner race contact		*Outer race contact*		*Inner race contact*		*Outer race contact*	
	Angle	*Force*	*Angle*	*Force*	*Angle*	*Force*	*Angle*	*Force*
Pre run	*54.8°*	*577.6 N*	*40.4°*	*525.8 N*	*59.4°*	*267.8 N*	*33.0°*	*422.9 N*
Run start	*54.8°*	*577.6 N*	*40.4°*	*525.8 N*	*52.0°*	*1337.4 N*	*45.3°*	*1481.7 N*
Run end	*61.1°*	*536.5 N*	*31.7°*	*889.9 N*	*55.8°*	*1268.4 N*	*40.9°*	*1600.6 N*
Post run	*61.1°*	*536.5 N*	*31.7°*	*889.9 N*	*65.7°*	*257.5 N*	*21.3°*	*645.8 N*

BEARCENT also calculated the size of the ellipsoid of contact between bearing ball and inner race. Using the width of the ellipsoid of contact, contact angles and bearing geometry, the author calculated the angular extremity of the ellipsiod of contact, λ (see Figure 4.4). Truncation occurred if λ was greater than 70°, the angle at which the extremity of the ellipsoid of contact would override the bearing inner race shoulder. The author did not predict truncation would occur under pre-run, run start, run end or post run conditions for either the single or tandem bearings.

The dynamic analysis of the turbine module bearing system performed using BEARCENT predicted bearing contact angles would remain low enough to prevent truncation of the bearings during ILPT facility operation, indicating the bearings were suitable for use in the turbine module. One can calculate bearing cage/shaft speed ratio from bearing contact angles and loads. Section 4.1.3 describes the methods for calculating bearing cage/shaft speed ratio.

4.1.3 Bearing cage/shaft speed ratio

The author predicted the inner race contact angle variation during ILPT facility operation (see Section 4.1.2). It remained sufficiently low at all conditions to prevent truncation occurring. A second consideration when analysing a bearings dynamic performance is bearing cage/shaft speed ratio. We can define cage/shaft speed ratio as the angular velocity of the bearing cage holding the balls, divided by the angular velocity of the bearing inner race which we derive from bearing geometry. We can more readily measure cage/shaft speed ratio (see Section 4.1.7) than contact angles. A predicted cage/shaft speed ratios that matches closely measured cage/shaft speed ratio is a good indicator that bearing contact angles are as predicted, and therefore truncation is not occurring. As such cage/shaft speed ratio can be used as a proxy for contact angle.

The author predicted the acceleration of the turbine during ILPT facility operation (see Section 3.3.2) at approximately 1,600 rads/s^2. At accelerations above 300 rads/s^2, the SKF General Catalogue (1981) warns that bearing skidding may occur. The Catalogue defines bearing skidding as gross slippage of the bearing cage relative to the inner raceway. Skidding occurs at high accelerations due to the inertia of the bearing cage and ball set. In essence, the bearing inner race accelerates (as it is attached to a shaft which is accelerating) so rapidly that the inertia of the bearing cage and ball set prevents it from accelerating quickly enough to keep up with the inner race. Consequently, the balls cease to roll on the inner race and slip, resulting in severe frictional heating of the bearing and their ensuing rapid failure. When skidding of a bearing occurs, cage/shaft speed ratio of the beating falls below the predicted level for pure rolling of the balls. Therefore, the author considered a prediction of cage/shaft speed ratio vital in order to ascertain whether bearing skidding was occurring during ILPT facility operation as a consequence of the high accelerations.

The author used the SKF code BEARCENT to predict cage/shaft speed ratio for the four run states which are in Table 4.3. The author made two predictions by making two sets of assumptions about the bearing balls' rolling axis. The first assumed "outer race control" of the balls and constitutes an upper limit of expected measured cage/shaft speed ratio. The second assumed "combination race control" of the balls and constitutes a lower limit of expected measured cage/speed ratio.

One can visualise the outer race control method of calculating cage/shaft speed ratio by considering bearing ball geometry, Figure 4.6. The bearing balls are held in place relative to one another in a cage. During normal bearing operation, the bearing inner race rotates at the angular velocity of the shaft, the outer race remains stationary and the balls roll between the two. The balls will roll about an unknown axis of rotation with angular velocity ω, in addition to the rotation, n, about the bearing centre line. Rotation about the bearing centre line gives rise to centrifugal forces which result in the outer race contact load being higher than the inner race contact load (as Figure 4.5 illustrates). Therefore, the outer race principally determines the ball's rolling axis contact angle. Once the author predicted the outer race contact angle (using the code BEARCENT, see Section 4.1.2), he could derive the bearing cage/shaft speed ratio from the bearing geometry. Engineers name cage/shaft speed ratios calculated in this mannor outer race controlled cage/shaft speed ratios.

Falcon and Andrew (1969) found the combination race control method of calculating bearing cage/shaft speed ratio in closer agreement with measured cage/shaft speed ratios than the outer race control method for bearings where the inner race contact load was of a similar magnitude to the outer race contact load. Consider a bearing ball rotating between inner and outer races where inner and outer contact loads are similar, Figure 4.7. There must be slip of both contact points as neither is coincident with the ball axis of rotation. The inner and outer race slip induces moments $M_{\alpha i}$ and $M_{\alpha o}$, which oppose each other. The code BEARCENT assumes no spin of the ball; therefore, $M_{\alpha i}$ and $M_{\alpha o}$, are equal and opposite. BEARCENT assumes the moments proportional to contact point load and width of the ellipsoid of contact at each contact point. Therefore, BEARCENT is able to calculate the angle φ, Figure 4.7, that equilibrium requires. Once a ball axis of rotation is astablished, one can derive the bearing cage/shaft speed ratio from bearing geometry. For normal operation of a bearing, one can expect reasonably the actual cage/shaft speed ratio no less than the combination race control prediction and no more than the outer race control prediction.

The author utilised the SKF code BEARCENT to predict outer race controlled and combination race controlled cage/shaft speed ratios from predicted inner and outer race contact angles, loads and ellipsoid of contact widths. Table 4.3 shows the four ILPT run-state predictions and Table 4.5 presents the predicted cage/shaft speed ratios. The author predicted ILPT run time (see Section 3.3.2) at 213 ms and used it in conjunction with predicted cage/shaft speed ratios to construct a predicted bearing cage/shaft speed ratio during ILPT facility operation.

Table 4.5
Bearing cage/shaft speed ratios during ILPT operation

ILPT run State	*Outer ring control C/S speed ratio*		*Combination ring control C/S speed ratio*	
	Single bearing	*Tandem bearing*	*Single bearing*	*Tandem bearing*
Pre-run	*0.469*	*0.489*	*0.462*	*0.469*
Run start	*0.469*	*0.463*	*0.462*	*0.461*
Run end	*0.495*	*0.470*	*0.472*	*0.463*
Post run	*0.495*	*0.546*	*0.472*	*0.507*

Outer and combination race control predictions for the single bearing, Figure 4.8, illustrate how increasing turbine speed results in an increase in ball centrifugal load with a corresponding reduction of outer race contact angle and, therefore, an increase in cage/shaft speed ratio. The prediction of cage/shaft speed ratio for a bearing in the tandem set adopts a stepped form due to the application of turbine blade and disc axial gas loads, Figure 4.9. The outer race contact angle increases as the axial loads apply as the radial centrifugal load becomes a lower proportion of the total applied load, resulting in a step drop in cage/shaft speed ratio.

The author instrumented the bearing system (see Section 4.1.7) in order to measure the cage speed of the single bearing and the tandem pair's upstream bearing. The author also measured turbine speed in order to derive bearing cage/shaft speed ratio for each ILPT run during facility commissioning (see Chapter 6). Measured cage/shaft speed ratio for the single bearing during ILPT Run 6384 fell between outer and combination race control predictions, Figure 4.10, giving confidence that the bearing was not skidding and that there was no truncation. The measured cage/shaft speed ratio of the upstream bearing of the tandem pair, Figure 4.11 was 2.2% lower than the combination race control prediction during ILPT run time, giving rise to an initial concern that the bearing might be skidding slightly. During the course of a short experimental programme (reported in Chapter 7) run to run variations in cage/shaft speed ratio were large enough, Figure 4.12, to give confidence that the tandem pair bearing was not skidding.

Stirling (1969) tested the bearings utilised in the turbine module design in a steady state rig by measuring bearing cage/shaft speed ratio over a comparable speed and axial load range to that relevant to the turbine module, Figure 4.13. The author found that his predictions and measured data of the nominal cage/shaft speed ratio of 0.45 were in broad agreement with Stirling's. This was a useful independent confirmation.

Overall, the author considered the bearings suitable for use in the turbine module in the proposed configuration. He did not predict bearing truncation under any of the ILPT facility run states. Measured cage/shaft speed ratios gave confidence that bearing skidding did not occur, despite the turbine's high acceleration during ILPT operation.

4.1.4 Bearing pre-load

The turbine module bearing system required pre-loading to avoid bearing skidding immediately prior to and after ILPT facility operation (see Section 4.1.1). The author designed the bearing system with a 10 kN axial pre-load applied to the outer race of a single 'floating' bearing, then on to the matched bearing pair via a spacer, Figure 4.3. The author had to apply the pre-load to the floating bearing outer race within the limited available space in the bearing system.

The author identified Belleville washers as a suitably compact means of applying axial load. He incorporated a circumferential ring of six sets of Belleville washers in double parallel quadruple configuration, Figure 4.14, into the bearing system, Figure 4.3. He experimentally determined the load/deflection characteristics of a set of Belleville washers, Figure 4.15. The author found Belleville washers' load deflection characteristics in reasonable agreement with the manufacturer's specification, with the exception of some hysteresis in the experimentally measured characteristics.

When fully assembled, the bearing system retaining flange was 10 mm from the bearing sleeve. The undeflected height of the Belleville washers was 12.6 mm; therefore, assembly of the bearing system resulted in a 2.6 mm compression of the Belleville washers, resulting in an 8 KN pre-load, Figure 4.15. The author achieved the required 10 KN pre-load by fitting a 0.3 mm plain washer under the Belleville washers to increase their deflection to 2.9 mm.

4.1.5 Carbon face seals

The author isolated the bearing system from the working section using Pioneer Western CAX5500/3 carbon face seals. Carbon face seals upstream of the single bearing and downstream of the matched bearing pair, Figure 4.3, prevented oil escaping from the bearing cavity and contaminating the working section. The carbon face seals are spring loaded, exerting a force of 130 N against the seal guide rings. Wallace (1988) investigated the seal contact load results in a seal power loss and derived a relationship for the retarding torque, Js, of a carbon face seal,

$$J_s = \kappa F_t^{'} \cdot \frac{D_m}{2}$$

where κ *= seal coefficient of friction*

D_m *= seal mean diameter*

$F_t^{'}$ *= total seal closing force*

The carbon face seal retarding torque was 1.13 Nm. One can calculate power loss from the retarding torque,

$$P_l = J_s n$$

$$P_l = 0.77\ kW\ @\ 6{,}500\ rpm$$

$$P_l = 1.18\ kW\ @\ 10{,}000\ rpm$$

The bearing coolant oil would remove some of the heat generated by the seal; however, the bearing housing on which the seals are mounted would absorb most of it. Therefore, the author neglected carbon face seal power loss during calculation of the bearing coolant oil temperature rise.

4.1.6 Oil system and supply

The bearing system design (see Section 4.1.1) called for an oil system supplying 4.5 l/min to the bearings through oil jets. The author conceived a twin oil jet arrangement to supply oil to the three bearings, Figure 4.16. The first oil jet (Injector 2) supplied oil to the single bearing and the upstream bearing of the matched pair. A second oil jet (Injector 1) supplied the downstream bearing of the matched bearing pair which was mounted in a small annular cavity between the single and matched bearing pair, Figure 4.3.

The bearing system design required oil cooling the downstream bearing of the matched bearing pair to pass through the bearing pair to reach the oil drain, situated between the single and matched bearing pair. Rolling element bearings act as a centripetal pump due to rotation of the bearing balls about the shaft centre line, and their own axis of rotation. Consider the matched bearing pair, Figure 4.17. Pre-load applied to the inner race results in contact points A, B, C and D. The rotation of the balls results in point AB and CD forming an ’equator’ with corresponding ’poles’ which constitute the axis about which the balls rotate, with angular velocity ω. Bearing balls also rotate about the shaft centre line which gives rise to a centripetal force. Oil on the bearing’s balls is thrown radially outward by the centripetal force. Rotation of balls about their own north-south axis results in oil on a ball at point P_1 carried from P_1 to P_2, as the ball rotates. At point P_1, the centripetal force due to rotation of the ball about the engine centre line will force the oil towards the 'north pole'. Oil moving towards the ball's ‘north pole’ will result in a net movement of oil through the bearings from right to left.

Bilstern (1982) investigated the pumping effect of rolling bearings and established an empirical method for predicting $\dot{q}$, the volume flow rate through a rolling element bearing,

$$\dot{q} = Q_{H=0}\left[1-\frac{H}{H_{Q=0}f_H(\nu)}\right]f_H(\nu)^{1\ 5}\,60{,}000 \qquad \mathit{1/min} \qquad - \quad 4.12$$

$$Q_{H=0} = 0.1\pi\left[d_m D_w - \frac{ZD^2}{4}\right]\frac{\pi\ n}{60}\left[1-\frac{D_w}{d_m}\cos\alpha_0\right]\frac{n}{2500} \qquad m^3/s$$

$$H_{Q=0} = \frac{K_1}{2g}\left\{1-\left[\frac{d_m - l\sin\alpha_0}{d_m + l\sin\alpha_0}\right]\right\}\left\{\frac{\pi\ n}{60}\left[1-\frac{D_w}{d_m}\cos\alpha_0\right]\frac{1}{2}\left[d_m + l\sin\alpha_0\right]\right\}$$

$$f_H(\nu) = 1.023 - 38.33x10^{-6}\nu$$

where $H = 0$ *(head against which the bearings pump)*

$d_m = 161.9$ *mm (mean bearing diameter)*

$D = 19.05$ *mm (bearing ball diameter)*

$Z = 22$ *(number of balls per bearing)*

$\alpha_0 = 40°$ *(nominal outer race contact angle)*

$K_1 = 0.75$ *(for ball bearings)*

$l = 15.24$ *mm (roller length, 80% of ball diameter)*

n = *shaft speed in rpm*

ν = *lubricating oil kinematic viscosity,* mm^2/s

$\rho = 900\ kg/m^3$ *(lubricating oil density)*

$g = 9.81\ m/s^2$ *(gravitational acceleration)*

Therefore $Q_{H=0} = 6.5x10^{-9}\ n^2$

$H_{Q=0} = 507.43x10^{-9}\ n^2$

The bearings are pumping against zero head; therefore, the head against which the bearings pumped, H, was zero. By assuming the oil temperature to be 20°C (ambient), the author was able to find oil viscosity, *v*, from the oil manufacturer's data sheets. Oil viscosity was 55 mm^2/s at 20°C. Using Equation 4.12 a turbine speed of 62 rpm is required to induce an oil flow rate of 1.5 l/min, Figure 4.18. At shaft speeds above 62 rpm, the bearings would pump a mixture of oil and air as they try to pump more than 1.5 1/min. At shaft speeds below 62 rpm, the cavity would fill with oil. Oil Injector 1 cavity, Figure 4.3, crucially required low oil pressure as a pressure greater than $30x10^3$ N/m^2 would exert a force of greater than 130 N on the carbon face seal (see Section 4.1.5) and therefore lift off the carbon face seal, allowing cooling oil into the working section. Stimpson (1989) estimated the pressure required to pass 1.5 1/min through the tandem bearing set between $0.1x10^3$ N and $1.0x10^3$ depending on oil viscosity. During facility commissioning (see Chapter 6), the author ran the bearing system continuously for 10 minutes, with no rotation of the turbine shaft. The author found no oil leaks from the carbon face seals, thus confirming that oil pressure in the Injector 1 cavity never reaches a high enough pressure to lift off the carbon face seal.

The oil supply system was located in and around the turbine module's core, making an estimate of the length and diameter of oil ways possible at an early stage of the turbine module design, Figure 4.19. The author assumed oil flow rate through the oil ways at 4.5 l/min; however, where the system branches into two, to feed the oil jets, each oil jet was fed with a different flow rate, the sum of which was 4.5 l/min. The author assumed head loss, H_l, through each branch of the system equal as pressure difference across the tandem bearing set was small, Figure 4.18 (pressure difference across the bearings was the head generated by the bearings as they acted as a pump). By a consideration of the losses through each branch of the oil system,

$$H_l = \sum \left[f \cdot \frac{l}{d} \cdot \frac{{v_l}^2}{2} + K \cdot \frac{{v_l}^2}{2} \right]$$

where l *= length of oil way*

d *= diameter of oil way*

v_l *= velocity of oil through oil way*

$f = \frac{64}{\mathrm{Re}}$ *(friction factor of laminar flow through oil way)*

K *= loss coefficient associated with sudden expansions bends and contractions*

the loss through each branch of the oil system were equal when oil flow rate through EFG, Figure 4.19, was 3.4 l/min and oil flow rate through HJK was 1.1 l/min. Using these flow rates, one can calculate head loss through the entire oil supply and return oil ways. Head loss through the supply oil ways was 3.3×10^5 N/m^2, and 0.4×10^5 N/m^2 through the return oil way. During commissioning of the turbine module, the author pressurised the bearing cavity to 0.5×10^5 N/m^2 to ensure good scavenging of the bearing cavity. With a bearing cavity pressure of 0.5×10^5 N/m^2 and a head loss of 3.3×10^5 N/m^2 through the supply oil ways, the author predicted an oil pressure of 3.8×10^5 N/m^2 to deliver 4.5 l/min of coolant oil. The author measured oil pressure of 3.4×10^5 N/m^2 and deliver rate of 5 l/min during facility commissioning.

The oil system predicted head loss was acceptable; however, the split of oil between the two oil jets resulted in the downstream bearing of the matched bearing pair receiving 1.1 l/min of coolant oil, not the Rolls-Royce plc recommended 1.5 l/min. In practice, the author minimised this problem by running the oil system with a flow rate of 5 l/min, increasing flow rate through the second oil jet to 1.26 l/min. A reduction of coolant oil flow rate to a bearing will result in an increase in coolant flow temperature. The author repeated bearing power loss calculations (see Section 4.1.1) with an oil flow rate of 1.26 l/min when he calculated the predicted coolant oil temperature rise at 36 K. The SKF General Catalogue (1981) recommends a maximum coolant oil temperature rise of 80 K, so a 1.26 l/min oil flow was acceptable.

From a knowledge of the air motor's performance (used to drive the turbine to its re-run speed, see Section 4.2) and bearing power loss, the author estimated the time it takes to spin the turbine to its pre-run speed, Figure 4.20. The author also estimated the time it takes for the turbine to spin down from its post run speed under the action of bearing, carbon face seal and disc windage loss (see Section 4.2). It took six minutes to accelerate the turbine to its pre-run speed and decelerate from its post run speed. The author considered an oil supply system capable of delivering 4.5 l/min of oil for approximately double the expected total run time desirable. The author devised an oil flow system similar to Doorly's (1983), Figure 4.21, which incorporated 50 litre reservoir and drain tanks giving eleven minutes operating time. Once the reservoir emptied, the author used a rotary pump to refill the reservoir. He fitted the reservoir with an audio alarm, which sounded when 10 litres (≈ 2 minutes) of oil remained.

4.1.7 Bearing system instrumentation

The author constantly monitored the bearing system performance whilst spinning the turbine. Critical bearing system parameters were: bearing temperature, cage/shaft speed ratio and vibration level. The author incorporated thermo-couples into the bearing system over each bearing, Figure 4.3, and in the oil return line. During facility commissioning (see Chapter 6), the author monitored bearing temperatures and shut down the turbine air motor air supply if bearing or oil exit temperatures exceeded a temperature rise of 80 K.

Bearing design calculations (see Section 4.1.3) predicted bearing cage/shaft speed ratios for pure rolling of the ball bearings. By monitoring bearing cage speed and turbine speed, the author calculated bearing cage/shaft speed ratios. The author measured cage/shaft speed ratio by mounting 5 mm lengths of 1.0 mm diameter steel rod into the bearing cage of the single bearing and the upstream bearing of the tandem pair. He mounted inductive proximity detectors in the bearing housing to detect the passing of the rods, enabling him to calculate cage speed. Limited space around the downstream bearing of the matched bearing pair prevented the mounting of an inductive proximity detector so the author could not measure the bearing cage speed. The author matched the bearing pair, splitting loads evenly between them. Cage/shaft speed ratio for the upstream bearing of the pair, therefore, should be identical to the downstream bearing.

A velocity transducer mounted over the matched bearing pair measured velocity of the bearing housing. The International Standard IS0 2372 (1974) specifies limit values for the vibration severity of machines, using root mean square velocity as a significant parameter for characterising vibration severity. ISO 2372 prefers bearing housing and machine mounting points as measurement locations.

The IS0 standard gives example limits for six machine classes. Table 4.6 provides the limits for the class which applies to the turbine module.

Table 4.6
I.S.O. Standard 2372, mechanical vibration of machines

BALANCE QUALITY	*VIBRATION LEVEL*
Precision quality	*< 1.8 mm/s*
Commercially acceptable	*1.8 - 4.5 mm/s*
In need of attention	*4.5 - 11.2 mm/s*
In need of immediate attention	*11.2 – 28 mm/s*

Lifshits et al. (1986) studied vibration limits of rotating machinery and proposed vibration severity limits based on statistical and consensus evaluation of vibration and failure data for many operating units. Table 4.7 provides Lifshits et al's vibration limits which apply to the turbine module.

Table 4.7
Vibration limits of rotating machinery
from LIFSHITS et al. (1986)

BALANCE QUALITY	*VIBRATION LEVEL*
No fault	*< 1.6 mm/s*
Acceptable	*1.6 – 3.2 mm/s*
Marginal	*3.2 – 6.3 mm/s*
Failure probable	*6.3 – 12.7 mm/s*
Danger of immediate failure	*> 12.7 mm/s*

During operation of the turbine module, the author adopted vibration severity limits of up to 4 mm/s for normal operation and 10 mm/s for immediate shut down. Vibration levels of 4-10 mm/s required balancing the turbine to reduce the turbine's residual unbalance and therefore reduce vibration levels to below 4 mm/s. Primary responsibility for the balancing of the turbine module rotating system lay with Dietz (1988).

4.2 TURBINE AIR MOTOR

4.2.1 Power requirement

The turbine required a motor that could spin its pre-run speed of 6,500 rpm (see Section 3.3.2) prior to ILPT operation. During commissioning trials (see Section 6.4), the author ran the turbine to its post run speed of 10,000 rpm to establish the rotating system's dynamic performance. Before the author could select a suitable motor, he required a power estimate. He predicted bearing and carbon face seal losses at 2.9 kW and 0.77 kW respectively at 6,500 rpm and 4.25 kW and 1.18 kW at 10,000 rpm (see Sections 4.1.1 and 4.1.5).

An additional loss for a motor to overcome was disc windage. Lawson (1970) investigated B22 turbine windage loss and established an empirical correlation for windage,

$$P_l = 4.0x10^{-3} \rho \, U^3 d^2 \qquad - \quad 4.13$$

where ρ *= 1.225 kg/m*^{3}*, density @ atmospheric pressure*

d = 0.56 m, disc diameter

U = 190 m/s, disc rim speed @ 6,500 rpm

The author conducted initial commissioning trials at turbine speeds up to 6,500 rpm at atmospheric working section pressure, to allow ease of access to the working section. Equation 4.13 gives a calculated windage loss at 6,500 rpm and atmospheric working section pressure of:

$$P_l = 10.62 \ kW$$

One can repeat the above calculation at 10,000 rpm and atmospheric working section pressure,

$$P_l = 46.30 \ kW$$

A 46.30 kW windage loss was unacceptably high, but could be reduced by evacuating the working section prior to high speed commissioning trials. The author could readily attain a vacuum of 0.1 atmospheres in the turbine module. A ten fold density reduction produced a corresponding windage power loss reduction to 4.63 kW. Total turbine power loss at 6,500 rpm and atmospheric working section pressure was the sum of bearing, carbon face seal and windage losses,

$$P_l = 14.29 \ kW$$

Similarly, we can calculate turbine losses at 10,000 rpm and 0.1 atmospheres,

$$P_l = 12.06 \ kW$$

The worst case condition was, therefore, spinning the turbine to its pre-run speed with atmospheric pressure in the working section. In order to ensure the rotating system's rapid acceleration, and therefore short total facility operation time, the author recognised as nesessary a motor capable of producing more power than that required for steady state operation (see Section 4.2.2).

4.2.2 Design considerations

The author considered electric motors which were large compared to the available space within the turbine module core. The author did not favour the concept of mounting the motor outside the turbine module and driving the turbine through a radial shaft and gear box due to the potential alignment problems associated with leading a shaft into the turbine module core.

Hilditch (1989) described the turbine shaft, designed to carry signal conditioning circuits, which could have been susceptible to noise generated by the rotating coils and magnets of a large electric motor. This, coupled with the problem of physically fitting an electric motor into the turbine module core, led Heditch to look for another method of driving the turbine.

Air motors are purely mechanical devices, and are physically very compact compared to electric motors of equivalent power. Low power, or "model" air motors are available, and engineers generally use them for applications where space is very limited. Manufacturers produce model air motors in small numbers for a specialist market which are correspondingly expensive compared to higher power, but larger air motors. The smallest air motor available, without resorting to model air motors, produced 40 kW at 6,500 rpm and was physically small enough to fit into the turbine module’s core (with some modification of its casing), Figure 3.2. The air motor was capable of a wide operating envelope, producing up to 110 kW at 36,000 rpm, Figure 4.22, so it was clearly substantially underutilised to overcome estimated losses. However, limiting the pressure difference across it could reduce air motor power. By limiting air motor differential pressure to 1.5×10^5 N/m^2, the author estimated time to spin the turbine up to its pre-run speed (from air motor performance characteristics, Figure 4.22, and calculated power losses) at four minutes, Figure 4.20. The author calculated a further two minutes for the turbine to spin down from its post run speed under the action of bearing, seal and windage losses. By designing an air supply that could provide the air motor with a differential pressure of up to 10×10^5 N/m^2, which could be regulated down to the lower levels envisaged, the air supply could provide flexibility to increase air motor power if required (to drive through an unforeseen turbine module natural frequency, for example). Power and cost considerations resulted in the author's decision to incorporate a high power air motor into the turbine module.

The author designed an air supply system capable of supplying air to the air motor at $10\text{x}10^5$ N/m^2 (see Section 4.2.4) after consideration of the pressure losses incurred ducting air into and away from the module core.

4.2.3 Air ducting through the turbine module

The design of the AGV (see Section 4.3) was such that the turbine module core was supported from thirty two radial struts with the implication that the air motor inlet and exit air supply must route into and out of the core via the struts.

Inspection of the AGV struts (see Section 4.3.1), indicates the practicality of a maximum hole diameter through the upstream strut section of 20 mm and 12 mm through the downstream strut section. Of the thirty two AGV spokes, twenty four of the downstream, and twenty six of the upstream section were available for the inlet and exhaust ducting of the air motor's air supply, Figure 3.2.

Air fed to the air motor through the twenty four holes in the downstream strut section, and exhausted through the twenty six holes in the upstream section. From the air motor performance characteristics, Figure 4.22, the author found power and driving air volume flow rate for any given turbine speed and driving air inlet pressure. The motor required an estimated 14.29 kW to maintain 6,500 rpm which require 10 standard m^3/min of air at $2.0\text{x}10^5$ N/m^2, therefore requiring a flow rate of 5 m^3 /min (one standard m^3 of air is one m^3 at $1\text{x}10^5$ N/m^2 and 25°C). By assuming ambient temperature at 298 K (25°C), one can calculate the speed of sound from which air motor inlet and exhaust flow Mach numbers can also be calculated,

$$a = \sqrt{\gamma RT}$$

$$\therefore \quad a = 346 \; m/s$$

$$Flow\ rate\ \dot{q} = 5\ m^3/min = 0.083\ m^3/s$$

$$For\ twenty\ four\ 12\ mm\ diameter\ holes\ area,\ A = 2.73x10^{-3}\ m^2$$

$$flow\ velocity\ v_l = \frac{\dot{q}}{A}$$

$$v_l = 30 \; m/s$$

$$Inlet\ Mach\ number\ M = \frac{v_l}{a}$$

$$M = 0.09$$

$$Similarly\ for\ the\ exhaust\ M = 0.06$$

The use of twenty four feed and twenty six exhaust lines to and from the air motor through the spokes of the AGV ensured that velocities at the predicted flow rates were low, minimising pressure loss through them. Low velocities through air motor supply and exhaust lines also ensured volume flow rate could increase substantially without compressible effects becoming significant.

4.2.4 Air supply and control

The high pressure air supply available within the Osney Laboratory provides air at $27x10^5$ N/m^2. This has to be regulated down to $10x10^5$ N/m^2, the maximum air motor inlet pressure. The author identified a Class C4 25 mm pressure regulator, manufactured by IMI Bailey Birkett Ltd, which could regulate up to $27x10^5$ N/m^2, down to $10x10^5$ N/m^2 and pass between 0 and 46 m^3/min. The pressure regulator specification met, or was in excess of, the air motor requirements estimated in Section 4.2.3.

The Class C4 pressure regulator's mode of operation introduced pressure fluctuations into the air supply downstream of the regulator. Pressure upstream of the regulator on the regulator valve was balanced by downstream pressure and a spring. When the force closing the valve due to the spring and downstream pressure equalled the force opening the valve due to upstream pressure, there was no flow through the regulator. When downstream pressure fell, due to the air motor accepting mass flow, higher upstream pressure forced open the regulator, creating flow. When downstream pressure rose sufficiently, the valve closed again, until the downstream pressure once again fell sufficiently to cause the cycle to repeat. The author overcame pressure fluctuations due to the 'puffing' action of the regulator by incorporating a 1.5 m^3 settling tank downstream of the regulator, Figure 4.23. The settling tank provided the air motor supply; it did not come directly from the regulator.

Air motor air supply calculations (see Section 4.2.3) lead to a total of twenty four separate feed pipes to the air motor. The author constructed a manifold that fitted under the turbine module, accepting a single 50 mm bore line from the settling tank and radiating twenty four 25 mm bore air supply lines to the turbine module. By keeping air supply lines large, velocity in them remained low to minimise pressure loss.

The twenty six air exit lines through the first AGV section feed into an annular manifold, Figure.3.2. The author tapped the annular manifold at two locations on each side of the turbine module, with adaptor fittings connecting the manifold to two 100 mm bore exhaust pipes. He then fitted the exhaust pipes to a 0.6 m diameter, 1.2 m long acoustic diffuser. The acoustic diffuser silenced the exhaust which was otherwise unacceptably noisy.

The air motor air supply system, Figure 4.23, linked into the turbine module control system. Hilditch (1989) is primarily responsible for the turbine module control system. Her turbine control programme operated three valves in the 50 mm bore air supply line. The control valve, Figure 4.23, opened in 2% increments, allowing for adjustment of mass flow into the air motor. The control programme monitored bearing temperature, cage/shaft speed ratio, oil supply level and vibration level (see Section 4.1.7), turbine rotational speed and slip-ring coolant temperature. If any of the monitored parameters strayed outside limits preset in the control program, the programme automatically closed the air admittance valve and opened a vent, shutting off the air motors air supply. A pressure switch fitted in the 50 mm bore line which was set to close the air admittance valve and open the vent independently of the control programme if line pressure exceeds 10×10^5 N/m^2. Additional pressure relief valves were fitted to both the settling tank and supply line, set to operate at 10×10^5 N/m^2 as a final safety precaution.

During commissioning trials of the turbine module (see Chapter 6), the air supply and exhaust system servicing the air motor performed reliably over the course of approximately five hundred spinning runs. The air supply enables the air motor to drive the turbine to its pre-run speed prior to ILPT facility operation in the manner envisaged during initial design of the turbine module.

4.3 DEVELOPMENT OF THE ANNULAR GATE VALVE AND INLET DUCT

4.3.1 Design requirements

The primary requirement of the Annular Gate Valve (AGV) was to separate the ILPT pump tube from the working section until the required point during ILPT facility operation when it would open to allow test gas to flow from the pump tube into the working section. Prior to ILPT facility operation, pressure upstream of the AGV would be 8.02×10^5 Pa, with the working section evacuated. The AGV was, therefore, required to withstand the differential pressure and seal to vacuum. As the turbine module working section was annular, it required an annular valve.

Schultz et al. (1977) originally developed the ILPT facility, incorporating a two dimensional cascade of airofoils into its working section. When fitted with a two dimensional cascade of aerofoils, Schultz et al. (1977) was able to utilise a slide value to separate the ILPT pump tube and working section. The slide valve was fitted with a pneumatic actuator which would open it in 40 ms, at the desired time during ILPT facility operation. The pneumatic actuator was held in the 'valve closed' position using a perspex cylinder and compressed air applied to one side of the actuator to open it, with only the integrity of the perspex cylinder keeping it shut. At the required point during ILPT facility operation, a small explosive charge destroyed the perspex cylinder allowing the slide valve to open. This mode of operation had proved reliable, and the required trigger mechanism already existed. The author therefore considered desirable an annular valve utilising the same concept as the slide valve that would open in a similar time.

In addition to separating the ILPT pump tube and working section, the AGV needed to provide a mounting face for the bearing assembly and, therefore, support the entire rotating system. The bearing oil system required 4.5 1/min of oil to duct into and away from the bearings, as well as the monitoring and controlling of the bearing cavity pressure. The AGV design was, therefore, required to provide a rigid mounting for the bearing system that could also supply bearing services in addition to separating the pump tube and working section.

The air motor design required the air motor to situate on the turbine module centre line, upstream of the bearing system. The AGV design was, therefore, required to accommodate the air motor and duct air into and away from it. Due to the air motor requiring large air supply volume flow rates (see Section 4.2.2), the author recognised the air motor air supply comprised a significant factor in the AGV design.

The AGV concept was of two fixed annular rings with radial slots, forming the fixed upstream and downstream sections of the AGV, Figure 4.24. Between the up and downstream sections was a centre section that was free to rotate. The centre AGV section contained radial slots which could rotate so that they were either in line with, or blocking, the radial slots in the up and downstream AGV sections. By rotating the AGV centre section it could, therefore, block the flow of test gas, or allow it into the working section.

The upstream section of the AGV provided the surface upon which the piston in the pump tube came to rest at the end of ILPT operation. The strut leading edges incorporated a flat consisting of 44% of axially projected strut area, which provided the support over the piston front face to withstand worst case differential pressure and deceleration loads. Allen (1988), primarily responsible for the current piston design, reports this fully.

An AGV concept utilising fixed upstream and downstream sections enabled the author to use the spokes between radial slots to duct bearing and air motor services into the turbine module core. The downstream AGV section provided the required bearing system mounting. The author accomplished rotation of the AGV centre section using two pneumatic actuators, therefore employing the same principle utilised in the two dimensional cascade slide valve, and consequently, the same trigger mechanism.

When designing the AGV, the number of radial holes (or radial spokes) was a free variable. The B22 turbine contained thirty six vanes in a ring upstream of the rotor. To avoid valve spoke wakes carrying through the vanes in a circumferentially periodic manner, the number of struts, n, could not be equal to, or an integer divider of thirty six (the number of vanes); therefore, 36/n could not be an integer. A C.N.C. milling machine machined the AGV sections. So as to facilitate ease and accuracy of programming, the number of degrees of rotation from one strut to the next had to be a real number. Thirty two struts gives an angular rotation from one strut to the next of 11.25°, which fulfilled the above requirements. Air motor air supply calculations (see Section 4.2.2), indicated that the required volume flow rate of air for the air motor could duct into and away from the air motor through twenty four and twenty six struts respectively; therefore, thirty two struts was acceptable. The actuator stroke required to open the AGV with thirty two spokes was 35 mm, similar to that of the two dimensional cascade's slide valve which had opened reliably in 40 ms. The final AGV design, Figure 4.25, fulfils the design requirements, utilising two pneumatic actuators to open the valve and provide the required mounting and services to the air motor and bearing system.

4.3.2 Model testing of the annular gate valve

When fully open, the AGV concept requires at least 50% flow blockage to close the valve. In practice, the required overlap for '0' ring grooves between rotating and stationary parts of the valve results in 64% blockage at the inner annulus. High blockage through the centre section of the AGV required high diffusion rates through the downstream section as the author could not increase inner annulus radius or reduce sufficiently the outer radius to eliminate diffusion. The author identified the aerodynamic design of the whole valve and inlet duct at an early stage in the turbine module's design as a potential problem area involving undesired flow separation.

In order to investigate flow through the AGV and inlet duct, the author built and tested a full size two dimensional linear wooden model with seven struts at the correct velocity, but one third Reynolds number (limited by the wind tunnel). As peak blockage was at the inner annulus, the author modelled struts on 10% height strut sections to allow investigation of the strut hub region.

Diffusion rate through the downstream AGV section was reduced by adding a 50 mm strut trailing edge extension, Figure 4.26, resulting in an area ratio of 1:1.68 through a 115 mm AGV diffusion length at the hub. The outer annulus diameter at the start of the valve needed to match the pump tube bore diameter. The pump tube bore diameter was 50 mm larger than the B22 turbine vanes outer diameter. Diffusion rate through the AGV downstream section was reduced by blending the pump tube bore diameter into a parallel inlet duct through the AGV downstream section. The inner annulus reduced to as low a diameter as possible, the air motor mounting, Figure 3.2, making the minimum diameter 16 mm less than the vane inlet duct diameter. The author used the available 8 mm increase of radius through the AGV downstream section to reduce inner annulus diffusion rates. The outer annulus contraction started and finished with ellipses to avoid discontinuities in curvature in the outer annulus line. The AGV front face blended into the valve inner annulus wing a 2:l ellipse, the major axis the length of the upstream valve section.

The author painted the model matt black and fixed "tufts" (five millimeter long white cotton strands) to the inner annulus, outer annulus and struts. The tufts clearly indicated reversed flow through the downstream AGV section on the inner annulus. Flow reattached to the inner annulus approximately 100 mm downstream of the strut trailing edge plane. The author concluded that diffusion rate through the downstream vane section was too high, resulting in a large separation bubble that started at the onset of diffusion and reattached 100 mm downstream of the strut trailing edge.

The author tested the AGV design model with the least diffusion through the downstream section possible within the limitations of the turbine module design. Diffusion rates through the downstream AGV section could reduce by lengthening the strut trailing edge pieces; however, this would have reduced the length of inlet duct available for strut wakes to mix out. Incorporating a "hump" into the inner annulus, Figure 4.27, reduced the diffusion rate through the downstream AGV section, designed to give a smooth diffusion rate through the downstream valve section.

The author modified the model to incorporate the inner annulus hump, and tufted again. He tested the model at one third design Reynolds number, all tufts through the AGV downstream section indicating attached flow. The tufts on the rediffusion section of the inner annulus, whilst mostly pointing downstream, would intermittently reverse direction indicating some transitory back flow. An 8° inner annulus diffusion angle caused the diffusion rate along the re-diffusion section of the inner annulus. Sandborn and Kline (1961) investigated turbulent boundary layer separation and concluded that for diffusion, angles of less than 5° separation does not occur. This author's efforts to eliminate separation on the inner annulus by eliminating separation through the downstream AGV section resulted in transitory back flow, similar to Sandborn and Kline's observation.

After model testing of the second AGV design, the author received a quasi three dimensional time marching finite volume fluid flow prediction code, Q3D, from Cambridge University. He used the code to analyse the flow through the downstream AGV section for the two designs model tested, and then to design a third. The code is inviscid, using a coarse grid, Figure 4.28, to allow modification and quick reanalysis of passage geometry. Mach number distributions over the inner and outer annulus for the first AGV design indicated rapid, but reasonably smooth flow diffusion, Figure 4.29. Mach number distributions over the inner and outer annulus for the second AGV design (incorporating the inner annulus hump) indicated a reduction in diffusion, Figure 4.30, but local troughs and peaks in Mach number.

The author used Q3D to investigate numerous variations on the AGV downstream section and inlet duct design. Design objectives were smooth, equal diffusion rates on the inner and outer annulus. Requirements of a final design were reduced diffusion rates compared to the first design and an inner annulus hump with a re-diffusion angle of less than 5°. The final design prediction, Figure 4.31, achieved the desired objectives through the use of low angle straight lines. Any attempt to eliminate discontinuities in curvature through the use of blending curves produced undesirable peaks in inner and outer annulus Mach number distributions. The final prediction involves a redesigned inner annulus hump, Figure 4.32, which results in a final AGV and inlet duct design made up entirely of straight lines apart from the inner annulus vane inlet contraction.

The author incorporated the redesigned inner annulus hump into the model that was then tufted and tested. A stroboscopic light at frequencies from 1 Hz to 1,000 Hz illuminated the tufts to help spot any momentary tuft reversal. There was no evidence of separation. The author concluded that the flow attached with no evidence of steady state or transitory flow separation.

During model testing of the first two AGV designs, the author conducted total pressure loss and turbulence area traverses, to help interpret the tuft flow visualisation. With the design of an AGV that did not produce separated flow, the author measured loss and turbulence area traverses over three planes, Figure 4.33. The loss coefficient was,

$$\frac{P_{or} - P_{om}}{\frac{1}{2}\rho\, v_r^{2}} \qquad - \quad 4.15$$

where P_{or} *= Total pressure at the reference point*

P_{om} *= Total pressure at the measurement point*

$\frac{1}{2}\rho\, v_r^{2}$ *= Dynamic head at the reference point*

This definition of loss eliminated the effects of day to day variation in atmospheric pressure and velocity in the tunnel, allowing the author to directly compare loss data measurements on one day with those on another. The author chose the reference point as minimum total pressure loss at the vane leading edge at the centre of plane 3, Figure 4.33. He used this method to measure loss to mount a total pressure probe at the reference point where he measured total and static pressure using water filled manometers, Figure 4.34. He connected a third manometer to a total pressure probe in the measurement plane which moved from point to point over the traversing plane to enable calculation of loss at grid points. The author calculated each point loss using measured water heights. Assuming Bernoulli's equation,

$$\frac{1}{2}\rho\, v_r^{\,2} = \rho_w g\left[\Delta H_r - \Delta H_{or}\right]$$

$$and \qquad P_{or} - P_{om} = \rho_w g\left[\Delta H_{om} - \Delta H_{or}\right]$$

$$\therefore \qquad \frac{P_{or} - P_{om}}{\frac{1}{2}\rho\, v_r^{\,2}} = \frac{\rho_w g\left[\Delta H_{om} - \Delta H_{or}\right]}{\rho_w g\left[\Delta H_r - \Delta H_{or}\right]}$$

$$\therefore \qquad Loss,\ C_l = \frac{\Delta H_{om} - \Delta H_{or}}{\Delta H_r - \Delta H_{or}} \qquad - \quad 4.16$$

Once the author calculated loss for a nine by six grid of measurement points in each measurement plane, he hand constructed contour plots of loss.

The author conducted turbulence level area traverses in the same three measurement planes in which he measured loss, using a constant current hot wire anemometer. Using King's (1914) method, he used the hot wire anemometer output A.C. and D.C. voltages to calculate turbulence level at each measurement point.

$$v^2 = A_k + B v_l^{\,p} \qquad (King's\ Law) \qquad - \quad 4.17$$

Taking logs of Equation 4.17 and differentiating,

$$2\frac{dv}{v} = \frac{pBv_l^{\,(p-1)}}{A_k + Bv_l^{\,p}} \cdot dv_l$$

$$= \frac{dv_l}{v_l} \cdot \frac{pBv_l^{\,p}}{A_k + Bv_l^{\,p}}$$

$$therefore \qquad = \frac{dv_l}{v_l} = \frac{dv}{v} \cdot \frac{2}{p} \cdot \frac{A_k + Bv_l^{\,p}}{Bv_l^{\,p}} \qquad - \quad 4.18$$

substituting Equation 4.17 into Equation 4.18,

$$\text{therefore} \quad = \frac{dv_l}{v_l} = \frac{2vdv}{p(v^2 - A_k)} \qquad - \quad 4.19$$

where v = *hot wire D.C. voltage*

dv = *hot wire A.C. voltage*

A_k = *hot wire 'no flow' D.C. voltage*

p = *power to which velocity is raised in Kings Law*

The author calibrated the hot wire against a pitot tube in steady flow in the tunnel he used to model test the A.V.G. and inlet duct. He mounted the hot wire in the centre of plane one, where turbulence level was low, and read D.C. voltages with one, two, three and four wind tunnel fans switched on, Figure 4.35. King's Law breaks down at low flow velocities as it assumes forced convection from the wire. Mee (1987) investigated the performance of constant current hot wire anemometers and concluded that at atmospheric pressure, natural convection from a hot wire was close to the forced convection that the author predicted, using King's Law when extrapolated to zero velocity. Therefore, the author obtained a fifth hot wire calibration point at zero velocity by placing the hot wire in a covered container and allowing it to stand. He then measured the hot wire D.C. output voltage.

When using hot wires, Lomas (1986) recommends evaluating the calibration constant A_k immediately prior to using the hot wire. This enables one to account for the effect of D.C. drift of the hot wire. The author found the calibration constant A_k by placing the hot wire in a closed container prior to use. The square root of the wire output voltage then gave the calibration constant A_k.

Turbulence levels that the author measured at plane one, Figure 4.36, indicated turbulence levels near the inner annulus characteristic of separated flow. Strut wakes were "washing out" in plane two, with circumferentially uniform turbulence by plane three. The author plotted plane two turbulence data in its "raw" form, Figure 4.37, to show the density of measured points from which he produced the contour plots.

Simpson et a1. (1981a) investigated the velocity fluctuations in backflow and found them of the same order as the free stream velocity. Simpson (1981b) defined incipient detachment as 1% backflow occurring for time periods sufficiently small to prevent cotton tufts responding to it.

Transient reversal of flow at the inner annulus will result in high loss in this region. Measurements, located at plane one, Figure 4.38, indicated high loss at the inner annulus. Strut wakes wash out (plane two) before the vane leading edge plane (plane three), giving a reasonably circumferentially uniform distribution of loss at plane three. Loss was highest at plane three on the inner annulus, indicating low momentum fluid (arising as a consequence of the diffusion through the downstream AGV section) transported along the inlet duct to the vane leading edge plane. As with turbulence data, Figure 4.39 plots the measured plane two loss data its "raw" form.

Flow visualisation using cotton tufts gave no indication of flow separation through the downstream valve section. The author used a second flow visualisation technique, painting a mixture of titanium dioxide and paraffin on the gate valve struts in the model. When the paraffin evaporated, streaks of titanium dioxide remained, forming a pattern of 'flow lines' on the surface. This technique was similar to that of Stalker (1956) who concluded that the direction indicated by 'streaks' was identical to that indicated by tufts. The resulting patterns of titanium dioxide showed clear evidence of a separation line at the AGV strut trailing edge blend line, Figure 4.40, with no similar separation lines on the strut itself, Figure 4.41. This was further evidence that the flow was attached to the struts.

The author found a solution to the high turbulence levels on the inner annulus when he fitted a fine wire gauze across the strut trailing edges. Engineers have used fine wire gauzes for many years in wind tunnels to reduce turbulence levels. Laws et a1. (1978) discussed a gauze pressure drop coefficient, k, that previous workers used as a means of characterising a gauze, where k is,

$$k = \frac{\Delta P}{\frac{1}{2}\rho\, U^2}$$

where ΔP *= pressure drop across the gauze*

ρ *= air density*

U *= mean gauze approach velocity*

Dryden et a1. (1947) suggested an optimum pressure drop coefficient of 2.8, concluding that at this value of k, the gauze obtained a uniform exit velocity profile regardless of input velocity profile. By fitting the gauze with a pressure drop coefficient close to 2.8, flow downstream should have a uniform velocity, and therefore loss profile. The presence of fine wire gauze would also reduce turbulence level. The author fitted gauze with a measured pressure loss coefficient of 2.2 across the strut trailing edges in the AGV model and repeated turbulence and loss area traverses in plane three, Figure 4.42 and 4.43. The effect on turbulence level was dramatic, reducing it to a radially and circumferentially uniform measured level of 2.5% ± 0.5%.

Annand (1953) identified pressure loss coefficient, k, as a function of Reynolds number and gauze porosity (where it defied gauze porosity as gauze open area divided by its total area), and proposed an empirical correlation relating the three parameters. Kempson and Watkins (1987) used the correlation of Annand, concluding that increasing Reynolds number to its design value would not change the authors measured pressure loss coefficient of 2.2. Kempson and Watkins continued the author’s work, measuring velocity and turbulence profiles, Figure 4.44, at plane one, mid-way between strut trailing edges. The improvement in flow characteristics as a consequence of the gauze was significant. After testing four different gauzes covering a range of pressure loss coefficients and porosity, Kempson and Watkins concluded that the gauze the author first used was best suited for the turbine module. The author therefore decided to fit a similar gauze to that model tested to the turbine module.

One can regard the AGV downstream section as a straight walled diffuser. Wilson (1984) investigated the performance of straight walled diffusers and defined a pressure rise coefficient $C_{pr(th)}$,

$$C_{pr(th)} = \frac{P_c - P_d}{\frac{1}{2}\rho\, v_l^{2}}$$

where P_c *= Static pressure at diffuser entry*

P_d *= Static pressure at diffuser exit*

$\frac{1}{2}\rho\, v_l^{2}$ *= Dynamic head at diffuser entry*

The third section of the AGV had an inlet to exit area ratio of 1.68. By assuming incompressible flow through the AGV, one can show that for an area ratio of 1.68,

$$\frac{P_c - P_d}{\frac{1}{2}\rho\, v_l^{2}} = 0.65$$

Wilson considered the performance of a range of straight walled diffusers, plotting theoretical pressure rise coefficient, $C_{pr(th)}$, against measured pressure rise coefficient, $C_{pr(ac)}$, over a range of Reynolds numbers, Figure 4.45. Wilson considered diffusers with wall angles between 3° and 8°. As the AGV downstream section had a wall angle of 6.8°, Wilson's method was suitable for predicting AGV performance. The method he used to account for Reynolds number was a coefficient, $Re_{\delta*}$,

$$Re_{\delta*} = \frac{2\delta_c^{*}}{Y_c}$$

where δ_c^{*} *= Boundary layer displacement thickness at diffuser entry*

Y_c *= 14 mm, width at diffuser entry*

In order to evaluate $Re_{\delta*}$, the author required an estimate of the AGV downstream section's inlet boundary layer displacement thickness. He could reasonably approximate the first two sections of the AGV to a 100 mm flat plate with zero pressure gradient. The Reynolds numbers in the model and turbine module (at design conditions) based on a length of 100 mm are,

$$Re_{(model)} = 0.374x10^6$$

$$Re_{(rig)} = 1.900x10^6$$

Shames (1982) cites the relationship between Reynolds number and boundary layer displacement thickness as,

$$\textit{For laminar boundary layers} \qquad \frac{\delta^*}{x} = 1.73\,\mathrm{Re}^{-0.5} \qquad - \quad 4.20$$

$$\textit{For turbulent boundary layers} \qquad \frac{\delta^*}{x} = 0.0463\,\mathrm{Re}^{-0.2} \qquad - \quad 4.21$$

with a critical laminar/turbulent transition Reynolds number of $3.5x10^5$, indicating that boundary layers in both the model and turbine module are turbulent at the start of diffusion. Using Equations 4.20 and 4.21, and assuming point transition when Reynolds number reaches the critical value, one can show that at the start of diffusion,

$$\delta^* = 0.294 \ \textit{mm (model)}$$

$$\delta^* = 0.248 \ \textit{mm (rig)}$$

therefore enabling one to evaluate Reynolds number coefficient, $Re_{\delta*}$,

$$Re_{\delta*} = 0.042 \ (model)$$

$$Re_{\delta*} = 0.035 \ (rig)$$

The author calculated the theoretical static pressure rise coefficient, $C_{pr(th)}$, as 0.65. Using Wilson's correlation, Figure 4.45, observe that the actual model pressure rise coefficient, $C_{pr(ac)}$, was higher for the turbine module than the model. Increasing the Reynolds number from the model to that in the turbine module at design conditions increased the actual diffuser performance. When tested, the linear model did not suffer from flow separation. The correlation of Wilson indicates the turbine module will be less likely to separate than the model; therefore, the author concluded that attached flow in the model would result in attached flow in the turbine module.

4.3.3 Flowfield predictions

Once the author achieved an AGV and inlet duct that did not produce separated flow when model tested, he analysed it using a Rolls-Royce plc axi-symmetric streamline curvature fluid flow prediction programme, Q263. In this way, he could predict the effect of applying the AGV design to an annular duct at B22 turbine design conditions. The Q263 programme could not model individual struts, but radial distribution of strut blockage could be input at different axial locations in Q263, allowing strut blockage simulation. The author used the inviscid Q263 AGV flow field prediction as input for a Rolls-Royce plc boundary layer code D06, allowing him to predict the state of the boundary layer on inner and outer annulus through the AGV.

The prediction of axial velocity at B22 turbine design conditions from Q263, Figure 4.46, was a mid-passage prediction. The results represent velocity distribution mid-way between two struts. Axial velocity peaks at 63 m/s on the valve inner annulus, a Mach number of 0.16 indicating that the flow remains incompressible through the AGV. Flow diffusion occurs through the first half of the valve downstream section, flow velocity falling to 42 m/s less than half way through the valve. While this can appear as undesirably rapid flow diffusion, boundary layers will be thinnest and have low shape factors in this region, and therefore are more able to withstand adverse pressure gradients than nearer the strut trailing edge.

Hoheisel and Seyb (1986) describe the boundary layer prediction code DO6, which uses an integral method to determine boundary layer parameters. They specified boundary layer thickness as zero at the AGV front face and specified turbulence level of 4% over the entire boundary layer length. DO6 requires specification of the boundary layer transition point using Shames's (1982) method, which calculates the transition point from laminar to turbulent boundary layer as 18 mm downstream of the AGV front face.

DO6 predicted boundary layer displacement thickness δ^*, Figure 4.46, and momentum thickness Θ. Schlichting (1979) defined boundary layer shape factor, H_* as δ^*/Θ. For turbulent boundary layers, Schlichting (1979) cites a value of shape factor of H_* of 2.274 as the value at which boundary layer separation occurs. Using displacement and momentum thickness calculated by DO6, the author calculated shape factor that had a peak value of two on the inner annulus near the strut trailing edges. This shape factor value was high, but not separated. Model testing of the final AGV design indicated that the flow was close to separation on the inner annulus at the strut trailing edge plane, but attached.

The results of DO6 gave the author confidence in the AGV design, indicating he could utilise it in an annular configuration. Wilson's method (1984) (see Section 4.3.2) indicated that increasing Reynolds number to that encountered in the turbine module would improve AGV performance. On this basis, the author concluded that the final AGV design model he tested was suitable for use in the turbine module.

4.4 THE SECOND THROAT

4.4.1 Design Requirements

The author required a throat downstream of the turbine in order to adjust turbine exit static pressure and, therefore, Mach number. The author required the 'second' throat (the vane throat being the first) to have a variable area to allow change to the turbine exit Mach number by altering the second throat area.

A second requirement of the second throat design was that the potential flow field around the second throat to exert no influence on the turbine exit flow field. Axial length was at a premium in the turbine module, so it required an axially compact means of decoupling turbine exit and second throat inlet flow fields.

4.4.2 The second throat design concept

The requirement that the turbine module should form a replacement ILPT facility working section placed severe constraints on its axial length. Decoupling turbine exit and second throat inlet flow fields using a step expansion downstream of the turbine provided a suitably compact means of decoupling the flow fields, Figure 3.2. The intense mixing immediately downstream of a step expansion would prevent the second throat exerting any influence on the turbine exit flow field.

The author incorporated a parallel annulus with a length equivenant to five mid-height blade axial chords downstream of the turbine. The parallel annulus facilitated measurement of turbine downstream total and wall static pressures. The author designed the second throat as two rings, each of which contained eleven equally spaced holes, Figure 4.47. The rings could rotate relative to one another, so that the holes in one ring either coincided with the holes in the second, or the spokes between them, to increase or reduce the second throat area. Therefore, by rotating the two rings relative to one another, one could adjust the second throat area.

4.4.3 Design calculations

The author's design calculations for the second throat were to determine the area necessary for the second throat to achieve the required B22 blade mid-height exit Mach number. The most basic assumption about the step expansion was that the flow crossing it lost a dynamic head; therefore, static temperature and pressure at rotor exit were equal to the total temperature and pressure upstream of the second throat. The author calculated static temperature and pressure at rotor exit (see Section 3.3.2) as 277.5 K and 2.81×10^5 Pa respectively. Mass flow rate through the turbine was calculated to be 29.13 Kg/s (Section 3.3.2). One can express the mass flow rate through the second throat as,

$$\dot{m} = \rho^* A^* U^*$$

as $\rho = P/RT$ and $U^* = M\sqrt{\gamma R T^*}$ so that,

$$\dot{m} = \frac{\rho^*}{\rho_0} \cdot \frac{P_0}{RT_0} \cdot A^* \cdot M \sqrt{\gamma R \frac{T^*}{T_0} T_0} \qquad - \quad 4.22$$

Assuming a Mach number of 1 at the throat,

$$\frac{T^*}{T_0} = 0.833 \quad and \quad \frac{\rho^*}{\rho_0} = 0.634$$

Substituting the above into Equation 4.22,

$$A^* = 43x10^{-3} \; m^2$$

The required second throat area will be larger than that predicted due to the discharge coefficient of the eleven holes that constitute the second throat. The complexity of the step expansion/second throat combination made an accurate estimate of second throat discharge coefficient difficult. The British Standard on the specification for square edged orifice plates, BS1042, Section 1.1 (1981) cites discharge coefficients of 0.6 as the lowest encountered in orifice plates, implying a required second throat area of 72x10^{-3} m^2. The author, therefore, concluded that the actual second throat area would be greater than 43x10^{-3} m^2 and less than 72x10^{-3} m^2. The author designed the second throat with the capacity to vary its area from 10x10^{-3} m^2 to 100x10^{-3} m^2. During fine tuning of the ILPT during facility commissioning (see Section 6.4), the author measured the second throat area required to achieve design rotor exit Mach number which was 52.8x10^{-3} m^2. The measured value fell between the upper and lower estimates of required second throat area and was within the range of second throat areas attainable. The author concluded that despite the difficulty associated with the accurate prediction of required second throat area, the crude first order method had proved adequate.

4.5 TURBINE SPEED AND POWER MEASURMENT

4.5.1 Introduction

The author accomplished turbine speed measurement using four ’shaft encoder’ discs mounted on the turbine shaft, Figure 4.3. A shaft encoder disc consists of a 74 mm clear plastic disc with black radial lines around the circumference. The author mounted a Light Emitting Diode (L.E.D.) on one side of each shaft encoder disc, with a photo-detector on the other. When a clear portion of shaft encoder disc separated an L.E.D. and photo-detector, the author connected the photo detector output such that its output voltage was +5v. When separated by a black line, the output voltage was -5v. The four shaft encoder discs had 1, 36, 60 and 200 lines around their circumferences respectively.

The author used a frequency to voltage converter using the square wave output from the photo-detector of the one line disc to provide a D.C. voltage, the magnitude of which was proportional to the input square wave voltage frequency, and therefore, turbine speed. He monitored the frequency to voltage converter output voltage via the turbine module control program, Figure 4.48, which displayed as a real time speed verses time trace, enabling him to see the turbine speed history.

The output from a frequency to voltage converter was a D.C. voltage with an A.C. component superimposed. The frequency of the A.C. component was equal to the frequency of the input square wave, and originated as a consequence of the frequency to voltage convertor’s mode of operation (see Section 4.5.2). The A.C. component on the output from a frequency to voltage converter using a square wave voltage of a one line disc as input was equivalent to ±25 rpm error in turbine speed measurement at design speed. This error was tolerable for setting the turbine pre-run speed before ILPT operation, but not for triggering the transient data recorders (see Section 4.5.3) during ILPT operation. By using the square wave voltage output from a 200 line disc as input for a frequency to voltage convertor, the output voltage A.C. component was two hundred times higher and could more easily be filtered out using a passive filter (see Section 4.5.2), reducing error in turbine speed measurement to ±1 rpm. The author used this accurate speed measurement as input for a voltage comparator. When the comparator input voltage reached the voltage equivalent to 8,380 rpm, the comparator output voltage changed from +5v to -5v, triggering the transient data recorders that proceeded to take data from blade mounted instrumentation for 7 ms. After 7 ms, turbine speed had reached 8,490 rpm, so passing through turbine design speed during the data acquisition period.

The transient data recorder recorded the square wave output voltages from the photo detectors of the 1, 36 and 60 line shaft encoder discs, in addition to the output of the blade mounted instrumentation. The author positioned the one line disc relative to its photo-detector such that its output changed state as the first instrumented blade passed the vane at turbine module top dead centre. The author fitted the turbine module with thirty six vanes; therefore, one cycle of the output from the 36 line disc represented the rotation of the disc required to move a blade from one vane to the same position relative to the next. The output from the 60 line disc photo-detector performs a similar function, as there are sixty blades. One cycle of the 60 line disc photo-detector represents the rotation of the disc required to move a blade to the same position relative to a vane as the previous blade.

The author measured both turbine speed and output of the comparator using the PDP11/34 computer (see Section 3.5.1). This allowed him to measure turbine speed during ILPT facility operation, as well as the transient recorder trigger point during an ILPT facility run. The slope of the speed/time trace was the turbine’s angular acceleration, from which the author was able to derived turbine power (see Section 4.5.4).

4.5.2 Speed Measurement

The author measured turbine speed using a one line shaft encoder disc fitted with an RS 304-560 slotted optical switch. The slotted optical switch comprised an infra-red Light Emitting diode (L.E.D.) and photo-detector with integral Schmitt trigger and output stage, Figure 4.3. The photo-detector +5v/-5v output square wave frequency was proportional to turbine speed, and used as input to an LM2917N-8 frequency to voltage converter Integrated Circuit (I.C.). The frequency to voltage converter I.C. works on a charge pump technique, Figure 4.49, and one can externally configure it to accept the required input frequency range. For a one line shaft encoder disc at 10,000 rpm (turbine peak speed), the author picked the photo-detector square wave frequency of 167 Hz as an upper limit on frequency. He chose an upper limit of +5v allowing the following I.C. external components calculation,

$$V_0 = I_0 R_*$$

where $V_0 = 5$ *v (max), I.C. output voltage*

$I_0 = 185$ *μA, from manufacturer's data sheet*

$$\therefore \quad R_* = 27 \ k\Omega$$

$$\textit{Pick standard component value, } R_* = 26 \ k\Omega, \ V_0 = 4.8 \, v$$

From manufacturer's data sheets,

$$I_0 = V_z f_{in} C_1$$

$$\therefore \quad V_0 = V_z f_{in} C_1 R_* k_i$$

$$C_1 = \frac{V_0}{V_z f_{in} R_* k_i}$$

where $V_z = 7.56$ *v, from manufacturer's data sheet*

$f_{in} = 167$ *Hz, input square wave frequency*

$K_i = 1$ *output circuit gain constant*

$$\therefore \quad C_1 = 146x10^{-9} \ F$$

The value of C_2, depends on acceptable I.C. response time and output voltage ripple, V_{ri}. For turbine speed control prior to ILPT operation, speed changes occurred over the course of seconds; therefore, a filter cut off frequency, f_c, of 5 Hz was acceptable, as the resistor R_1, and capacitor C_2, acted as an RC filter,

$$f_c = \frac{1}{2\pi} \cdot \frac{1}{R_1 C_2}$$

$$\therefore \quad C_2 = \frac{1}{2\pi R_1 f_c}$$

$$\textit{therefore} \quad C_2 = 1.00x10^{-6}\ F$$

Using C_2 and the other calculated component values, ripple voltage, V_{ri}, one can calculate from Equation 4.23 (from manufacturer's data sheet),

$$V_{ri} = \frac{V_z}{2} \cdot \frac{C_1}{C_2}\left[1 - \frac{V_z f_{in} C_1}{I_0}\right] \qquad - \quad 4.23$$

Using Equation 4.23 with an input frequency of 108 Hz, equivalent to a turbine speed of 6,500 rpm,

$$V_{ri} = 0.196\ \ v\ \textit{(peak to peak)}$$

In practice, the turbine control program interpreted this output voltage ripple as a ±25 rpm uncertainty in speed measurement, as the software samples the I.C.'s output voltage fifty times, then averages, before applying the appropriate calibration and displaying turbine speed.

The 5 Hz cut off frequency and ±25 rpm uncertainty in turbine speed was adequate for turbine speed control prior to ILPT facility operation; however, ILPT facility operation required a low ripple measurement of turbine speed to trigger the transient data recorders (see Section 3.1.3). The author devised a second independent method of measuring turbine speed for triggering data transient recorders in order to keep turbine control and data acquisition systems separate. The author utilised the same concept as that used previously of a shaft encoder disc and slotted optical switch, this time in conjunction with a 200 line shaft encoder disc. The author picked a filter cut off frequency of 1 kHz as an upper limit of likely turbine speed change. At the turbine design speed, 8,434 rpm, the 200 line disc photo-detector output frequency was 28 KHz. The frequency to voltage convertor output stage extended to a 5 pole Butterworth filter to eliminate the 28 kHz voltage ripple. A five pole filter requires one decade in order to work effectively; therefore, a 1 kHz cut off was acceptable.

The output stage of the frequency to voltage convertor I.C. forms the single pole of the five pole filter, Figure 4.50, standard component values for the filter giving rise to filter cut off frequencies close to 1 kHz. The practical realisation of the low ripple measurement of turbine speed, Figure 4.51, utilises two of the four operational amplifiers in an LM324 quadruple operational amplifier I.C., measured output ripple less than 1 mv at 28 kHz, which was equivalent to a ±1 rpm error in speed. A five pole Butterworth filter introduced time shift into the output signal at 0.5 ms, which resulted in the measured turbine speed lagging approximately 5 rpm behind the turbine's actual speed. A mercury switch measured the time response of the entire frequency to voltage I.C. and filter to switch the input square wave from 10 kHz to 27 kHz, representing a step change in speed from 3,000 rpm to 8,000 rpm (assuming output from a 200 line shaft encoder disc). The circuit output took 2 ms to stabilize at the new output voltage after switching the input, corresponding to a rate of rise of 2,500 rpm per ms, an order of magnitude faster than the turbine speed changed during ILPT operation. This gave the author confidence in the circuit's ability to follow actual turbine speed changes.

4.5.3 Transient recorder trigger

The author utilised the low ripple output voltage measurement of turbine speed as input to a comparator that linked to the external trigger of the transient data recorders. The author used an LM339 I.C. containing four operational amplifiers as a basis for a dual comparator, Figure 4.52, one of which triggered the transient data recorders.

Prior to ILPT facility operation, the author set the comparator reference voltage to trigger the transient data recorder at 8,380 rpm. He achieved this by setting a square wave generator to 27.93 kHz and connecting it to the low ripple output voltage speed measurement systems input. He then turned down the comparator reference voltage until the output changed state, at which point reference voltage and frequency to voltage converter I.C. output voltage were equal.

4.5.4 Power measurement

The author measured turbine speed using the PDPl1/34 computer to establish turbine acceleration during ILPT operation. A least square line of best fit through the speed/time trace enabled the author to calculate average acceleration during ILPT facility operation, Figure 4.53, as the slope of the line was angular acceleration, $\dot{\omega}$. The author measured the moment of inertia of the turbine rotating system at 1.64 kgm^2 (see Section 5.4). With known moment of inertia and turbine design speed plus measured turbine angular acceleration each time the ILPT facility was operated, the author was able to calculate turbine power during each "run" as,

$$Turbine\,power\;\; P_w = J\omega$$

where J *= torque, Nm*

ω *= turbine speed, rad/s*

$$also \qquad J = I\dot{\omega}$$

where I *= rotating system moment of inertia, kgm*^{2}

ω *= turbine angular acceleration, rad/s*^{2}

Measured turbine power will be less than total turbine power due to bearing, seal and disc windage losses,

$$\textit{Therefore total turbine power, } P_w = I\omega\dot{\omega} + P_l \qquad - \quad 4.37$$

where P_l *= bearing seal and windage power loss*

In practice, power losses were approximately 7 kW (see Section 6.4.3). The turbine produced 2.36 MW and therefore neglecting power losses resulted in an error of 0.3%. The author considered the error associated with neglecting power loss small and consequently, did not consider it during analysis of the turbine performance (see Chapter 7). When calculating time varying turbine non and quasi non dimensional groups during ILPT facility operation, the code ROTOR (see Appendix 1) utilised measured turbine speed and acceleration. Hilditch used the transient data recorder trigger to facilitate measurement of blade heat transfer rates at turbine design speed fully reported in Hilditch (1989).

CHAPTER FIVE

STRESS ANALYSIS OF THE TURBINE DISC AND BLADE

5.1 THE REQUIRMENT FOR STRESS ANALYSIS

Rolls-Royce plc designed the B22 turbine and calculated stress levels in the turbine disc and blade using hand calculations. As a result, the author did not know the detailed disc and blade stress distribution. The proposed mode of operation of the turbine module (see Section 3.1.3) involved the turbine module accelerating from 6,500 rpm to 9,800 rpm during the 213 ms ILPT run time, with gas loads applied and removed from the turbine at the start and end of ILPT facility operation. The novelty of this application was such that no literature reported a comparable turbine test facility. Thus, the author concluded that a detailed prediction of the turbine module rotating system behaviour under load was desirable.

Ainsworth et al. (1989) planned to instrument the B22 turbine's blades at their mid-height section with thin film thermometers, or "gauges". Hilditch (1989) used the thin film gauges to study blade heat transfer rates and fully reported this. The prime reason for conducting the three dimensional blade stress analysis was to establish the uniformity of the strain distribution around the blade mid-height section under design condition loads, as the thin film gauges were strain sensitive. Hand calculations of the expected blade stress levels gave the author confidence that there was no danger of reaching the blade material's Ultimate Tensile Strength (U.T.S.), but gave no information about the uniformity of the stress distribution at the blade mid-height section.

Moir (1987) described the finite element analysis software FESDEC and solid modelling software MODEL. The author used FESDEC and MODEL to perform the stress analysis, running both on a Hewlett Packard 9836 mini computer.

5.2 STRESS ANALYSIS OF THE TURBINE DISC

5.2.1 Modelling assumptions

The turbine rotating assembly was axi-symmetric (with the exception of bolt holes) and, therefore, the author could accurately model it as an axi-symmetric problem, Figure 5.1. The author suppressed all radial and axial movement of the model along the bearing outer race and modelled the turbine shaft and bearings using few elements to allow the concentration of elements in areas of the model where he anticipated high stress levels.

One can derive the forces on an accelerating rotating assembly by considering the transformation from a coordinate system rotating with the assembly to a stationary one. Consider the point P, Figure 5.2, on a disc that has angular velocity ω, relative to a stationary coordinate system xyz. By writing the displacements l and r in vector form displacement, one can write velocity and acceleration of point P,

$$\beta = l + r$$

$$\dot{\beta} = \dot{l} + \dot{r} + \omega r$$

$$\ddot{\beta} = \ddot{l} + \ddot{r} + \omega(\omega r) + \dot{\omega} r + 2\omega\dot{r} \qquad - \quad 5.1$$

where $\ddot{l}$ = *linear acceleration of the disc in the x direction*

$\ddot{r}$ = *linear acceleration of the disc in the radial direction*

$\omega^2 r$ = *radial centripetal acceleration*

$\dot{\omega} r$ = *tangential acceleration due to the angular acceleration of the disc*

$2\omega\dot{r}$ = *Coreolis, or gyroscopic, acceleration*

The constrains used by the author prevented the turbine disc from moving radially or axially, the only permitted motion was rotation about x, the disc centreline, therefore,

$$\ddot{l} = \ddot{r} = \dot{r} = 0$$

$$\therefore \quad 2\omega\dot{r} = 0$$

Therefore, Equation 5.1 reduces to,

$$\ddot{\beta} = \omega^2 r + \dot{\omega} r$$

At the turbine design point ω = 883 rads/s, $\dot{\omega}$ = 1,630 rads/s^2 and the radius of the turbine disc r = 0.255 m,

$$\textit{Centripetal acceleration } \omega^2 r = 199{,}00 \ m/s^2$$

$$\textit{linear tangential acceleration } \dot{\omega} r = 416 \ m/s^2$$

As the centripetal acceleration was three orders of magnitude larger than the tangential acceleration, the author neglected tangential acceleration when loading the disc/shaft model.

Additional sources of load on the turbine disc/shaft model arise as a consequence of the turbine blades. The loads imposed on the disc by the blades comprised of a radial centrifugal load due to the blades (and their root fixing) finite weight, and tangential and axial gas loads due to the pressure difference and momentum change across the blade (see Section 4.1). One can calculate the radial force on the blades and their root fixing due to rotation as force, F_f expressed as $m\omega^2 r$. Given the centroid radius, r, and mass, m, of the blades and their root fixings, the radial force on the turbine disc imposed by the blades and their root fixing due to rotation at turbine design speed was 1.17×10^6 N.

5.2.2 Model loading and constraints

The author built the disc/shaft model from nine separate models, Figure 5.3, where each model was an individual part of the rotating system. The author then restrained the nine sections of the disc/shaft model as realistically as possible to simulate the presence of bolted flanges and interfaces between adjacent pieces. The restraints around the blade root take into account the absence of the turbine blade. The presence of the blade platform would limit motion of the front and rear blade retaining ring. By assuming the blade infinitely stiff, radial motion of the front and rear blade retaining rings must equal radial motion of the root fixing. The author restrained movement of the front and rear blade retaining rings to equal radial motion of the root fixing. The author applied the radial force of the blades and their root fixings as a distributed load.

5.2.3 Load case results

The author loaded the axi-symmetric disc/shaft model in three ways to provide information about its behaviour under load. First, the author loaded the model centrifugally, then centrifugally with radial blade load and finally with centrifugal, radial blade and axial gas loads. In this way, the author could assess the effect of the radial blade and axial gas load on disc stress and deflection.

Using FESDEC, the author loaded the disc/shaft model centrifugally at design speed. The results predicted a peak stress on the disc inner bore of 180 MN/m^2, Figure5.4. Using Baumister's (1978), one can calculate rotating disc stress. At design speed, the peak hoop stress on the inner bore of a rotating disc, with the same inner and outer radius as the turbine disc, was 266 MN/m^2. This result was plausible as the disc was not a simple disc, but heavily cut away, thus reducing the load on the inner bore. The author then modified the disc/shaft model by the addion of the centrifugal radial load imposed on the disc by the blades and their root fittings. The author re-ran FESDEC and observed the predicted stress levels generally increasing, with peak stresses of 240 to 260 MN/m^2 in the fillet radii around the mini disc/main disc interface, Figure.5.5 and 220 MN/m^2 on the disc inner bore. The addition of axial gas load has the effect of slightly increasing stress levels in the downstream half of the split disc, Figure 5.6, so that peak stress in the disc inner bore increased to 240 MN/m^2. The radial growth of the turbine blade root fixing was 137x10^{-6} m (0.0054") with an axial movement of 130x10^{-6} m (0.0051").

The disc material was JETHETE, with a yield stress of 1,150 MN/m^2 at ambient temperature. The author predicted stress concentration factors of 1.5 around non axi-symmetric features (such as bolt holes) using Peterson's (1974) method; therefore, a maximum stress level of 750 MN/m^2 in the axi-symmetric model was acceptable before localised yielding of the disc occurred. The author used FESDEC to predict the stress distribution through the disc/shaft model with radial blade and centrifugal loads due to rotation at 14,000 rpm, Figure 5.7, and 16,000 rpm, Figure 5.8. There was no sign of yielding at 14,000 rpm, but the author observed stress levels above 750 MN/m^2 at 16,000 rpm, indicating local yielding of the disc around non axi-symmetric features.

One can define a turbine disc's bursting speed as the rotational speed at which stress levels in the turbine disc exceed the disc material's yield stress. When considering the bursting speed of a turbine disc, Kerrebrock (1981) recommends that bursting speed should be design speed multiplied by 1.4. During operation, the turbine module's peak speed is typically 10.000 rpm. A bursting speed of 14,000 rpm was therefore consistent with Kerrebrock's recommendations. The author concluded that there was no danger of the turbine disc bursting during the course of normal ILPT facility operation when the peak speed was 10,000 rpm.

5.3 STRESS ANALYSIS OF THE TURBINE BLADE

5.3.1 Modelling assumptions

The author modelled the centrifugal load imposed on the turbine disc by the blades while rotating at design speed as a radially distributed load in the disc/shaft analysis. This enabled the author to model the effect of the sixty rotor blade's presence on the stress distribution through the disc. However, it provided no information about the stress levels in the blade. The turbine blades are made up of a dove-tail root fixing, a platform that forms part of the working section inner annulus and a shroudless aerofoil. Rolls-Royce plc defined the aerofoil at 0% and 100% aerofoil height, with the aerofoil itself generated by straight ruling between them.

The author modelled the blade in three sections, Figure 5.9, with the root, platform and aerofoil initially separate. The root and platform models mesh together exactly and, after elimination of coincident nodes at their interface, form a single model. The aerofoil and platform were so different in shape that it was not possible to obtain a similar mesh on both. The author moved nodes on the aerofoil base that were close to nodes on the platform for coincidence, then tied them together using constraint equations. This method of attaching two parts of the model led to spurious stresses in the aerofoil/platform interface, which whilst undesirable, had only a local effect so the author did not consider them significant.

The final blade model, Figure 5.10, was geometrically accurate; however, the relatively coarse grid required the omission of fillet radii. Sharp corners in a finite element model can lead to high stress concentration factors. One must view the results of the blade stress analysis with caution around sharp comers; however, spurious stresses in these regions will be local and therefore do not affect the overall result.

5.3.2 Model loading and constraint

Rotation of the blades at design speed gives rise to a centripetal acceleration and its corresponding radial force. The blade gas load gives rise to tangential and axial forces. The author calculated the axial gas load at 14.1 kN (235 N per blade) at the turbine's design point (see Section 4.1.1). For a turbine generating 2.36 MW at 8,434 rpm,, the tangential gas load is 6.7 kN, corresponding to a 112 N tangential load per blade. The axial and tangential gas loads will act through the aerofoil's pressure centre, but the author assumed they acted through its centroid as he did not know the centre of the pressure's position.

The gas loads will result in moments, Mx and -My, Figure 5.11, at the aerofoil root. The aerofoil centroid was 20 mm above the root section. The moment about the root at the axial direction, M_x, was, therefore, 4.70 Nm and the moment about the root in the tangential direction, M_y, was -2.24 Nm. By considering the aerofoil as a straight beam of asymmetric section, one can use Howatson et al's (1977) method to calculate the direct stress around the aerofoil,

$$\sigma_r = \frac{\left(M_x I_y - M_y I_{xy}\right)y + \left(M_y I_x - M_x I_{xy}\right)x}{I_x I_y - I_{xy}^{\ 2}} \qquad - \quad 5.2$$

where $I_{xx} = \int x^2 \delta A = 9.460x10^{-9}\ m^4$

$I_{yy} = \int y^2 \delta A = 1.278x10^{-9}\ m^4$

$I_{xy} = \int xy\delta A = 6.7000x10^{-11}\ m^4$

Substituting the known values of M_x and M_y into Equation 5.2,

$$\sigma_r = \frac{6.16x10^{-9}y - 21.5x10^{-9}x}{12.1x10^{-18}} \qquad - \quad 5.3$$

where x and y are the distances of any point in the aerofoil root section from the axial and tangential neutral axis, peak stresses occur around the aerofoil's edge, Figure 5.11, with a peak value of 22 MN/m^2 at the blade Bailing edge.

The finite element software was unable to apply adequately the gas load to the blade model. The author loaded the blade model centrifugally at turbine design speed with no attempt to model gas loads. Principle stress vectors in the aerofoil are radial (except very near the root), so one can gauge the effect of gas load on aerofoil results by superimposing the stress distribution around the aerofoil root that the gas loads generate on the model results. For a simple cantilever with a uniformly distributed load over its length bending moment, and therfore stress, is a function of distance squared from the cantilever's free end. A cantilever with linearly decreasing distributed load from built in to free end bending moment is a function of distances cubed from the cantilever's free end. At the blade mid-height section (the location of blade mounted instrumentation) gas loads will fall to 25% of their root value, Figure 5.11, assuming that the aerofoil is uniformly loaded and 0.8% of their root value, assuming one loads the aerofoil with a linearly decreasing distributed load.

5.3.3 Load case results

FESDEC's blade stress analysis results predict a blade rotating at a constant speed of 8,434 rpm with no applied gas loads. Section 5.3.2 considers the effect of gas loads which one must apply as a correction to the results in this section.

One can best view blade stress distribution as a set of colour filled contours, Figure 5.12. Peak stresses occur around the root region and also appear on the blade platform, Figure 5.13. The blade root area was larger than that of the 0% height aerofoil section, resulting in similar stress levels in the two, despite the root having to carry the platform's additional load.

Blade stress analysis results of 100 - 110 MN/m^2 in the root region compare well with hand calculated stress levels of 105 MN/m^2. Stress levels of 40 MN/m^2 at the aerofoil mid-height section also compare well with hand calculated values of 36 MN/m^2. The B22 blades were manufactured from JE'I'HETE, with blades that were instrumented manufactured from INCO-718. Both materials have a yield stress in excess of 1,000 MN/m^2 at ambient temperature. Manufacturers produce turbine blades from high strength material because they must withstand the applied centrifugal and gas loads at elevated temperatures in the engine environment. Elevated temperature reduces the material's Ultimate Tensile Strength (U.T.S.) dramatically, Figure 5.14. Blade metal temperatures remained close to ambient during ILPT facility operation, with the consequence that the blade material stress remained well below the material's U.T.S.

The predicted aerofoil stress levels were reasonably one-dimensional[2] at the blade mid-height section, but were more complex around the aerofoil/platform interface. The aerofoil and platform joined at the interface by constraining coincident nodes on both surfaces to move together. The author did not attempt to model fillet radii. One must view the

---

[2] Stress levels around the two-dimensional aerofoil were almost uniform across a constant radius aerofoil section. Stress level through the aerofoil varied only with radius from the centre line. One can regard the stress distribution around the two-dimensional aerofoil as a function of only radius, and therefore varies one-dimensionally.

results of the modelling method around the aerofoil/platform interface with caution. Whilst results around the aerofoil/platform interface are error prone, they are consistent with hand calculated stress levels of 100 MN/m^2 in this region.

The reasonably one dimensional stress distribution around the aerofoil mid-height section will result in a uniform strain distribution at this location. The Young's Modulus of INCO-718 at 25°C is 205x10^9 N/m^2, assuming a stress level of 40 MN/m^2. This implies instrumentation mounted at the blade mid-height section will experience a strain, ε, of 195x10^{-6}.

Predicted blade deflected shape, Figure 5.15, indicate that the aerofoil centroid lines up radially with the root centroid. The asymmetric shape of the aerofoil results in the aerofoil having a high second moment of area in the tangential direction in comparison with the root. As a consequence the aerofoil and platform rotate about the root. When designing a turbine blade, Kerrebrock (1981) recommends that aerofoil position relative to the root should be such that at the turbine design point, tangential gas loads exactly oppose the moment set up by offset aerofoil and root centroids. This method will minimise bending moments at the aerofoil/platform interface and therefore, minimise stress. Tangential gas loads will increase the load on the B22 turbine blade aerofoil, not reduce it, which contradicts Kerrerbrock’s recommendations. Whilst undesirable, the blade material’s U.T.S. was an order of magnitude higher than predicted stress levels in the blade during ILPT facility operation. Therefore, the author did not consider the addition of the applied gas loads due to centrifugal loads significant.

5.4 ROTATING SYSTEM MOMENT OF INERTIA

The author used a method to calculate the B22 turbine's speed rise and power during ILPT facility operation (See Section 3.3.2), which required knowledge of the moment of inertia of the turbine module's rotating system. He measured the rotating system's moment of inertia experimentally and later used FESDEC to predict moment of inertia.

One can measure the moment of inertia of an object using the trifiler suspension technique, which requires supending the object by three long wires. After a small angular displacement of the object, one measures its time period of oscillation, τ. It can be shown that,

$$I = \frac{Wr^2\tau^2}{4\pi^2 l} \qquad - \quad 5.4$$

The author measured all parameters in Equation 5.4, Table 5.1, allowing him to calculate disc/shaft system moment of inertia.

Table 5.1 *Trifiler suspension parameters*	
Weight of disc and blades	56.90 *kg*
Weight of shaft	18.80 *kg*
Total weight, W	75.70 *kg* ± 50 *g*
Radius of disc, r	0.18 *m* ± ½ *mm*
Length of suspending wires, l	1.948 *m* ± 1.5 *mm*

The author timed one hundred oscillations of the rotating assembly at 3 minutes 49 seconds, giving a time period of oscillation, τ, of 2.29 seconds; therefore, the moment of inertia of the disc shaft system, I, was 1.64 kgm^2. One can measure the error with measured moment of inertia by taking logs of Equation 5.4 and differentiating. The error in measured moment of inertia was ±1.2%; therefore, the error in moment of inertia was ±0.02 kgm^2.

Finite element analysis of the turbine disc (see Section 5.2) and turbine blade (see Section 5.3) enabled the author to predict their respective moments of inertia. For this, the author calculated the disc/shaft model as 1.471 kgm^2, with a value of 0.0026 kgm^2 for the blade. With a total of sixty blades, this makes the blade ring's total predicted moment of inertia 0.157 kgm^2.

The disc/shaft model did not include the non axi-symmetric root fixings that form part of the disc and did include the non-rotating bearing outer races. For an axi-symmetric ring of material, one can calculate moment of inertia, I, as moment of inertia expressed as (Mr^2)/2. One can calculate the moment of inertia of the disc root fixing and bearing outer races from their mass and centroid radius, Table 5.2.

Table 5.2
Moment of inertia of the rotating systems individual components

	Mass kg	*Centroid radius m*	*Moment of inertia Kgm^2*
Disc/shaft (FESDEC)	51.7	*Not calculated*	1.471
Blades (FESDEC)	5.2	*Not calculated*	0.157
Disc root fixing	0.8	0.218	0.019
Bearing outer races	3.5	0.090	0.014

The total moment of inertia for the rotating system is the sum of the disc/shaft, blades and disc root fixing moment of inertia minus the moment the bearing outer races' inertia, which came to 1.633 kgm^2. Moment of inertia determined experimentally, using the trifiler suspension technique, was 1.64 kgm^2 ±0.02 kgm^2. The author predicted the rotating system of inertia using FESDEC. The value of moment of inertia predicted fell within the error bars of the measured value, giving confidence in the experimental method and accuracy of turbine disc and blade modelling in FESDEC.

The author predicted the stress distribution around the blade mid-height section at 40 MN/m^2 at turbine design conditions, which were reasonably one dimensional. One can therefore assume that the strain imposed on instrumentation mounted at blade mid-height is 195x10^{-6} and purely radial. The deflected shape of the turbine disc/shaft model indicated a radial growth of the disc of 137x10^{-6} m and axial movement of 130x10^{-6} m under design condition loads. The author used this prediction during assembly of the turbine module when machining the blade overtip seal (see Section 6.1) to ensure it achieved design blade tip clearance at turbine design conditions.

The stress analysis of the B22 turbine disc/shaft system and the blade gave confidence in the turbine module rotating system's ability to withstand the loads to which the author would subject it during ILPT facility operation. The author concluded that the novel use of the B22 turbine in a transient turbine test facility was practical despite it originally being designed for steady state, not transitory, operation.

CHAPTER SIX

FACILITY CONSTRUCTION AND COMMISSIONING

6.1 CONSTRUCTION AND ASSEMBLY

The prime approach to turbine module assembly and commissioning was to pre-assemble the AGV (see Section 4.3) and bearing system (see Section 4.1), then commission them before installation in the ILPT. This was to minimise ILPT down-time. Once the author finalised the turbine module design, manufactur was initiated of the parts necessary to assemble the AGV and bearing system. AGV components were manufactured first, enabling the author to assemble and test it (see Section 6.2). The manufacture of parts nesessary to assemble the bearing system where then completed. After assembly the bearing system was then mounted on the AGV to allow development of the air motor air supply and enable low speed rotation of the turbine shaft.

Rolls-Royce plc two-plane balanced the disc/shaft assembly prior to the final bearing system assembly. Before the author could undertake bearing system commissioning trials, the air motor required an air supply. Experience gained by Hilditch (1989), of a similar air motor was utilised by the author during design of the air motor air supply (see Section 4.2).

The bearing oil system was adapted from that used by Doorly's (1983) (see Section 4.1.6). Construction and assembly of the turbine module took place in parallel to the continued operation of the ILPT facility. Consiquently the oil system was not available during turbine module assembly and commisioning. The author conducted initial bearing system trials at low speed (below 1,000 rpm) using an oil bath lubrication system. The author undertook full commissioning of the bearing system after mounting the turbine module in the ILPT facility (see Section 6.4).

The author commenced turbine module installation into the ILPT facility with the AGV which mounted on the ILPT 'A' frame, Figure 4.25, and bolted to the pump tube. The author then added the bearing system, followed by inner and outer annulus casings up to, and including, the vane ring.

After building the turbine module up as far as the vane ring, the author cut the blade overtip seal using a disc mounted cutter, Figure 6.1. The disc mounted cutter specifically cuts the blade overtip seal, the cutter blade having the correct turbine blade hade angle of 11°. Stress analysis of the turbine disc (see Section 5.2) predicted that the turbine disc would grow $137x10^{-6}$ radially and move $130x10^{-6}$ axially under design condition loads. The 11° hade angle resulted in the disc axial movement increasing the tip clearance by $25x10^{-6}$ m; therefore, the combined effect of a $137x10^{-6}$ m radial growth and $130x10^{-6}$ m axial movement was an $112x10^{-6}$ m reduction in blade tip clearance. Rolls-Royce plc specified a dynamic tip clearance of 380 $x10^{-6}$ m at design turbine speed; therefore, a static tip clearance $492x10^{-6}$ m was required.

The author mounted the turbine disc on its shaft with the cutter and fifty seven of the sixty blades. The author made radial cuts of $25x10^{-6}$ m by turning the blade cutter positioning screw through one revolution and spinning the disc by hand. The author repeated this process until the cutter removed abradable material around the entire overtip seal circumference. Tip clearance over the fifty seven blades was then measured using a feeler gauge. Maximum blade-to-blade tip clearance variation was $175x10^{-6}$ m due to the variation of blade span. The author considered this unacceptable as $175x10^{-6}$ m was approximately 50% of the required clearance at design conditions.

The author ground the turbine blades to a uniform length by mounting the fully bladed turbine disc on a lathe with a grinding wheel mounted on the headstock, Figure 6.2. The disc was rotated at 60 rpm and the grinding wheel used to take successive cuts until all blades were of equal length. After grinding the turbine blades to length, the author remounted the bladed disc and cutter on the shaft and cut successively until static blade tip clearance was $492x10^{-6}$ m $\pm 10x10^{-6}$ m.

Following machining of the blade overtip seal, the author cut the upstream labyrinth seal clearance, δ_{cl}, to size, then continued the turbine module assembly to the second throat allowing the downstream labyrinth seal to be cut. The method used to machine the labyrinth seals was to remove the turbine disc, mount a dial gauge from the shaft and mark the seal's high and low points. The seal was then removed, mounted on a lathe face plate, and the measured eccentricity reproduced. The author cut the seal to the correct diameter and remounted it on the turbine module. The dial gauge was used to check the seal's concentricity. In this way, the author set front and rear labyrinth seal clearances, δ_{cl}, to 125×10^{-6}m, $\pm 25 \times 10^{-6}$ m. Once all seal clearances were set, the turbine module assembly was complete.

6.2 THE ANNULAR GATE VALVE

6.2.1 Valve opening and prediction

The two dimensional working section installed in the ILPT facility by Schultz et al. (1977) utilised a slide valve to separate the ILPT pump tube and working section. The change from a two dimensional to an annular working section required the author to replace the slide valve with an annular valve, the AGV (see Section 4.3). The slide valve had opened in 40 ms, with ILPT run times of a similar length to those the author expected when fitted with the turbine module. The author chose an AGV opening time of 40 ms as a logical target as it had proved satisfactory in the past.

Once the author had overseen manufactured the AGV's parts, they were assembled and bolted to a large metal block to allow commissioning trials. The author fited a linear displacement transducer to one of the actuators used to open the AGV, Figure 4.25, the ouptup voltage being captured on a digital storage scope during AGV opening trials. This provided a means of monitoring AGV opening characteristics.

The actuators comprise of a pair of pistons in cylinders, Figure 6.3. Immediately prior to ILPT facility operation, the actuators were used to close the AGV that was then held closed with a perspex cylinder in each cylinder. The author set the actuator driver pressure to approximately $5x10^5$ N/m^2 and assumed the pressure downstream of the pistons, P_2, to be atmospheric pressure as the downstream side of the actuator was vented to atmosphere. When the perspex cylinder was explosively removed, the piston started to move down the cylinder under the action of the pressure difference across it. Once the inner seal reaches the inner cylinder, a "cushioning" volume of air was trapped and compressed as the actuator continued its stroke. The compression of air in the cushioning volume reduced the pressure difference across the piston causing the actuator to decelerate towards the end of its stroke.

The author could adjust the piston's position relative to the cylinder casing; therefore, changing the time during the opening sequence when the cushioning volume was trapped and deceleration of the piston began. Also a needle valve could be opened to allow air in the cushioning volume to bleed out, therefore reducing cushioning. Aditionally the initial pressure, P_1 , could be varied, which in conjunction with the variable starting position and intensity of cushioning, allowed variations in the AGV opening characteristics.

The adjustment of actuator driver pressure, stroke and cushioning to optimise the AGV opening characteristics was recognised by the author as a potential problem area early in the AGV design. The author consequently wrote a computer code, OPEN, to predict the velocity, acceleration and opening time of the AGV during its opening sequence. The code helped the author gain insight into the behaviour of the AGV prior to commissioning and to understand the opening characteristics during commissioning.

6.2.2 Test sequence and results

The author used a test sequence to commission the AGV, with the objective of optimising the actuator driver pressure and cushioning to achieve the desired opening characteristics.

Immediately prior to opening the AGV, pressure upstream of the AGV in the pump tube was 8.02x10^5 N/m^2 (see Section 3.3.2). The author evacuated the working section prior to ILPT facility operation and applied the full tube pressure across the AGV. The effect of a pressure difference across the AGV was to press the valve centre section against the rear section, compressing the 'O' rings between them. Compression of the 'O' rings increases the AGV static friction; therefore, it required a larger force to open the AGV with a pressure difference across it.

The author mounted the AGV on a large metal block, Figure 6.4, with a 25mm steel blanking plate across its front face. Once the AGV was assembled and closed, the volume between AGV and blanking plate was presurised, simulating the conditions immediately prior to AGV opening. Once the AGV started opening, the pressure between AGV and blanking plate fell to atmospheric. In the ILPT, pressure downstream of the AGV rose to the upstream total pressure. During commissioning trials, pressure upstream of the AGV fell to atmospheric pressure. In both cases, the differential pressure across the AGV fell to zero as it opened. The author considered pressurising the front face of the AGV during commissioning trials a good simulation of actual ILPT operation.

Figure 6.5 shows an air supply capable of applying up to 7.0x10^5 N/m^2 across the actuators. By pressurising the actuator reservoir to the required pressure, then opening the valve for the actuator forward stroke by hand, the author applied pressure to the side of the actuators which opened the AGV.

The AGV commissioning trials strove for an opening time of 40 ms, achieved in a controlled manner without valve "bounce" under representative ILPT operating conditions. The author defined valve bounce as the AGV partially closing again after fully opening. Commissioning trials commenced with no pressure difference across the AGV. The author pressurised the actuator reservoir to 1.0x10^5 N/m^2, the valve for the actuator forward stroke opened by hand and they recorded displacement transducer output. The author used displacement transducer output in conjunction with the opening characteristics predicted by OPEN as a guide to varying the actuator settings to achieve the AGV's smooth opening in the desired 40 ms. The author could set up the AGV to open in 40 ms with cushioning commencing after 25 mm of the 35 mm stroke, Figure 6.6.

Applying 3.7×10^5 N/m^2 to the AGV front face increased AGV static friction, such that it required a minimum of 2.7×10^5 N/m^2 actuator driver pressure to open it. The author increased actuator cushioning to a maximum 35 mm out of a 35 mm stroke. The author opened the valve for the actuator forward stroke by hand. The resulting displacement transducer output, Figure 6.7, indicated 10 ms of bounce after the AGV opened despite increased actuator cushioning to a maximum of 35 mm. OPEN predicted high deceleration of the AGV towards the end of the actuator stroke, but not high enough to stop the actuator completely before the end of the stroke. Reducing the actuator driver pressure would have enabled the cushioning to decelerate the actuator before the end of the stroke; however, this was not possible due to the static friction of the AGV which the actuator had to be overcome before it would open.

Application of 8.02×10^5 N/m^2 across the AGV compounded the situation witnessed at 3.7×10^5 N/m^2, Figure 6.8. The code OPEN predicts opening time reasonably. The tabulated output, Table 6.1, clearly demonstrates the high deceleration towards the end of the actuators stroke as a consequence of the cushioning. Actuator velocity was, however, still significant at the end of the stroke, resulting in valve bounce. The inadequate cushioning was a consequence of the 5.1×10^5 N/m^2 actuator driver pressure the actuator required to overcome the AGV static friction. Opening time was 20 ms plus an additional 20 ms of valve bounce. No mechanical damage occurred as a consequence of the actuator's contacting the nylon end stops with significant velocity. Therefore, the author deemed the opening characteristics of Figure 6.8, acceptable in view of this, as well as the 40 ms total opening time.

Table 6.1
Tabulated output of the program OPEN, predicting the opening characteristics of the AGV with an 8.02x10^5 N/m^2 differential pressure across it

Displacement (mm)	*Velocity (m/s)*	*Acceleration (m/s^2)*	*Time (ms)*
1	0.727	264.1	2.752
2	1.027	262.9	3.893
3	I .247	250.0	4.773
4	1.427	240.9	5.501
5	1.581	232.5	5.186
6	1.717	224.4	6.792
7	I.837	212.8	7.354
8	I .944	201. I	7.884
9	2.039	189.5	8.386
10	2.124	177.8	8.866
11	2.201	165.9	9.329
12	2.270	153.9	9,776
13	2.331	141.7	10.211
14	2.386	129.2	10.635
15	2.434	116.3	11.050
16	2.476	102.9	11.457
17	2.512	89.0	11.858
18	2.541	74.5	12.254
19	2.364	59.1	12.645
20	2.581	42.9	13.034
21	2 391	25.5	13.421
22	2.594	6.8	13.806
23	2.589	-13.4	14.192
24	2.574	-35.5	14.580
25	2.55I	-59.9	14.970
26	2 3 7	-87.1	15.364
27	2.470	-117.6	15.766
28	2.407	452.4	16.177
29	2.326	-192.4	16.599
30	2.221	-239.0	17.038
31	2.084	-294.4	17.502
32	1.903	-360. I	18.004
33	I .654	-443.2	I8.566
34	I .282	-546.6	19.248
35	0.531	-680.4	20.351

6.3 WORKING SECTION INLET AND EXIT FLOWFWFIELDS

6.3.1 Introduction

The author first installed the turbine module in the ILPT without fitting the turbine disc. The author filled the gap left by the turbine disc in the inner annulus with a wooden ring to enable him to assess the working section inlet and exit flow fields.

The author fitted wall static pressure tappings in the working section, Figure 6.9, 10 & 11, and connected them to National semiconductor differential pressure transducers (Nationals) mounted on the turbine module outer casing. The author also used a pitot mounted Kistler piezoelectric pressure transducer upstream of the vanes at Plane A to measure total pressure in the working section.

Facility run times of 0.5 seconds with low piston oscillations were available if the author tuned the ILPT to design condition at a gas to wall temperature ratio of 1.0 (see Section 3.4.1). The ILPT required long run times and constant total pressure as the static pressure tappings connected to Nationals via long lengths of hypodermic tubing, with a 200 ms fill time for the longest tubes.

6.3.2 Vane inlet flowfield

Circumferential inner and outer surface static pressure distributions at Plane B, Figure 6.12, exhibited very little variation, indicating uniform flow from the AGV. The author positioned the total pressure probe at Plane A mid-way between two AGV struts at mid-passage height to minimise the likelihood of AGV strut wakes influencing the probe. The author mounted a total pressure probe in Plane B, downstream of a strut trailing edge, which moved between runs to form an eleven point radial total pressure traverse. The author measured reference total, P_{ref}, and traverse total, P_{tra}, to an accuracy of ±½%, so to measure the ratio P_{tra}/P_{ref} to ±1%. The eleven point inlet total pressure traverse, Figure 6.13, fell well within the limits of experimental error. The ratio of total pressure in Plane B to total pressure in Plane A was greater than one. This unexpected result was attributed to experimental error as the author measured P_{tra} in an AGV strut wake and P_{ref} between wakes. The effects of measurement error dominated over any genuine total pressure loss downstream of the AGV strut, indicating that any total pressure loss was small. The uniform radial total pressure traverse and circumferential inner and outer annulus static pressure measurements led the author to conclude that the vane inlet flow field was radially and circumferentially uniform.

Izsak (1988) investigated turbulence level at Plane B and measured the radial distribution of turbulence at the same location that the author used to measure the radial total pressure profile. Izsak measured 2.5% turbulence, Figure 6.14, rising to over 4% near both inner and outer annulus. Izsak obtained his results using a hot wire anemometer with a gauze fitted across the AGV trailing edges. This compared well with the 2.5% ± 0.5% turbulence level measured by the author during final AGV design model testing (see Section 4.3.2).

6.3.3 Vane exit flow field

The author measured circumferential static pressure distributions at Plane C in conjunction with measured upstream total pressure to calculate Mach number distributions on the inner and outer annulus, Figure 6.15. The ±1% error in total to static pressure ratio at a Mach number of 1.0, resulted in a ±0.8% error in Mach number. The Mach number's run to run variation fell well within a ±0.8% Mach number error band; however, a significant point to point variation of Mach number around both the inner and the outer annulus occurred. Maximum circumferential Mach number variation on the outer annulus was 0.15 and 0.1 on the inner annulus, an order of magnitude greater than the error band on Mach number. Mach number run to run variation was within the limits of experimental error, but this could not account for the variation of Mach number around both the inner and outer annulus.

The author assembled the turbine module with care to minimise misalignment between inner and outer annulus casings. There was, however, inevitable nonconcentricity between them, due to manufacturing tolerances and imperfect alignment. The author measured tolerance on distance between inner and outer annulus at ±0.125 mm, which he suspected was responsible for Mach number point to point variation.

Consider the working section as two concentric rings, outer radius R_0, with a radial distance h separating inner and outer annulus.

$$A = \pi\left[{R_0}^2 - \{R_0 - h\}^2\right] \qquad - \quad 6.2$$

For isentropic compressible flow,

$$\frac{A}{A^*} = \frac{1}{M}\left[\frac{2}{\gamma-1}\left(1+\frac{\gamma-1}{2}M^2\right)\right]^{\frac{(\gamma+1)}{2(\gamma-1)}} \qquad - \quad 6.3$$

By substituting Equation 6.2 into Equation 6.3 and rearranging in terms of h,

$$h = R_0 - \left\{\frac{A^*}{M\pi}\left[\frac{2}{\gamma+1}\left(1+\frac{\gamma-1}{2}M^2\right)\right]^{\frac{(\gamma+1)}{2(\gamma-1)}}\right\}^{\frac{1}{2}} \qquad - \quad 6.4$$

where R_0 = 261.4 *mm (Plane C)*

A^* = 0.0396 m^2 *(Vane exit area)*

γ = 1.4

Using Equation 6.4 demonstrates that a change in Mach number from 0.9 to 1.0 (approximately design value vane exit Mach number ±0.05) occurs as a consequence of a 0.24 mm change in h, which was consistent with the manufacturing and assembly tolerances.

The author recalibrated, changed and recalibrated the pressure transducers to measure static pressure at Plane C. The author observed the same variation in circumferential vane exit Mach number and concluded that measurement error was not responsible for the observed circumferential variation of Mach number at Plane C. The author measured the vane throat area at 4% lower than its design value, with a 3% variation in throat area between individual vane passages. The variation indicated significant tolerance on Rolls-Royce plc manufactured items in the turbine module. The author considered the effect of inner and outer annulus eccentricity using a simple one-dimensional approach, indicating that the measured eccentricity was consistent with the measured variation in Mach number. The author concluded that manufacturing and assembly tolerances were responsible for the observed circumferential variation in Mach number at Plane C.

A ±0.05 circumferential variation in vane exit Mach number results in a ±3° circumferential variation in blade incidence. Whilst this was undesirable, Hilditch (1989) measured mean mid-height blade heat transfer rates on the B22 turbine and found that they remained almost constant during ILPT operation. Blade mid-height incidence changed by over 30° during ILPT operation, Figure 7.5, indicating a remarkable insensitivity of blade heat transfer rate to incidence variation. Due to the apparent insensitivity of blade heat transfer rates to incidence variation, the circumferential variation in vane exit Mach number, and therefore incidence, due to manufacturing and assembly tolerances, was concluded by the author to be tolerable.

Mach number distributions at Plane D, Figure 6.16, were similar to those at plane C. Circumferential variation of Mach number at Plane D was 0.2, attributable to the manufacturing and assembly errors of the turbine and turbine module. As with Plane C, run to run variations in Mach number were small.

6.4 DYNAMIC COMMISSIONING

6.4.1 Introduction

The author commissioned the turbine module rotating system in three stages. First stage commissioning established the satisfactory performance of the bearing and rotating system without the turbine disc. The second stage commissioned the bearing and rotating system with the fully bladed turbine disc. The third stage commissioned the bearing and full rotating system with flow through the working section.

Stage one commissioning involved spinning the rotating system to 10,000 rpm over the course of twenty runs. Stage two commissioning involved rotating the full rotating assembly to 10,000 rpm over the course of twenty five runs. Stage three commissioning involved firing the ILPT and assessing bearing and rotating system performance during ILPT operation. Stage three commissioning started from a low speed, ¼ Reynolds number starting point, with full turbine design conditions reached by the end of commissioning trials. At the conclusion of stage three commissioning, the bearing and rotating system performed satisfactorily at turbine design conditions.

6.4.2 Stage one commissioning, the bearing and rotating system without turbine disc

Stage one commissioning objectives were to run the rotating system to its overspeed condition of 10,000 rpm incrementally to ensure the bearing system, oil system and rotating system performed satisfactorily. The author monitored bearing cage/shaft speed ratio to assess the bearing system performance. The oil system performance was judged by monitoring bearing temperature, bearing cavity oil exit temperature and flow rate. The rotating system performance was judged using vibration limit criteria based on IS0 Standards (see Section 4.1.7).

During the course of twenty runs, the author increased turbine speed to 10,000 rpm. The "stepped form of the speed/time trace, Figure 6.17, was due to the low inertia of the rotating system caused by the turbine disc's absence. A small increase in air flow rate to the air motor resulted in the turbine’s rapid initial acceleration, then a levelling off of speed as bearing and shaft windage losses rose to equal air motor power.

The author measured the turbine shaft speed and the speed of the single bearing's cage during each ILPT run. This facilitated calculation of the bearing's cage/shaft speed ratio, allowing the author to plot cage/shaft speed ratio as a function of turbine speed, Figure 6.18. Section 4.1 considers bearing cage/shaft speed ratio with a nominal value of 0.45 typical for the single bearing. If cage/shaft speed ratio fell below 0.2 or rose above 0.8, the bearings would no longer roll, but would "skid" (see definition in Section 4.1.3), which would result in the bearings' rapid frictional heating and subsequent failure. Measured cage/shaft speed ratio remained close to its nominal value of 0.45 over the turbine's speed range, giving the author confidence that the ball bearings were rolling, not skidding.

Rolls-Royce plc two-plane balanced the turbine shaft before the bearing system's final assembly. This resulted in very low vibration levels during stage one commissioning. Vibration levels did not exceed 1.0 mm/s at any speed up to 10,000 rpm.

6.4.3 Stage two commissioning, the bearing and rotating system with fully bladed turbine disc

Stage two commissioning objectives were similar to those of stage one, with the addition of the fully bladed turbine disc to the rotating system. During the course of fifteen runs, the author increased the turbine speed to 4,500 rpm with the speed/time trace for run 29, Figure 6.19, being typical. Turbine speed rose more slowly than during stage one commissioning with the addition of the turbine disc increasing the rotating system's inertia and windage loss. The author conducted the first fifteen runs with the working section at atmospheric pressure. This resulted in disc and blades windage loss which prevented the air motor from driving the turbine past 4,500 rpm.

After evacuation of the working section, the author confirmed the bearing's satisfactory performance by spinning the turbine to 5,000 rpm. Examination of the relevant IS0 Standards on rotating machine vibration levels (see Section 4.1.7) led the author to the decision to balance the rotating system if they recorded vibration levels of 4-10 mm/s. The author recorded vibration levels in the 4-10 mm/s range as the turbine passed through a resonance at 4,000 and 4,500 rpm. Dietz (1988) carried out an investigation of turbine dynamic performance, whilst balancing the rotating system. In all, Dietz identified six modes of vibration in the 0 to 10,000 rpm speed range which Table 6.2 illustrates.

Table 6.2
Turbine module modes of vibration,
reproduced from Dietz (1988)

Vibrating Component	*Frequency*	
	Hz	*rpm*
Bearing Housing	29	1750
Facility support structure	33	2000
Dump tank	40	2400
Disc/shaft assembly	66	4000
Facility support structure	75	4500
Facility support structure	110	6600

After balancing the rotating system, the author increased turbine speed in increments to 10,000 rpm, Figure 6.20. The vibration modes that Dietz identified are clearly visible on the vibration/time trace, Figure 6.21; however, at no point do they exceed 4 mm/s, indicating the rotating system was well balanced. Bearing temperature and bearing cavity oil exit temperatures remained within 5 K of each other, with a peak rise of 30 K at 10,000 rpm. A 30 K rise in oil temperature across the bearings with an oil flow rate of 5 l/min indicated 3.9 kW of power removed from the bearings in the form of heat. The predicted power loss for steady state running at 9,800 rpm, assuming no heating of the bearing housing, was 4.25 kW (see Section 4.1.1). The oil removed approximately 90% of the power dissipated in the bearings. The oil probably removed less than 90% of the power dissipated as heat in the bearings, indicating that the prediction of bearing power loss was probably low. The author's main consideration was that oil temperature rise should remain below 80 K, and that the bearing cage shaft speed ratio remained close to its nominal value. Meeting these criteria, the author concluded that the beating system was performing satisfactorily at rotational speeds of up to 10,000 rpm.

In order to determine total bearing/seal losses at 6,500 rpm, the author ran down the turbine pre-run speed through 6,500 rpm after cutting off flow through the air motor. The working section was evacuated to 500 N/m^2, thus reducing disc windage to 25W (using Lawson's (1970) method - see Section 4.2.1), which was small enough to be ignored. One can use the turbine run down curve, Figure 6.22, to find deceleration, slope of the speed/time trace at 6,500 rpm. One can express power as,

$$P_w = Q\omega$$

$$\text{and torque} \quad Q = I\dot{\omega}$$

$$\text{therefore} \quad P = I\omega\dot{\omega} \qquad - \quad 6.5$$

where $I = 1.633\ kgm^2$ *(see Section 5.4)*

$\omega = 6{,}500\ rpm = 680\ rad/s$

Measured turbine deceleration, $\dot{\omega}$, with 50x10^3 N/m^2 pressure in the working section was 12.5 rads/s^2. Using Equation 6.5, this gave a power loss of 13.88 kW at 6,500 rpm. Measured turbine deceleration with 500 N/m^2 pressure in the working section was 7 rads/s^2; using Equation 6.5 this gave a power loss of 7.77 kW at 6,500 rpm. Conducting Run 51 at a pressure near vacuum, one can attribute the difference between power loss during Run 62 and 61, 6.11 kW to the disc windage and blade churning losses the author encountered during Run 62. Using Lawson's method to calculate disc windage (described in Section 4.2.1), with a pressure of 50x10^3 N/m^2, the author prediced a 5.31 kW windage loss. The predicted and measured windage losses were in close agreement, with the difference ascribed to blade churning.

At 6,500 rpm, the predicted bearing power loss (see Section 4.1.1) and seal loss (see Section 4.1.5) were 2.9 and 0.77 kW respectively, giving a total predicted power loss of 3.67 kW. The total measured power loss on Run 61 was 7 kW, almost twice the predicted value. The author repeated the bearing power loss calculations, and found that careful manipulation of the empirical constants within the relevant equations allowed him to achieve predicted power loss close to that measured. The author concluded that the bearing power loss calculation method was good, but uncertainties in the correct choice of empirical constants in the relevant equations resulted in a low prediction of bearing power loss. Despite the ability to model empirical constants in the relevant equations to give the measured value of bearing power loss, the author considered it more appropriate to leave a genuine prediction of bearing power loss in Section 4.1.1.

Once the author ran the turbine to its overspeed condition with satisfactory performance of both the bearing and oil supply systems, he considered stage two commissioning complete.

6.4.4 Stage three commissioning, the bearing and full rotating system with flow through the working section

The objective of stage three commissioning was to run the turbine through design speed during ILPT operation. It achieved full design condition speed and Reynolds number from a low speed, ¼ Reynolds number starting point.

The first full facility operation, Run 6362, was at ¼ design Reynolds number, with a target gas to wall temperature ratio of 1.3 and initial turbine speed of 500 rpm, Figure 6.23. During ¼ Reynolds number runs, temperature ratio was between 1.2 and 1.3; however, the author left ILPT fine tuning to a temperature ratio of 1.3 until the completion of stage three commissioning. The authors chosen ILPT mode of operation involved running the turbine to a higher speed than the required pre-run speed, point A (Figure 3.4), then cuting the air supply to the air motor and leting the turbine speed fall back to that required, point B, whereupon the ILPT fired. Using low rotational speeds, bearing cavity oil exit temperature remained unchanged. Due to a triggering problem, the author captured the cage/shaft speed ratio only during the latter part of Run 6362. Bearing cage/shaft speed ratio during the facility run time remained stable, Figure 6.24, and close to the predicted nominal value of 0.45.

After the success of the first ¼ Reynolds number run, the author increased turbine speed over the course of three runs, until turbine speed passed through design speed during ILPT operation.

After the ¼ design Reynolds number runs, the author increased Reynolds number to ½ design value with an initial turbine speed of 1,000 rpm, Figure 6.25. ILPT operation resulted in a sharp, but small, rise in bearing cavity oil exit temperature, which was consistent with the speed rise during ILPT operation. Bearing cage/shaft speed ratio remained stable, Figure 6.26, and close to the nominal predicted value of 0.45. There was some evidence of the matched bearing pair cage/shaft speed ratio dropping during ILPT operation, then increasing with the gas load removal at the end of the run (see prediction in Section 4.1.3). At reduced Reynolds numbers, the turbine gas load also reduces; therefore, the author expected the apparent insensitivity of cage/shaft speed ratio to applied gas load.

During successive runs, the author increased initial turbine speed until it achieved design speed during ILPT run time. Following successful operation at ½ design Reynolds number, the author tuned the ILPT to full design Reynolds number. For the first run at design Reynolds number, the author reduced initial turbine speed to 1,000 rpm, Figure 6.27. Bearing cage/shaft speed ratio matched predicted cage/shaft speed ratio (see Section 4.1.3) closely, Figure 4.28. Measured single bearing cage/shaft speed ratio increased constantly during ILPT operation, and the matched bearing pair adopted the stepped form due to the applied gas load during ILPT operation (see prediction in Section 4.1.3).

The author increased the turbine speed over successive runs until it reached design speed, Figure 6.29, during ILPT facility operation. He recorded a peak temperature rise in the bearing cavity oil exit temperature of 40 K, well below the 80 K SKF recommended maximum. Vibration levels remained below the 4 mm/s level at which the rotating system required balancing, except during the actual ILPT operation where the author recorded a peak level of 7 mm/s, Figure 6.29. The author could associate this peak in vibration level, with the piston in the pump tube striking the AGV front face at the end of ILPT operation, and therefore was not a balancing problem.

Once the turbine achieved design speed and Reynolds number, the facility was fine tuned to a temperature ratio of 1.3, with design inlet and exit Mach numbers. During stage three commissioning, the author left the second throat fully open, resulting in the vanes choking. The author closed the second throat incrementally over successive runs until vane mid-height exit Mach number reduced to 0.946. ILPT fine tuning continued over several runs to bring the turbine as close to design condition as possible.

Stage three commissioning concluded with tuning to turbine design condition. All mechanical systems operated satisfactorily, with uniform flow field at the vane leading edge plane during ILPT operation. Conclusion of stage three commissioning allowed commissioning of the turbine module in-shaft electronic signal processing system and instrumentation to commence, which Hilditch (1989) reported.

Following successful commissioning of the in-shaft electronics and instrumentation, a short experimental program was undertaken to enable the author to study the B22 turbine's performance and Hilditch to study turbine blade mid-height heat transfer rates. Hilditch was responsible for heat transfer measurements, and fully reports them in Hilditch (1989). Chapter 7 considers the accuracy with which the ILPT facility simulated and achieved the B22 turbine design point, and presents the assessment of the vane flow field and turbine performance.

CHAPTER SEVEN

TURBINE STAGE PERFORMANCE

7.1 INTRODUCTION

Once the turbine module was fully commissioned, the author undertook a short test program to fulfil two functions: (i) to study the variation of turbine non and quasi non dimensional groups during ILPT facility operation and (ii) to measure turbine blade mid-height heat transfer rates at turbine design conditions. Hilditch was responsible for heat transfer rate measurements and fully reports them in Hilditch (1989).

Section 7.2.1 shows the calculation of time varying turbine non and quasi non dimensional groups which enabled the author to assess the accuracy with which the ILPT facility was able to achive the turbine design point. Section 7.2.2 considers parameters that can by used to characterise a turbine's performance, and derives the range of conditions over which the B22 turbine passed during ILPT facility operation. Section 7.3.1 shows the calculation of time varying non and quasi non dimensional groups which enabled the author to assess their impact on the vane flow field and therefore, quantify the significance of their variation. Section 7.3.2 assesses the accuracy of the engine condition simulation. Section 7.4.2 shows measured vane static pressure distributions in conjunction with measured vane upstream total pressure. The author used these to calculate vane Mach number distributions and compared them with predictions and linear cascade data. Section 7.4.3 describes the flow visualisation carried out on the vane surface and end walls and concluded the chapter with a consideration of the implication of flow visulisation results for the vane flow field.

7.2 WORKING SECTION CONDITIONS

7.2.1 Time varying non dimensional groups

Rolls-Royce plc defined the B22 turbine design point in terms of non and quasi non dimensional groups (see Section 3.2.2). In order to assess the closeness to the design point, the author required the actual variation of non and quasi non dimensional groups during the course of ILPT facility operation. The author observed that during ILPT operation, the turbine non and quasi non dimensional groups continuously changed for two reasons. First, turbine speed was rising continuously. Second, piston oscillations (see Section 3.4.2) result in the working section total temperature and pressure oscillating about their design values, with resulting oscillations in non and quasi non dimensional groups.

The author wrote the program ROTOR (see Appendix 1) to calculate turbine non and quasi non dimensional groups. For each ILPT run, the author used ROTOR to input the measured vane upstream total temperature and pressure, vane and blade exit inner and outer annulus static pressures, turbine speed and acceleration. The ILPT low speed data acquisition system (see Section 3.5.1) sampled each channel every 2.3 ms, allowing the author to calculate turbine non and quasi non dimensional groups for approximately ninety time steps during ILPT operation.

The author used ROTOR to calculate non and quasi non dimensional groups for facility runs 6382, 3, 4 and 6445, 6 and 7. The turbine performance proved very repeatable; therefore, the author only presents and discusses results of one run, 6384, here.

The author evacuated the ILPT working section during the facility set up procedure (see Section 3.1.3). As ILPT facility operation commenced, the author opened the AGV (see Section 4.3), and pressure in the working section increased from near vacuum to its design value. The author connected the National pressure transducers, used to measure inner and outer annulus static pressures, to the static pressure tappings with lengths of hypodermic tubing, the lengths of which varied from 200 mm to 400 mm. The hypodermic tubing's fill time was approximately 30 ms. The author measured the upstream total pressure using a Kistler pressure transducer mounted in the head of the total pressure pitot probe. He did not associate fill time with the total pressure measurement. The low initial measured static pressure resulted in an erroneously high total pressure to static pressure ratio, Figure 7.1, during the hypodermic tube fill time. After the first 30 ms of ILPT operation, the piston oscillations resulted in both pressure ratio and Mach number crossing and recrossing their design values.

Chapin (1983) investigated the amplitude and phase response of different lengths and diameters of hypodermic tubing between a sinusoidal pressure source and pressure sensing module. The hypodermic tubing the author used in the turbine module was 1 mm bore. Chapin studied 1 mm bore hypodermic tubing of lengths 340 mm, 610mm and 760 mm. Since the results of most relevance to the turbine module are those from the 340 mm length tubing, all further comment will be with respect to these results.

Using Brooks and Jones' (1989) method, one can predict the time period of piston oscillation, Figure 3.12. For a temperature ratio of 1.3, Brooks and Jones predicted a piston oscillation time period of 0.07 seconds, equivalent to 14 Hz. For a frequency of 14 Hz, Chapin measured a phase lag of 2½° and a reduction of amplitude of 2%. He calculated the theoretical response of the hypodermic tubing using the method of Bergh and Tijdeman's (1965), which was in close agreement with experimental data. Chapin studied the effect of bending and coiling the hypodermic tubing, and concluded that the effect was negligible for frequencies of less than 15 Hz. Chapin's work led the author to conclude that the amplitude and phase response of the hypodermic tubing in the turbine module over the encountered frequency range did not change significantly by the presence of 200 mm to 400 mm lengths of 1 mm bore hypodermic tubing. He verified this conclusion by overlaying the output signal from the total pressure transducer (a Kistler pressure transducer mounted in the probe head) with the output signal from a static pressure transducer on the inner annulus at the vane exit plane (incorporating the longest length of hypodermic tubing). The two signals' phase were in good agreement, Figure 7.2, after the 30 ms tube fill time.

The author predicted total pressure oscillations of 12% at a temperature ratio of 1.3 (see Section 3.4.2), which was in close agreement with the measured piston oscillations. The 12% oscillations in total pressure result in a similar predicted oscillation of mass flow rate and Reynolds number, which the author observed in practice, Figure 7.3. Once again, piston oscillations result in the actual value of parameters crossing and recrossing their design value.

The author calculated turbine specific speed and specific work number for Run 6384 using the method described in Appendix 1. Turbine specific speed and specific work number are functions of turbine speed, and therefore rise continuously throughout ILPT facility operation, Figure 7.4. Turbine specific speed is defined as $N/\sqrt{T}$. The effect of taking the square root of temperature is to reduce piston oscillations to the root of their value, with the consequence that the rising turbine specific speed trace incorporates only slight oscillations passing through its design value once. Turbine specific work number has the full piston oscillations imposed on its rising trajectory, with the consequence that it passes through its design value three times.

Blade mid-height incidence angle and turbine vane exit Mach number, Figure 7.5, are significant parameters as their accuracy at turbine design speed determines the accuracy of the blade inlet velocity triangle. The turbine reached design conditions during time steps 142.6 ms and 144.9 ms into Run 6384 (see Section 7.2.2). During this time period incidence and Mach number coincided closely with their design values, giving confidence that the run achieved the design blade inlet mid-height velocity triangle during high speed data acquisition (see Section 3.5.1).

Overlay for Table 7.1

The content of each column of Table 7.1, and the design value of the parameter listed in the column, are itemized below. The 7 ms high speed data acquisition period durring Run 6384 extended from time step 140.3 ms to 144.9 ms and is shown cross hatched.

Turbine blade mid-height incidence angle, design value, 0.0°

Mass flow number, design value, 7.03x10^{-4} msK$^{1/2}$

Inlet totel to down stream static pressure ratio, design value, 2.872

Specific Speed design value, 435.885 rpm/K$^{1/2}$

Specific work number, design value, 216.3 J/kg K

Mass flow rate, design value, 29.13 kg/s

Reynolds Number, design value, 2.7x10^{6}

Mid-height vane exit Mach number, design value, 0.946

Turbine speed, design value, 8,434 rpm

Vane inlet total temperature, design value, 374 K

Vane inlet total pressure, design value, 8.02x105 Pa

Time after the start of low speed data acquisition

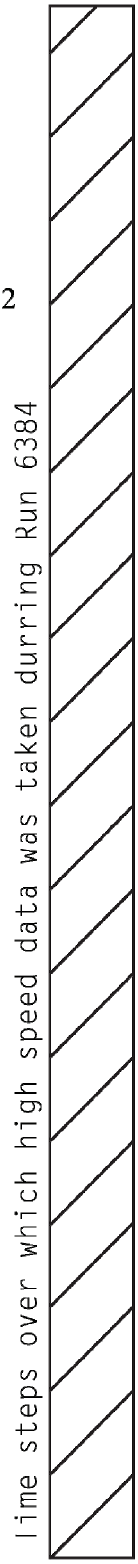

Table 7.1

Turbine non and quasi non dimensional groups using ROTOR for each measure point during Run 6384

TIME	P.TOT	T.TOT	T.SPD	MA.NO.	RE.NO.	M.DOT	CPDT/T	N/RT	PR	MRT/P	INC.
0.0690	772695.0	376.2	7184.8	0.944	2576091.8	28.26	207.92	370.42	2.80	0.000710	8.72
0.0713	764804.0	375.9	7224.2	0.933	2542323.3	27.99	211.29	372.60	2.82	0.000710	8.01
0.0736	771021.0	374.6	7263.5	0.925	2567066.5	28.26	211.11	375.29	2.81	0.000710	7.36
0.0759	790869.0	374.4	7302.9	0.950	2657992.0	29.00	206.97	377.41	2.87	0.000710	8.14
0.0782	798043.0	373.9	7342.3	0.965	2698938.0	29.28	206.35	379.69	2.92	0.000710	8.44
0.0805	804260.0	374.3	7381.6	0.962	2713545.3	29.50	205.47	381.51	2.95	0.000710	8.11
0.0828	830325.0	375.3	7421.0	0.965	2795121.5	30.41	200.08	383.06	2.98	0.000710	8.05
0.0851	843716.0	376.1	7460.4	0.958	2826244.5	30.87	197.74	384.66	2.97	0.000710	7.59
0.0874	847781.0	377.0	7499.7	0.956	2829671.8	30.98	197.59	386.23	2.92	0.000710	7.32
0.0897	871215.0	378.6	7539.1	0.977	2911389.8	31.77	192.88	387.46	3.00	0.000710	8.02
0.0920	879107.0	380.1	7578.4	0.966	2913899.3	32.00	191.77	388.71	3.00	0.000710	7.44
0.0943	876476.0	379.8	7617.8	0.934	2876719.0	31.91	193.42	390.88	2.91	0.000710	5.74
0.0966	885324.0	381.9	7657.2	0.937	2888371.5	32.14	191.94	391.79	2.88	0.000710	5.77
0.0989	877672.0	381.5	7696.5	0.941	2871846.0	31.88	194.71	394.02	2.85	0.000710	5.69
0.1012	864042.0	382.2	7735.9	0.930	2809071.3	31.36	198.61	395.67	2.83	0.000710	4.92
0.1035	857107.0	381.8	7775.2	0.906	2764940.3	31.12	201.34	397.89	2.76	0.000710	3.37
0.1058	835586.0	381.9	7814.6	0.883	2669509.5	30.34	207.56	399.88	2.67	0.000710	1.78
0.1081	815977.0	381.0	7854.0	0.888	2619467.3	29.66	213.86	402.37	2.65	0.000710	1.65
0.1104	800673.0	379.7	7893.3	0.896	2589982.5	29.15	219.41	405.05	2.69	0.000710	1.72
0.1127	780586.0	378.7	7932.7	0.879	2515411.8	28.46	226.48	407.62	2.64	0.000710	0.29
0.1150	763369.0	376.8	7972.0	0.867	2460495.8	27.90	233.32	410.65	2.61	0.000710	-1.09
0.1173	754283.0	375.4	8011.4	0.878	2456382.3	27.62	237.74	413.47	2.62	0.000710	-0.74
0.1196	745674.0	374.4	8050.8	0.894	2452916.3	27.34	242.00	416.06	2.67	0.000710	-0.16
0.1219	742565.0	374.6	8090.1	0.905	2542156.8	27.22	244.12	417.96	2.72	0.000710	0.26
0.1242	746152.0	372.5	8129.5	0.905	2482635.3	27.43	244.80	421.21	2.75	0.000710	-0.22
0.1265	754522.0	372.5	8168.8	0.915	2519603.3	27.74	243.28	423.25	2.77	0.000710	0.03
0.1288	768391.0	372.3	8208.2	0.947	2597588.8	28.25	240.08	425.36	2.86	0.000710	1.66
0.1311	787999.0	372.8	8247.6	0.964	2681181.0	28.98	235.34	427.57	2.97	0.000710	2.26
0.1334	809999.0	372.0	8286.9	0.957	2750223.0	29.80	230.05	429.64	3.02	0.000710	1.56
0.1357	832955.0	374.4	8326.3	0.949	2797933.0	30.54	224.05	430.30	2.99	0.000710	1.00
0.1380	853042.0	375.4	8365.6	0.965	2870929.3	31.24	219.56	431.75	3.02	0.000710	1.73
0.1403	867389.0	382.9	8405.0	0.971	2852387.8	31.45	214.75	429.48	3.06	0.000710	2.38
0.1426	870737.0	378.7	8444.4	0.942	2876617.5	31.75	216.13	433.91	3.01	0.000710	0.06
0.1449	862368.0	378.7	8483.7	0.904	2809206.5	31.46	219.24	435.93	2.87	0.000710	-2.74
0.1472	844194.0	379.3	8523.1	0.890	2727876.5	30.75	224.81	437.58	2.76	0.000710	-4.08
0.1495	817651.0	379.2	8562.5	0.882	2633845.3	29.79	233.22	439.67	2.70	0.000710	-5.10
0.1518	789673.0	354.1	8601.8	0.869	2755226.3	29.77	251.03	554.07	2.65	0.000710	-9.72
0.1541	765282.0	373.1	8641.2	0.850	2476719.0	28.11	253.52	447.33	2.58	0.000710	-9.54
0.1564	749261.0	375.6	8680.5	0.847	2402322.0	27.43	259.26	447.89	2.54	0.000710	-9.88
0.1587	746631.0	374.8	8719.9	0.877	2440006.5	27.34	261.85	450.79	2.63	0.000710	-7.71
0.1610	743044.0	372.6	8759.3	0.899	2464143.0	27.31	264.84	453.73	2.71	0.000710	-6.40
0.1633	556286.0	367.6	8798.6	0.568	1443378.1	20.59	357.77	458.88	2.04	0.000710	-12.90

Overlay for Table 7.1

The content of each column of Table 7.1, and the design value of the parameter listed in the column, are itemized below. The 7 ms high speed data acquisition period durring Run 6384 extended from time step 140.3 ms to 144.9 ms and is shown cross hatched.

Table 7.1

Turbine non and quasi non dimensional groups using ROTOR for each measure point during Run 6384

- Time after the start of low speed data acquisition
- Vane inlet total pressure, design value, 8.02x105 Pa
- Vane inlet total temperature, design value, 374 K
- Turbine speed, design value, 8,434 rpm
- Mid-height vane exit Mach number, design value, 0.946
- Reynolds Number, design value, $2.7x10^6$
- Mass flow rate, design value, 29.13 kg/s
- Specific work number, design value, 216.3 J/kg K
- Specific Speed design value, 435.885 rpm/$K^{1/2}$
- Inlet total to down stream static pressure ratio, design value, 2.872
- Mass flow number, design value, $7.03x10^{-4}$ ms$K^{1/2}$
- Turbine blade mid-height incidence angle, design value, 0.0°

TIME	P.TOT	T.TOT	T.SPD	MA.NO.	RE.NO.	M.DOT	CPDT/T	N/RT	PR	MRT/P	INC.
0.0690	772695.0	376.2	7184.8	0.944	2576091.8	28.26	207.92	370.42	2.80	0.000710	8.72
0.0713	764804.0	375.9	7224.2	0.933	2542323.3	27.99	211.29	372.60	2.82	0.000710	8.01
0.0736	771021.0	374.6	7263.5	0.925	2567066.5	28.26	211.11	375.29	2.81	0.000710	7.36
0.0759	790869.0	374.4	7302.9	0.950	2657892.0	29.00	206.97	377.41	2.87	0.000710	8.14
0.0782	798043.0	373.9	7342.3	0.965	2698938.0	29.28	206.35	379.69	2.92	0.000710	8.44
0.0805	804260.0	374.3	7381.6	0.962	2713545.3	29.50	205.47	381.51	2.95	0.000710	8.11
0.0828	830325.0	376.3	7421.0	0.965	2795121.5	30.41	200.08	383.06	2.98	0.000710	8.05
0.0851	843716.0	376.1	7460.4	0.958	2826244.5	30.87	197.74	384.66	2.97	0.000710	7.59
0.0874	847781.0	377.0	7499.7	0.956	2829671.8	30.98	197.59	386.23	2.92	0.000710	7.32
0.0897	871215.0	378.6	7539.1	0.977	2911289.8	31.77	192.88	387.46	3.00	0.000710	8.02
0.0920	879107.0	380.1	7578.4	0.966	2913899.3	32.00	191.77	388.71	3.00	0.000710	7.44
0.0943	876476.0	379.8	7617.8	0.934	2876719.0	31.91	193.42	390.88	2.91	0.000710	5.74
0.0966	885324.0	381.9	7657.2	0.937	2888371.5	32.14	191.94	392.79	2.88	0.000710	5.77
0.0989	877672.0	381.5	7696.5	0.941	2871846.0	31.88	194.71	394.02	2.85	0.000710	5.69
0.1012	864042.0	382.2	7735.9	0.930	2809071.3	31.36	198.61	395.67	2.83	0.000710	4.92
0.1035	857107.0	381.8	7775.2	0.906	2764940.3	31.12	201.34	397.89	2.76	0.000710	3.37
0.1058	835546.0	381.9	7814.6	0.883	2669509.5	30.34	207.56	399.88	2.67	0.000710	1.78
0.1081	815977.0	381.0	7854.0	0.888	2619467.3	29.66	213.86	402.37	2.65	0.000710	1.65
0.1104	800673.0	379.7	7893.3	0.896	2589982.5	29.15	219.41	405.05	2.69	0.000710	1.72
0.1127	780586.0	378.7	7932.7	0.879	2515411.8	28.46	226.48	407.62	2.64	0.000710	0.29
0.1150	763369.0	376.8	7972.0	0.867	2460495.8	27.90	233.32	410.65	2.61	0.000710	-1.09
0.1173	754283.0	375.4	8011.4	0.878	2456382.3	27.62	237.74	413.47	2.62	0.000710	-0.74
0.1196	745674.0	374.4	8050.8	0.894	2452916.3	27.34	242.00	416.06	2.67	0.000710	-0.16
0.1219	742565.0	374.6	8090.1	0.905	2542156.8	27.22	244.12	417.96	2.72	0.000710	0.26
0.1242	746152.0	372.5	8129.5	0.905	2482635.3	27.43	244.80	421.21	2.75	0.000710	-0.22
0.1265	754522.0	372.5	8168.8	0.915	2519603.3	27.74	243.28	423.25	2.77	0.000710	0.03
0.1288	768391.0	372.3	8208.2	0.947	2597588.8	28.25	240.08	425.36	2.86	0.000710	1.66
0.1311	787999.0	372.8	8247.6	0.964	2681181.0	28.98	235.34	427.57	2.97	0.000710	2.26
0.1334	809999.0	372.0	8286.9	0.957	2750223.0	29.80	230.05	429.64	3.02	0.000710	1.56
0.1357	832955.0	374.4	8326.3	0.949	2797933.0	30.54	224.05	430.30	2.99	0.000710	1.00
0.1380	853042.0	375.4	8365.6	0.965	2870929.5	31.24	219.56	431.75	3.02	0.000710	1.73
0.1403	867389.0	382.9	8405.0	0.971	2852387.8	31.45	214.75	429.48	3.06	0.000710	2.38
0.1426	870737.0	378.7	8444.4	0.942	2876617.5	31.75	216.13	433.91	3.01	0.000710	0.06
0.1449	862368.0	378.7	8483.7	0.904	2809206.5	31.46	219.24	435.93	2.87	0.000710	-2.74
0.1472	844194.0	379.3	8523.1	0.890	2727876.5	30.75	224.81	437.58	2.76	0.000710	-4.08
0.1495	817651.0	379.2	8562.5	0.882	2633845.3	29.79	233.22	439.67	2.70	0.000710	-5.10
0.1518	789673.0	354.1	8601.8	0.869	2755226.3	29.77	251.03	554.07	2.65	0.000710	-9.72
0.1541	765282.0	373.1	8641.2	0.850	2476719.0	28.11	253.52	447.33	2.58	0.000710	-9.54
0.1564	749261.0	375.6	8680.5	0.847	2402322.0	27.43	259.26	447.89	2.54	0.000710	-9.88
0.1587	746631.0	374.8	8719.9	0.877	2440006.5	27.34	261.85	450.79	2.63	0.000710	-7.71
0.1610	743044.0	372.6	8759.3	0.899	2464143.0	27.31	264.84	453.73	2.71	0.000710	-6.40
0.1633	556286.0	367.6	8798.6	0.568	1443378.1	20.59	357.77	458.88	2.04	0.000710	-12.90

Time steps over which high speed data was taken durring Run 6384

The tabulated output of ROTOR for Run 6384, Table 7.1, clearly indicated the accuracy with which the run achieved design conditions during ILPT facility operation. The error bars associated with each of the parameters in Table 7.1 (calculated in Appendix 1) indicate that during the 7 ms high speed data acquisition period, the run achieved turbine design conditions within the accuracy of the measurement.

7.2.2 Measured turbine performance

Recall that Section 3.2 considered the dynamic similarity requirements for a correct simulation of the turbine flow field where, following Horlock's (1966) method,

$$\frac{\dot{m}\sqrt{T}}{P}, \frac{C_p \Delta T}{T} = f\left\{\frac{N}{\sqrt{T}}, P_r, \mathrm{Re}, \gamma\right\} \qquad - \quad 3.3$$

For performance considerations, Horlock found the Reynolds number unimportant if large enough[3]. One can regard over the temperature range encountered in the working section γ as constant; therefore, Equation 3.3 reduces to two possible equations, giving $\dot{m}\sqrt{T}/P$ and $C_p\Delta T/T$ as functions of $N/\sqrt{T}$ and P_r. The assumption made in calculating $\dot{m}\sqrt{T}/P$ (see Appendix 1) that the vanes are always choked, results in $\dot{m}\sqrt{T}/P$ as constant. The independent and non constant variables relevant to turbine performance are, therefore, $C_p\Delta T/T$, $N/\sqrt{T}$, and P_r. One can, therefore, reduce Equation 3.3 to,

$$\frac{C_p \Delta T}{T} = f\left\{\frac{N}{\sqrt{T}}, P_r\right\} \qquad - \quad 7.1$$

where the function, f, was unknown. During ILPT run time, turbine power and speed rise continuously, therefore $C_p\Delta T/T$ and $N/\sqrt{T}$ rise continuously. ILPT piston oscillations (see Section 3.4.2) result in oscillations of vane upstream total pressure and temperature. The

---

[3] The run achieved both design Reynolds number and gas to wall temperature ratio during ILPT operation as they were significant parameters when measuring heat transfer.

oscillations in vane upstream conditions, in turn, result in oscillations in turbine pressure ratio (see Section 7.2.1). Continually rising $N/\sqrt{T}$, with an oscillating $C_p\Delta T/T$ and P_r, results in the turbine tracing out a path across its performance "map", Figure.7.6 a&b. From the measured values of $C_p\Delta T/T$, $N/\sqrt{T}$ and P_r, one can infer the turbine's performance map using a surface fitting routine. The surface in Figure 7.6 a&b is the function in Equation 7.1, and characterises the performance of the B22 turbine about its design point. The overlays illustrate the actual path the turbine followed over its performance map during ILPT facility operation.

The function in Equation 7.1 will be different from turbine to turbine; however, it will not change with time for an individual turbine, assuming turbine geometry remains constant. If turbine geometry should change (for example, turbine tip clearance may increase as the turbine wears), then the function in Equation 7.1 will change. By assuming the geometry of the B22 turbine remains constant, the author assumed that the function in Equation 7.1 was unique and constant with time. Assuming one can approximate the function in Equation 7.1 to a second order polynomial in the locality of the design point, one can write Equation 7.1 as,

$$\frac{C_p\Delta T}{T} = aP_r + b\frac{N}{\sqrt{T}} + c\{P_r\}^2 + d\left\{\frac{N}{\sqrt{T}}\right\}^2 \qquad - \quad 7.2$$

Using the values of $C_p\Delta T/T$, P_r and $N/\sqrt{T}$ from Table 7.1 at the measure points for time 140.3 ms to 147.2 ms, one can evaluate the constants in Equation 7.2,

$$\frac{C_p\Delta T}{T} = -778P_r + 6.09\frac{N}{\sqrt{T}} + 130\{P_r\}^2 + 6.70x10^{-3}\left\{\frac{N}{\sqrt{T}}\right\}^2 \qquad - \quad 7.3$$

Substituting design values of $N/\sqrt{T}$ and P_r into Equation 7.3 yields $C_p\Delta T/T$ = 215.94 J/kgK, with error bars (see Appendix 1) of +3% and *-5%.* Design $C_p\Delta T/T$ was 216.3 J/kgK, indicating that it was achieved at design values of $N/\sqrt{T}$ and P_r, within the accuracy of the measurement.

One can linearly interpret the run time at which measured $C_p\Delta T/T$, $N/\sqrt{T}$ and P_r was achieved from their measured values close to the design point by assuming,

$$t = a\frac{C_p\Delta T}{T} + b\frac{N}{\sqrt{T}} + cP_r$$

Evaluating the constants yields,

$$t = 7.0x10^{-3}\frac{C_p\Delta T}{T} + 398x10^{-3}\frac{N}{\sqrt{T}} - 10.5P_r \qquad - \quad 7.4$$

Substituting into Equation 7.4 design values of $N/\sqrt{T}$ and P_r and a $C_p\Delta T/T$ of 215.94 JkgK gives a time of 144.8 ms. Therefore, the ILPT Run 6384 achieved design conditions after 144.8 ms. The time step closest to 144.8 ms was at 144.9 ms (see Table 7.1), therefore, one can assume that Run 6384 achieved design conditions at the time step 144.9 ms into Run 6384. The author chose $C_p\Delta T/T$, $N/\sqrt{T}$ and P_r in Equation 7.4 to maintain consistence with Equation 7.3; however, he could have used other variables from Table 7.1, or $C_p\Delta T/T$, $N/\sqrt{T}$ and P_r. Turbine speed, vane exit Mach number, $C_p\Delta T/T$ and blade incidence angle are all closer to their design value at the time step 142.6 ms into Run 6384; therefore, one must regard the run achieving design conditions over a time period that spans the measure points 142.6 ms and 144.9 ms into Run 6384.

This thesis focuses on the design and commissioning of a new working section for the ILPT facility that would enable run times to achieve turbine design conditions; therefore, the author did not perform experimental work at "off-design" conditions. However, the author regarded the turbine module’s ability to cover a range of conditions during a single ILPT run as one of the facility's major strengths. Future experimental programmes will utilise the turbine's ability to cover a range of conditions during a single ILPT run, enabling future generations of research students to study the turbine flow field at design and off-design conditions.

7.3 THE VANE STATIC PRESSURE FIELD

7.3.1 Piston oscillations

The author considered the mechanisms responsible for piston oscillations in Section 3.4.2, and predicted them as 12% (peak to peak) of total pressure at turbine design conditions. This section quantifies the significance of piston oscillations on the vane flow field.

The author utilised Rolls-Royce plc’s blade-to-blade prediction code FINSUP to assess the effect of piston oscillations on the vane flow field. FINSUP enabled the author to construct a finite element grid around a vane section, Figure 7.7. He could then calculate the inviscid flow field from specified inlet total temperature, pressure and exit Mach number. Once the inviscid flow field was calcualted, FINSUP used an integral boundary layer calculation to predict boundary layer displacement thickness, δ^*, over vane suction and pressure surface. FINSUP assumed that one could account for the boundary layer blockage by adding the boundary layer displacement thickness to the specified vane profile, therefore slightly modifying it. FINSUP then recalculated the inviscid blade-to-blade flow field for the modified profile, and then recalculated the boundary layer. FINSUP iterated between flow field and boundary layer calculations until it reached a converged solution. In this way, FINSUP accounted for boundary layer blockage when calculating the inviscid blade-to-blade flow field.

In order to ascertain the effect of piston oscillations on the vane mid-height blade-to-blade flow field, the author ran FINSUP to the conditions in Table 7.1 at time steps 121.9 ms and 142.6 ms, a "trough" and "peak" in piston oscillations which straddled the design value of total pressure.

The predicted Mach number distributions for time steps 121.9 ms and 142.6 ms were in good agreement, Figure 7.8, except over the latter half of the suction surface. At time step 121.9 ms, ROTOR calculated a vane exit Mach number of 0.9047. At time step 142.6 ms, ROTOR calculated a vane exit Mach number of 0.9420. This change in vane exit Mach number likely was responsible for the discrepancy between the two predicted Mach number distributions, not the change in inlet total pressure. The time step 144.9 ms was still close to the piston oscillation peak, but with an exit Mach number of 0.9044, very close to that for time step 121.9 ms. The author conducted a FINSUP prediction for time step 144.9 ms, which overlaid the predicted Mach number distribution for time step 121.9 ms exactly, confirming that the change in exit Mach number, not inlet total pressure, was responsible for the deviation between Mach number distributions at time steps 121.9 ms and 142.6 ms.

Piston oscillations result in a change of vane exit Reynolds number from 2.45×10^6 at time step 121.9 ms, to 2.87×10^6 at time step 142.6 ms. One can show boundary layer displacement thickness, δ^*, for a turbulent boundary layer as $0.0463 Re^{-0.2}$ (from Shames, 1982); therefore, increasing Reynolds number should result in a decrease in predicted boundary layer displacement thickness. The boundary layer displacement thickness for time step 142.6 ms was less than that for time step 121.9 ms, Figure 7.9, consistent with the expected trend, but the magnitude of the difference was negligibly small.

FINSUP's blade-to-blade flow field predictions indicate that oscillations in total pressure have a secondary effect on the vane flow field compared to changing vane exit Mach number. The change in boundary layer blockage due to oscillations in Reynolds number has a small effect on the vane flow field which one can ignore.

7.3.2 Accuracy of engine condition simulation

Recall that Chapter 3 considered simulation of the B22 turbine design point and showed that the ILPT, as a short duration air supply, could achive all non and quasi non dimensional groups used to define the turbine design point. The ILPT provided the turbine module with compressed air that had a ratio of specific heats, γ, of 1.4 (the rig γ). A ratio of specific heats for the combustion products entering a high pressure turbine in the engine environment of 1.275 would be typical (the engine γ). This section will quantify flow field simulation error incurred in the ILPT facility as a consequence of using a working fluid with a γ of 1.4, rather than 1.275.

Using the Rolls-Royce plc blade-to-blade prediction code FINSUP described in Section 7.3.1, the author predicted the vane mid-height flow field at B22 turbine design conditions using the rig and engine γ, Figure 7.10. The two predictions were virtually indistinguishable, with only the slightest variation on the crown of the suction surface. The effect of changing γ from 1.4 to 1.275, whilst keeping all other design point non dimensional groups constant, was to reduce, slightly, turbine mass flow rate. As the vanes are not quite choked, a slight reduction in mass flow rate will result in a slight reduction in Mach number at the throat. This observation is consistent with the observed trend (Figure 7.10), but the magnitude is so small that one can ignore it.

Predicted vane suction surface boundary layer displacement thickness, Figure 7.11, was in close agreement for the rig and engine γ. The engine γ prediction of boundary layer displacement thickness was slightly lower than that for the rig γ at the crown of the suction surface, Figure 7.11. In order to maintain vane exit design conditions (a Mach number of 0.946 and Reynolds number of 2.7x106), the B22 turbine required a vane inlet total pressure of 8.02×10^5 Pa at the rig γ and 8.63×10^5 Pa at engine γ. Assuming that Mach number was unity at the blade throat for both rig and engine γ, it can be shown that for the required vane inlet conditions to achieve the design outlet conditions in both cases, Reynolds number will be slightly higher at the throat for the engine γ than the rig γ. Boundary layer displacement thickness for a turbulent boundary layer can be shown to be $0.0463\mathrm{Re}^{-0.2}$ (from Shames, 1982); therefore, the slightly higher throat Reynolds number at the engine γ will result in a slightly lower boundary layer displacement thickness consistent with the predictions in Figure 7.11. Due to the small effect on boundary layer displacement thickness of changing γ, one can regard the change in boundary layer blockage from rig to engine γ as negligibly small.

The author quantified the overall effect of changing from the engine to the rig γ, concluding that the change had a small effect on the vane flow field and boundary layers. The change in the vane flow field as a consequence of using a working fluid with a γ of 1.4 instead of 1.275 was therefore concluded to be negligible.

7.4 VANE STATIC PRESSURE DISTRIBUTIONS

7.4.1 Pressure tapping locations

The B22 turbine contains a ring of thirty six vanes, instrumented with six pressure tappings. Each instrumented vane has a pressure tapping at the leading edge and every 10% axial chord up to, and including, 90% axial chord. One can divide the instrumented vanes into three groups of two, covering the suction and pressure surface at 10%, 50% and 90% stream tube heights, Figure 7.12. The author mounted each pair of instrumented vanes to form an instrumented passage, Figure 7.13.

One can visualise the location of pressure tapped pairs of vanes in the vane ring by considering the turbine module when viewed downstream from the working section. Imagine the vanes numbered one to thirty six in an anti-clockwise direction, with vane one at top dead centre. The tip suction surface instrumented vane would be number fourteen, and the pressure surface instrumented vane number fifteen. Similarly, the root suction and pressure surface instrumented vanes would be numbers seventeen and eighteen, and the mid-height vanes numbers twenty and twenty one. Each instrumented vane pair was at least one vane away from another instrumented pair, or vane cassette.

7.4.2 Vane Mach number distributions

The author used measured static pressures around the 50% height vane section in conjunction with measured vane upstream total pressure to calculate vane Mach number distributions. Measured and predicted Mach number distributions (predicted using FINSUP, see Section 7.3.1) compared well at vane mid-height, Figure 7.14, with minimal run to run variation of the measured data. The agreement between predicted vane mid-height Mach number distributions at design conditions, and those at time step 142.6 ms (from Table 7.1, see Figure 7.8) was excellent, with the two predictions overlaying exactly. The good agreement between predicted design condition Mach number distributions, and at time step 142.6 ms demonstrates the accuracy with which the ILPT facility achieved the design flow field. The good agreement between predicted and measured Mach number distributions indicated that the flow field was essentially two dimensional at the vane mid-height section.

Nicholson (198l) measured the static pressure distribution around the B22 vane mid-height section in the ILPT facility when fitted with a linear cascade, Figure 7.15. The change from a linear to annular cascade cannot explain the discrepancy between two dimensional cascade data and the prediction, as the two dimensional prediction matched B22 turbine blade mid-height section results well. The explanation for the discrepancy was Nicholson and the author’s use of the difference between their definitions of "mid-height section". Rolls-Royce plc supplied the B22 turbine with vanes that were pressure tapped at l0%, 50% and 90% stream sections, Figure.7.12. Stream sections are an attempt to follow a fluid streamline through the vane passage and therefore, do not have a constant radius from the engine centre line. One can define plane sections as those with a constant radius from the engine centre line. Nicholson's B22 mid-height section was a plane section. The author's mid-height section in contrast was a stream section.

Nicholson defined the mid-height section as 280.8506 mm from the engine centre line for a section that was 68.275% engine size, giving a full size engine radius of 411.352 mm. The radius of the mid-height vane streamline section on the B22 turbine vane at the trailing edge was 255.04 mm for a section that was 62% engine size, giving a full size engine radius of 411.355 mm. Clearly, the author's stream section and Nicholson's plane section are coincident only at the trailing edge. It was ironic that the B22 turbine vanes only pressure tapped to 90% axial chord, so the author could not make a direct comparison between Nicholson's and his Mach number distributions at the coincident point. The author concluded that if a prediction of vane mid-height Mach number distribution was performed using Nicholson's definition of mid-height, agreement with Nicholson's measured data would probably be as good as that achived by the author.

Facility repeatability at vane tip sections was excellent, Figure 7.16, with the two dimensional prediction in good agreement with measured data. Secondary flows were strong at the vane tip (see Section 7.4.3); however, the two dimensional prediction was able to predict the Mach number distribution well, indicating that the flow was essentially two dimensional on the vane surface.

The hub prediction was in good agreement with the measured data, except over the latter half of the suction surface, Figure.7.17. The form of the measured data suggested that the actual vane exit Mach number was higher than the design value, resulting in the measured Mach numbers over the latter part of the suction surface being higher than predicted.

One can explain the discrepancy between measured and predicted hub Mach numbers by considering the vane passage shape. The high inner annulus curvature at the vane hub will result in a radial pressure gradient being set up to establish the required streamline curvature in the flow. This static pressure gradient will result in the static pressure on the inner annulus being lower that it would have been had Rolls-Royce plc not incorporated inner annulus curvature into the vane design. Engineers at Rolls-Royce plc designed the B22 turbine using two dimensional blade-to-blade and meridional prediction codes. The meridional solver was of the streamline curvature type, with no calculation stations within the blade row. For this reason, the strong hub meridional curvature was not well modelled during the design of the B22 turbine. The vane exit static pressure will, therefore, be lower than design at the root, thus the exit Mach number will be higher than that predicted using the two dimensional prediction code. This is a primary flow effect that arises as a consequence of the three dimensionality of the vane passage shape.

7.4.3 Vane surface flow visualization

The author designed the turbine module with two "cassettes" holding four vanes each, Figure 3.2, mounted on either side of the turbine module. One could remove these vane cassettes prior to and following ILPT facility operation. The author used each cassette for a different flow visualisation technique. The first, a two colour flow visualisation technique, involved mixing coloured dye with paraffin and painting it over the vanes and end walls. The author used red dye on the end walls and green on the vane suction and pressure surface. After facility operation, the red and green dye locations indicated where secondary flows had swept blade fluid onto the end walls, and end wall fluid onto the vanes. The second, an oil dot flow visualisation technique, involved mixing titanium-dioxide (a white powder) and paraffin to form a slurry, which was applied to the vanes as dots, in what the author considered strategic locations on both vane surface and end walls. After facility operation, the dots formed streaks indicating the flow direction. The streaks' length approximately indicated flow velocity. The author took care to ensure that he painted the dots as uniformly as possible.

Recall that Section 2.2 considered the mechanisms responsible for three dimensional flow phenomena in a cascade. Goldstein and Spores' (1988) model, Figure 2.6, was a useful guide when interpreting the results of other workers. The author uses it here to help interpret flow visualisation results.

The two colour flow visualisation on the vane suction surface, Figure 7.18, gives an excellent indication of the extent of the secondary flow development on the inner and outer vane annulus. The secondary flow swept large quantities of red end wall dye onto the vane suction surface on the outer annulus, with virtually no transport on the inner annulus. The author was not surprised by the minor secondary flow development on the vane inner annulus as the vane exit Mach number at the hub was (see Section 7.4.2) above its design value in this region. A high vane exit Mach number at the hub will result in under turning of the flow in this region. The inner annulus boundary layer will be turned more due to the lower velocities in the boundary layer, but not enough to allow boundary layer fluid to sweep up the vane suction surface as it was at the tip. The radial pressure gradient at vane exit also acts to keep low momentum fluid on the inner annulus and encourage migration in the tip region. Therefore, the author expected more dramatic flow visualisation results at the vane tip.

Goldstein and Spores' model predicts a down flow of fluid from the vane pressure surface onto the end wall. The author saw this effect in the outer annulus two colour flow visualisation, Figure 7.19, where green dye from the suction surface predominately replaced the red end wall dye. In the third vane passage, Figure 7.19, the author did not paint the vane's suction surface; therefore, the green dye on it indicates that the pressure surface transported the dye across the outer annulus and up the suction surface. The observed up flow on the suction surface was also in agreement with Goldstein and Spores' model.

The oil dot flow visualisation of the vane suction surface, Figure 7.20, indicates the "lift off" of the pressure/passage vortex (see Section 2.2) as it reaches the suction surface's crown after migrating across the outer annulus. The pressure gradient that builds up through the vanes was responsible for driving the outer annulus pressure/passage vortex towards the hub, the angle of the oil dots at lift off, indicating that the pressure/passage vortex will be driven down to approximately 80% vane trailing edge height.

Oliver (1989) studied the B22 turbine in a low Reynolds number facility and conducted a traverse of total pressure loss at design $C_p\Delta T/T$, $N/\sqrt{T}$ and P_r[4] 10% vane axial chord downstream of the vane trailing edge plane, Figure 7.21. The loss cores that one associates with inner and outer annulus pressure/passage vortexes are similar to those Binder (1982) saw, Figure 2.11, with the outer annulus loss core centre located at approximately 80% vane trailing edge height, as the oil dot flow visualisation indicated.

The radial pressure gradient at vane exit has a major influence on flow in the vane trailing edge region. Under ultraviolet light, the author could see the streak of red dye from the tip secondary flow down the trailing edge, Figure 7.22. The author had difficulty photographing the inner annulus wake region, Figure 7.23; however, he could see the presence of green dye from the vane surface. Green dye swept off the vane surface into the wake, then deposited onto the inner annulus under the action of the radial pressure gradient.

The author established the qualitative nature of the flow field leaving the B22 turbine's vanes, with strong secondary flow development at the vane tip, and minor secondary flow development at the hub. The identification of higher than design value vane exit Mach number at the vane hub will result in under turning the flow in this region, with secondary flows at the tip resulting in the flow overturn there. The secondary flow development on the outer annulus was consistent with Goldstein and Spores' model, and of a comparable magnitude to Binder's observations.

---

[4] $C_p\Delta T/T$, $N/\sqrt{T}$, and P_r are the important non and quasi non dimensional groups that engineers must match in a turbine test facility, if the turbine performance in the rig and engine is to be similar (see Section 7.2.2).

The author concluded that the large inner annulus contraction suppressed the migration of high loss fluid towards the suction surface. However, Oliver's observation of the high loss region at the vane hub indicates there was some secondary flow development in the hub region. Measured vane mid-height Mach number distributions matched design condition prediction closely, indicating that the mid-height vane flow field was essentially two dimensional, and therefore outside the influence of hub meridional curvature and tip secondary flows. The small variation of vane static pressure field with piston oscillations, coupled with the accuracy with which turbine non and quasi non dimensional groups were achived during the high speed data aquasition period, led the author to conclude that the engine flow field simulation in the turbine module was adequate to allow future generations of research students to meaningfully investigate the turbine flow field.

CHAPTER EIGHT

SUMMARY AND CONCLUSIONS

Scholars have used a large number of experimental facilities to test two dimensional cascades of aerofoils for many years to provide information about the turbine flow field, but inevitably fail to model three dimensional and rotational effects. Engine manufacturers are moving towards three dimensional design techniques in the never ending quest for higher efficiency engines; therefore, there is a need for a turbine test facility capable of rigorously simulating all aspects of the turbine flow field at engine representative conditions. Such a turbine test facility would enable the study of previously neglected phenomena and the physical mechanisms responsible for them. The detailed measurements made during the course of an experimental investigation of the turbine flow field would also provide an ideal test case against which to validate the three dimensional aero-thermo-dynamic design codes that engine manufacturers are developing currently.

The B22 turbine is a high pressure turbine, with an operating point typical of modem high-bypass ratio gas turbines. Cascades of B22 turbine mid-height vane and blade sections have been the focus of a major research effort at Oxford for many years. The data available on the aerodynamics of and heat transfer to the B22 turbine vane and blade mid-height sections has led to an understanding of the flow field around these sections in cascade. Doorly (1983), Doorly & Oldfield (1985) and Doorly et a1. (1985) used a rotating bar wake generator to simulate wake passing in a two dimensional cascade of B22 turbine blade mid-height sections. This work elucidated the wake passing process, and in particular, the effect of the wake passing process on the flow field around the B22 turbine blade mid-height section. The wealth of data available on both the B22 turbine vane and blade mid-height sections made the B22 turbine a logical choice for inclusion in a new turbine test facility capable of a full three dimensional, rotating simulation of the turbine flow field.

The Oxford University Engineering Laboratory Isentropic Light Piston Tunnel (ILPT) was used by generations of research students to conducte the previous two dimensional cascade testing of the B22 turbine vane and blade mid-height sections. The ILPT supplied compressed air to the working section containing the aerofoils for approximately 300 ms at the required temperature and pressure to correctly simulate the turbine flow field. The author considered the ILPT as a possible short duration air supply for a full B22 turbine stage, and found it capable of supplying it with air for 213 ms at the appropriate temperature and pressure for correct turbine flow field simulation.

When the author considered those parameters relevant to the turbine flow field simulation, it proved practical to model them all, with the exception of the ratio of specific heats, γ. The combustion products entering a high pressure turbine in an engine environment would, typically, have a ratio of specific heats of 1.275. The ILPT's working fluid, compressed air, had a ratio of specific heats of 1.4. The error incurred as a consequence was assessed and judged to be small, thus the author concluded that the turbine flow field simulation was good.

Having established the need for a new turbine test facility capable of simulating all flow features found in the engine environment and the suitability of the ILPT as a short duration air supply for the B22 turbine, the author had to design a new working section for the ILPT that incorporated the B22 turbine. The design of a new working section, the "turbine module", fell broadly into two areas: (i) the aerodynamic design of the working section and (ii) the turbine module's mechanical design.

The author conducted the aerodynamic design of the working section inlet duct in parallel with the the aerodynamic design of the Annular Gate Valve (AGV). The AGV is used to separate the working section from the ILPT pump tube. The author studied the final AGV design performance by wind tunnel testing a linear wooden model of seven AGV spokes. The final AGV design did not suffer from any separated flow regions, resulting in a radially and circumferentially uniform flow field at the vane leading edge plane.

One can subdivide the turbine module's mechanical design into two areas:(i) the bearing system design for the turbine disc and shaft and (ii) the turbine module rotating system's stress analysis.

The turbine module bearing system was required to operate over the range of conditions encountered during ILPT operation. The author made a prediction of total bearing load for four ILPT run states (pre-run, run start, run end and post run) and proposed a bearing system. He utilised an SKF prediction code to predict bearing contact angles and loads for the four run states. Bearing truncation did not occur and it did not exceed maximum bearing load, giving the author confidence in the bearing system design's suitablility for use in the turbine module.

The acceleration of the turbine during ILPT operation was sufficiently high to raise concern over the possibility of the bearings skidding. When a bearing skids, its cage/shaft speed ratio falls below the predicted value for pure bearing ball rolling. The author predicted bearing cage/shaft speed ratio for pure bearing ball rolling, which he measured during ILPT operation. The results matched the prediction well, giving him confidence that the bearings operated in a pure rolling mode.

The author undertook a rigorous axi-symmetric stress analysis of the turbine module rotating system. Under design condition loads, the author predicted that the turbine would grow $137x10^{-6}$ m radially and deflect $130x10^{-6}$ axially. He used this prediction when cutting the blade over-tip seal, setting a static tip clearance of $492x10^{-6}$ m to achieve the Rolls-Royce plc specified $380x10^{-6}$ m clearance at design conditions. Peak stress levels in the rotating system occurred on the turbine disc inner bore when the author centrifugally loaded the model at design speed. He predicted a peak stress level of 266 MN/m^2 using hand calculations and 180 MN/m^2 using the finite element analysis. He considered the discrepancy reasonable as the turbine disc is not a parallel sided plain disc, but is heavily cut away, therefore reducing the bore's load. When the author applied radial blade and axial gas loads to the finite element model in addition to centrifugal loads, stress level in the turbine disc bore increased to 240 MN/m^2, with a peak value of 260 MN/m^2 in the fillet radii around the main disc/mini disc interface. The author considered turbine disc bursting speed, and predicted bursting speed of 14,000 rpm. During normal ILPT operation the B22 turbine reaches a peak speed of 10,000 rpm. This was consistent with recommended practice that bursting speed should be 1.4 times peak operating speed.

The author constructed and analysed a three dimensional model of the turbine blade using three dimensional "brick" elements. He considered centrifugal and gas loading effects on the blade, and modelled centrifugal load at design turbine speed. He found the stress distribution around the blade mid-height section essentially two-dimensional, indicating that strain on instrumentation mounted at this location was purely radial. Stress levels in the blade were low compared to those in the turbine disc, enabling him to confirm that it was safe for Dietz (1988) to remove small quantities of material on the blade's aerofoil to facilitate the installation of flush mounted pressure transducers. The author predicted stress levels of 100-110 MN/m^2 to occur in the blade root region, which matched the hand calculated value of 105 MN/m^2 well. Predicted stress levels of 40 MN/m^2 around the aerofoil mid-height section also matched the hand calculated stress level of 36 MN/m^2 well, thus implying instrumentation installed at this location would experience a strain, ε, of $195\text{x}10^{-6}$.

The author illustrated the accuracy of the rotating system and blade finite element models when he used them to predict the rotating system's moment of inertia. The predicted moment of inertia fell within the measured value's error bars, giving the author confidence in both the finite element models and the measurement technique.

Upon completion of the turbine module aerodynamic and mechanical design, the author took responsibility for the turbine module's assembly and installation in the ILPT. After installing the turbine module, the author commissioned the new ILPT turbine test facility.

Turbine module commissioning trials culminated with the turbine achieving design conditions during ILPT facility operation. The author wrote a program, ROTOR, to calculate time varying turbine non and quasi-non dimensional groups during ILPT facility operation. He used ROTOR to establish turbine design condition accuracy and confirmed that turbine design conditions were achieved during ILPT facility operation. During ILPT Run 6384, 7 ms of high speed data were aquired and during those 7 ms the ILPT facility achieved in the working section a value of $Cp\Delta T/T$ of 216.13, $N/\sqrt{T}$ of 435.93 and a P_r, of 2.87. These values were within 0.10%, 0.01% and 0.06% of their design values respectively, which was within the estimated uncertainty of the measurements. The ILPT facility operation also achieved a vane exit Mach number, Reynolds number and $\dot{m}\sqrt{T}/P$ of 0.942, 2.81×10^6, and 7.1×10^{-4} respectively during the 7 ms high speed data acquisition period, within 0.40%, 4.07% and 1.00%, respectively, of their design values and within the uncertainty of the measurements.

The range of conditions covered by the B22 turbine during ILPT facility operation was primarily a means for the author to assess the accuracy with which the turbine achieved its design point. However, during this assessment the author discovered that he could utilise the turbine's ability to cover a range of conditions during ILPT facility operation in a future work programme, to study the turbine performance at off design conditions.

During the new facility's commissioning trials, vane flow visualisation revealed significant secondary flow development at the vane tip. Secondary flow development at the vane hub was low, which the author concluded was due to the high inner annulus curvature. This over-accelerated the flow in the hub region, suppressing the migration of low momentum fluid. Blade-to-blade vane hub predictions, mid-height and tip Mach number distributions matched those calculated from measured vane static and upstream total pressure, except over the latter half of the hub suction surface. Design peak Mach number at the root was just over 1 at the crown of the suction surface, at an x/s of 0.5. The measured peak Mach number was over 1.2 and occurred at an x/s of 0.8. At this location, the high inner annulus curvature resulted in flow over accelerating, and consequently the exit Mach number was higher than its design value. This observation was consistent with the flow visualisation results.

The first results from the new ILPT working section have illustrated the viability of achieving the required values of all parameters necessary for a rigorous simulation of the turbine flow field. The next phase in the project will make detailed measurements of both pressure (Dietz, 1988) and heat transfer rate (Allan, 1988) on the turbine blade in order to better understand the mechanisms responsible for unsteady and three dimensional flow phenomena in the rotating frame of reference. The author recommends further investigation of the turbine performance at off design conditions, which could be extended to include a study of the effects of varying blade tip clearance on turbine performance.

REFERENCES

Ainsworth, R.W., Allen, J.L., Davies, M.R.D., Doorly, J.E., Forth, C.J.P., Hilditch, M.A., Oldfield, M.L.G. & Sheard, A.G., Developments in Instrumentation and Processing for Transient Heat Transfer Measurement in a Full Stage Model Turbine, Trans. ASME, J. of Turbomachinery, Vol. 111, pp 20-27, 1989.

Aimworth, R.W., Schultz, D.L., Davies, M.R.D., Forth, C.J.P., Hilditch, M.A., Oldfield, M.L.G. & Sheard, A.G., A Transient Flow Facility for the Study of the Thennofluid-Dynamics of a Full Stage Turbine Under Engine Representative Conditions, ASME 88-GT-144, 1988.

Allan, W.D.B., Unsteady Heat Transfer Measurements About the Rotor Blades in a Fully Three Dimensional Rotating Turbine Stage in a Transient Facility, First Year Report, University of Oxford, 1988.

Ashworth, D.A., LaGraff, J.E., Schultz, D.L. & Grindrod, K.J., Unsteady Aerodynamic and Heat Transfer Processes in a Transonic Turbine Stage, ASME 85-GT-128, 1985.

Annand, W.J.D., The Resistance to Air Flow of Wire Gauzes, J. of the R.Ae.S., Vol. 57, March 1953.

Baines, N.C., Oldfield, M.L.G., Jones, T.V., Schultz, D.L., King, P.I. & Daniels, L.C., A Short-Duration Blowdown Tunnel for Aerodynamic Studies on Gas Turbine Blading, ASME 82-GT-312, 1982.

Baumeister, T., Avallone, E.A. & Baumeister, T., Mark's Standard Handbook for Mechanical Engineers, McGraw-Hill, Eighth Edition, 1987.

Bergh, H. & Tijdeman, H., Theoretical and Experimental Results for the Dynamic Response of Pressure Measuring Systems. Nat. Luchtvaartlab (Amsterdam), Report No. NLR-TR F.238, 1965.

Bilstern, C., Pumping Effect of Single Row Rolling Bearings, SKF, Report. NO. GT82D 2001, 1982.

Binder, A. & Romey, R., Secondary Flow Effects and Mixing of the Wake Behind a Turbine Stator, ASME 82-GT-46, 1982.

Binder, A., Forster, W., Kruse, H. & Rogge, H., An Experimental Investigation Into the Effect of Wakes on the Unsteady Turbine Rotor Flow, Trans. ASME, J. of Eng. for Gas Turbines and Power, Vol. 107, pp 458-466, 1985.

Binder, A., Turbulence Production Due To Secondary Vortex Cutting in a Turbine Rotor, ASME 85-GT-193, 1985.

Binder, A, Forster, W., Mach, K. & Rogge, H., Unsteady Flow Interaction Caused by Stator Secondary Vortices in a Turbine Rotor, ASME 86-GT-302, 1986.

Bindon, J.P., The Measurement and Formation of Tip Clearance Loss, ASME 88-GT-203, 1988.

Blair, U.F., Dring, R.P. & Joslyn, H.D., The Effects of Turbulence and Stator/Rotor Interaction on Turbine Heat Transfer: Part 1 - Design operating Conditions, Trans. ASME, J. of Turbomachinery, Vol. 111, pp 87-96, 1989.

British Standard, Fluid Flow in Closed Conduits, Part 1 - Pressure Differential Devices, Section 1.1 - Specification for Square Edged Orifice Plates, Nozzles and Venturi Tubes Inserted in Circular Cross-Section Conduits Running Full, BS1042, British Standards Institution, 1981.

Brooks, A.J. & Jones, T.V., The Use of Short Duration Facilities for Testing Gas Turbine Blading, Procedings of the Joint European Propulsion Forum on Modern Techniques and Developments in Engine and Component Testing, 1989.

Chapin, G.C., Dynamic-Pressure Measurements Using an Electronically Scanned Pressure Module, NASA, Technical Memorandum 84650, 1983.

Dentton, J.D. & Cumpsty, N., Loss Mechanisms in Turbomachines, Proc. I.Mech.E., Int. Conf. Turbomachinery - Efficiency Prediction and Improvement, Paper C260/87, 1987.

Dickins, T.E., The Aerodynamics of High Performance Turbine Blading, M.Sc. Thesis, University of Oxford, 1989.

Dietz, A.J., Unsteady Aerodynamic Studies on a Three Dimensional Rotating Turbine Stage in a Transient Facility, First Year Report, University of Oxford, 1988.

Doorly, D.J., A Study of the Effect of Wake Passing on Turbine Blades, D.Phil. Thesis, University of Oxford, 1983.

Doorly, D.J. & Oldfield, M.L.G., Simulation of the effects of shock wave passing on a turbine rotor blade, ASME 85-GT-112, 1985

Doorly, D.J., Oldfield, M.L.G. & Scrivener, C.T.J., Wake-passing in a turbine rotor cascade, Procs. of Symp., AGARD-CP-390, 1985.

Dring, R.P. & Joslyn, H.D., Measurement of Turbine Rotor Blade Flows, Trans. ASME, J. of Eng. for Power, Vol. 103, pp 401-405, 1981.

Dring, R.P., Joslyn, H.D., Hardin, L.W. & Wagner, J.H., Turbine Rotor-Stator Interaction, ASME 82-GT-3, 1982.

Dring, R.P. & Joslyn, H.D., The Relative Eddy in Axial Turbine Rotor Passages, ASME 83-GT-22, 1983.

Dryden, H.L. & Schubauer, G.B., The Use of Damping Screens for the Reduction of Wind Tunnel Turbulence, J. of Aero. Sci., Vol. 14, pp 221-228, 1947.

Dunn, M.G. & Hause, A., Measurement of Heat Flux and Pressure in a Turbine Stage, J. of Eng. for Power, Vol. 104, pp 215-223, 1982.

Dunn, M.G., Turbine Heat Flux Measurements: Influence of Slot Injection on Vane Trailing Edge Heat Transfer and Influence of Rotor on Vane Heat Transfer, ASME 84-GT-175, 1984.

Dunn, M.G., Rae, W.J. & Holt, J.L., Measurement and Analyses of Heat flux Data in a Turbine Stage: Part 1 - Description of Experimental Apparatus and Data Analysis, Trans. ASME, J. of Eng. for Power, Vol. 106, pp 229-233, 1984.

Dunn, M.G., Heat-Flux Measurements for the Rotor of a Full-Stage Turbine: Part 1 - Time-Averaged Results, ASME 86-GT-77, 1986.

Dunn, M.G., Seymour, P.J., Woodward, S.H., George, W.K. & Chupp, R.E., Phase-Resolved Heat-Flux Measurements on the Blade of a Full-scale Rotating Turbine, ASME 88-GT-173, 1988.

Epstein, A.H., Guenette G.R. & Norton R.J.G., The M.I.T. Blowdown Turbine Facility, ASME Paper 84-GT-116, 1984.

Falcon, K.C. & Andrew, C., Angular Contact Ball Bearings: Track Position at High Speeds, Proc. I.Mech.E., Vol. 184 Part 1 No. 19, pp 351-369, 1970.

Fitt, A.D., Forth, C.J.P., Robertson, B.A. & Jones, T.V., Temperature Ratio Effects in Compressible Turbulent Boundary Layers, Int. J. of Heat and Mass Transfer, pp. 159-164, Vo1.29, 1986.

Goldstein, R.J. & Spores, R.A., Turbulent Transport on the Endwall in the Region Between Adjacent Turbine Blades, Trans. ASME, J. of Heat Transfer, Vol. 110, pp 862-869, 1988.

Gregoryy-Smith, D.G. & Graves, C.P., Secondary Flows and Losses in a Turbine Cascade, AGARD CP351 No.17, 1983.

Guenetta, G.R., Epstein, A.H., Giles, M.B. & Haimes, R., Fully Scaled Transonic Turbine Rotor Heat Transfer Measurements, ASME 88-GT-171, 1988.

Haywood, R.W., Analysis of Engineering Cycles, Third Edition, Pergamon Press, 1980.

Hilditch, M.A., Unsteady Heat Transfer Measurements in a Rotating Gas Turbine Stage, D.Phi1. Thesis, University of Oxford, 1989.

Hodson, H.P., Boundary Layer and Loss Measurements on the Rotor of an Axial-Flow Turbine, Trans. ASME, J. Eng. for Gas Turbines and Power, Vo1.106, pp 391-399, 1984.

Hodson, H.P., An Inviscid Blade-to-Blade Prediction of a Wake-Generated Unsteady Flow, ASME 84-GT-44, 1984.

Hoheisel, H. & Seyb, N.J., The Boundary Layer Behaviour of Highly Loaded Compressor Cascade at Transonic Flow Conditions, AGARD-CP-401 'Transonic and Supersonic Phenomena in Turbomachhes', 1986.

Horlock, J.H., Axial Flow Turbines Fluid Mechanics and Thermodynamics, Krieger, First Edition, 1966.

Hartan, F.G., Aerodynamic and Heat Transfer of Turbine Blading, D.Phil Thesis, University of Oxford, O.U.E.L. 1598/85, 1985.

Howatson, A.M., Lund, P.G. & Todd, J.D., Engineering Tables and Data, Chapman and Hall, 1977.

International Standard, Dynamic Capacity of Rolling Element Bearings, I.S.O. 281, Switzerland, 1977.

Internatonal Standard, Mechanical Vibration of Machines With Operating Speeds From 10 to 200 res/s - Basis for Specifying Evaluation Standards, I.S.O. 2372, Switzerland, 1974.

Ireland, P.T., Wang, Z., Jones, T.V. & Byerley, A.R., A Cold Heat Transfer Tunnel Employing Liquid Crystals For Measuring Full Surface Heat Transfer Coefficients Over Turbine Blade Passages, Procedings of the 9th Symposium of "Measuring Techniques for Transonic and Supersonic Flow in Cascades and Turbomachines", 1988.

Ireland, P.T., Heat Transfer Measurements Under the Horseshoe Vortex, Submitted for publication, 1989.

Ishii, J. & Honami, S., A Three Dimensional Turbulent Detached Flow with a Horseshoe Vortex, ASME 85-GT-70, 1985.

Izsak, M.S., Wakes and Transition in a Rotating Gas Turbine Stage, M.Sc. Thesis, University of Oxford, 1988.

Jeal, B., Moving Towards the Non-Metallic Aero Engine, The Rolls-Royce Magazine, No.36 pp 23-27, Rolls-Royce plc., March 1988.

Jones, T.V. & Schultz, D.L., A Study of Film Cooling Related to Gas Turbines Using Transient Techniques, Aero. Res. Council, Report No. A.R.C. 32420, 1970.

Jones, T.V., Schultz, D.L. & Henley, A.D., On the Flow in an Isentropic Light Piston Tunnel, Aero. Res. Council, R.and M. No. 3731, 1973.

Kempson, A. & Watkins, P.A., The Design of a Turbulence Suppressing Gauze for the Isentropic Light Piston Tunnel, Third Year Report, University of Oxford, 1987.

Kmbrok, J.L., Aircraft Engines and Gas Turbines, The M.I.T. Press, Fourth Printing, 1981.

King, L.V., On the Convection of Heat from Small Cylinders in a Stream of Fluid: Determination of the Convection Constants of Small Platinum Wires with Applications to Hot Wire Anemometry, Phil. Trans. Roy. SOC. A., Vol. 241, pp 373-432, 1914.

King, P.I., Aerodynamics of High Performance Turbine Blading, D.Phi1. Thesis, University of Oxford, O.U.E.L. 1632/86, 1986.

Klein, A., Unterschungen uber die Einfluss der Zustromgrenzschicht auf die Sekundiirstrzimung in den Beschaufelungen von Axialturbinen. Forsch. Ing., Bd 32, Nr 6, 1966; English translation "Investigation of the entry boundary layer on the secondary flows in the blading of axial turbines". BHRA T 1004, 1966.

Langston, L.S., Nice, M.L., & Hooper, R.M., Three Dimensional Flow Within a Turbine Cascade Passage, J. of Eng. for Power, pp 21-28, 1977 Laws, E.M. and Livesey, J.L., Flow Through Screens, Ann. Rev. Fluid Mech., Vol. 10, pp 247-226, 1978.

Lawson, S., Turbine Windage Loss, Rolls-Royce plc, report No. TRR 90055, 1970.

Letcourt, M.D., An Investigation Into Unsteady Blade Forces in Turbomachinery, ASME J. of Eng. for Power, Oct. 1965, pp 345-354, 1965.

Lifshits, A., Simmons, H.R. & Smalley, A.J., More Comprehensive Vibration Limits for Rotating Machinery, ASME 86-GT-148, 1986.

Lomas, C.G., Fundamentals of Hot Wire Anemometry, Cambridge University Press, First Edition, 1986.

Mee, D.J. & Dickins, T.E., O.U.E.L. Blowdown Wind Tunnel Inlet Turbulence Measurement, University of Oxford Turbo Machinery Group Internal Report, 1987.

Moir, P.J., Manifold - Design Analysis Software on Desk Top Computers, E.T.A. Engineering Consultants Ltd., 1987.

Morphis, G. & Bindon, J.P., The Effects of Relative Motion, Blade Edge Radius and Gap Size on the Blade Tip Pressure Distribution in an Annular Cascade with Clearance, ASME 88-GT-256, 1988.

Nicholson, J.H., Experimental and Theoretical Studies of the Aerodynamic and Thermal Performance of Modern Gas Turbine Blades, D.Phil. Thesis, University of Oxford, O.U.E.L. 1362/81, 1981.

Oldfield, M.L.G., Jones, T.V. & Schultz, D.L., On Line Computer for Transient Turbine Cascade Instrumentation, I.E.E.E. Trans. on Aero. and Electronic Systems, Vol. AES-14 NOS pp 738-749, 1978.

Oldfield, M.L.G., Schultz, D.L. & Nicholson, J.H., Loss Measurements Using a Fast Traverse in an ILPT Transient Cascade, Procs. of the Symp. on Measuring Techniques, Lyon, France, 1981.

Oldfield, M.L.G., Bryanston-Cross, P.J., Nicholson, J.H. & Scrivener, C.T.J., A Study of Passage Flow through a Cascade of Turbine Blades Using Image Plane Holographic Interferometry. AGARD-P-399, 1986.

Oliver, M.J., Private communication with Mr. M.J. Oliver, Rolls-Royce plc, Manager-Turbine Research, 1989.

Parker, R. & Watson, J.F., Interaction Effects Between Blade Rows in Turbomachines, 1.Mech.E. Proceedings Vol. 186 21/72, pp 331-340, 1972.

Paulon, J., Reboux, J. & Sovrano, R., Comparison of Test Results Obtained on Plane and Annular, Fixed and Rotating Supersonic Blade Cascades, Trans. ASME, J. Eng. Power, Vol. 97 pp 245, 1975.

Peterson, R.E., Stress Concentration Factors, Wiley, First Edition, 1974.

Rigby, M.J., A Study of Shock Wave and Wake Passing on the Heat Transfer to a Transonic Turbine Blade, Oxford University, D.Phil. thesis, 1989.

Sandborn, V.A. & Kline, S.J., Flow Models in Boundary Layer Stall Inception, J. of Basic Eng., pp 317-327, Sept. 1961.

Schlichting, H., Boundary-Layer Theory, McGraw-Hill, Seventh Edition, 1979.

Schultz, D.L., Jones, T.V., Oldfield, M.L.G. & Daniels, L.C., A New Transient Cascade Facility for the Measurement of Heat Transfer Rates, AGARD CP No. 229, 'High Temperature Problems in Gas Turbine Engines', 1977.

Schultz, D.L., Ainsworth, R.W., Scrivener, C.T.J., The Role of Short Duration Facilities in Gas Turbine Research, 8th Symp. of ISABE 87-7031, 1987.

Shames, L.H., Mechanics of Fluids, McGraw-Hill, Second Edition, 1982.

Shelly, T., Turbine Blade Implants, Eureka, Vol. 8(No. 12), pp 24, 1988.

Sieverding, C.B., Secondary Flows in Straight and Annular Turbine Cascades, Thermodynamics and Fluid Mechanics of Turbomachinery (Edited by Ucer, Stow and Hirsch), Vol. 2, pp 621-664, NATO Series, 1985.

Simpson, R.L., Chew, Y.T. & Shivaprasad, B.G., The Structure of a Separating Turbulent Boundary Layer, Part 1, Mean Flow and Reynolds Stresses, J. of Fluid Mech., Vol. 113, pp 23-51, 1981.

Simpson, R.L., Review - A Review of Some Phenomena in Turbulent Flow Separation, Trans. of the ASME, vol. 103, pp 520-532, Dec. 1981.

SKF General Catalogue, SKF Group Publication 3200E, 1981.

Stalker, R.J., A Note on the China-Film Technique for Boundary Layer Indication, J. of the R.Ae.S., vol. 60, pp 543-544, August 1956.

Stimpson, N., Private. communication with Mr N.Stimpson, S.K.F. plc bearing specialist, 1989.

Stirling, K.C., Thrust Bearing Performance, Rolls-Royce plc Report No. MRD/3259/71, 1969.

Wallace, N.M., Basic Concepts of Seal Function and Design, 1.Mech.E. Guides for the Process Industries 'Mechanical Seal Practice for Improved Performance', The I.Mech.E., 1988.

Wilson, D.G., High-Efficiency Turbomachinery and Gas Turbines, The M.I.T. Press, First Edition. 1984.

APPENDIX ONE

TURBINE NON AND QUASI NON DIMENSIONAL GROUPS

A.1 INTRODUCTION

At an early stage in the turbine module design, the author recognised that he would need to assess the accuracy of turbine design point during each ILPT run. He calculated the non and quasi non dimensional groups that he had used to define the turbine design point as functions of facility run time for each ILPT run. He had to achieve this using parameters which he could readily measure in the turbine module. These were vane inlet total temperature and pressure, vane and rotor exit (Plane C and D, see Figure 6.9) inner and outer annulus static pressures and turbine speed.

The ILPT low speed data acquisition system, TOPSY (see Section 3.5.1), samples each measurement channel every 2.3 ms, enabling one to calculate turbine non and quasi non dimensional groups at approximately ninety time steps during a typical ILPT run. To calculate this, the author wrote a programme, ROTOR, which used TOPSY output data files as input. The output from ROTOR was a single array, Table 7.1, of the twelve parameters, which the author considered most important to achieve turbine design conditions. He then used a commercial graph plotting package, GRAPHER and surface fitting package SURFER, to pick up the array and plot, cross plot and surface fit the data.

A.2 THE PROGRAMME ROTOR

The author wrote ROTOR in FORTRAN on the Oxford university turbo machinery group μVAX. Whilst writing ROTOR, the author ensured that it was as easy to modify and expand as possible, so that future generations of research students could adapt it to their requirements. His approach to ROTOR was to write a short top programme that called sub-routines to perform each separate calculation. In this way, one can easily modify the programme to call another subroutine written at a later date.

The structure of ROTOR can be understood by reference to Figure A.1. The top programme, ROTOR initially opens an input data file ROTOR.DAT, Figure A.2. The data file contains all constants relevant to the calculation of non and quasi non dimensional groups, the names of TOPSY files containing the required input data and the name of an output file. ROTOR then initialises all variables and arrays using the subroutine INIT, includes parameters from the three files and reads the TOPSY data files for all time steps using RDFILE. All input variables for time step one then pass to the subroutine CALC, which proceeds to call eight subroutines in succession, until it calculates all non and quasi non dimensional groups for that time step, whereupon it passes them back to ROTOR. ROTOR writes the non and quasi non dimensional groups for the first time step into the first row of the output file, then updates all input data to that of the second time step (2.3 ms later in the run), calls CALC and repeats the calculation of non and quasi non dimensional groups. ROTOR repeats this procedure until it reaches the end of the TOPSY data files (the end of the run), whereupon it closes the output data file and stops the programme. A section of the output data file for Run 6384, Table 7.1 illustrates the output of ROTOR.

A.3 CALCULATION METHOD AND ERROR ANALYSIS

Below is the method the author useed in ROTOR to calculate the turbine non and quasi non dimensional groups and an estimate of the measurement error of each group. The author assumed static pressure at Plane C (see Figure 6.9) to vary linearly from inner to outer annulus, enabling him to calculate mid-height vane exit static pressure,

$$P_{c(mid)} = \frac{P_{c(inner)} + P_{c(outer)}}{2}$$

Assuming a ±½ % error in measured pressures, $P_{c(mid)}$ will have an associated error of ±½ %.

For compressible flow,

$$\frac{P_0}{P} = \left[1 + \frac{\gamma - 1}{2} M^2\right]^{\frac{\gamma}{\gamma - 1}}$$

$$\therefore \quad M_{c(mid)} = \left(\frac{2}{\gamma - 1} \left\{ \left[\frac{P_{0A}}{P_{c(mid)}} \right]^{\frac{\gamma - 1}{\gamma}} - 1 \right\} \right)^{\frac{1}{2}} \qquad - \ A.1$$

One can find error in Equation A.1 by taking logs of the equation, differentiating it then assuming the error in P_{0A} and $P_{c(mid)}$ are both equal to ±½ %. Using this method one can show that error in $M_{c(mid)}$ was ±1.1 %, providing $M_{c(mid)}$ does not fall below 0.7.

One can express Reynolds number as $\rho_c U/\mu$, where c is the vane axial chord and ρ, U and μ are based on vane exit mid-height static conditions,

$$\rho_{c(mid)} = \frac{P_{c(mid)}}{RT_{c(mid)}}$$

$$T_{c(mid)} = \frac{T_{oA}}{\left[1 + \frac{\gamma - 1}{2} M_{c(mid)}{}^2\right]}$$

The author measured vane inlet total temperature, T_{0A}, to ±½ % and the error in $M_{c(mid)}$ was calculated as ±1.1 %. One can show the resulting error in $T_{c(mid)}$ as ±1.0 %, assuming $0.7 \leq M_{c(mid)} \leq 1.0$. Once one knows the error in $P_{c(mid)}$ and $T_{c(mid)}$, one can calculate the error in $P_{c(mid)}$ as ±1.5 %. One can express vane exit mid-height velocity, $U_{c(mid)}$, as,

$$U_{c(mid)} = M_{c(mid)} \sqrt{\gamma R T_{c(mid)}}$$

which can be shown to have an error of ±1.6 %. One can find fluid viscosity using Sutherlands law,

$$\mu_{c(mid)} = \mu_{ref} \left[\frac{T_{c(mid)}}{T_{ref}} \right]^{1\ 5} \left[\frac{T_{ref} + 110}{T_{c(mid)} + 110} \right]$$

Assuming a ±1.0 % error in $T_{c(mid)}$, the error in $\mu_{c(mid)}$ is ±2.2 %. One can find the error in Reynolds number using the calculated values of error in $T_{c(mid)}$, $U_{c(mid)}$ and $\mu_{c(mid)}$ as ±5.3%.

One can write mass flow rate as,

$$\dot{m} = \rho^* A^* U^*$$

and as ρ=P/RT and $U^* = M\sqrt{\gamma R T^*}$ it can be shown that,

$$\dot{m} = \frac{\rho^*}{\rho_0} \cdot \frac{P_0}{RT_0} \cdot A^* \cdot M \sqrt{\gamma R \frac{T^*}{T_0} T_0} \qquad - \quad A.2$$

$$and \quad \frac{T^*}{T_0} = \frac{1}{\left[1 + \frac{\gamma - 1}{2} M^2\right]} \qquad and \quad \frac{\rho^*}{\rho_0} = \frac{1}{\left[1 + \frac{\gamma - 1}{2} M^2\right]^{\frac{1}{\gamma - 1}}}$$

If one assumes the vanes to be choked, which they very nearly are, and γ=1.4, then T^*/T_0=0.833 and ρ^*/ρ_0=0.6339. The author estimated boundary layer blockage through the vanes at 1.0%, therefore reducing actual vane throat area to 99% effective area. Assuming R=287 m^2/s^2K, then Equation A.2 reduces to,

$$\dot{m} = 40x10^{-3} \frac{P_{0A} 0.99 A^*}{\sqrt{T_{0A}}} \qquad - \quad A.3$$

The author estimated the error in vane throat area at ±1% [5], therefore that error in mass flow rate is ±1.75%. The error associated with assuming that the vanes are choked was quantified by assuming that in a worst case, the Mach number can fall as low as 0.9, in which case the mass flow rate calculated using Equation A.3 will fall by less than 1%. Therefore, one can write the error bar on mass flow rate as +0.75% -2.75%.

One can calculate turbine specific work number from a consideration of turbine power, which one can expressed thermodynamically and dynamically,

$$Q = \dot{m} C_p \Delta T$$

$$and \quad Q = I\omega\dot{\omega}$$

---

[5] The author measured the B22 turbine vanes throat area at 0.0176520 m^2, which was 4% below the design value of 0.0165322 m^2. ROTOR used the measured value (see Figure A2). The ±1% error in the throat area refers to the author's estimate of the accuracy with which he measured the throat area.

$$\therefore \quad \frac{C_p \Delta T}{T} = \frac{I\omega\dot{\omega}}{\dot{m} T_{0A}}$$

The error in turbine rotating system moment of inertia was ±1.2% (see Section 5.4). The author calculated the error in measured speed at ±l rpm at design speed (see Section 4.5.2), which is equivalent to an error of ±0.01%. The best-line fit through the turbine speed/time trace was relatively poor, giving rise to an estimated ±l% error in turbine acceleration. One can show the error in $C_p\Delta T/T$ at ±4.4%, with the 1% over estimate of mass flow giving rise to a total estimated error of -5.4% to +3.4%.

One can define blade incidence angle as blade inlet gas angle minus inlet gas angle. One can calculate blade inlet gas angle from a consideration of the blade inlet velocity triangle, Figure 3.7. Section 3.3.2 shows that,

$$M_b = \frac{rN}{\sqrt{\gamma R T_{0A}}}$$

$$M_3 = \sqrt{M_{c(mid)}{}^2 + M_b{}^2 - 2M_{c(mid)} M_b \sin\alpha}$$

Therefore, blade inlet gas angle, ξ,

$$\xi = \cos^{-1}\left[\frac{M_{c(mid)} \cos\alpha}{M_3}\right]$$

One can show the error in M_{b2} as ±0.25%, and ±3.8% in M_3, at the turbine design point, from which the error in blade incidence angle is ±4%.

Errors in the remaining turbine non and quasi non dimensional groups, $N/\sqrt{T}$, P_r and $\dot{m}\sqrt{T}/P$ are ±0.25%, ±1.0% and +1.5% to -3.5% respectively. Table 7.1 summarises the errors the author associated with the measured values of those parameters listed in in Table A.l.

Table A.1
Errors associated with turbine parameters calculated from TOPSY measured data

Parameter	*Error, %*
Total pressure	±0.5%
Total temperature	±0.5%
Turbine speed	±0.01%
Vane exit mid height Mach number	±1.1%
Reynolds number	±5.3%
Mass flow rate	+0.75%, -2.75%
Turbine specific work number	-5.4% *to* +3.4%
Turbine specific speed	±0.25%
Turbine pressure ratio	±1.0%
Turbine mass flow number	-1.5% *to* +3.5%
Blade mid-height incidence	±4%

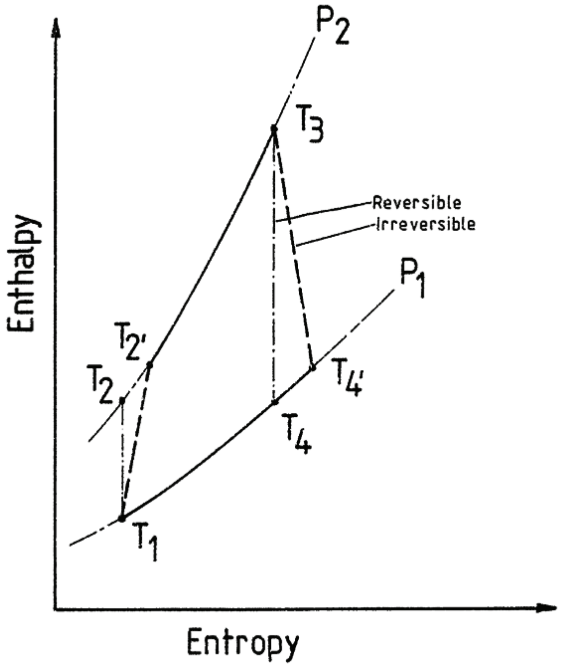

Figure 1.1: Enthalpy–entropy diagram for reversible and irreversible Joule cycle

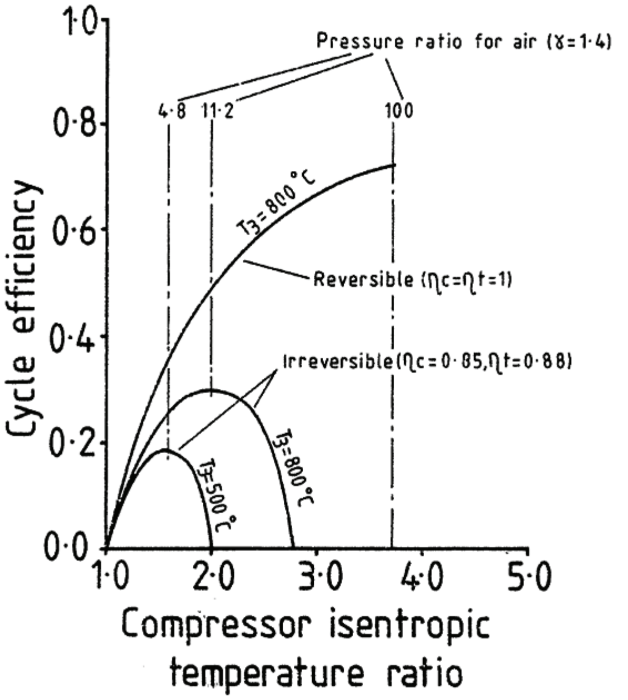

Figure 1.2: Variation of Joule cycle efficiency with pressure ratio, illustrating departure of actual cycle efficiency from ideal due to irreversible effects

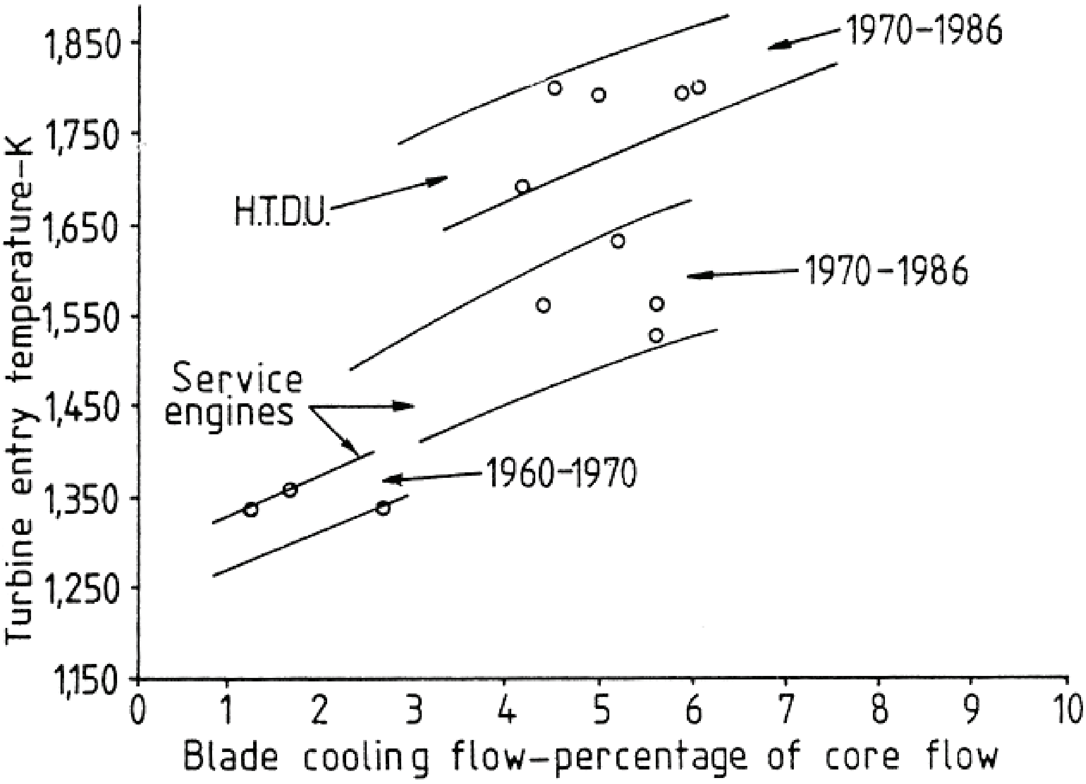

Figure 1.3: Advances in turbine-cooling technology achieved with in-service engines and high-temperature demonstrator units, illustrating increasing trend in both TET and blade-coolant mass flow over the past twenty years

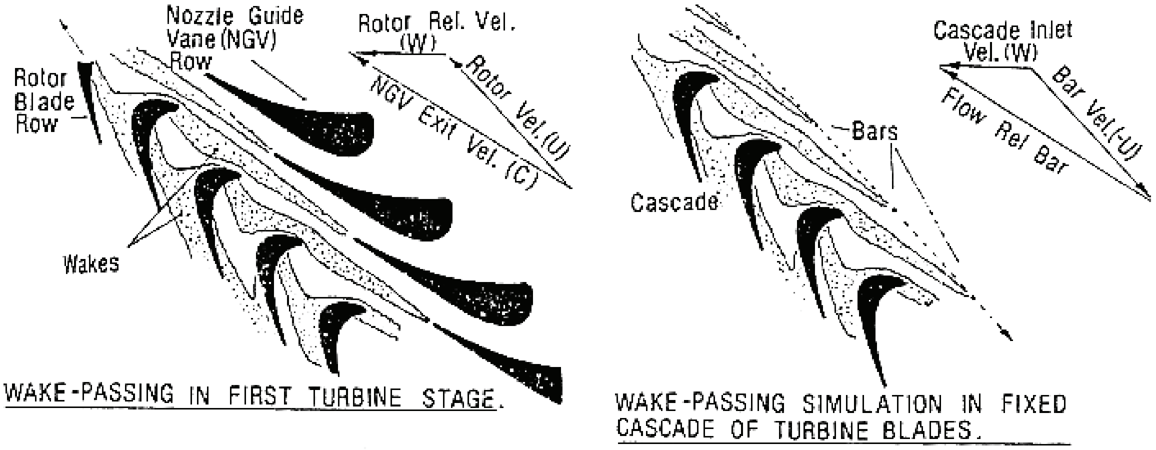

Figure 2.1: Convection of vane wakes into rotor passage, and use of bars for wake and correct velocity triangle simulation (adapted from Doorly, 1983)

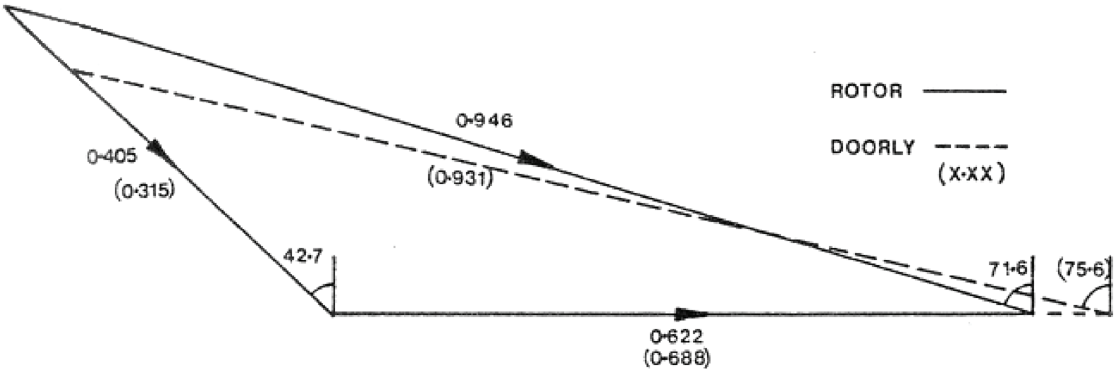

Figure 2.2: Design condition blade inlet mid-height velocity triangle achieved by Doorly (1983), compared with that of B22 turbine blade

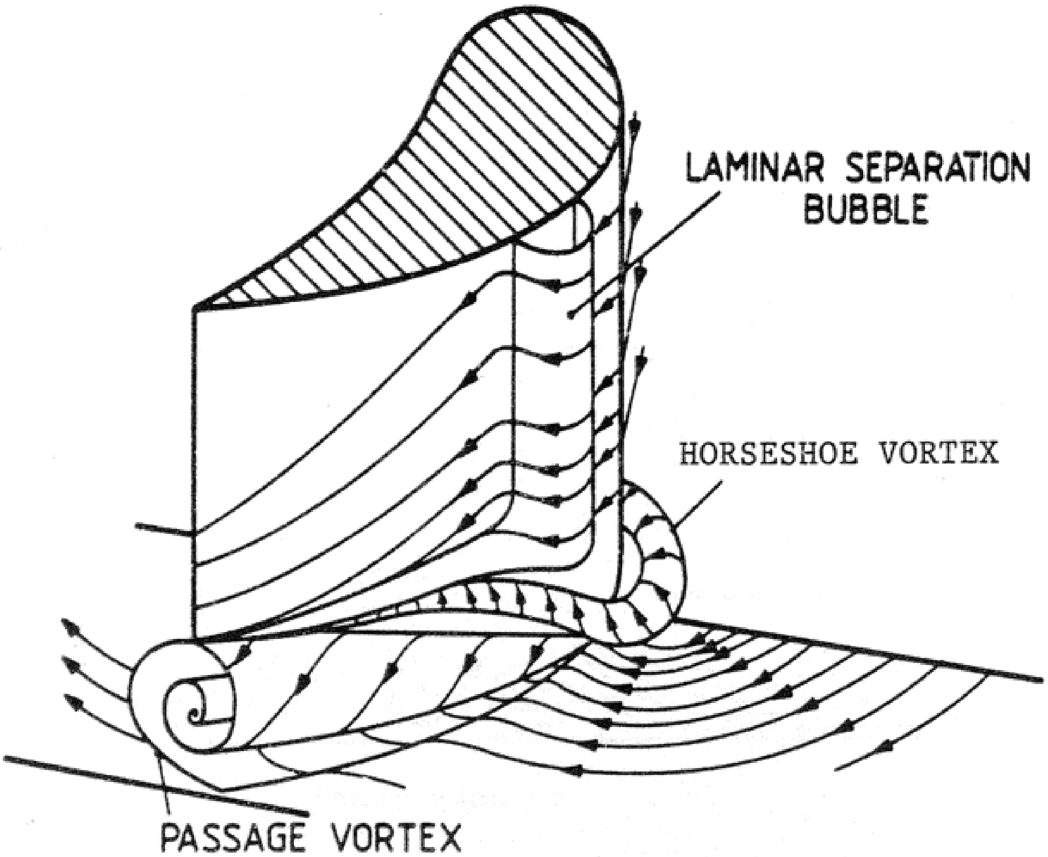

Figure 2.3: Development of 'passage vortex' in end-wall region of cascade of aerofoils (adapted from Klien, 1966)

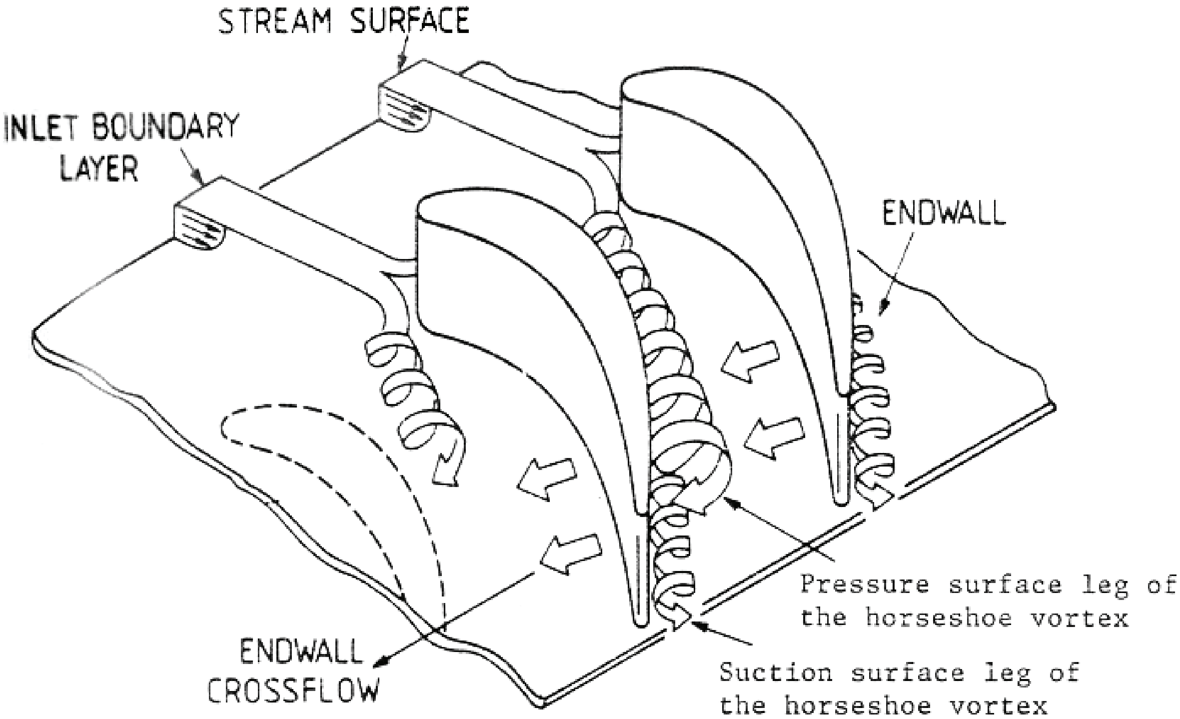

Figure 2.4: Development of 'horseshoe vortex' in end-wall region of cascade of aerofoils (adapted from Langston et al., 1977)

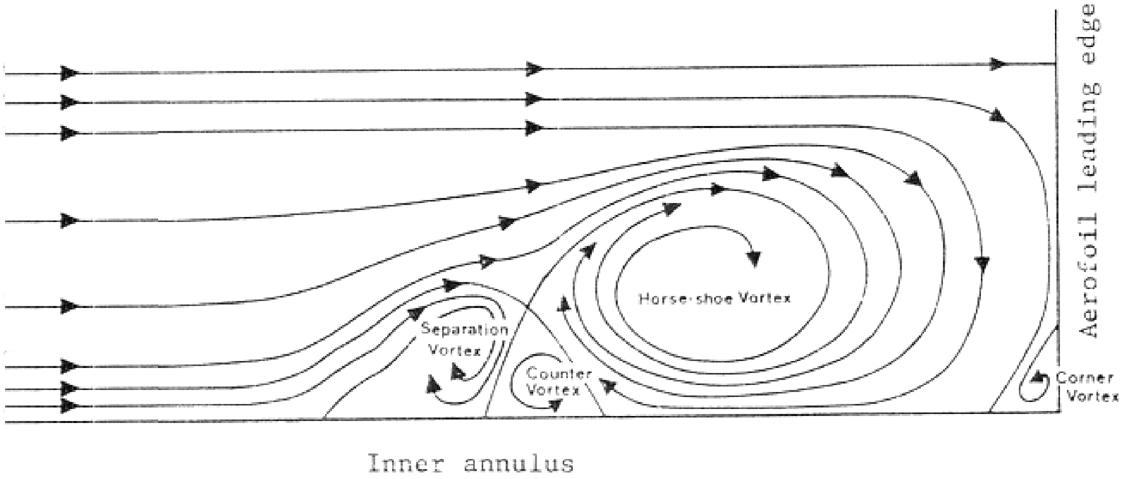

Figure 2.5: Flow model of three-dimensional turbulent detached region in stagnation plane at aerofoil/end-wall intersection (adapted from Ishii & Honami, 1985)

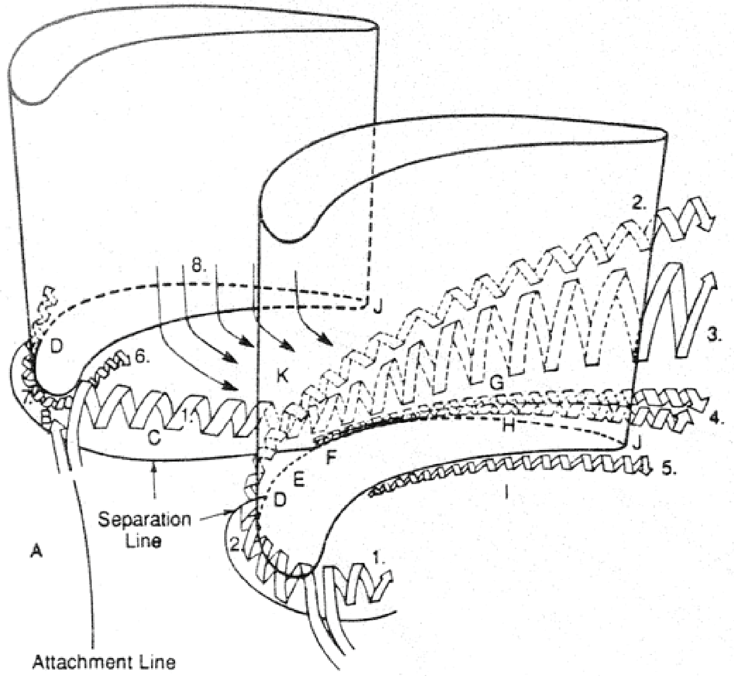

1. Pressure surface leg of the horseshoe vortex
2. Suction surface leg of the horseshoe vortex
3. Passage vortex
4. Suction surface corner vortices
5. Pressure surface corner vortex
6. Pressure surface corner vortex
7. Suction surface corner vortex
8. Downward velocity component on the pressure surface

Figure 2.6: Three-dimensional flow field in end-wall region of cascade of aerofoils (adapted from Goldstein & Spores, 1988)

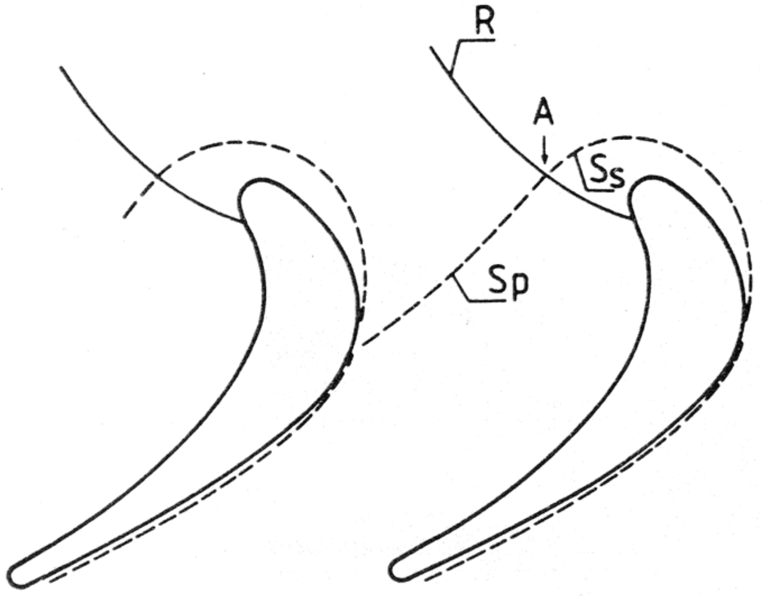

Figure 2.7: End-wall separation and stagnation streamlines for rotor blade in cascade (adapted from Langston et al., 1977)

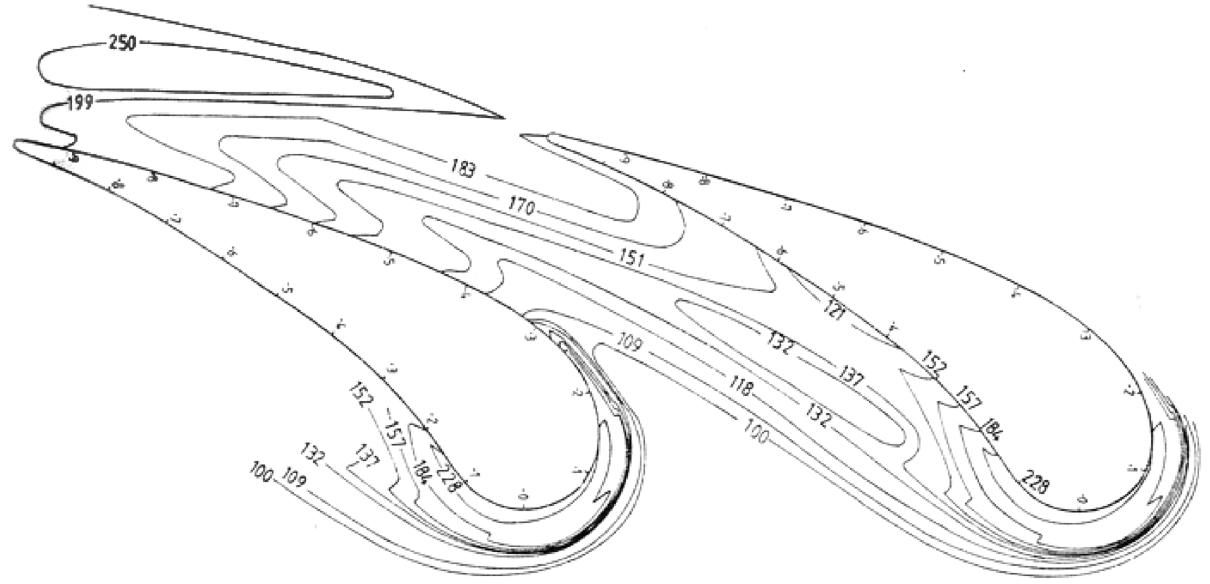

Figure 2.8: Contours of heat-transfer coefficient (W/m² K) on end wall; smaller numbers on vanes (x/s and x/p) represent suction and pressure surfaces respectively (adapted from Ireland et al., 1988)

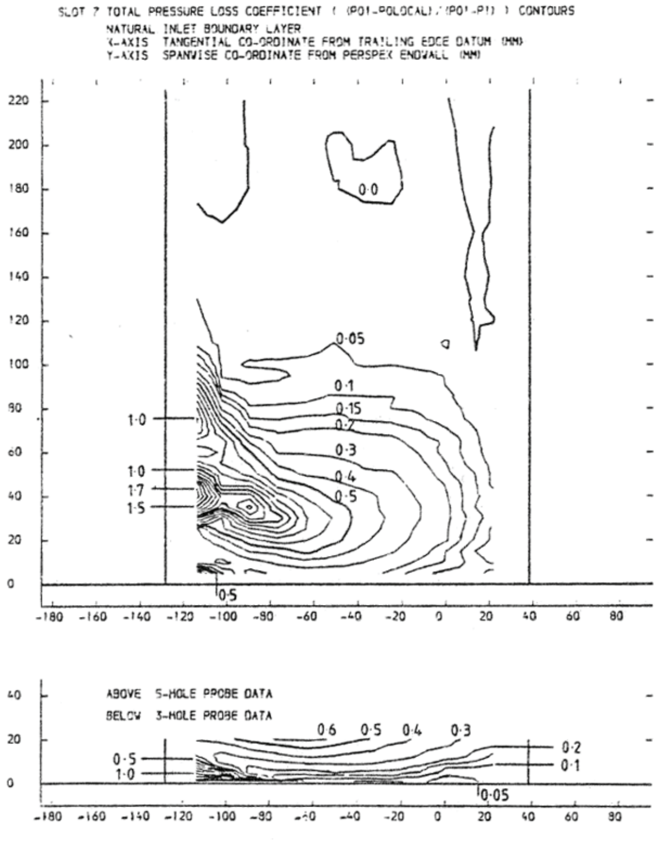

Figure 2.9: Three- and five-hole probe loss measurements in end-wall region of cascade of aerofoils (adapted from Gregory-Smith & Graves, 1983)

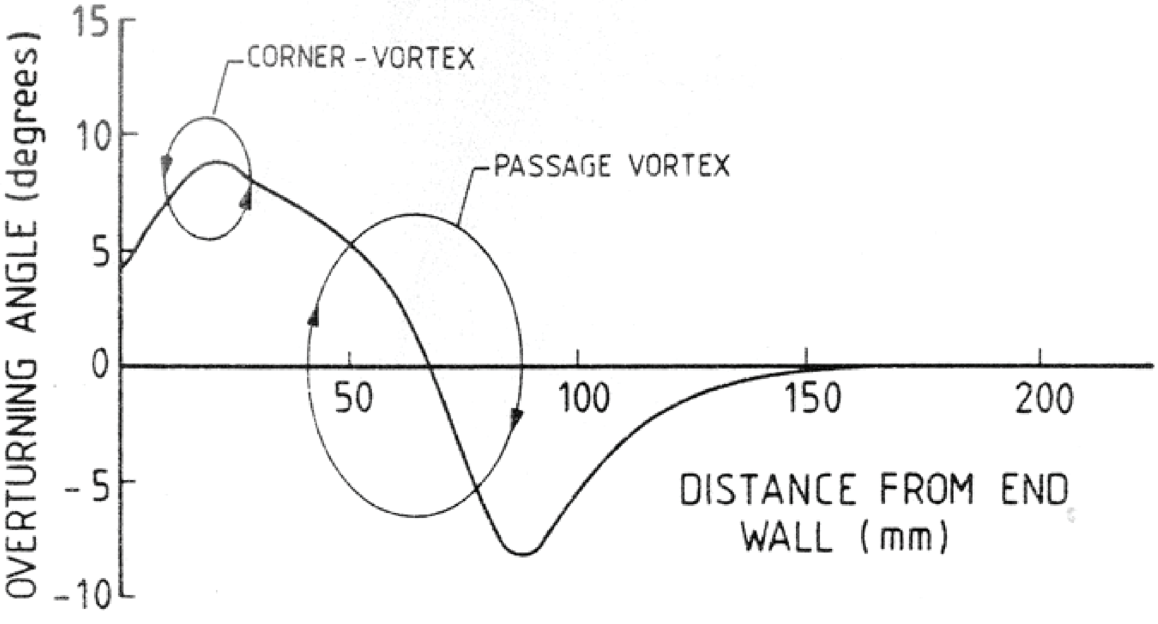

Figure 2.10: Over- and under-turning of flow near end wall due to secondary flow vortices (adapted from Gregory-Smith & Graves, 1983)

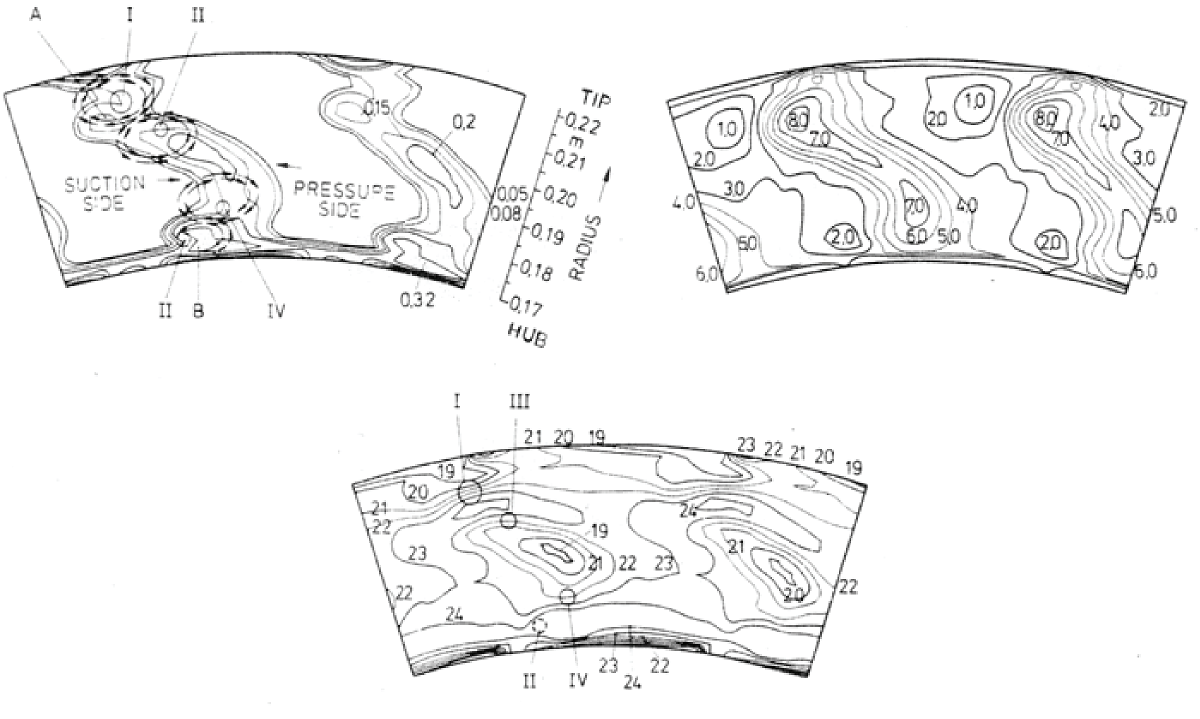

Figure 2.11: Isobar plot of total pressure (2.11a), top left; isocline 166 plot of slope (2.11b), top right; yaw angle (2.11c), bottom (design exit yaw angle equals 21º); adapted from Binder (1982)

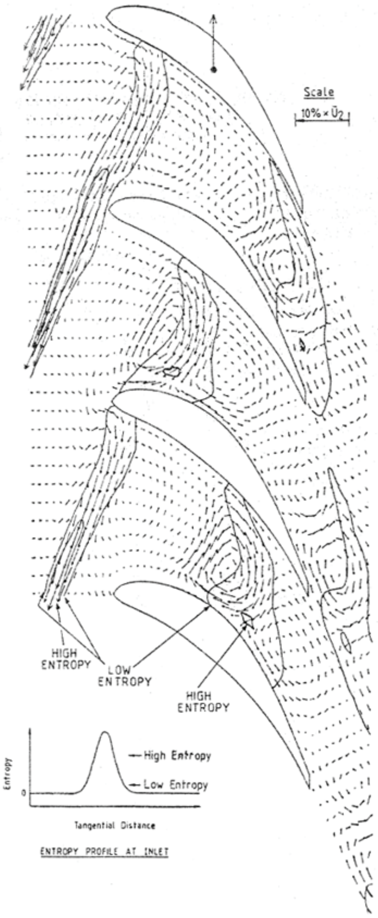

Figure 2.12: Unsteady velocity vectors and entropy contours (adapted from Hodson, 1984b)

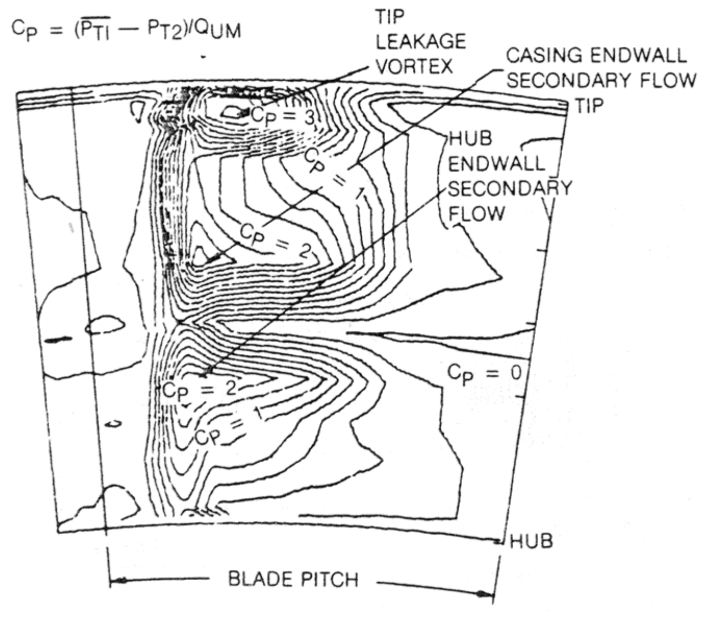

Figure 2.13: Relative frame total pressure contours 6.8% blade axial chord downstream of turbine rotor blade (adapted from Dring & Joslyn, 1981)

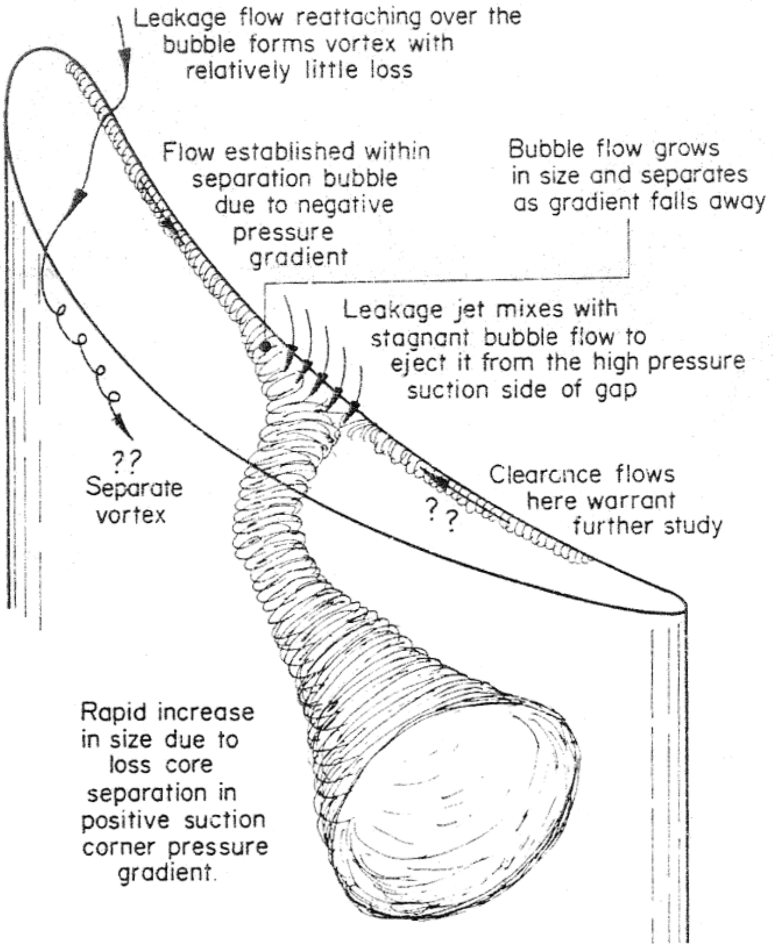

Figure 2.14: Suggested history and effect of clearance-gap separation bubble in terms of loss formation internal to gap, and in the suction corner mixing zone (adapted from Bindon, 1988)

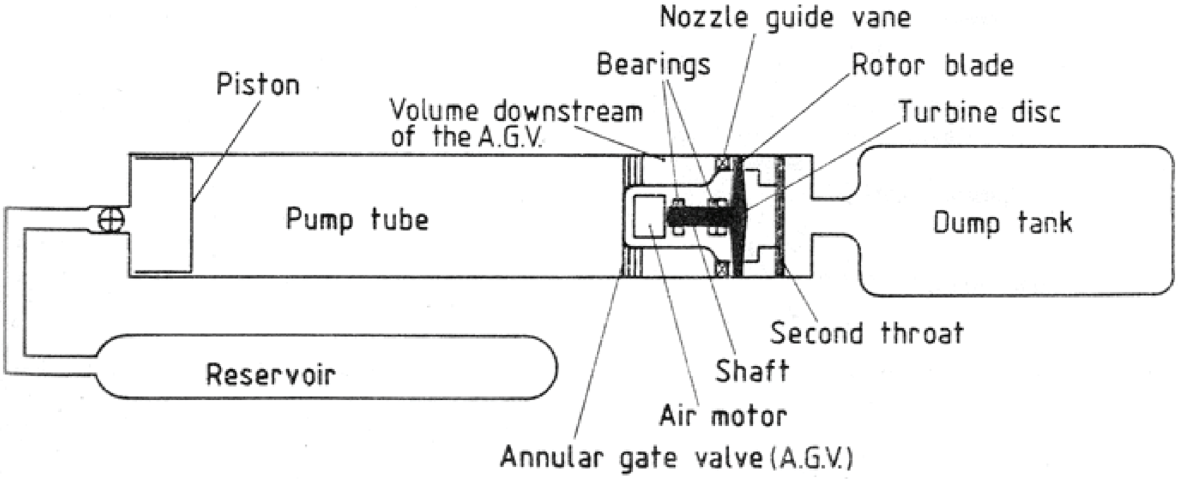

Figure 3.1: Layout of OUEL transient turbine-test facility

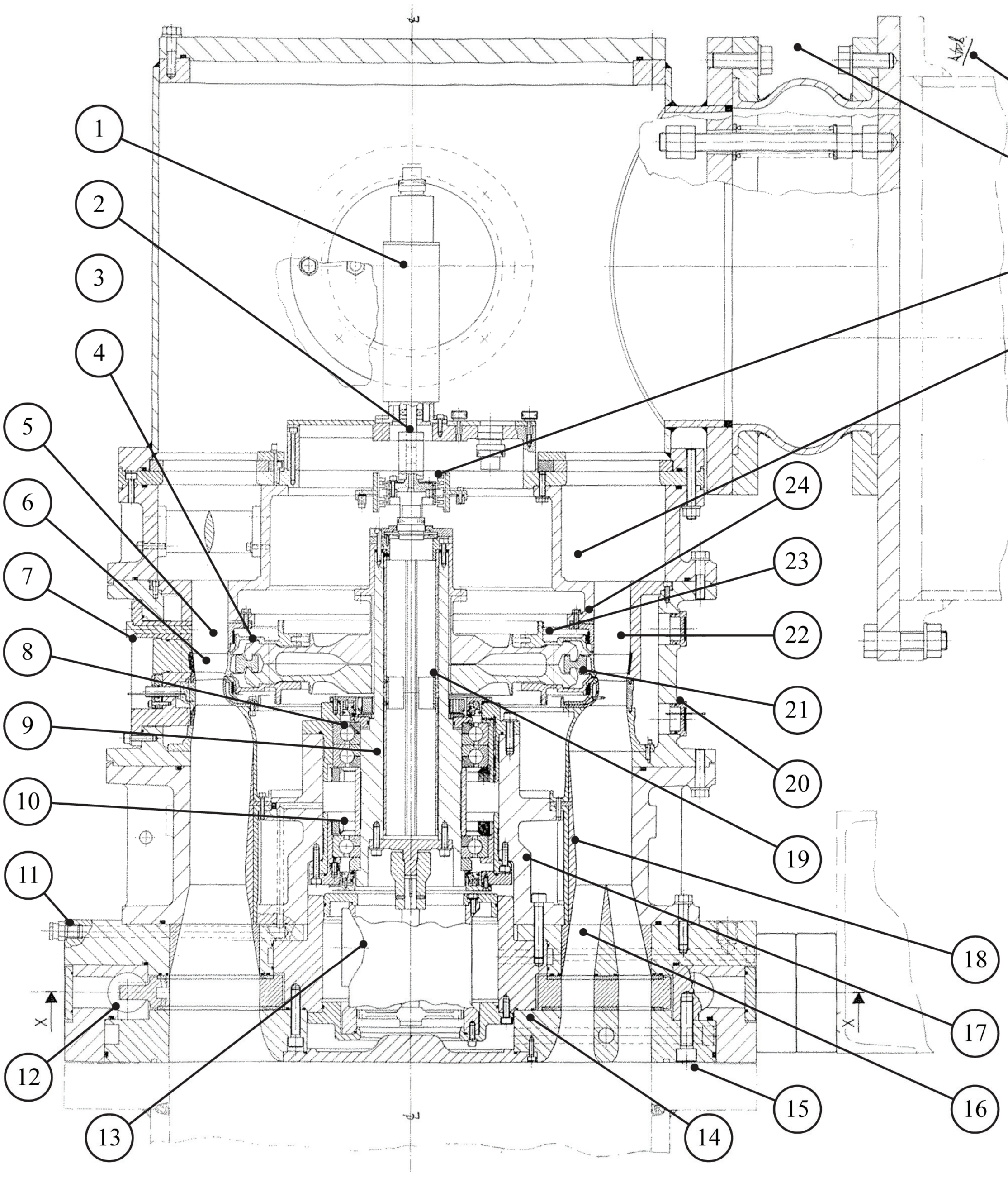

1	Slip ring
2	Flexible coupling
3	Second throat
4	Mini-disc
5	Rotor blades (60)
6	Vanes (36)
7	Cassette of four vanes
8	Matched bearing pair
9	Turbine shaft
10	Single bearing
11	Annular gate valve
12	Annular manifold
13	Air motor
14	Air motor exhaust lines (26)
15	ILPT pump tube
16	Air motor air feed lines (24)
17	Bearing housing
18	Inlet duct inner wall 'hump'
19	Instrumentation carrier
20	Brass boss
21	Upstream labyrinth seal
22	Blade overtip abradable seal
23	Split turbine disc
24	Downstream labyrinth seal
25	Step expansion
26	Shaft encoder assembly
27	Flexible seal
28	ILPT dump tank

Figure 3.2: General arrangement of turbine module, OUEL transient turbine-test facility working section

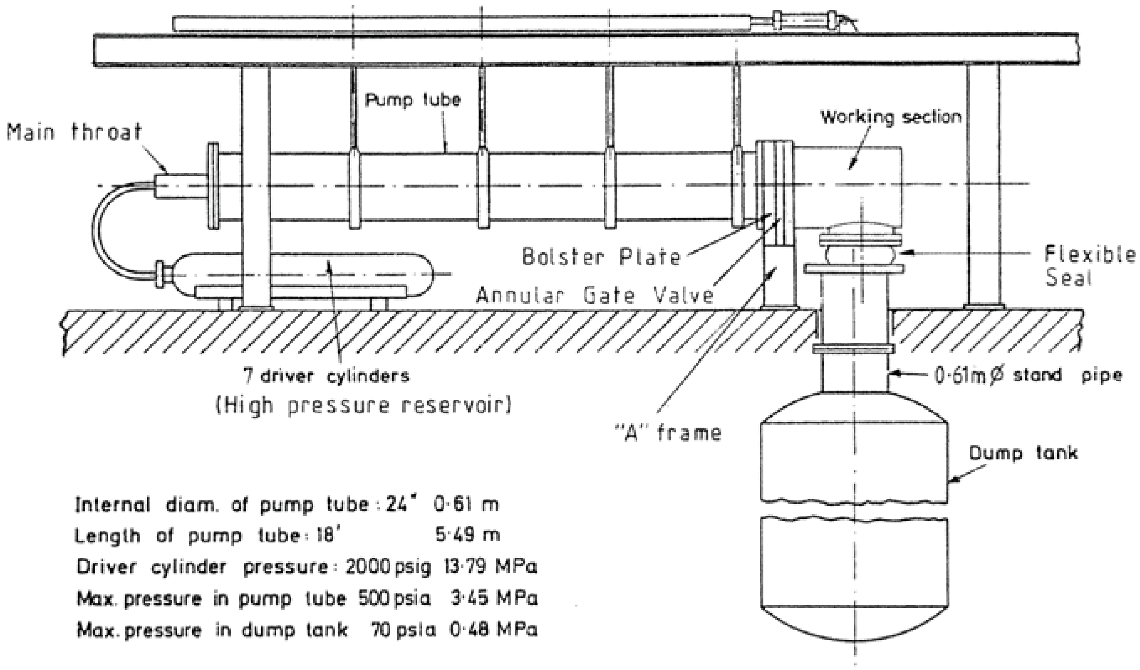

Figure 3.3: General arrangement of OUEL transient turbine-test facility

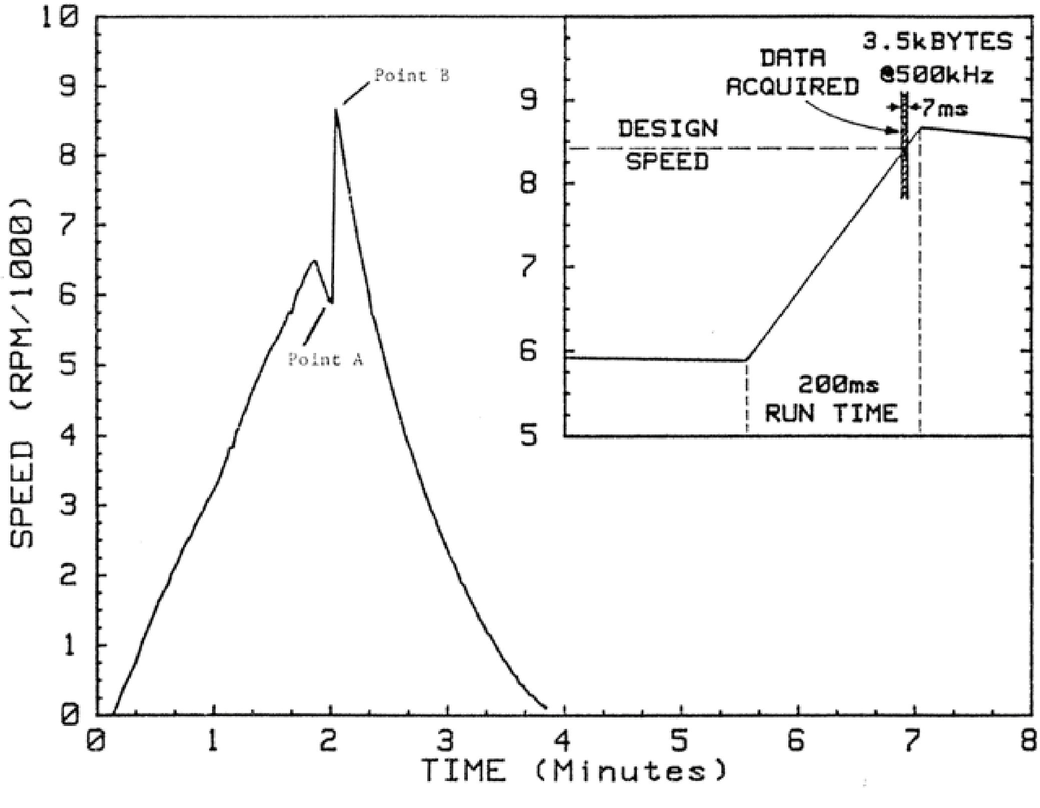

Figure 3.4: Operating sequence of OUEL transient turbine-test facility

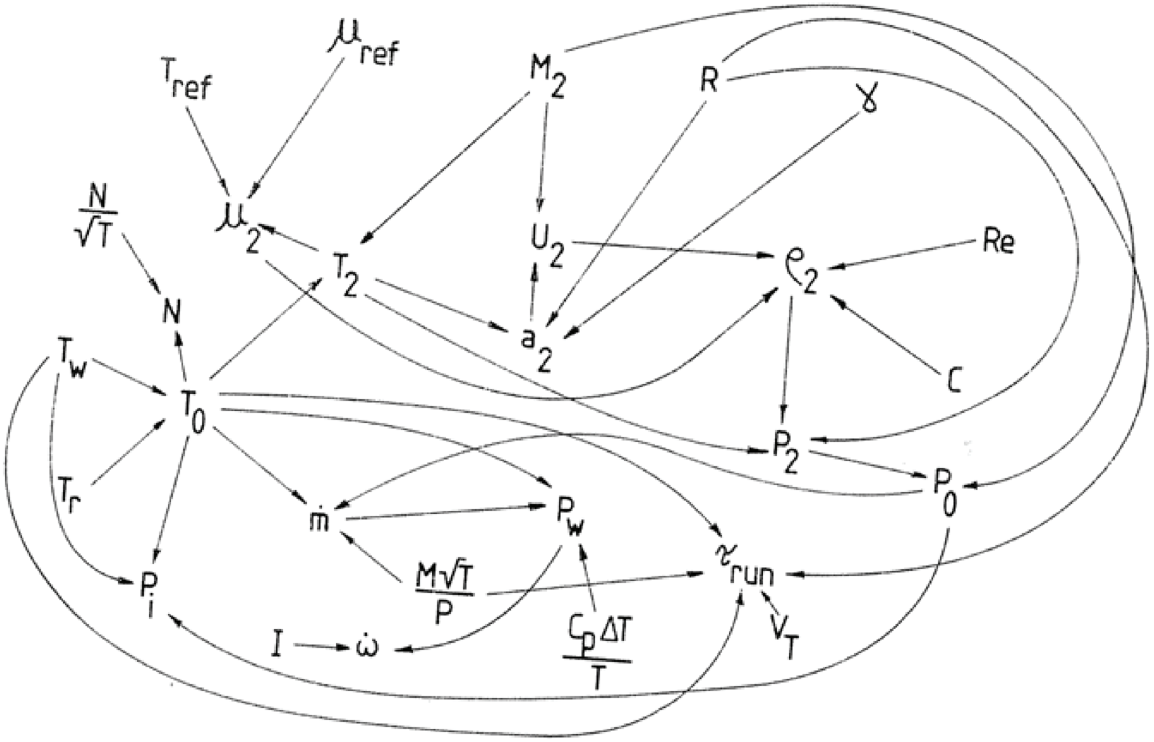

Figure 3.5: Flow chart of design condition calculations

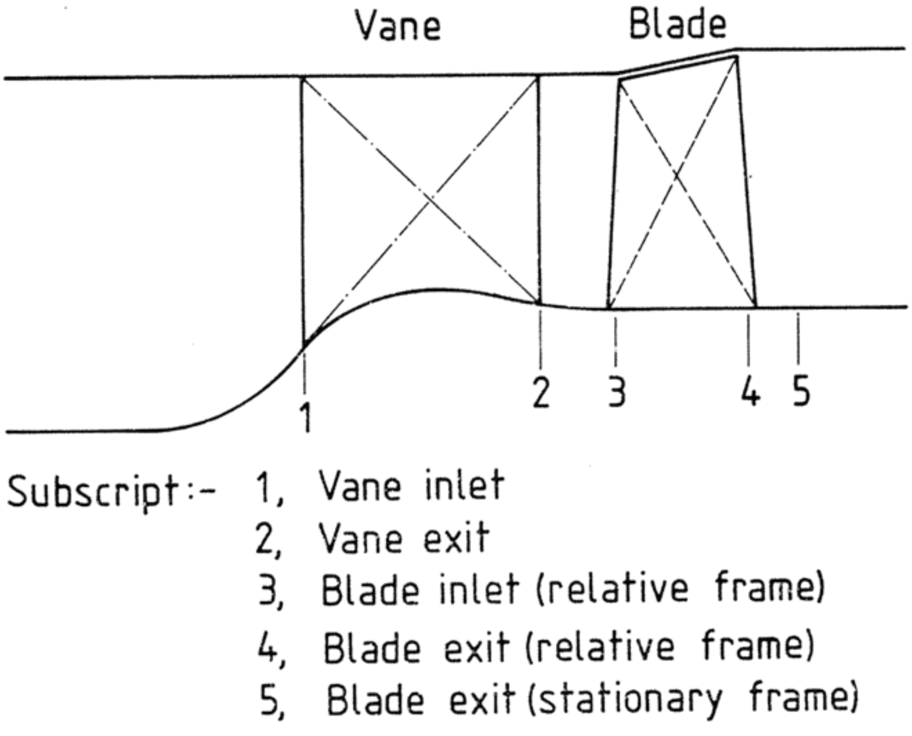

Figure 3.6: Definition of axial turbine stations

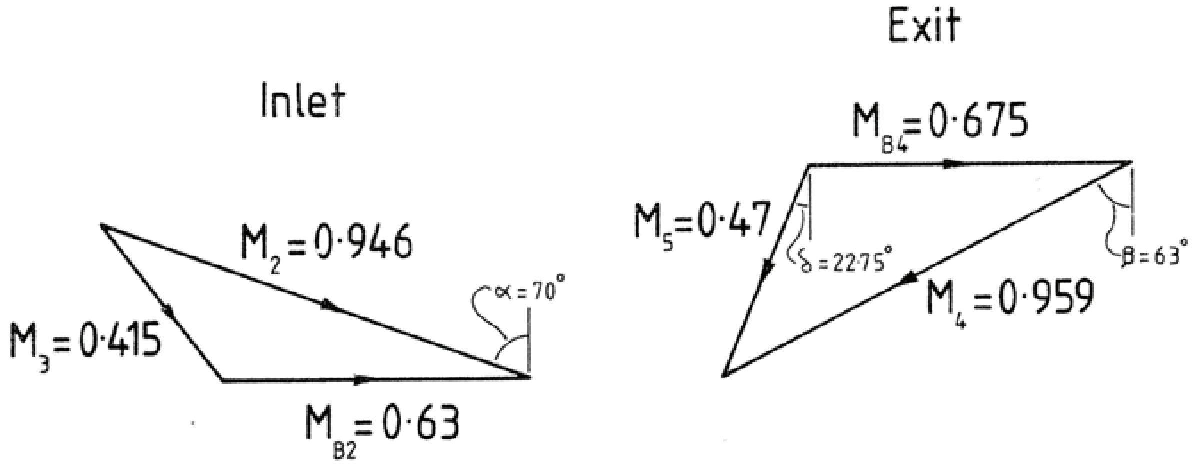

Figure 3.7: Blade mid-height design condition inlet (left) and exit (right) velocity triangles

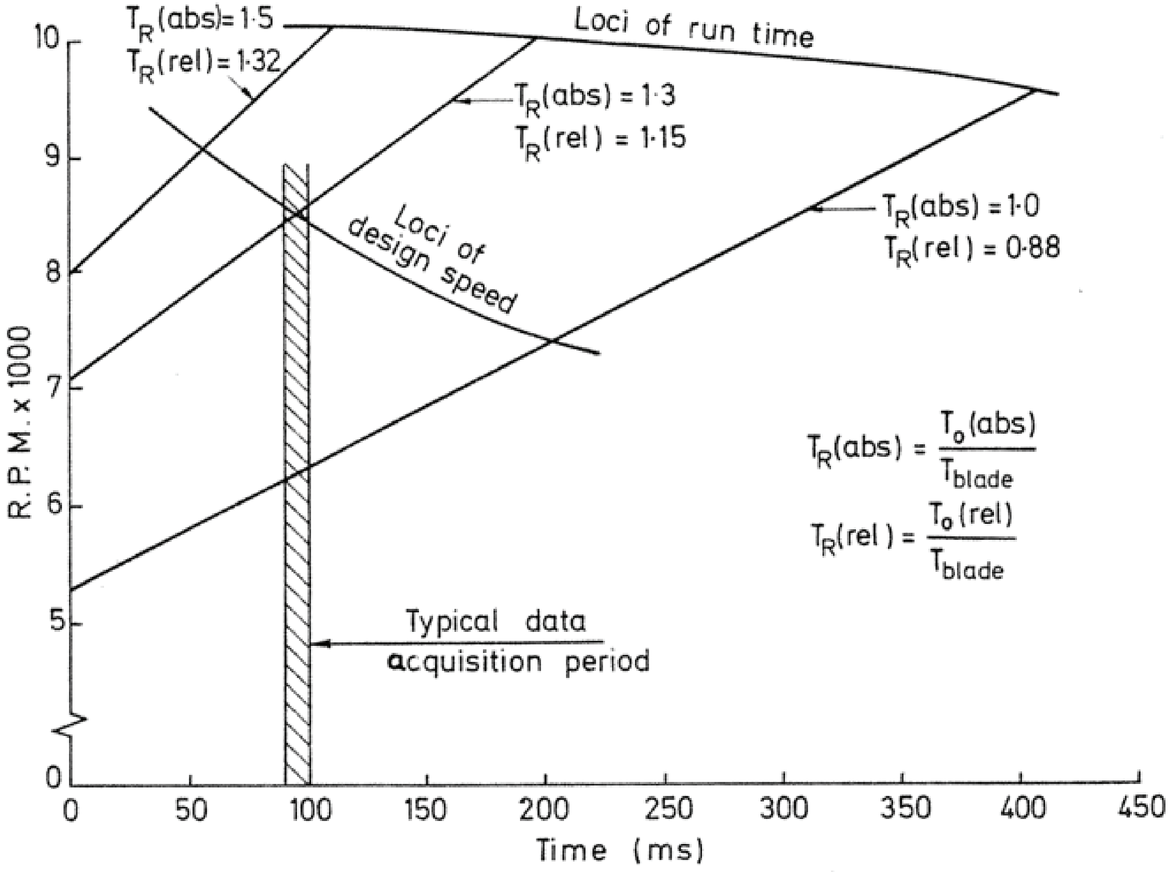

Figure 3.8: Working section operating envelope

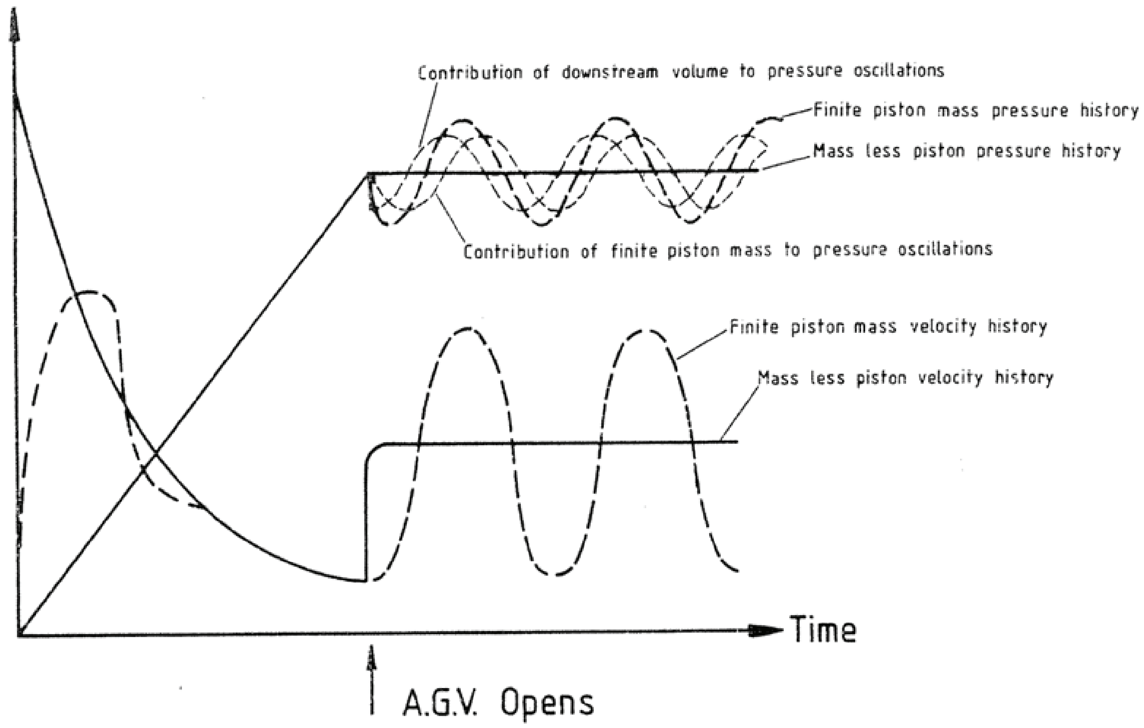

Figure 3.9: **Theoretical velocity history and tube pressure history illustrating effect of finite piston mass and AGV downstream volume on working section inlet pressure and piston velocity**

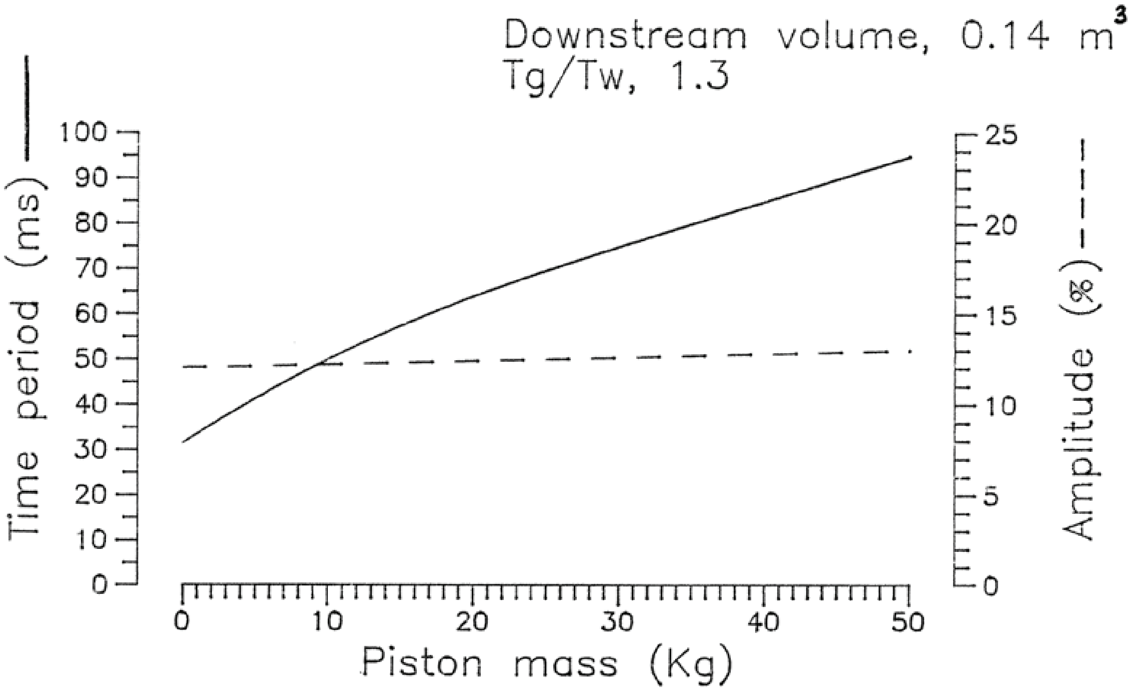

Figure 3.10: **Prediction of piston oscillation amplitude and time period as a function of piston mass, using method of Brooks & Jones (1989)**

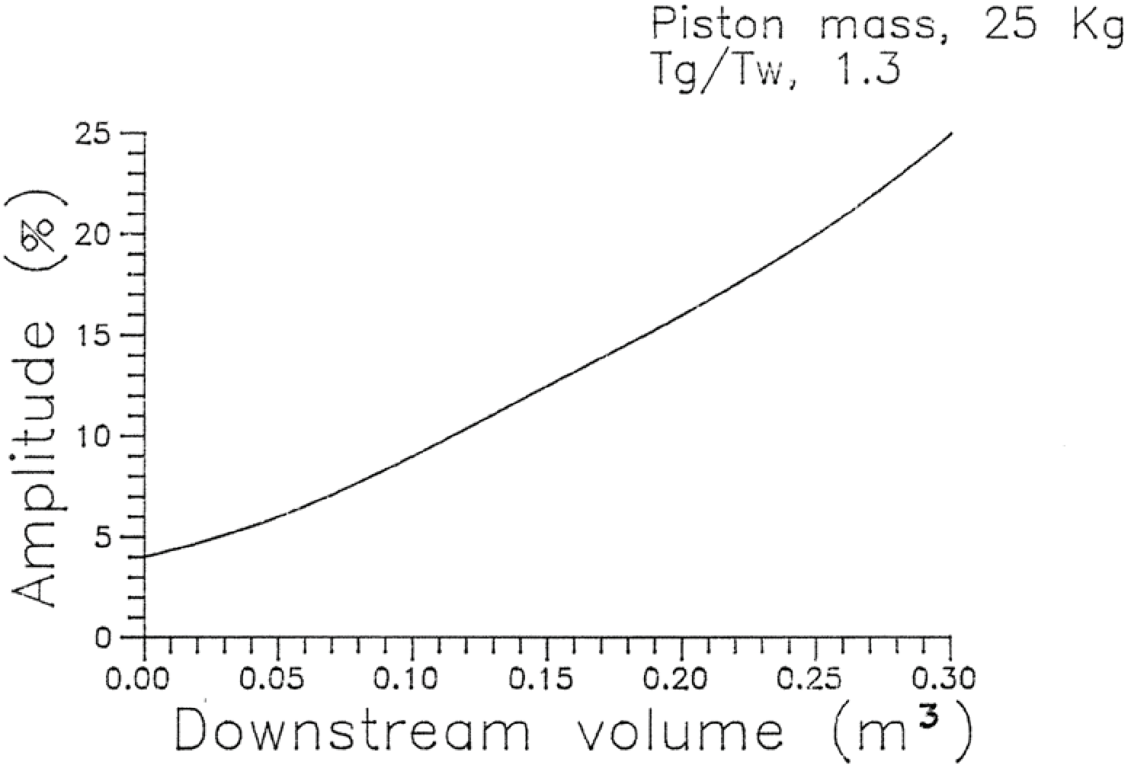

Figure 3.11: Conditions in pump tube and working section during facility operation, taken from UV trace of a typical run

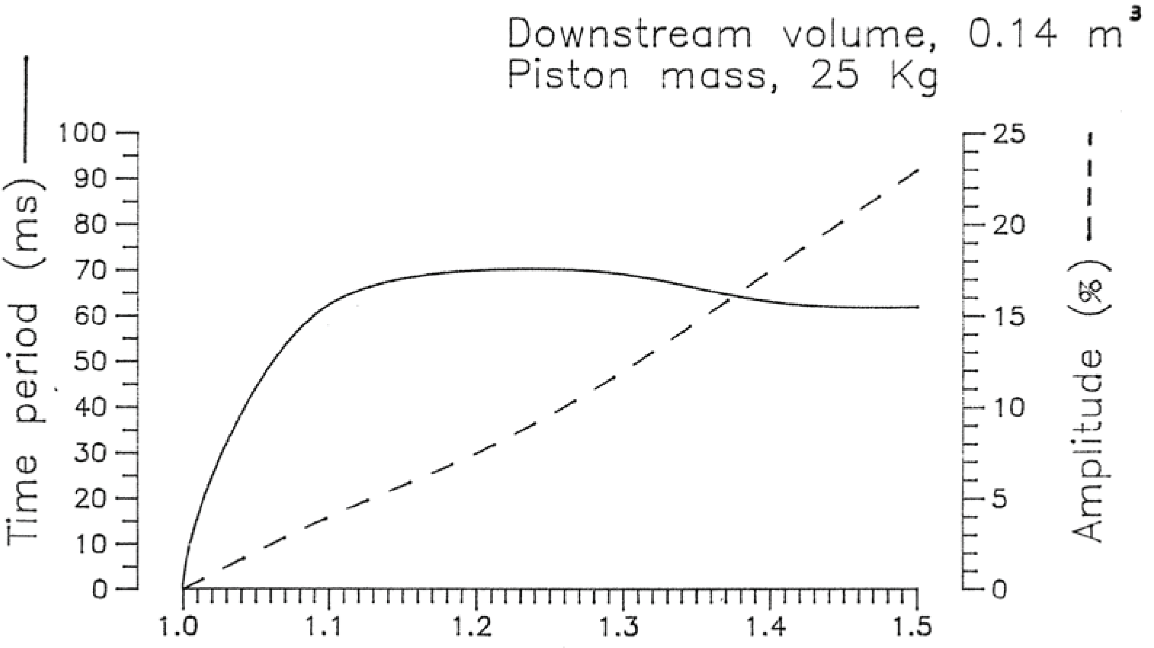

Figure 3.12: Prediction of piston oscillation amplitude and time period as a function of working-section temperature ratio, using method of Brooks & Jones (1989)

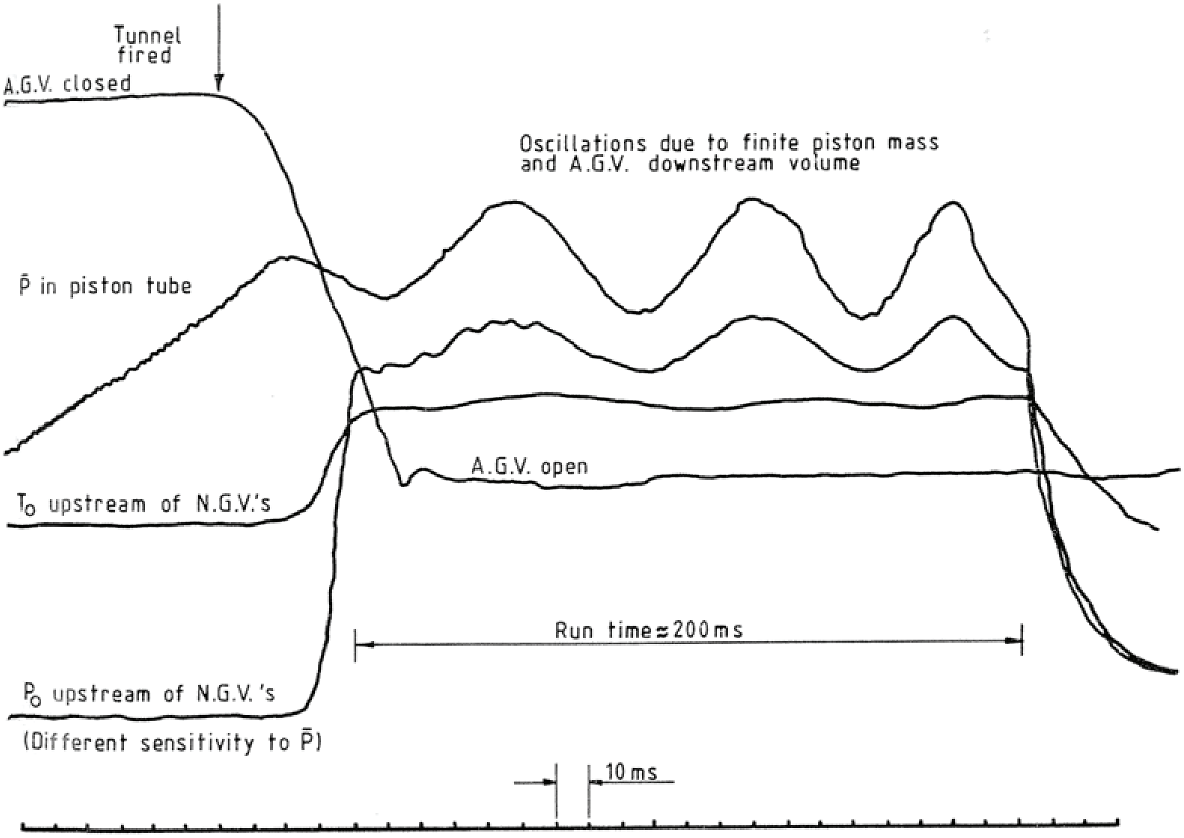

Figure 3.13: Conditions in pump tube and working section during facility operation, taken from UV trace of a typical run

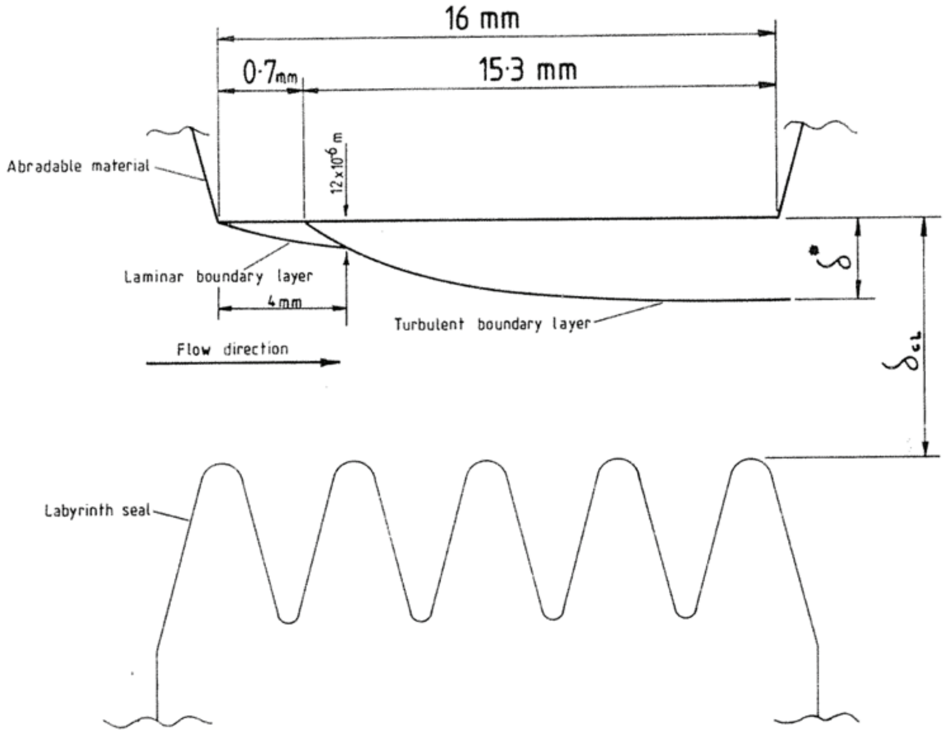

Figure 4.1: Schematic view of boundary-layer development through turbine disc upstream labyrinth seal

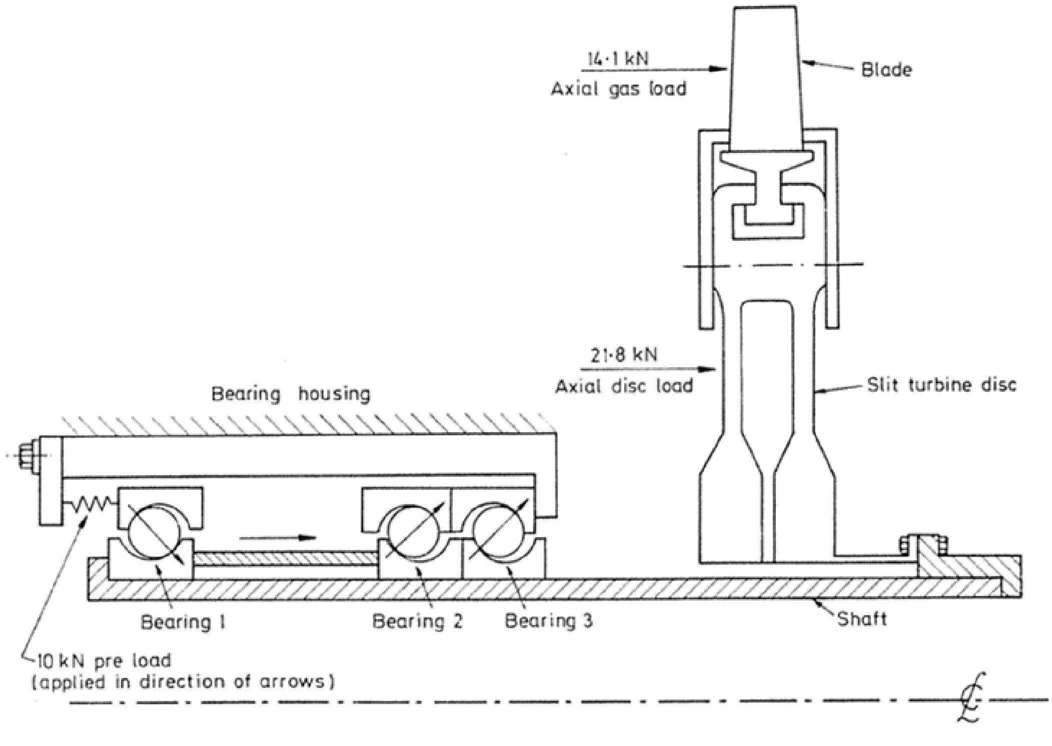

Figure 4.2: Proposed concept for single-sided bearing system for use in turbine module

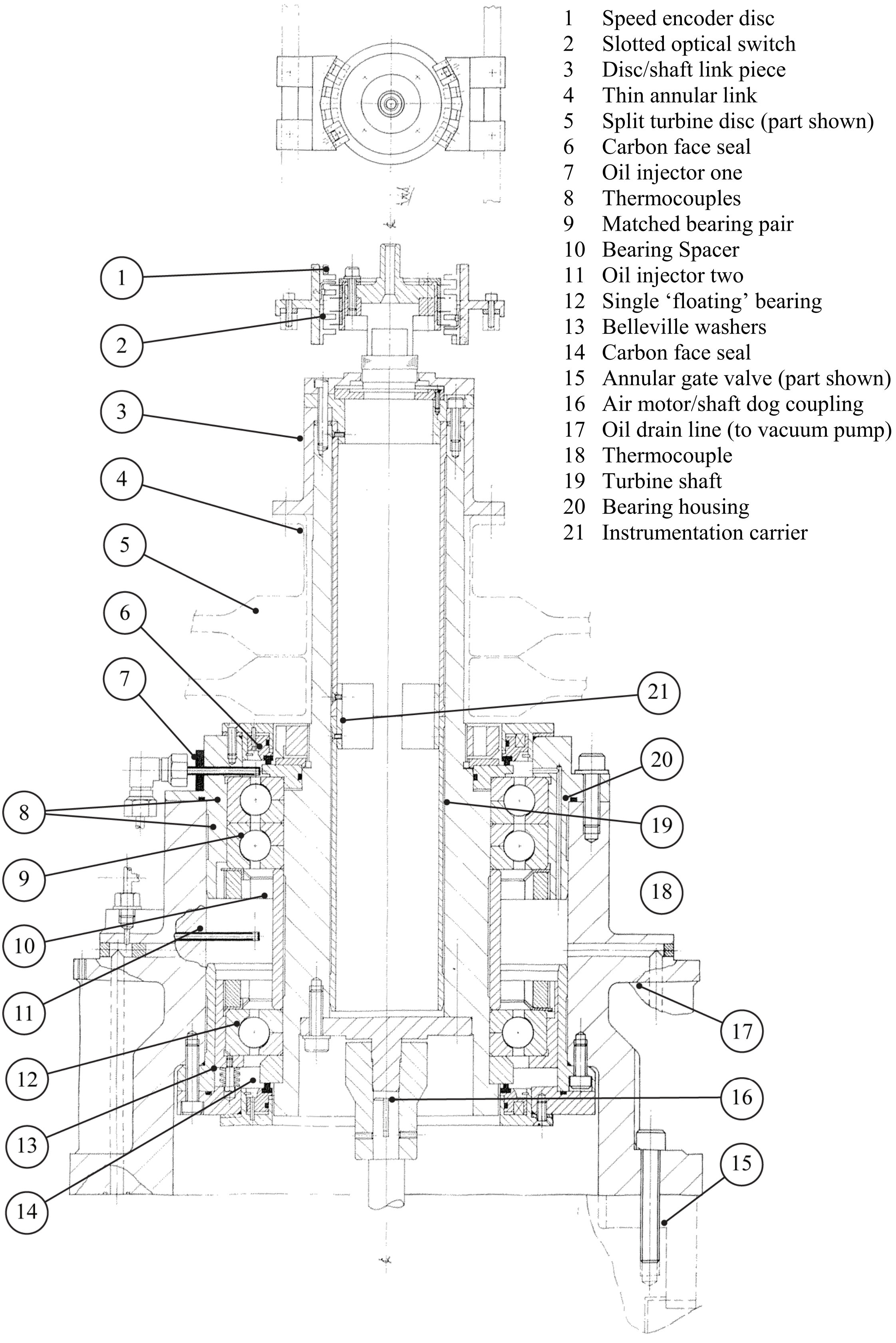

1	Speed encoder disc
2	Slotted optical switch
3	Disc/shaft link piece
4	Thin annular link
5	Split turbine disc (part shown)
6	Carbon face seal
7	Oil injector one
8	Thermocouples
9	Matched bearing pair
10	Bearing Spacer
11	Oil injector two
12	Single ‘floating’ bearing
13	Belleville washers
14	Carbon face seal
15	Annular gate valve (part shown)
16	Air motor/shaft dog coupling
17	Oil drain line (to vacuum pump)
18	Thermocouple
19	Turbine shaft
20	Bearing housing
21	Instrumentation carrier

Figure 4.3: General arrangement of turbine module bearing system

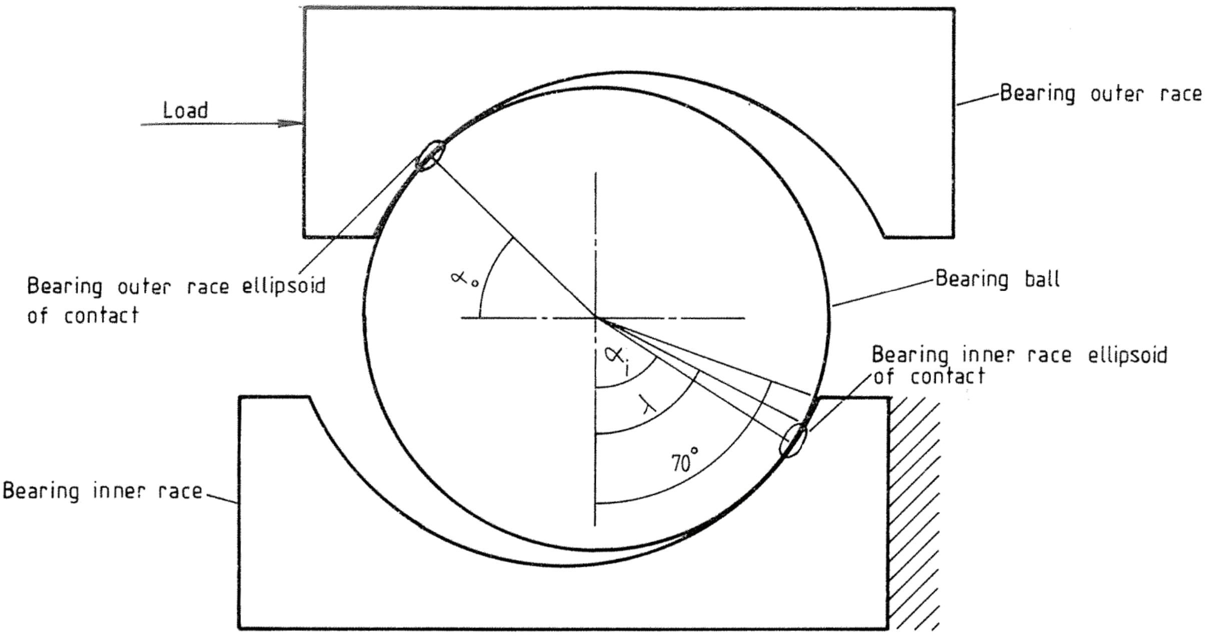

Figure 4.4: Ball-bearing geometry under axial load

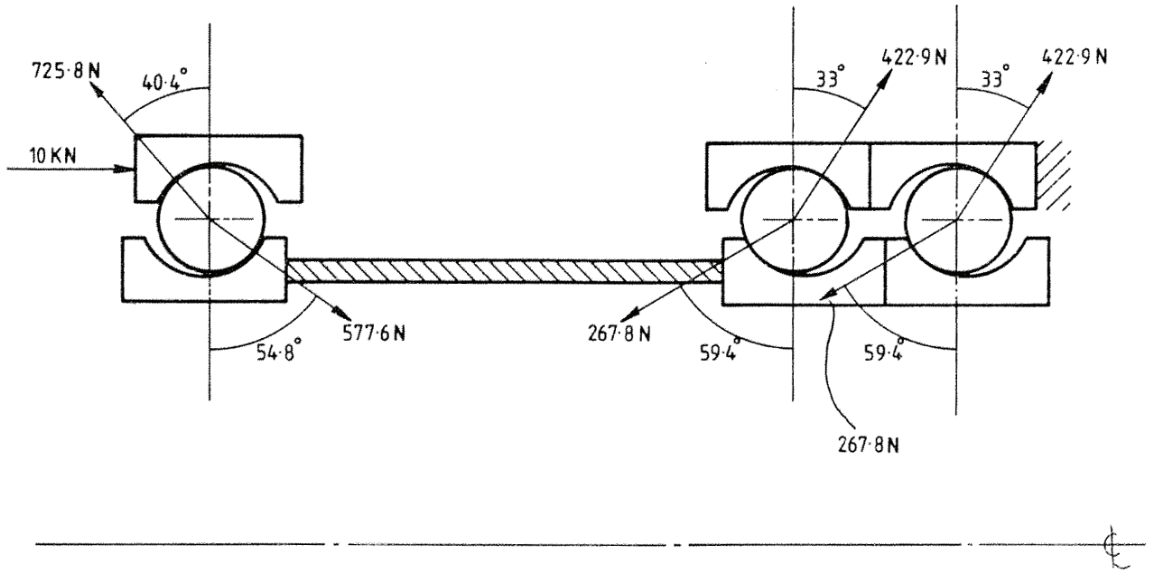

Figure 4.5: Contact angles and loads in single bearing and a bearing from tandem set with ILPT in pre-run state, predicted using SKF code BEARCENT

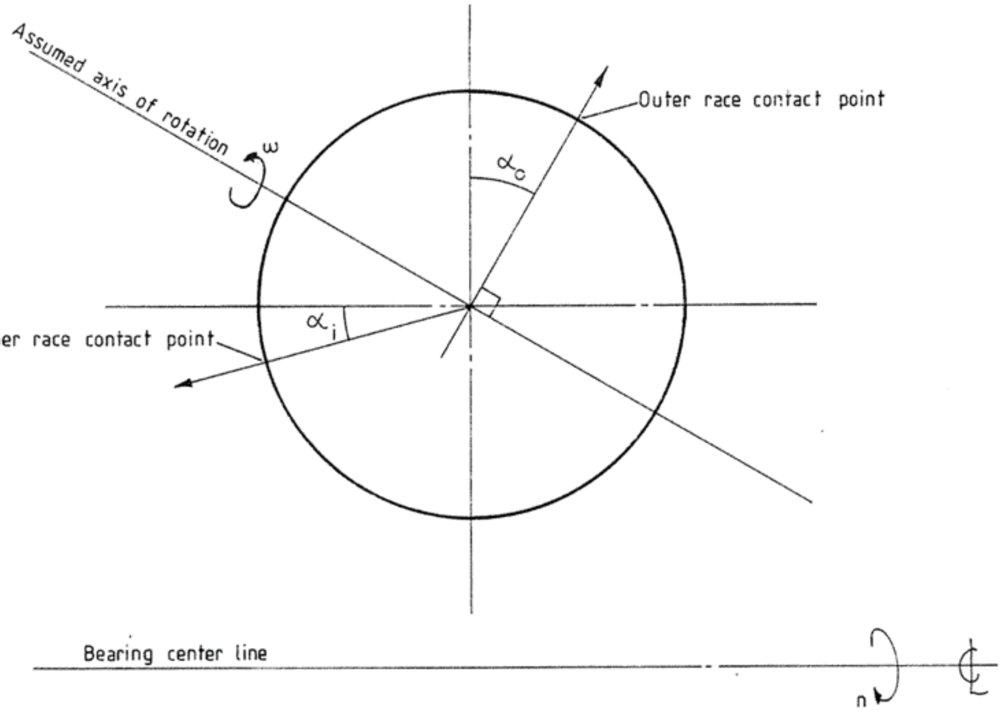

Figure 4.6: **Ball-bearing geometry and assumed axis of rotation for 'outer race control' calculation of bearing cage/shaft speed ratio**

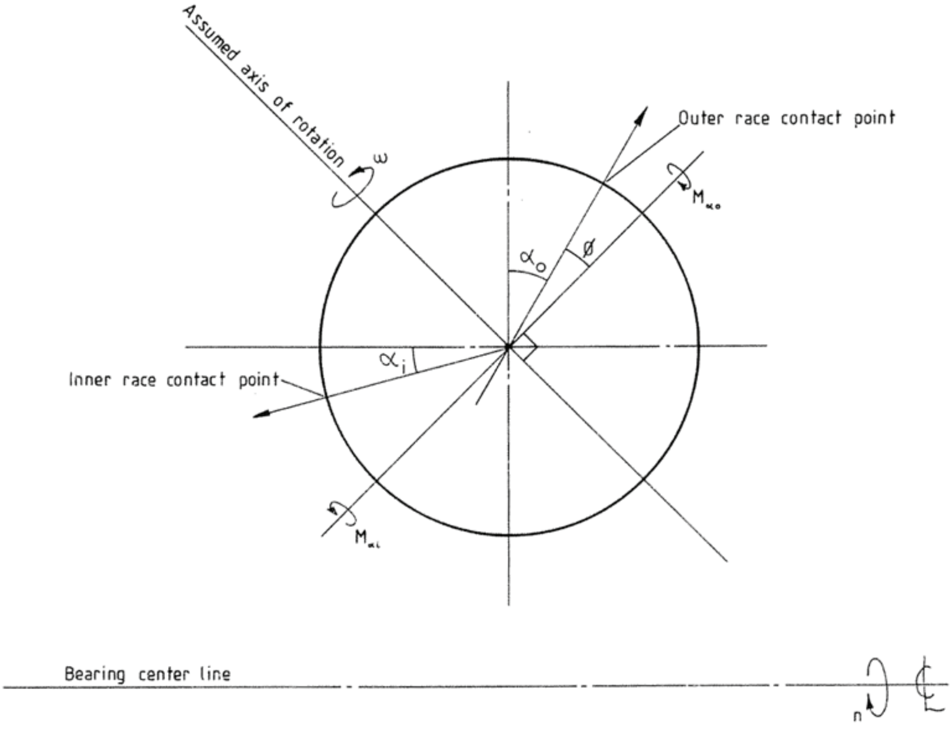

Figure 4.7: **Ball-bearing geometry and assumed axis of rotation for 'combination race control' calculation of bearing cage/shaft speed ratio**

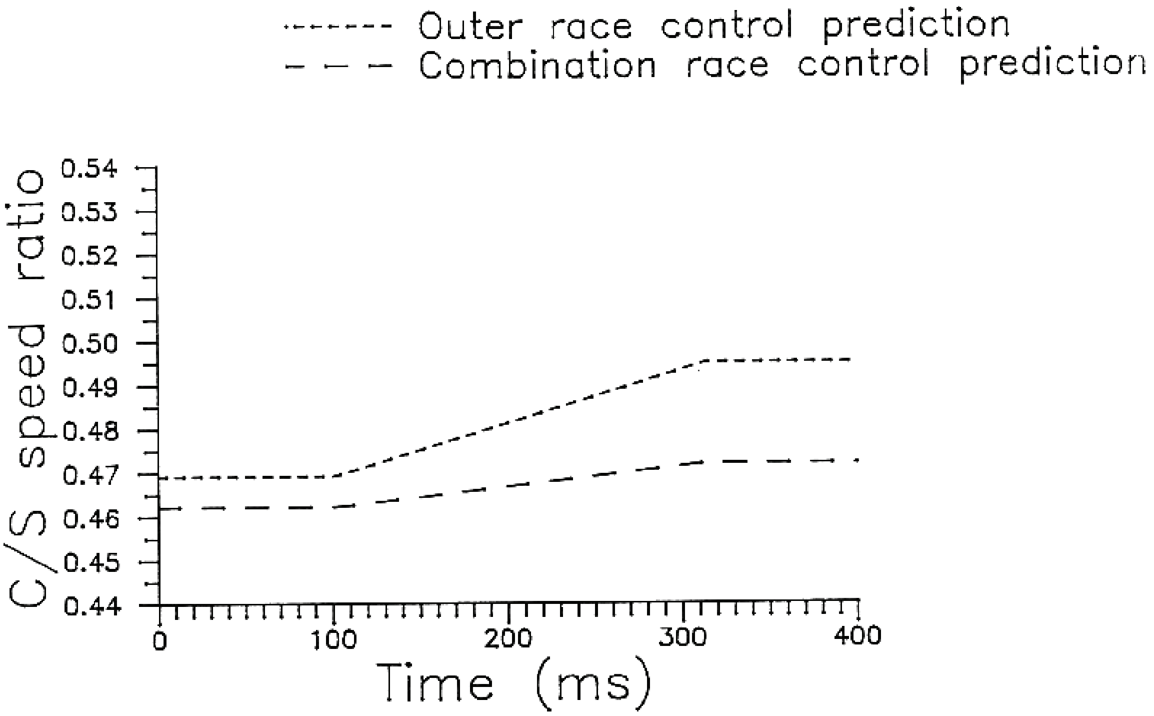

Figure 4.8: **Outer and combination race control predictions of single bearing cage/shaft speed ratio during ILPT operation**

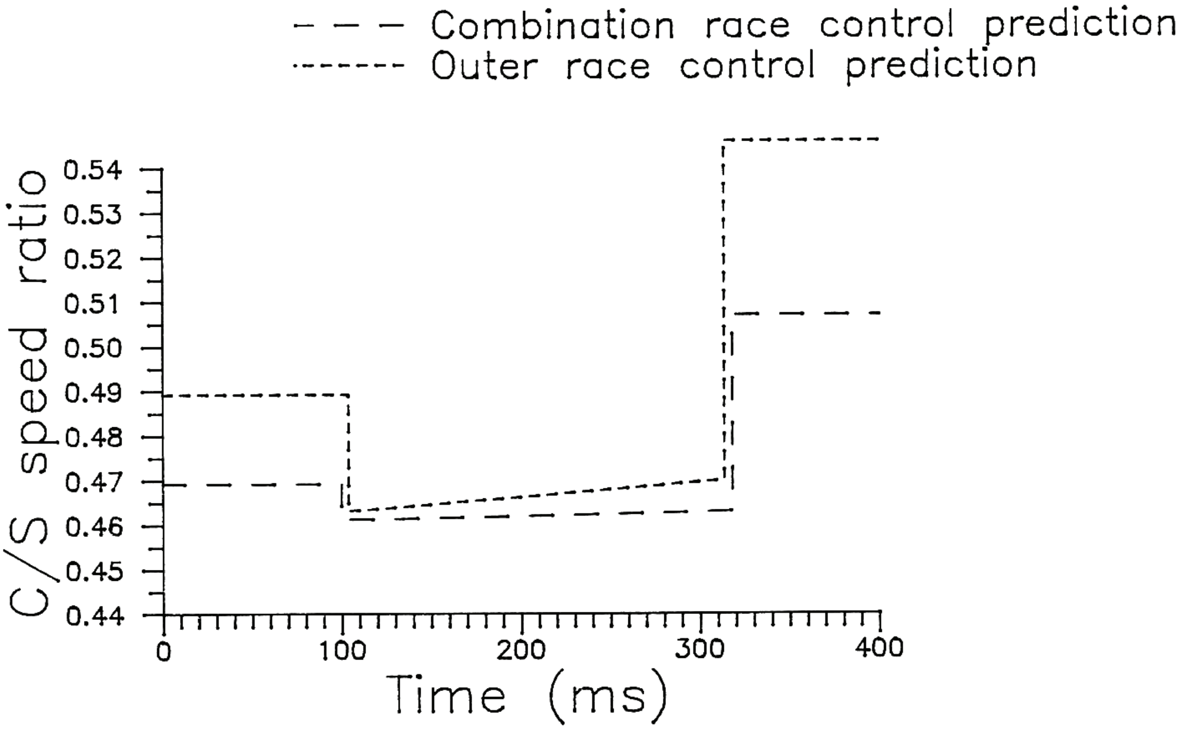

Figure 4.9: **Outer and combination race control predictions of cage/shaft speed ratio for bearing in the tandem set during ILPT operation**

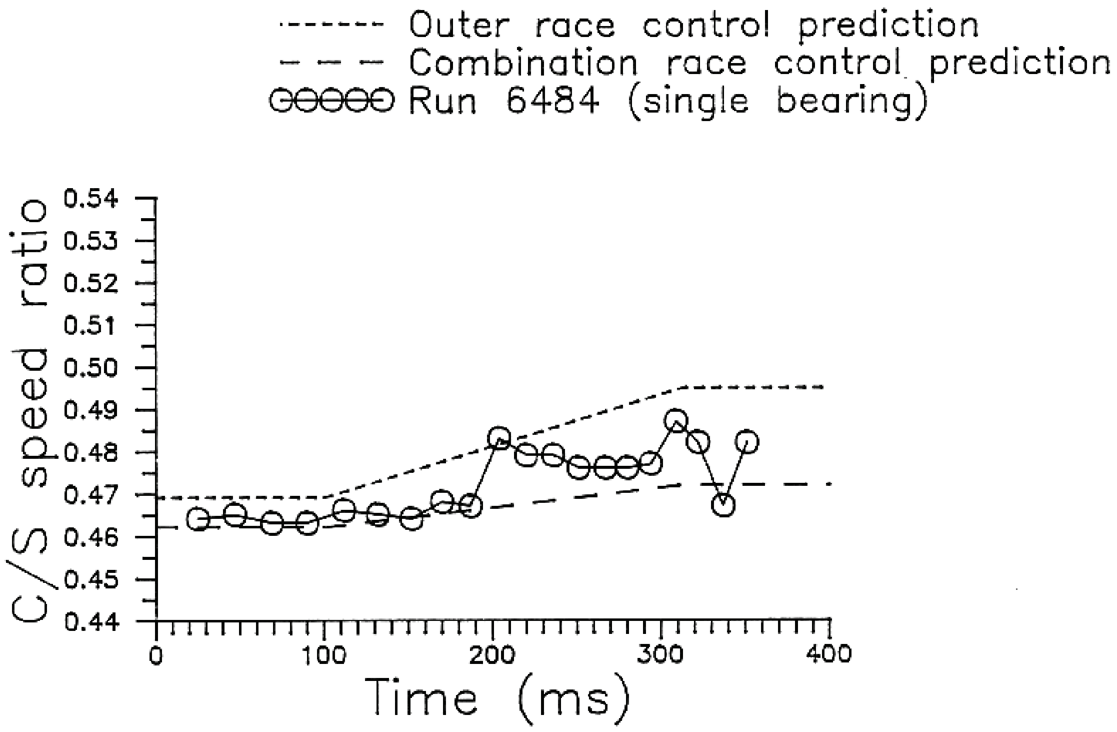

Figure 4.10: Cage/shaft speed ratio measured for single bearing during ILPT Run 6384 and comparison with predictions

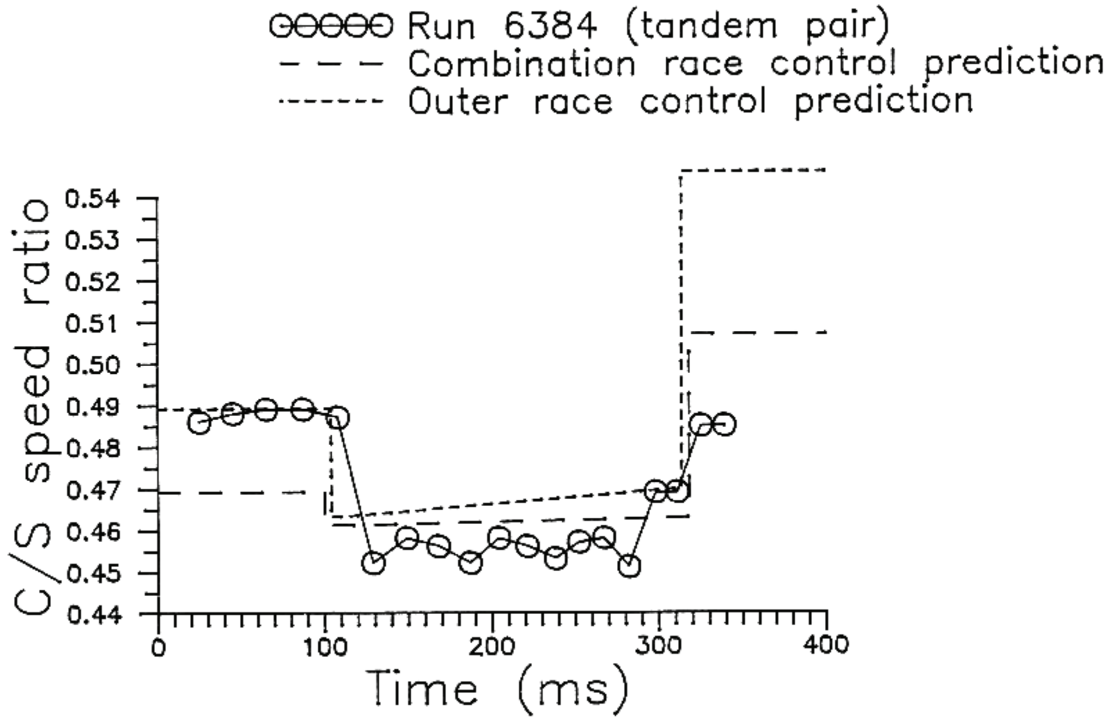

Figure 4.11: Cage/shaft speed ratio measured for upstream bearing of tandem set during ILPT Run 6384 and comparison with predictions

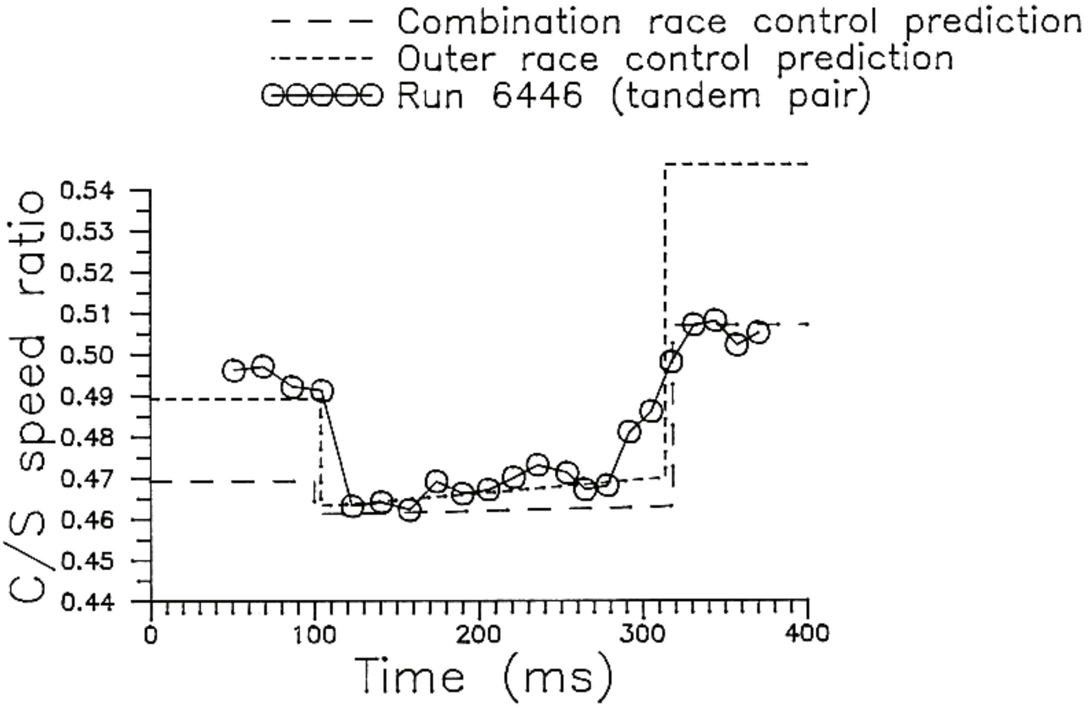

Figure 4.12: Cage/shaft speed ratio measured for upstream bearing of tandem set during ILPT Run 6446 and comparison with predictions

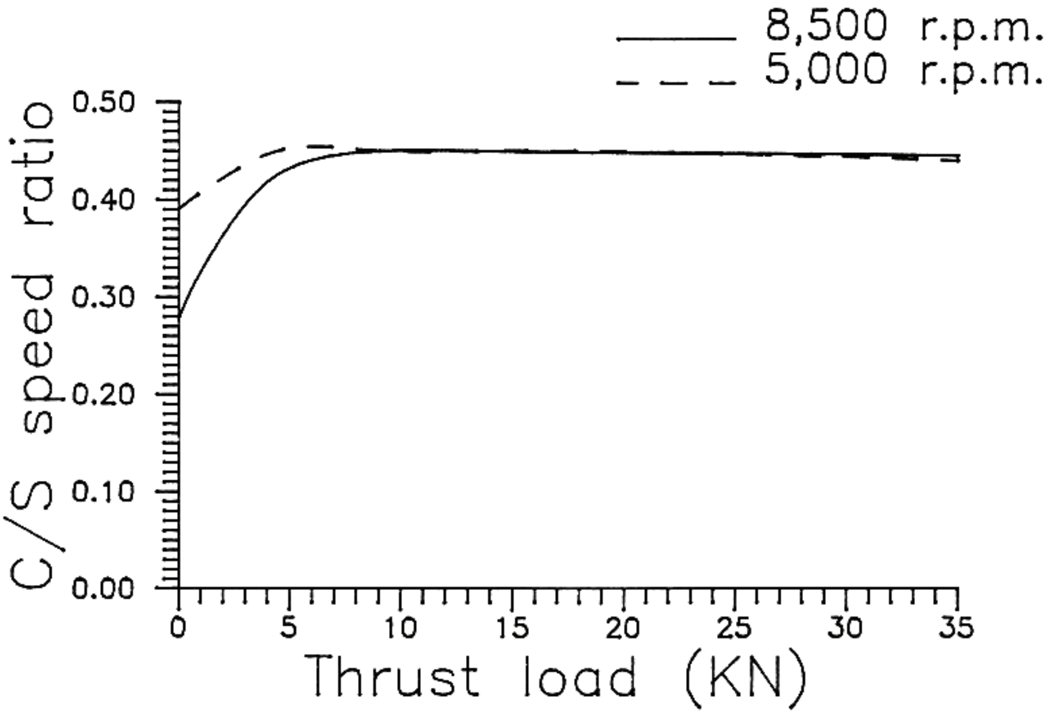

Figure 4.13: Measured cage/shaft speed ratio versus thrust for single-bearing row, for similar bearings to those supplied with B22 turbine (adapted from Stirling, 1969)

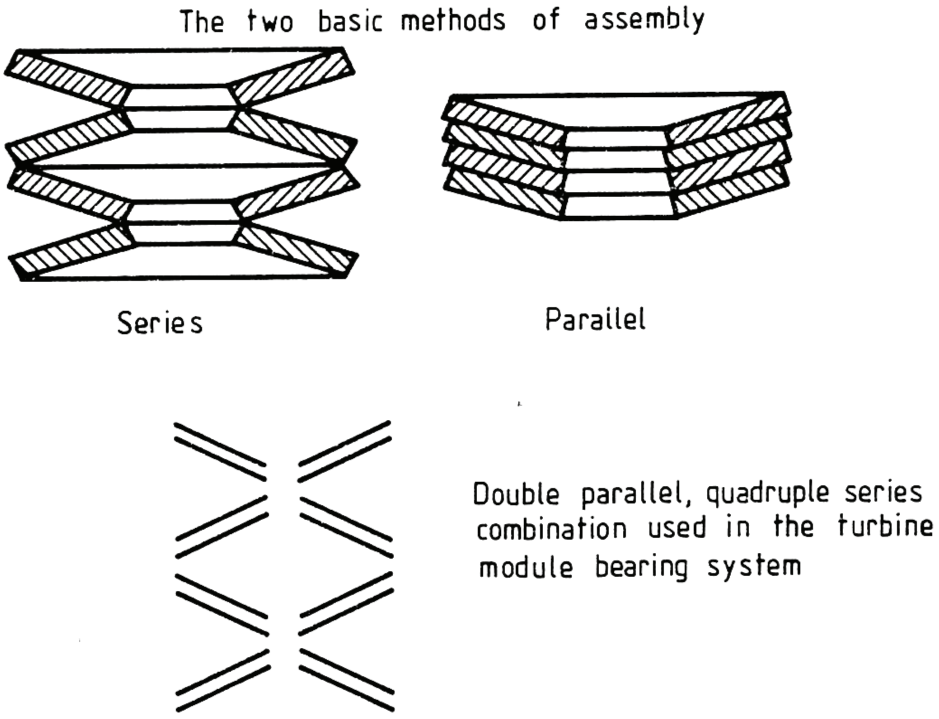

Figure 4.14: Belleville washer stack configurations

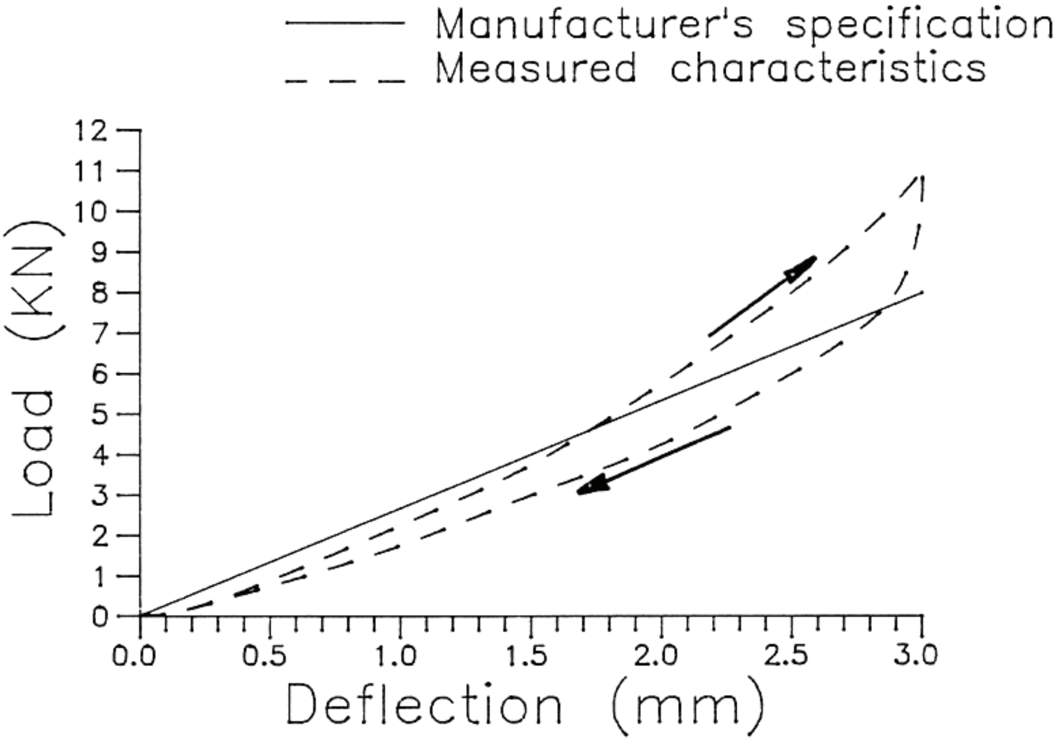

Figure 4.15: Measured load/deflection characteristics of set of Belleville washers assembled in triple parallel quadruple series configuration

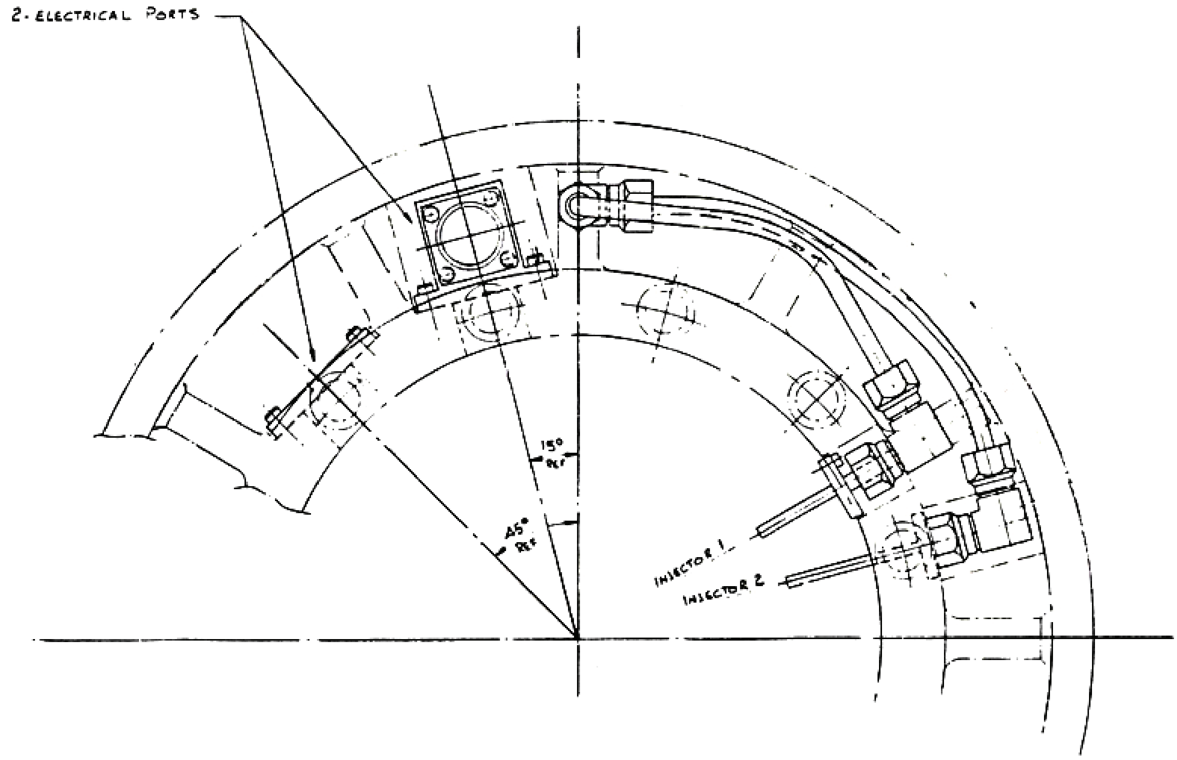

Figure 4.16: Bearing assembly oil-injector system layout

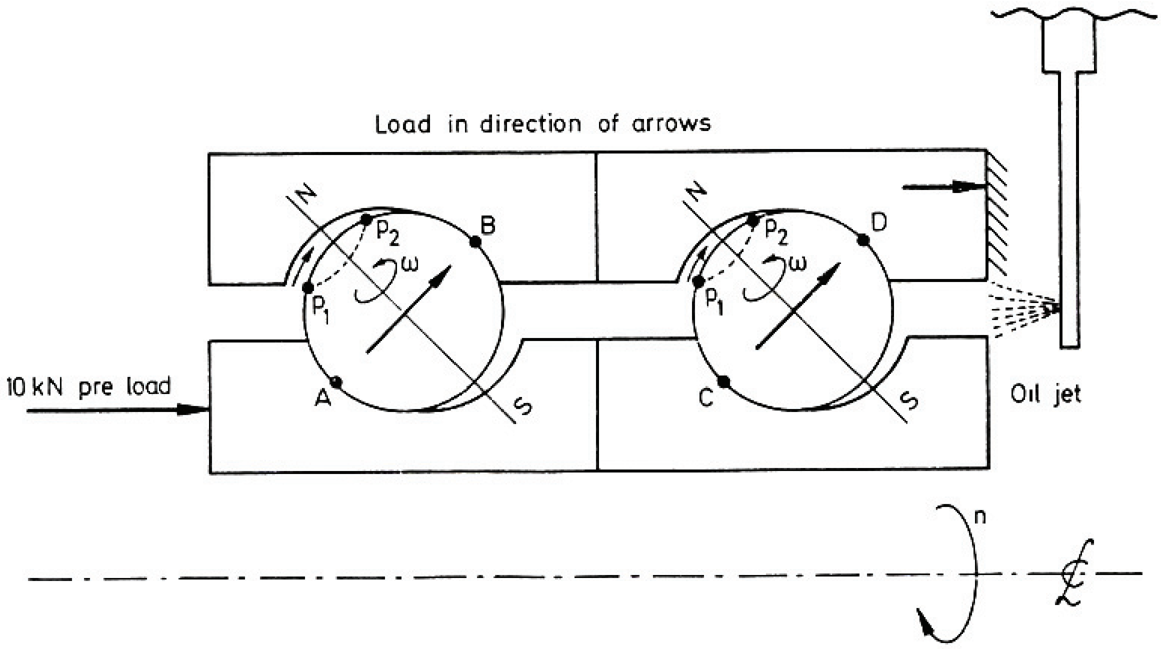

Figure 4.17: Schematic view of tandem set of deep-groove ball-bearing geometry under load, resulting in bearings acting as a centripetal pump

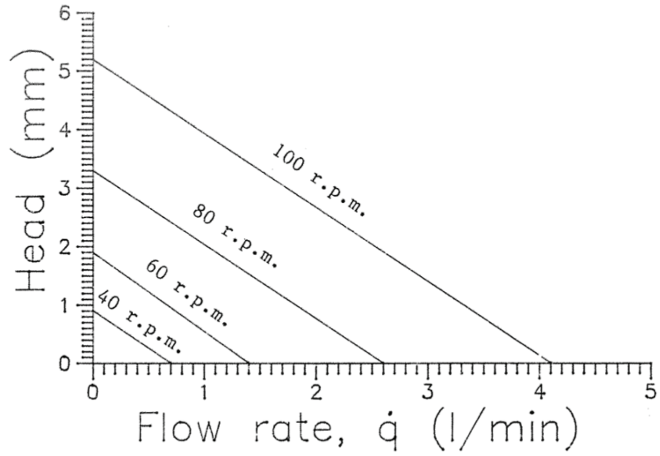

Figure 4.18: Predicted pump performance of tandem set of deep-groove ball bearings, following method of Bilstern (1982)

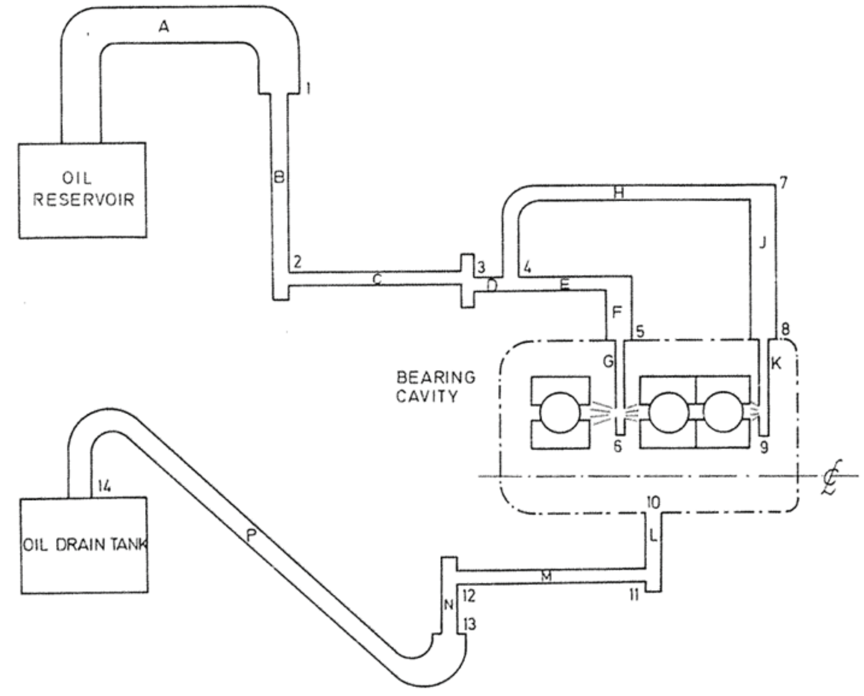

Oil way restriction	Restriction type	Loss coefficient K	Oil way section	Diameter (m)	Length (m)
1	Contraction $A_2/A_1=0.25$	0.32	A	0.025	3.500
2	90° bend	0.90	B	0.012	0.280
3	Double T	3.60	C	0.008	0.150
4	Standard T	1.80	D	0.005	0.075
5	Contraction $A_2/A_1=0.36$	0.29	E	0.005	0.180
6	Sharp edged entry and exit	1.50	F	0.005	0.035
7	90° bend	0.90	G	0.003	0.033
8	Contraction $A_2/A_1=0.36$	0.29	H	0.005	0.240
9	Sharp edged entry and exit	1.50	J	0.005	0.035
10	Sharp edged entry	0.50	K	0.003	0.055
11	90° bend	0.90	L	0.008	0.050
12	90° bend	0.90	M	0.008	0.150
13	Sudden expansion	1.12	N	0.012	0.280
14	Sharp edged exit	1.00	P	0.025	3.000

Figure 4.19: Schematic view of oil ways between oil reservoir, bearing assembly, and oil drain tank

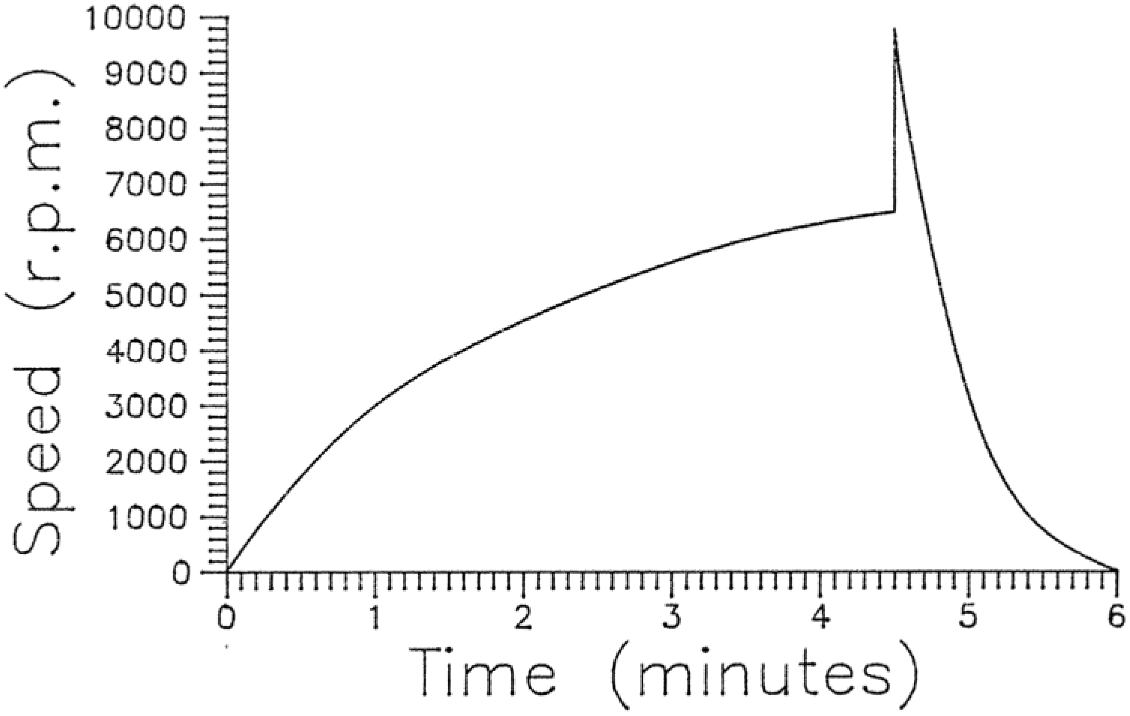

Figure 4.20: Predicted facility speed/time characteristics

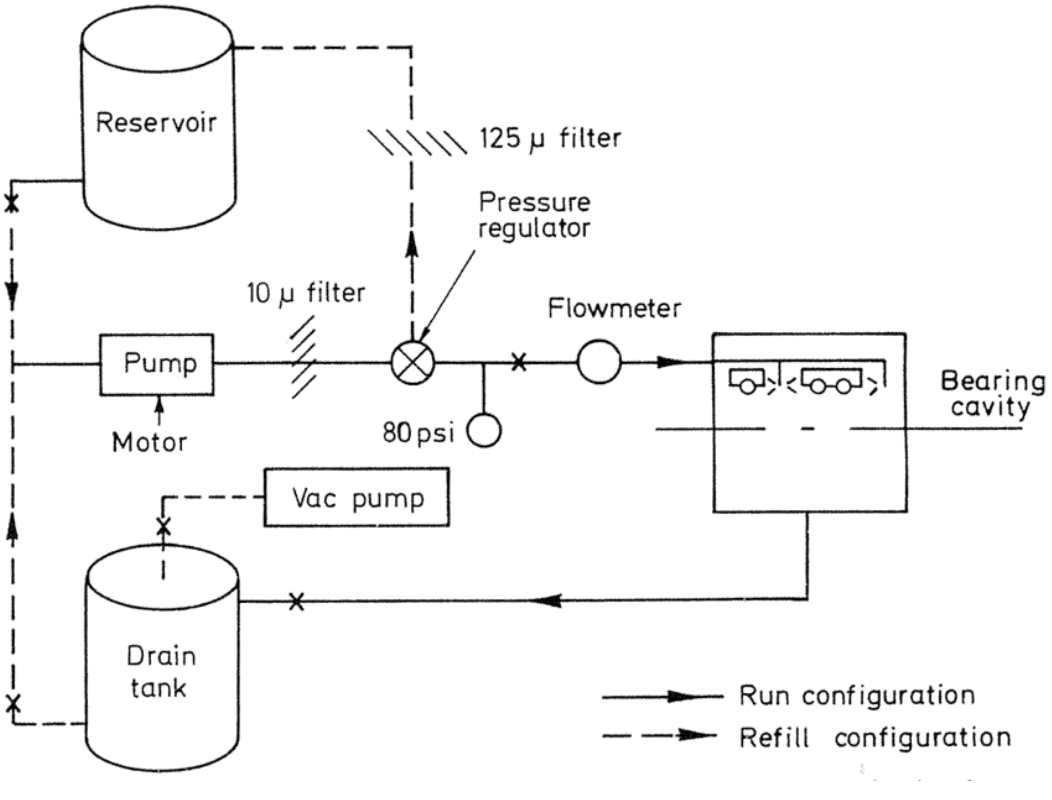

Figure 4.21: Schematic view of oil-supply system to bearings

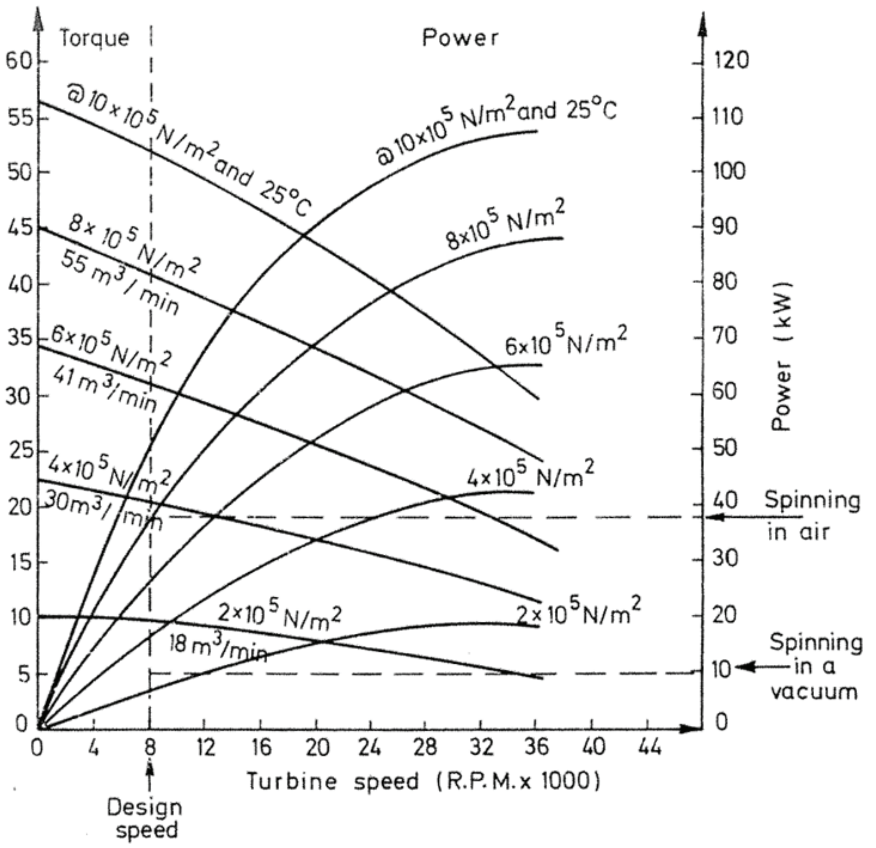

Figure 4.22: Air-motor performance characteristics (from manufacturer's data)

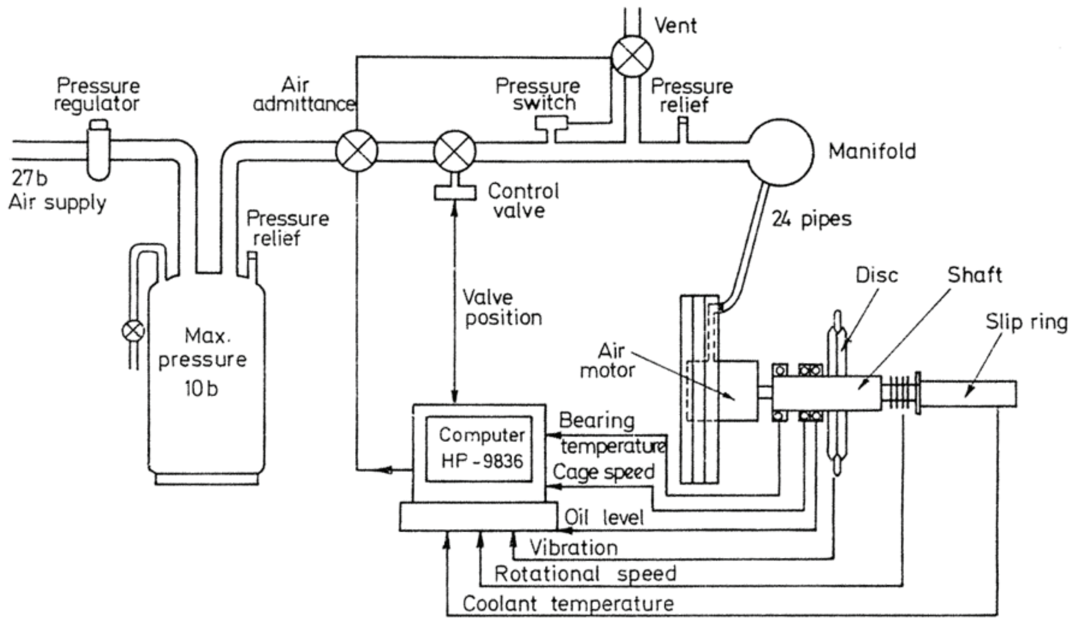

Figure 4.23: Air supply and control system for air motor and turbine module

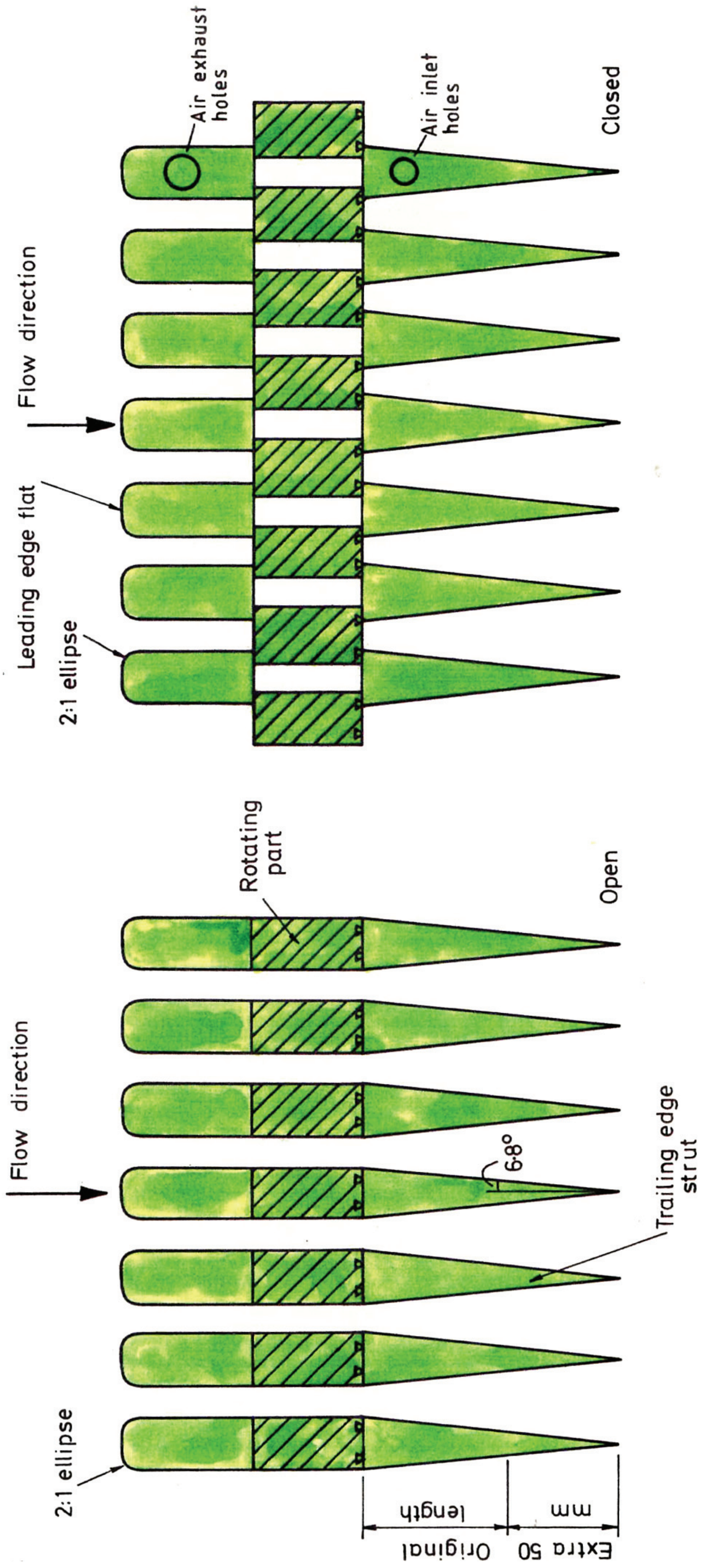

Figure 4.24: Schema of annular gate-valve operation

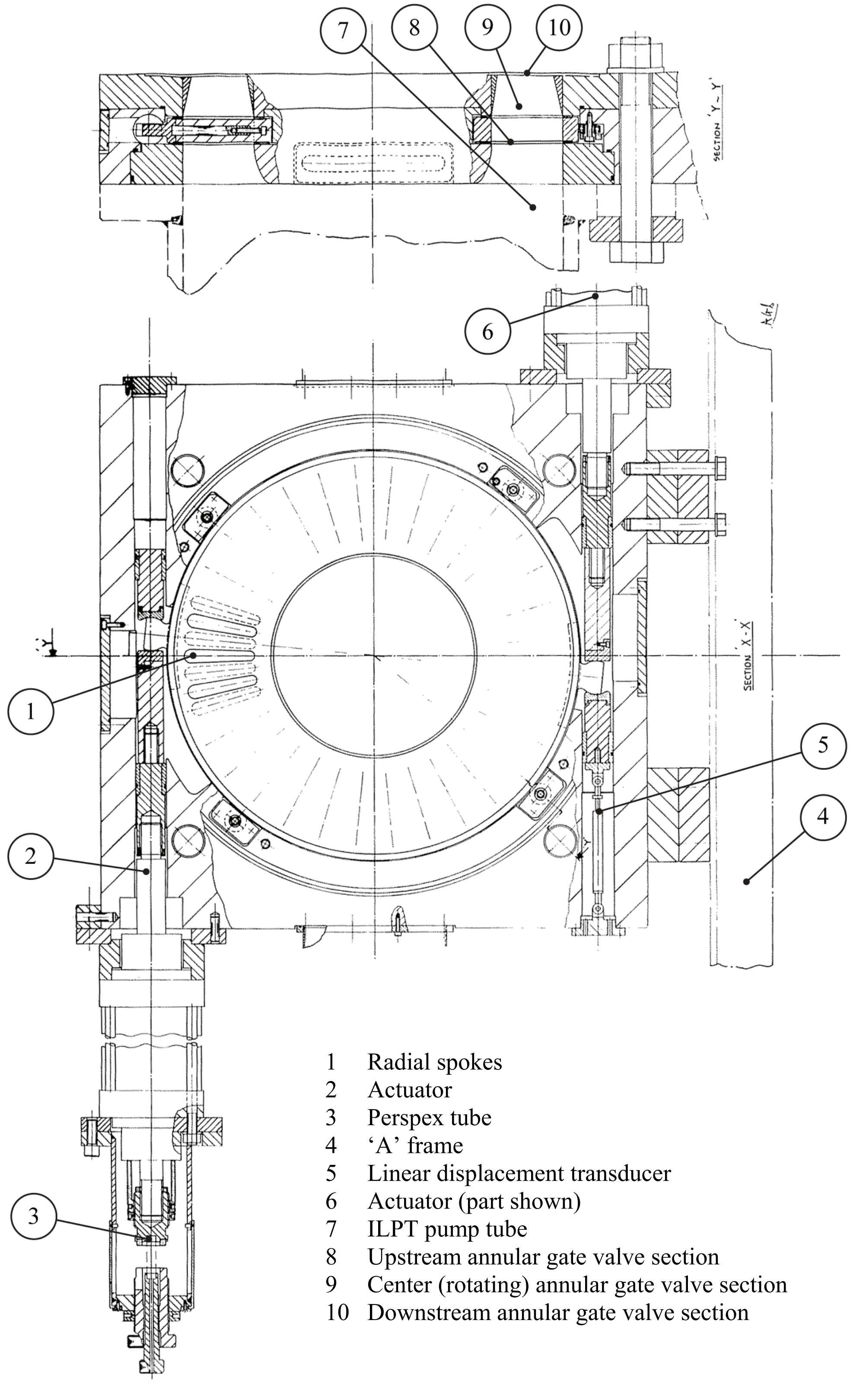

1 Radial spokes
2 Actuator
3 Perspex tube
4 'A' frame
5 Linear displacement transducer
6 Actuator (part shown)
7 ILPT pump tube
8 Upstream annular gate valve section
9 Center (rotating) annular gate valve section
10 Downstream annular gate valve section

Figure 4.25: General arrangement of annular gate valve

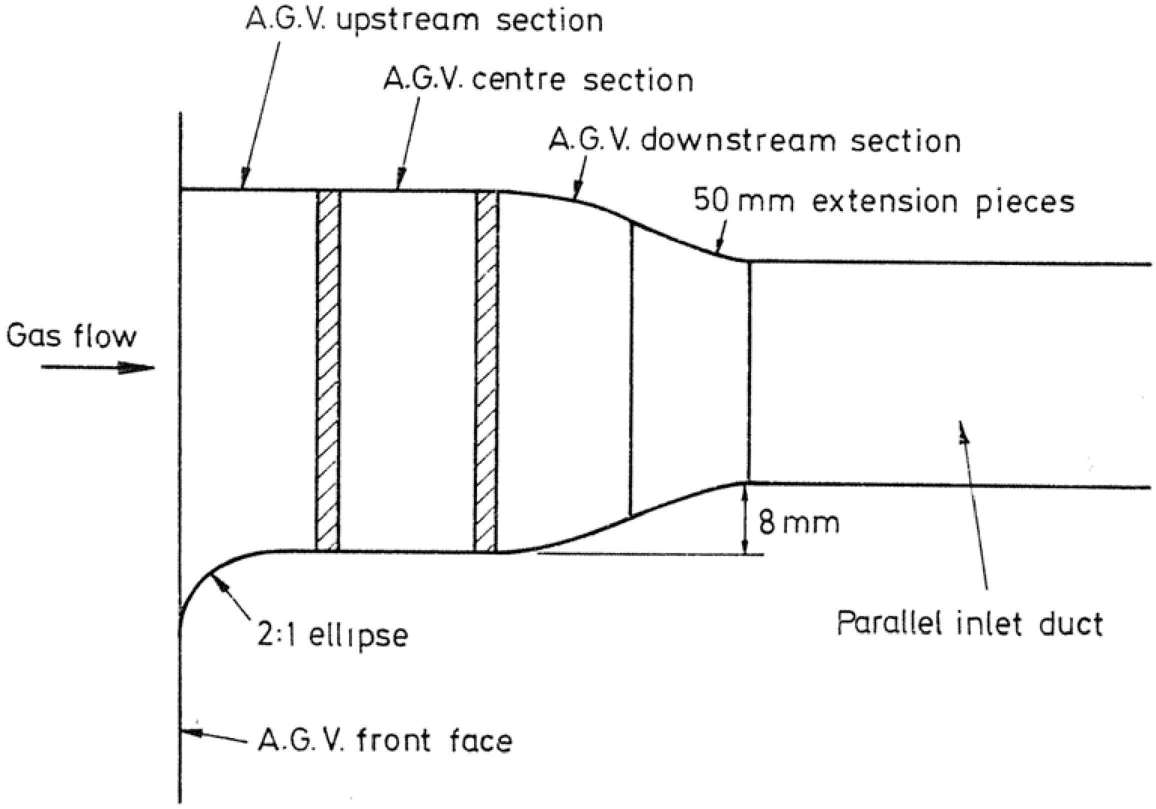

Figure 4.26: Geometry of annular gate valve and inlet duct

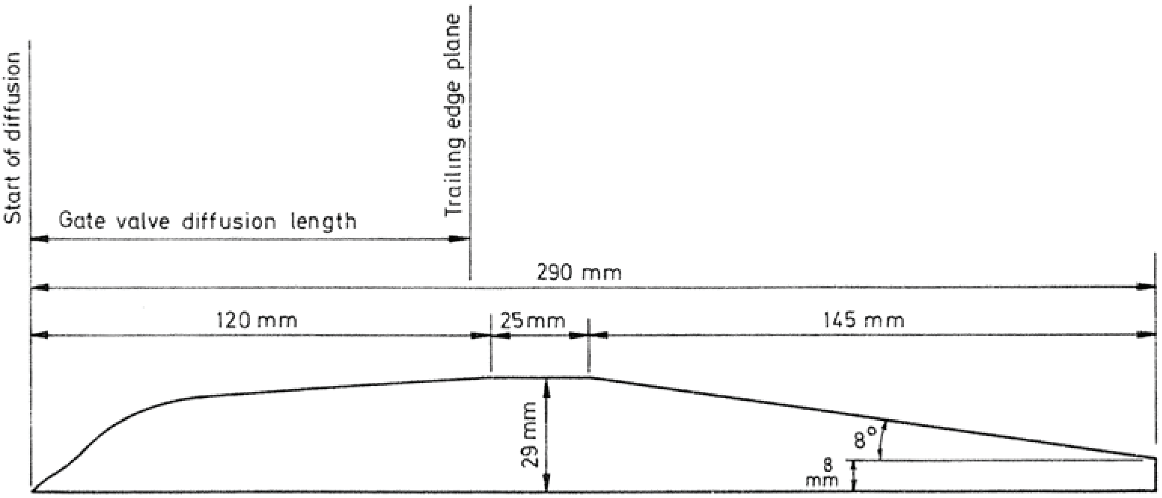

Figure 4.27: First inner annulus profile design incorporating a ‘hump’

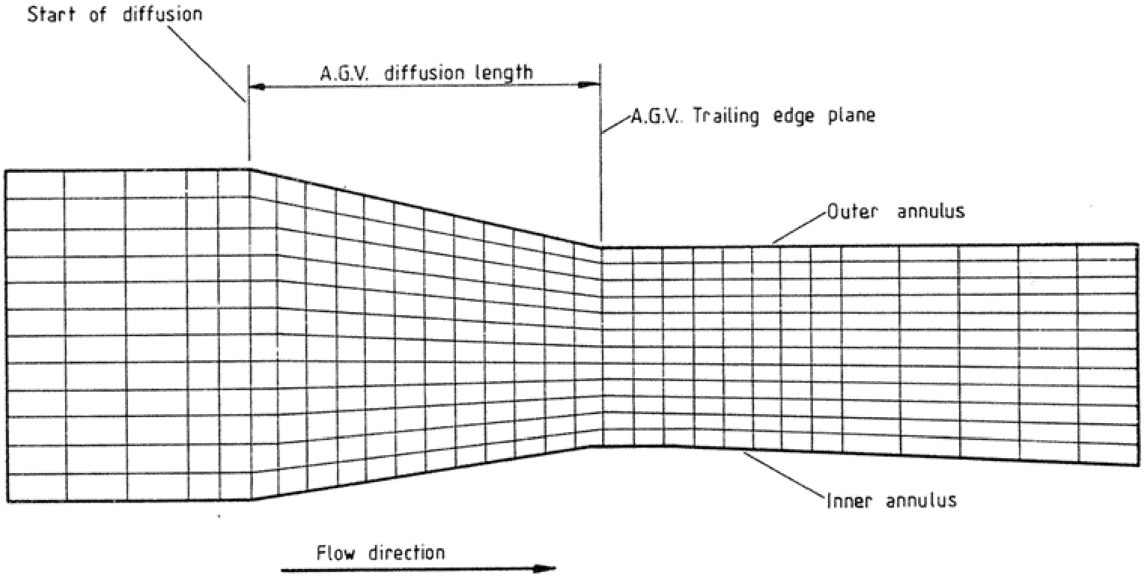

Figure 4.28: Typical quasi-3D (Q3D) code finite-volume grid used to analyse possible AGV downstream diffusing section designs

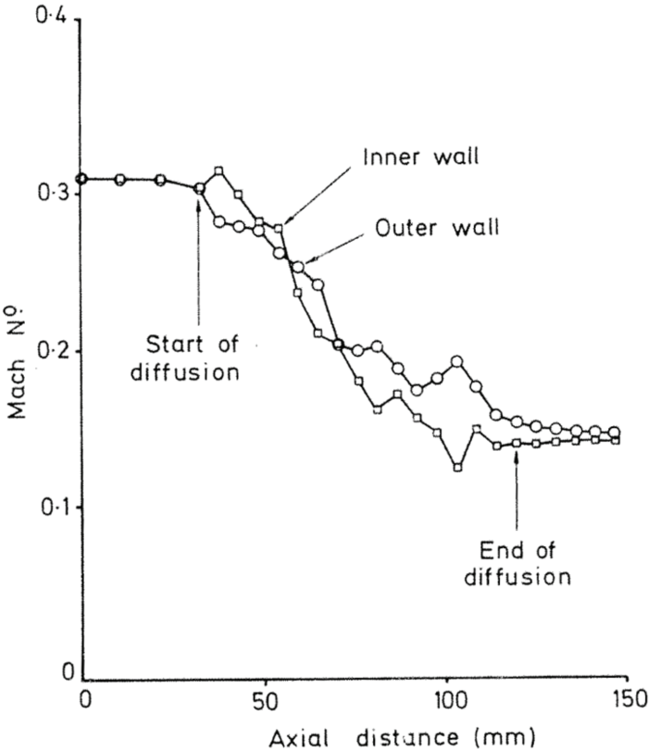

Figure 4.29: Mach number distribution predicted using Q3D finite-volume code for first AGV downstream section design

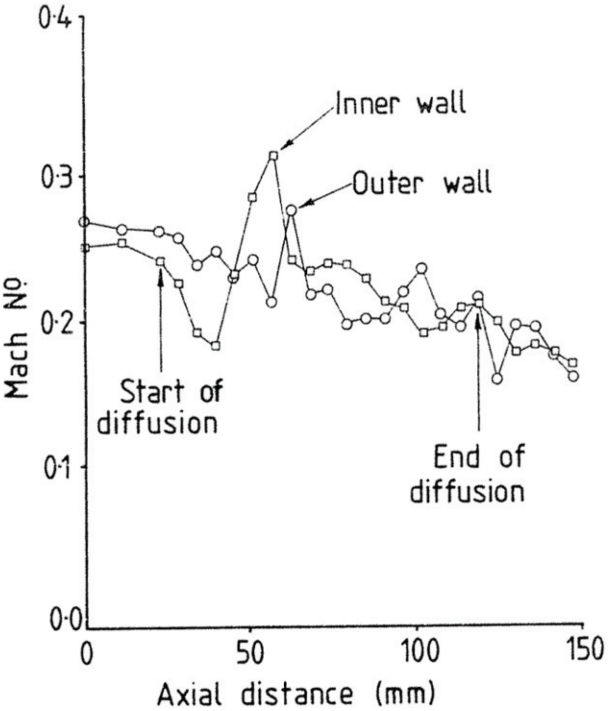

Figure 4.30: Mach number distribution predicted using Q3D finite-volume code for AGV downstream section incorporating first inner annulus 'hump'

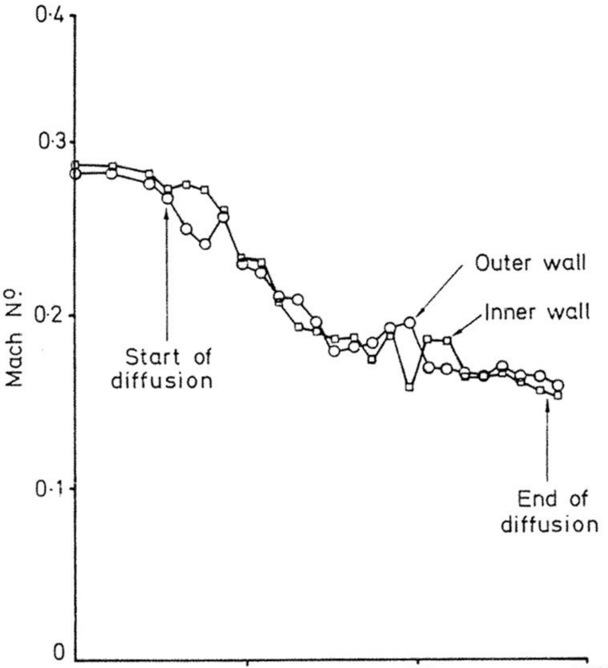

Figure 4.31: Mach number distribution predicted using Q3D finite-volume code for AGV downstream section including final inner annulus 'hump'

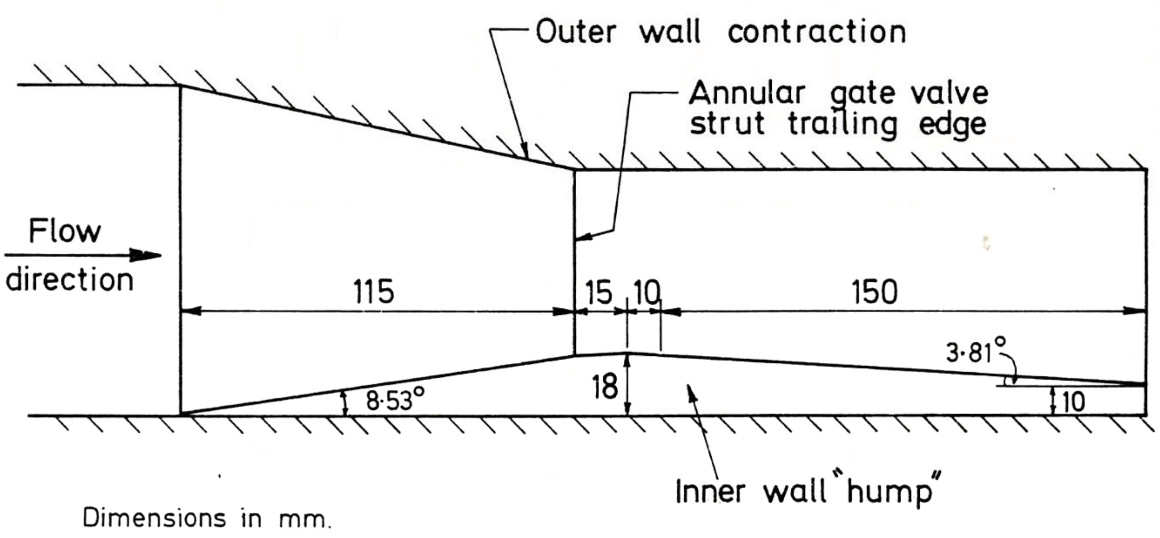

Figure 4.32: Final inner annulus design

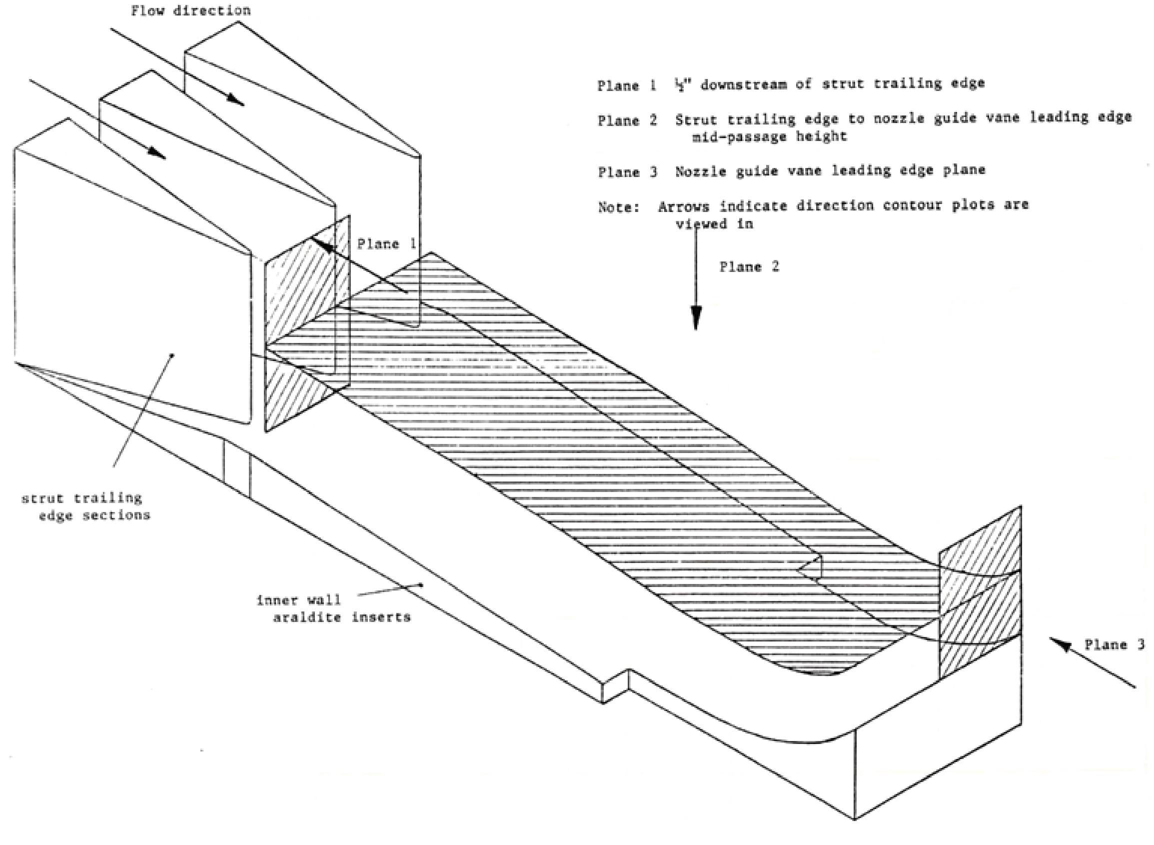

Figure 4.33: Three planes, and viewing direction, over which area traverse data were taken during model testing of final AGV and inlet duct design

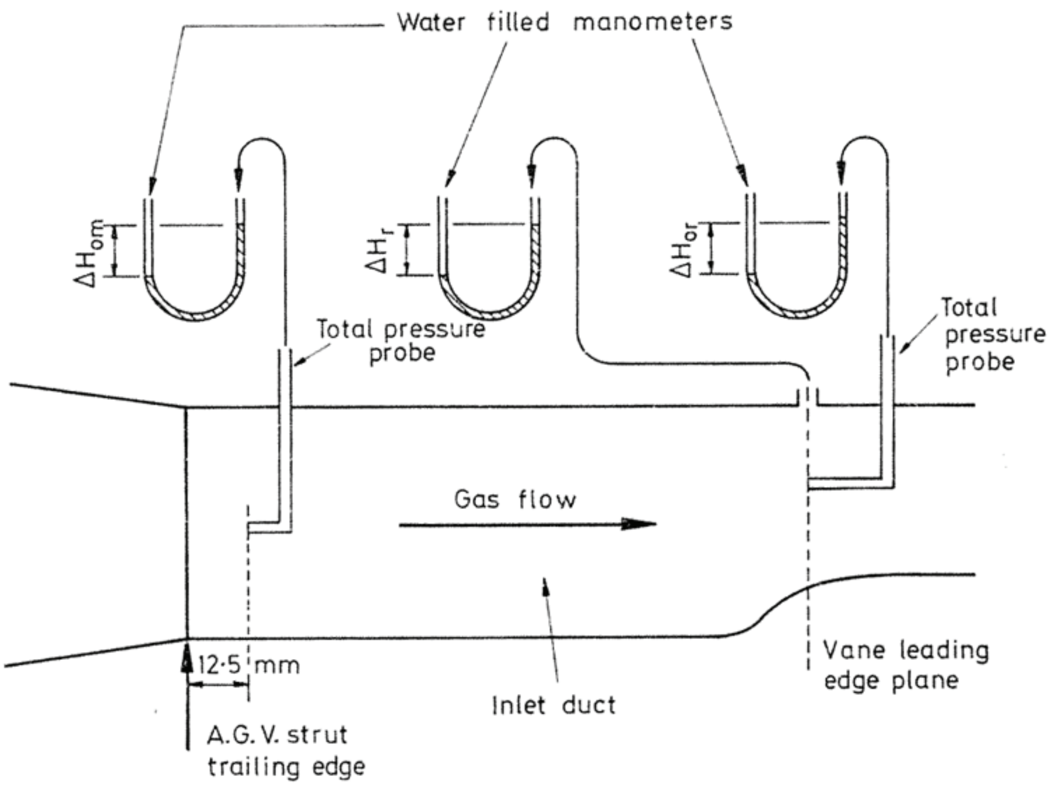

Figure 4.34: Manometer configuration used when measuring loss data in AGV linear model

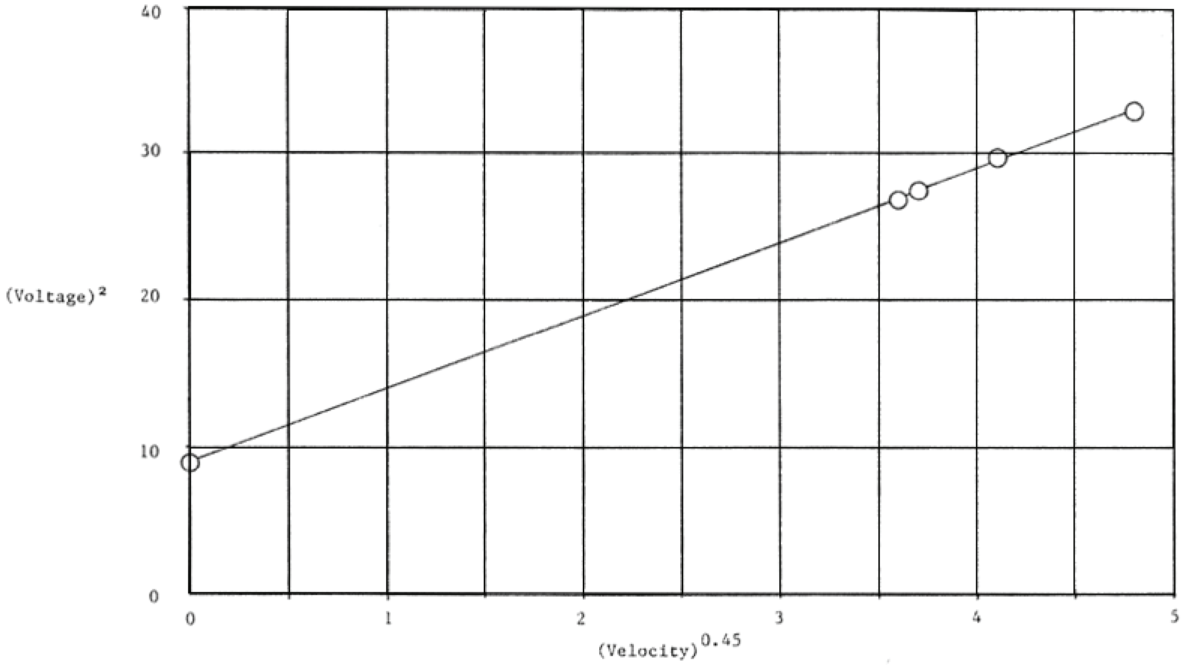

Figure 4.35: Calibration curve of hot wire used for all turbulence measurements

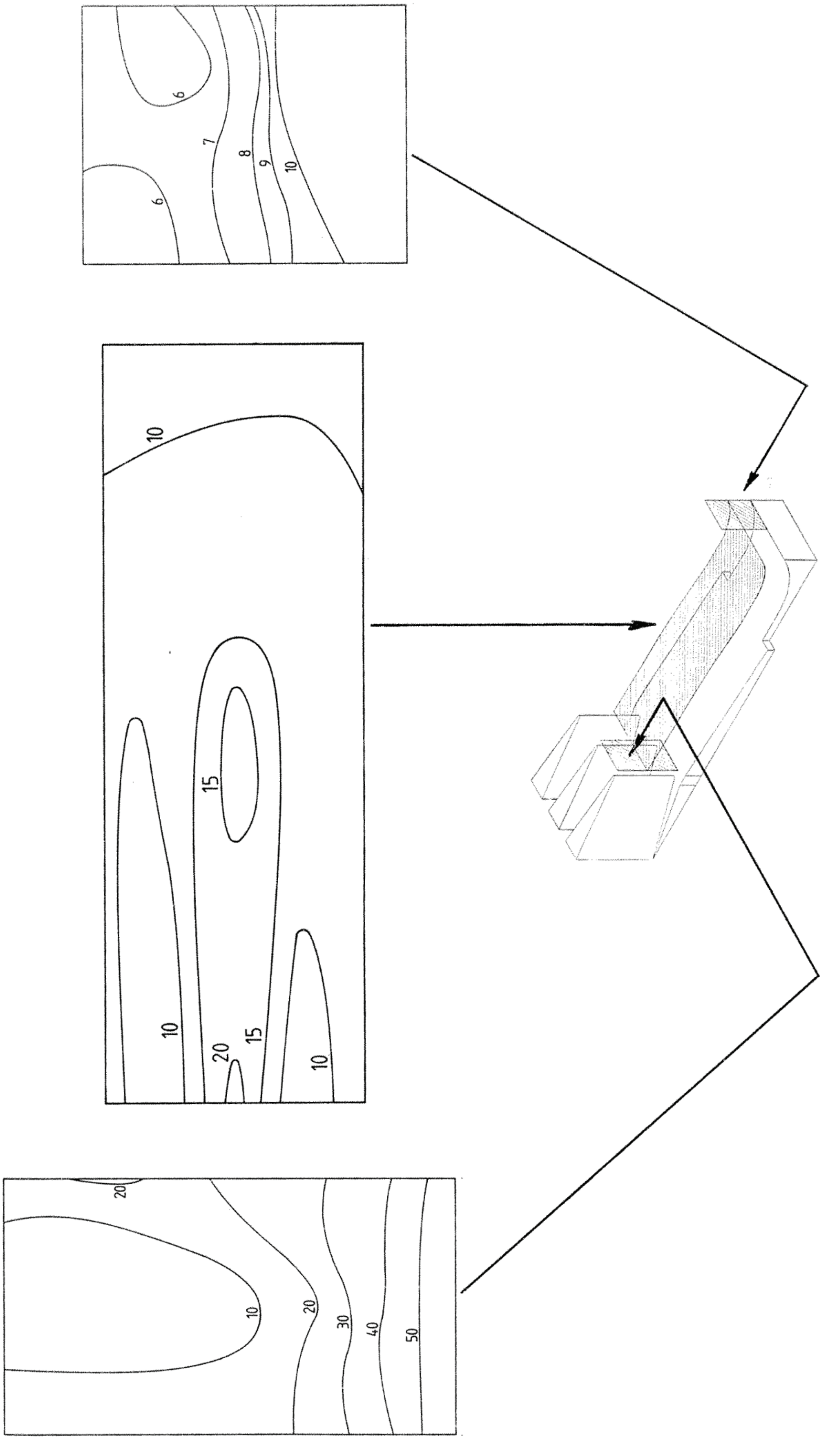

Figure 4.36: Contour plots of measured turbulence level in planes one, two, and three

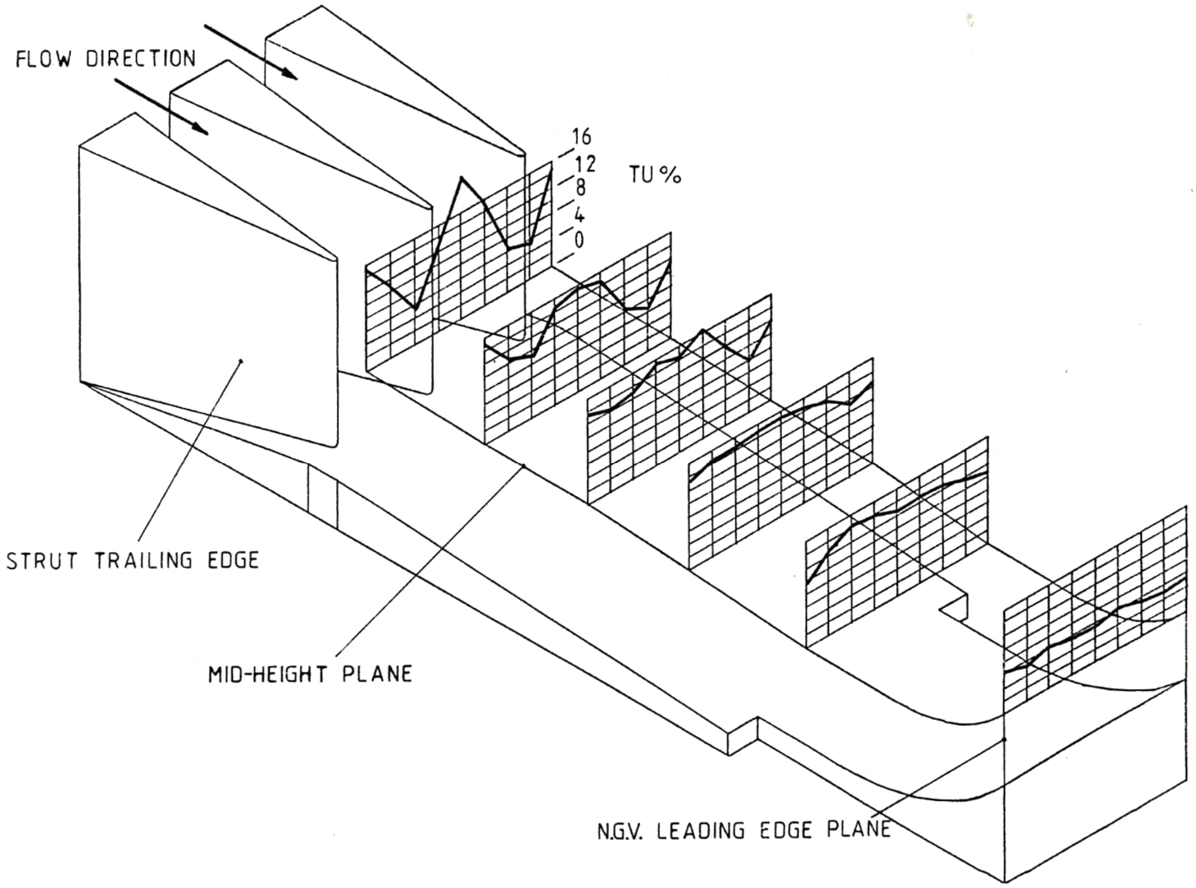

Figure 4.37: Measured turbulence data (plane 2) plotted in 'raw' form

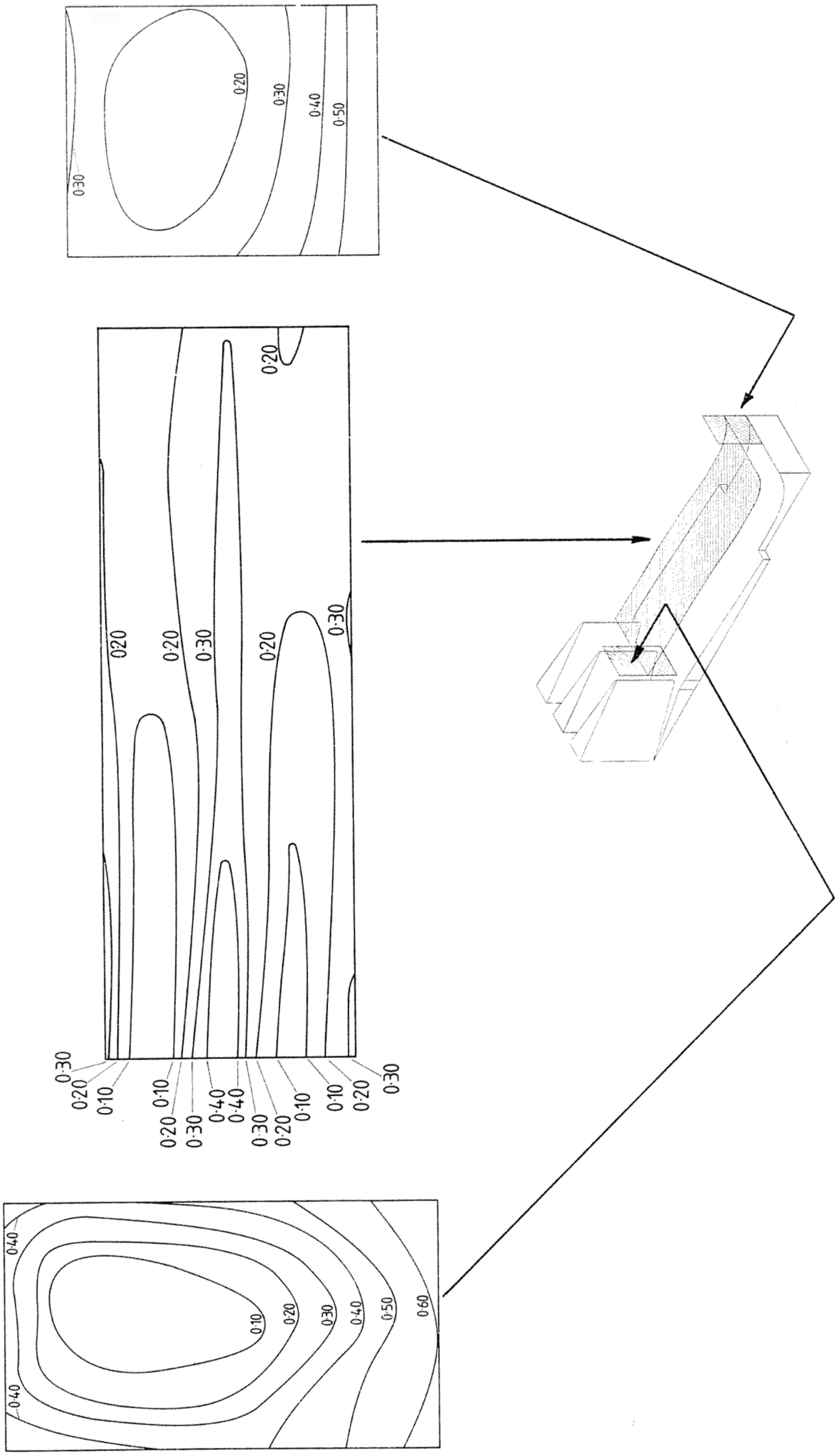

Figure 4.38: Contour plots of measured loss data, planes one, two, and three

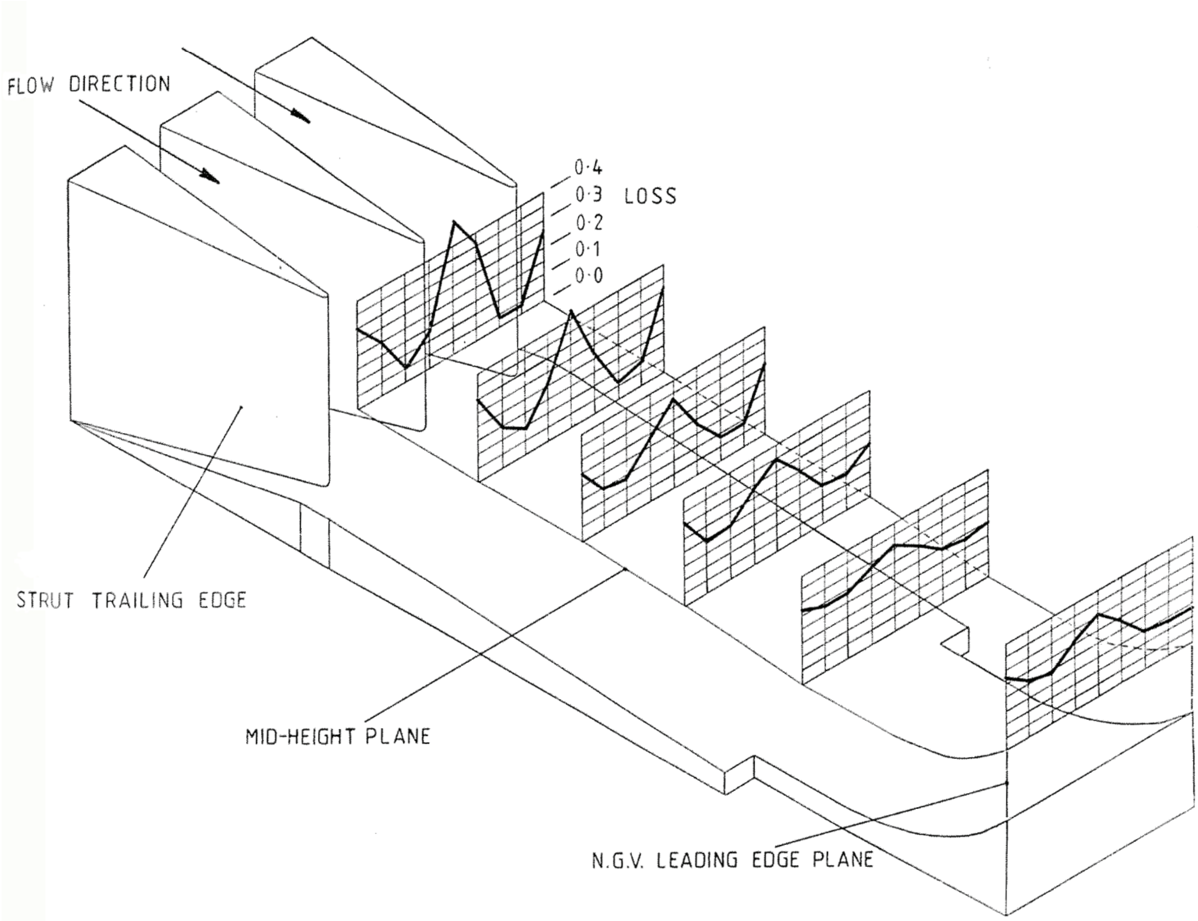

Figure 4.39: Measured loss data (plane 2) plotted in ‘raw’ form

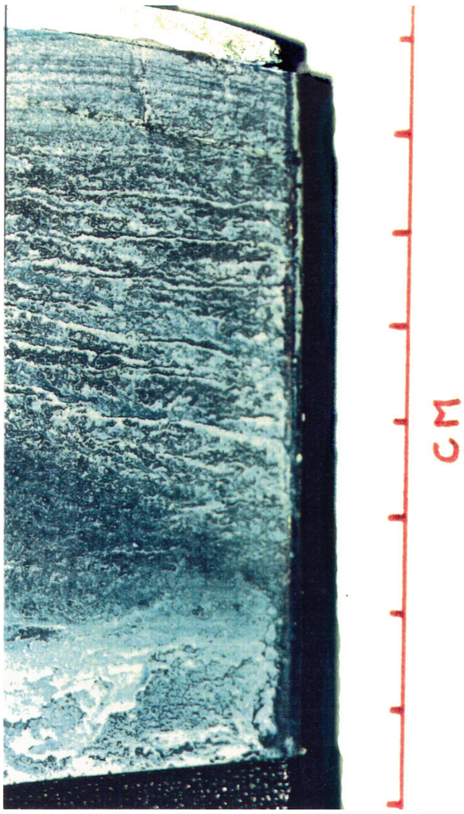

Figure 4.40: Flow visualisation on strut of final AGV design; flow separates at trailing-edge radius on final design, indicating flow is attached to strut until this point

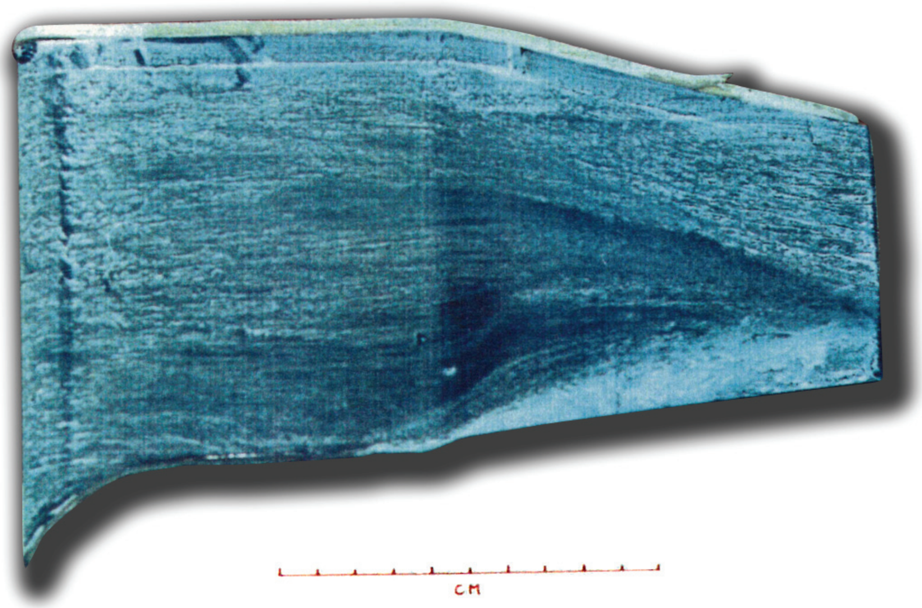

Figure 4.41: Flow visualisation on strut of final AGV design; flow separation evident in early builds not present in flow visualisation of final design

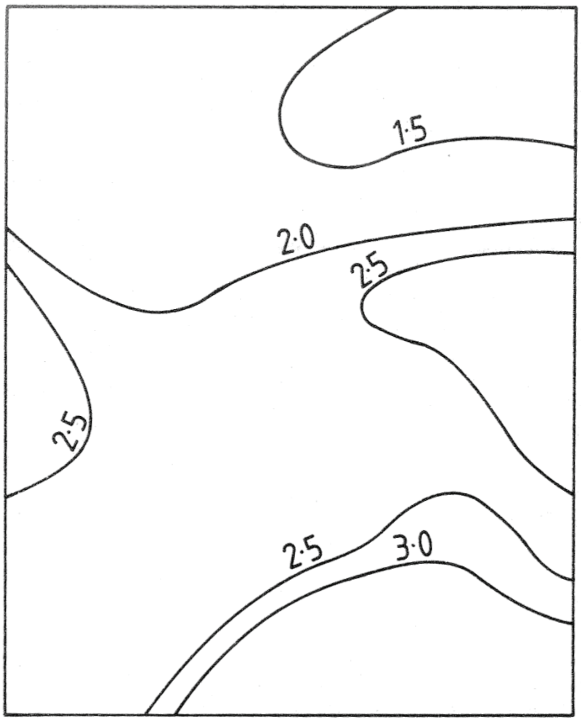

Figure 4.42: Contour plot of measured turbulence level, plane 3, with gauze fitted across AGV strut trailing edges

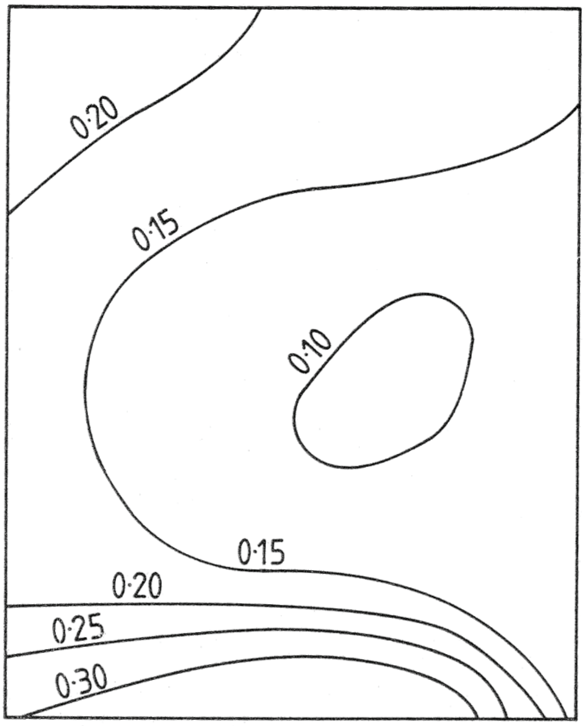

Figure 4.43: Contour plot of measured loss, plane 3, with gauze fitted across AGV strut trailing edges

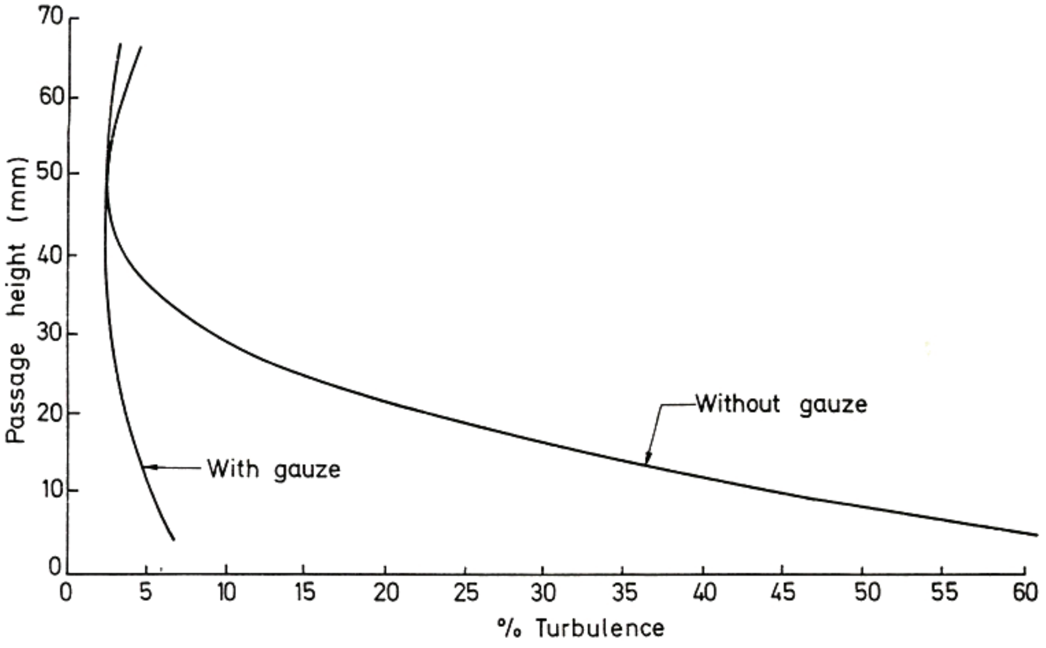

Figure 4.44: Measured mid-passage radial turbulence level, plane 1 (adapted from Kempson & Watkins, 1987)

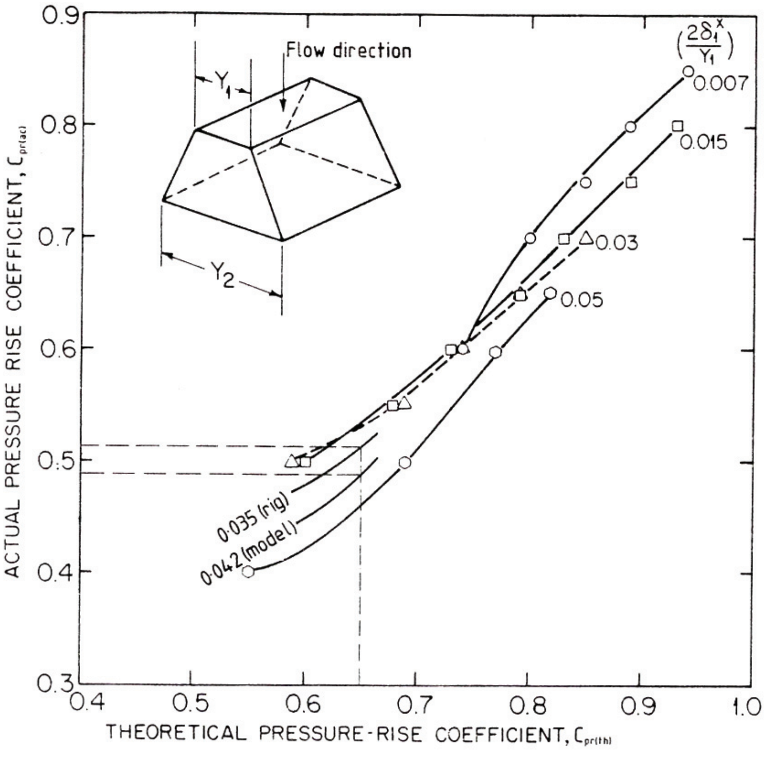

Figure 4.45: Actual pressure-rise coefficient versus theoretical pressure-rise coefficient for range of Reynolds number coefficients for straight-walled diffusers (adapted from Wilson, 1984)

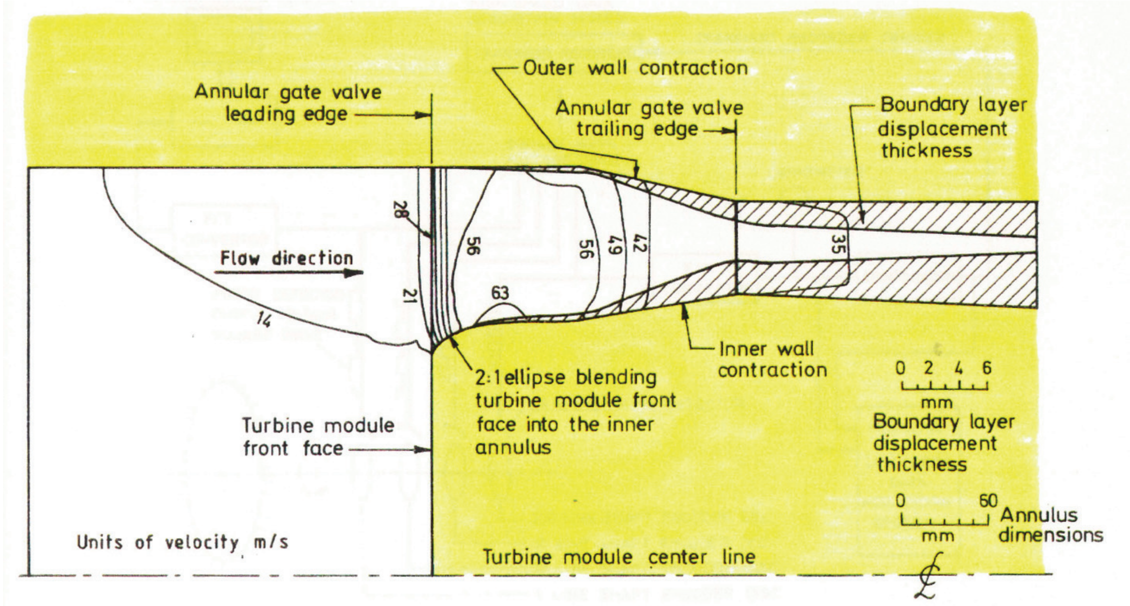

Figure 4.46: Axi-symmetric streamline curvature prediction of axial velocity through annular gate valve and inlet duct, with boundary-layer displacement thickness shown ten times thickness for clarity

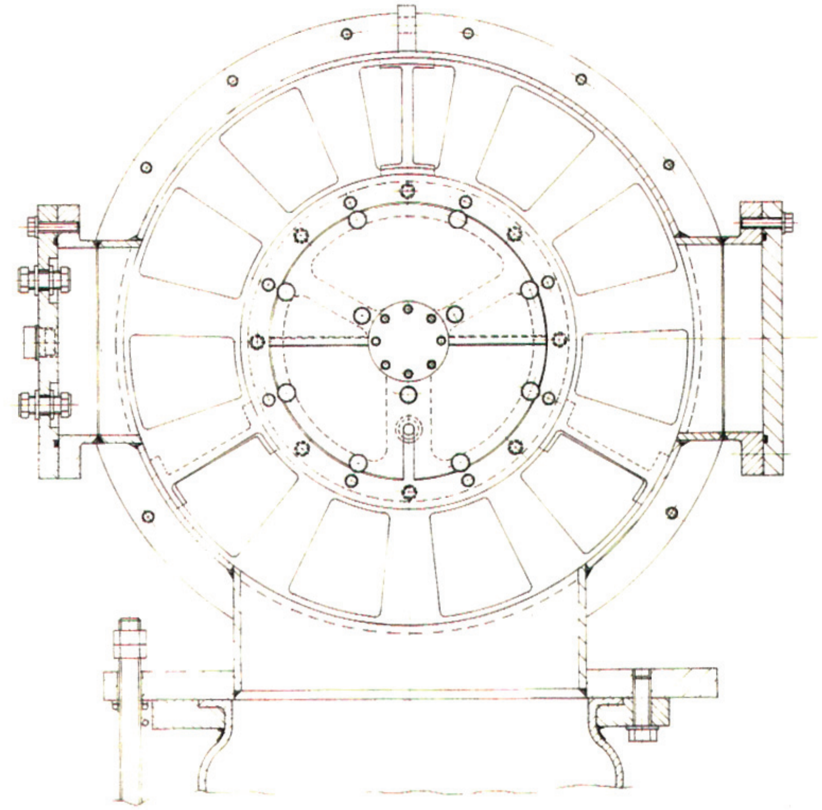

Figure 4.47: Sectional view through turbine module second throat

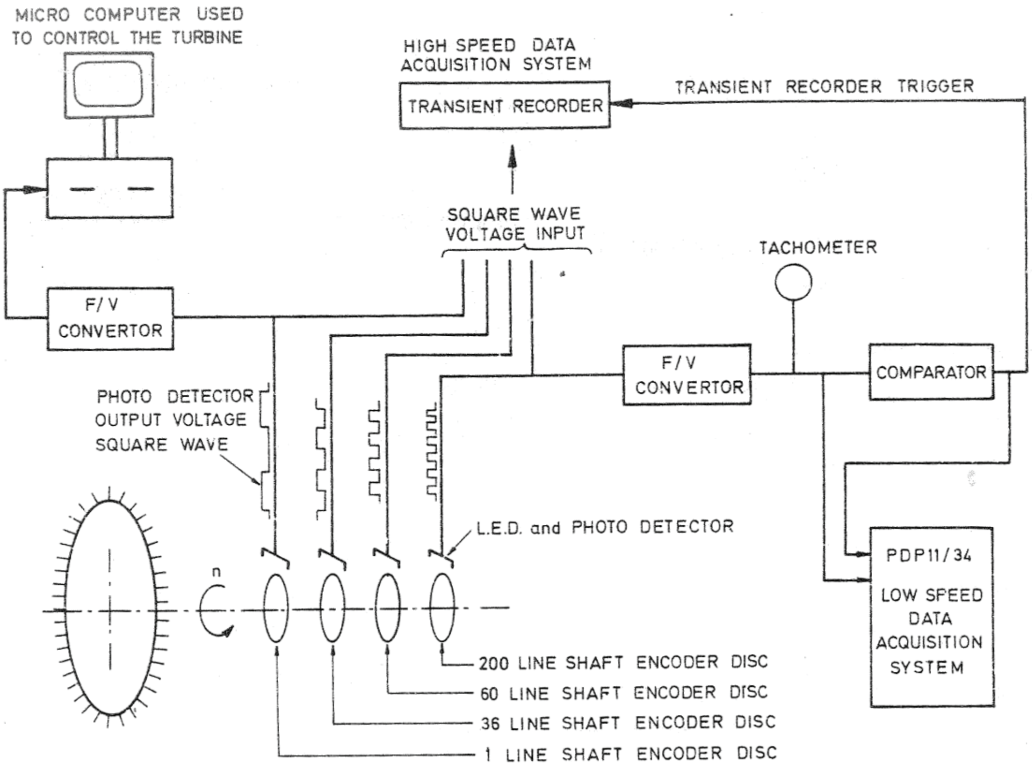

Figure 4.48: Shaft encoder disc configuration utilised in turbine test facility

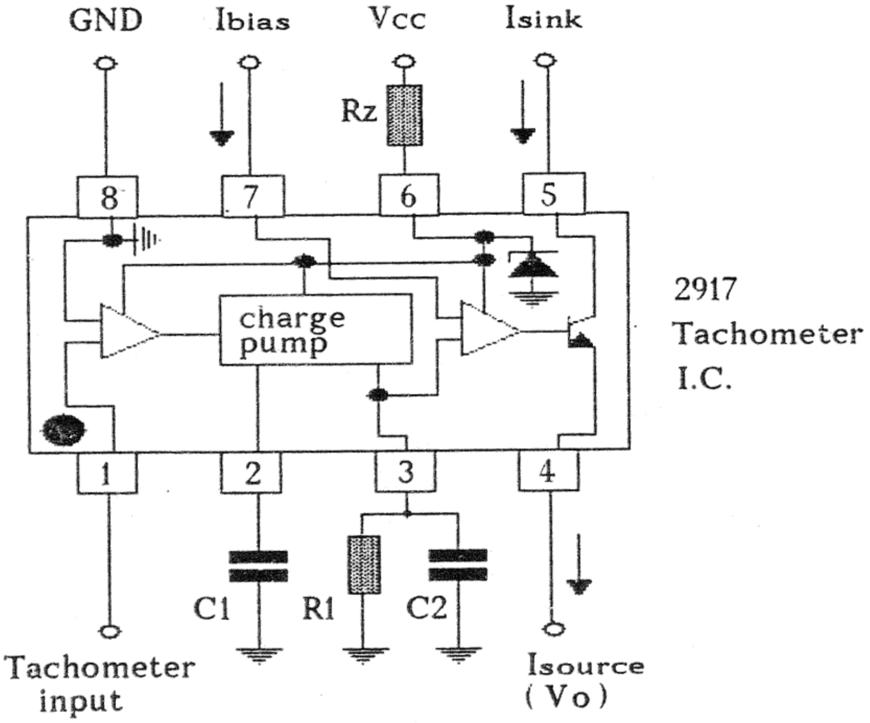

Figure 4.49: Tachometer chip used in frequency-to-voltage converters

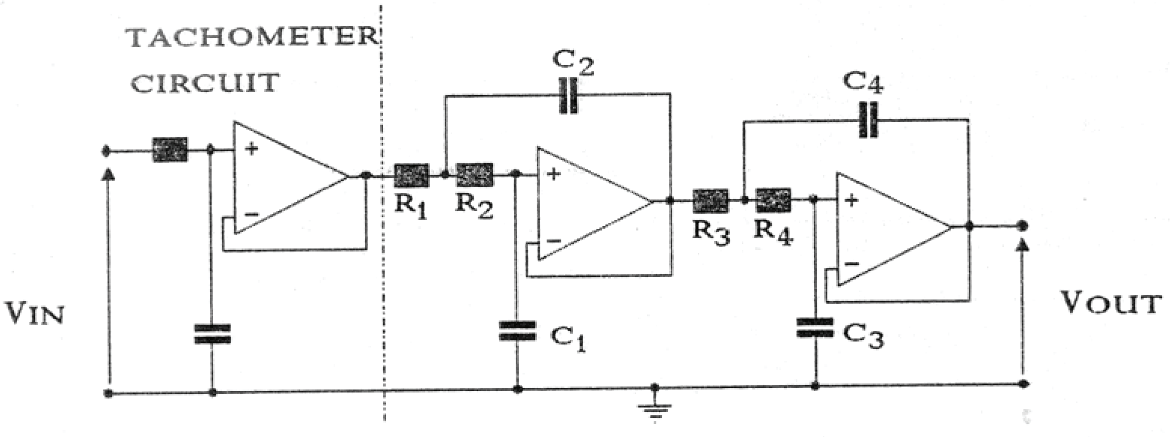

R_1 = 36K
R_2 = 10K
C_1 = 2.2nF
C_2 = 33nF

R_3 = 43K
R_4 = 13K
C_3 = 4.7nF
C_4 = 10nF

Figure 4.50: Layout and component values for low-pass filter used to eliminate AC noise on output from 200-line frequency-to-voltage converter

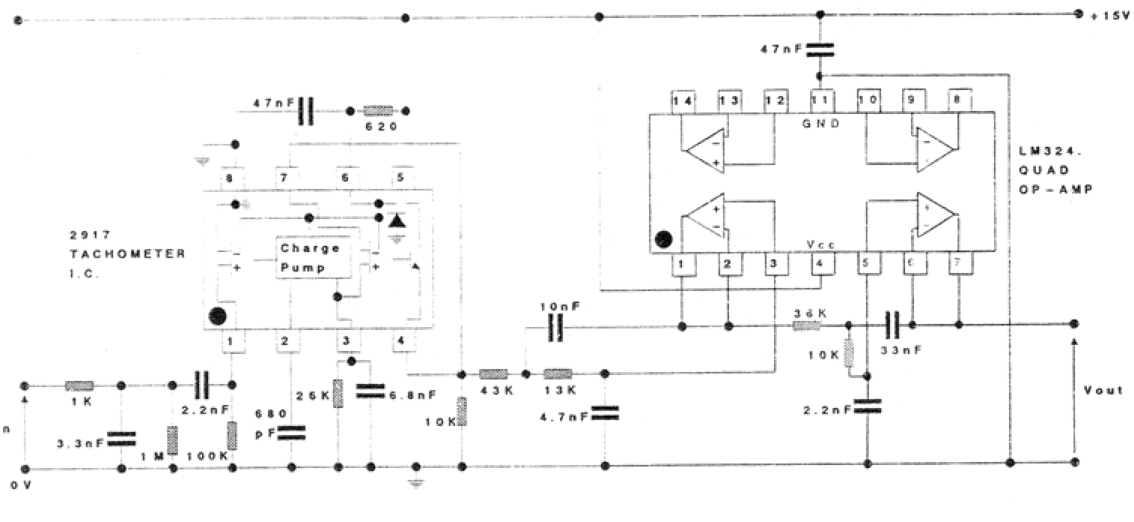

Figure 4.51: Layout of tachometer chip and five-pole Butterworth filter with component values for 200-line shaft encoder disc and 1000-Hz cut-off frequency

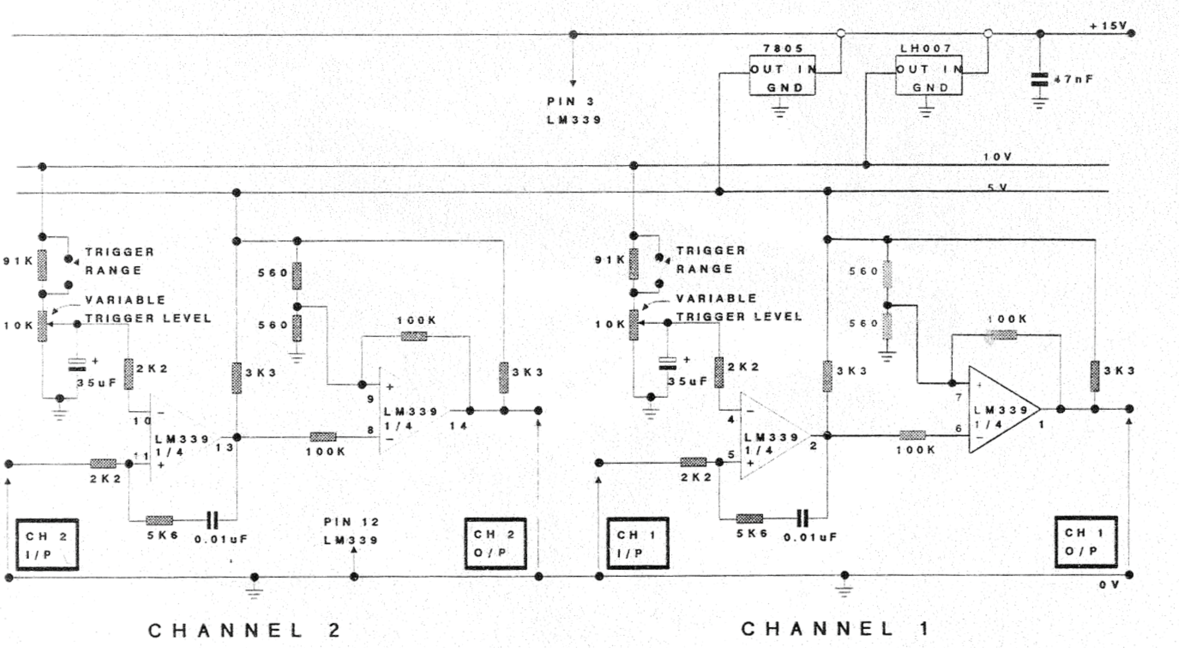

Figure 4.52: Layout and component values for dual comparator; input comes from 200-line frequency-to-voltage converter output; output used as a transient recorder trigger

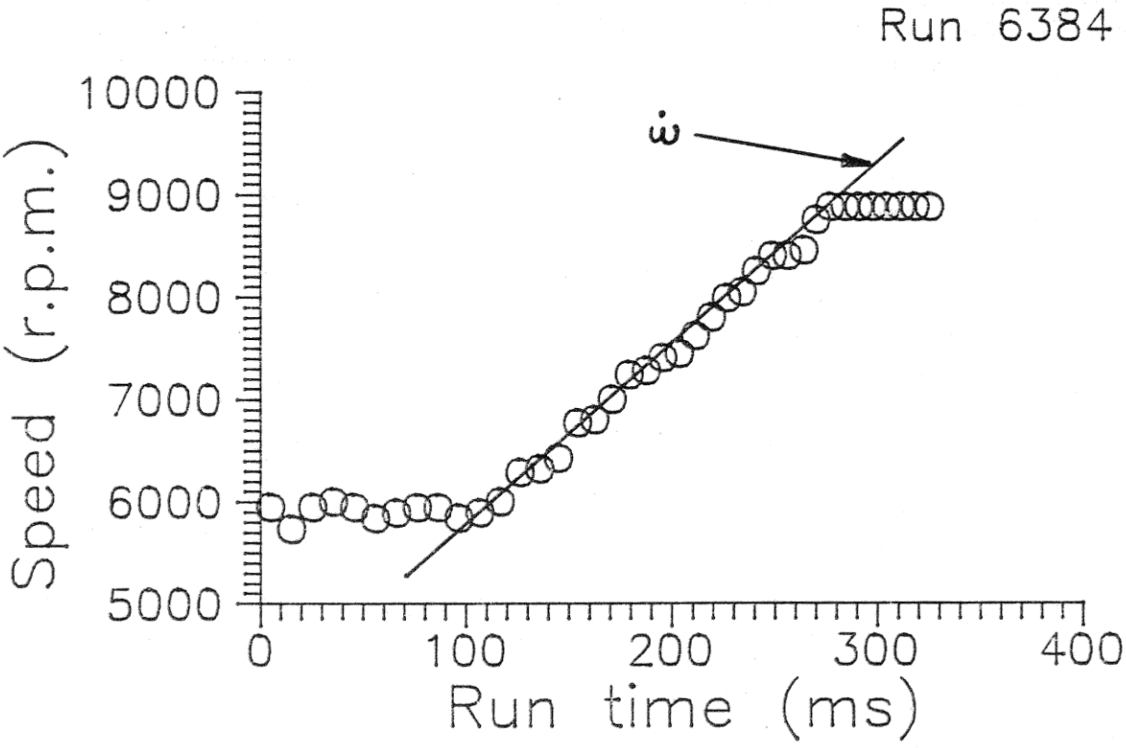

Figure 4.53: Measured turbine-speed data, with least-square best-line fit used to establish turbine acceleration during ILPT operation

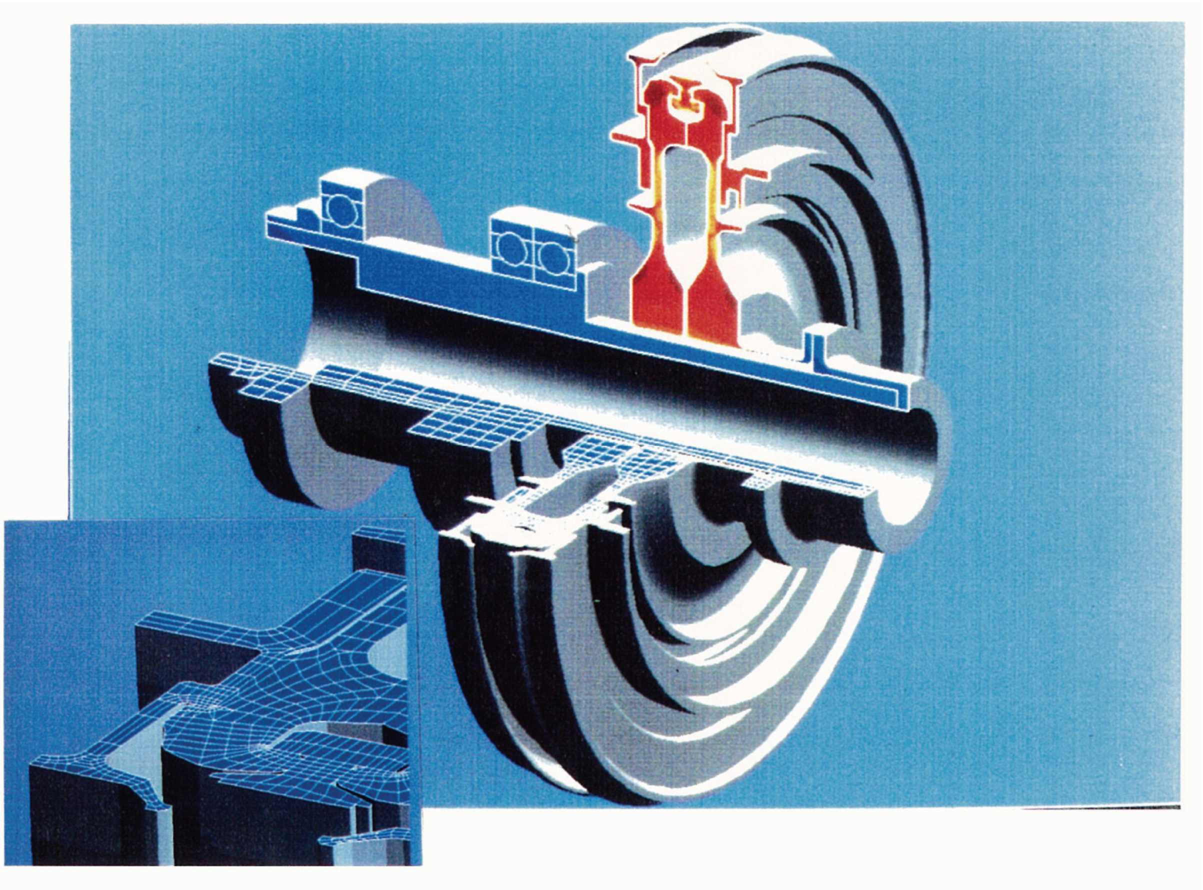

Figure 5.1: Axi-symmetric disc/shaft finite-element model, with stress contours due to design condition loading on vertical face (see Figure 5.5 for scale); mesh used on horizontal face shown as insert (close up around root fixing)

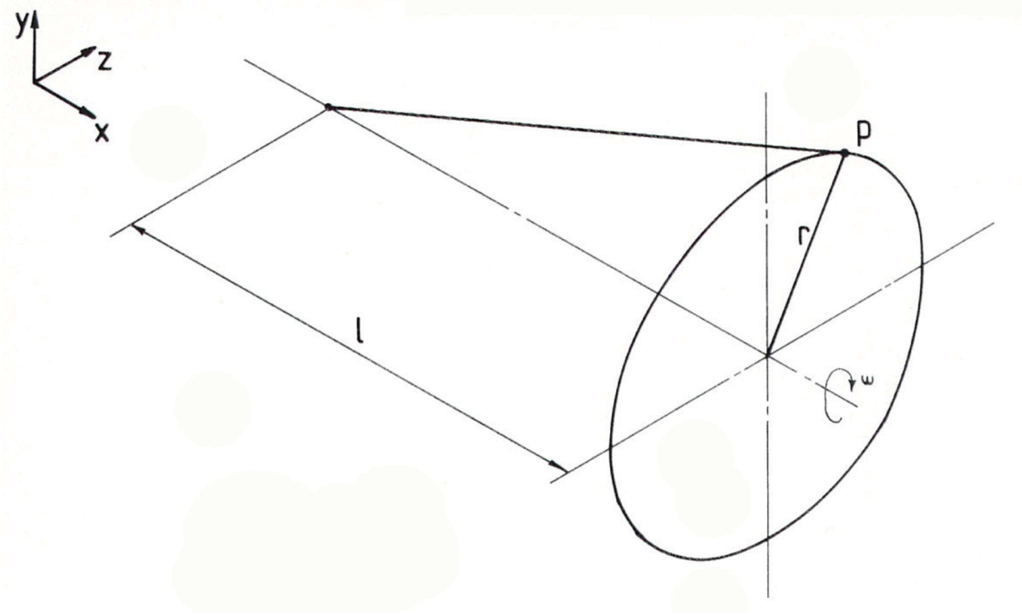

Figure 5.2: Stationary and rotating coordinate systems

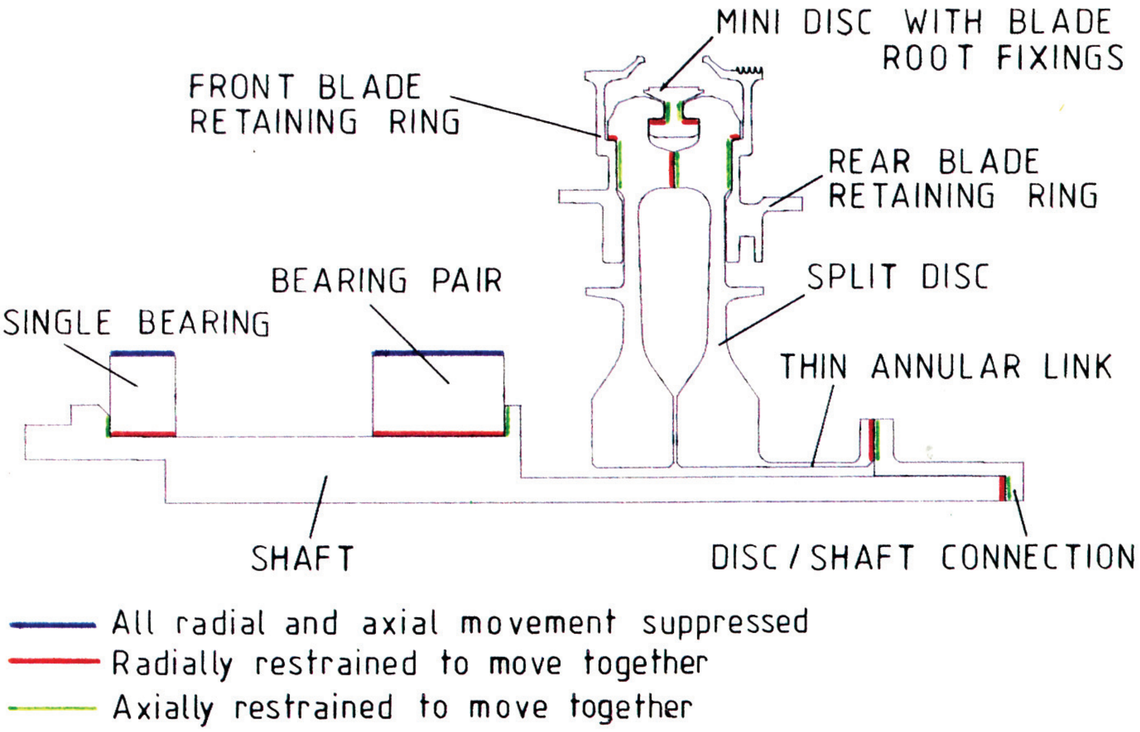

Figure 5.3: **Nine-component axi-symmetric finite-element models using eight noded elements, as utilised in axi-symmetric disc/shaft model; and the direction in which coincident faces were restrained**

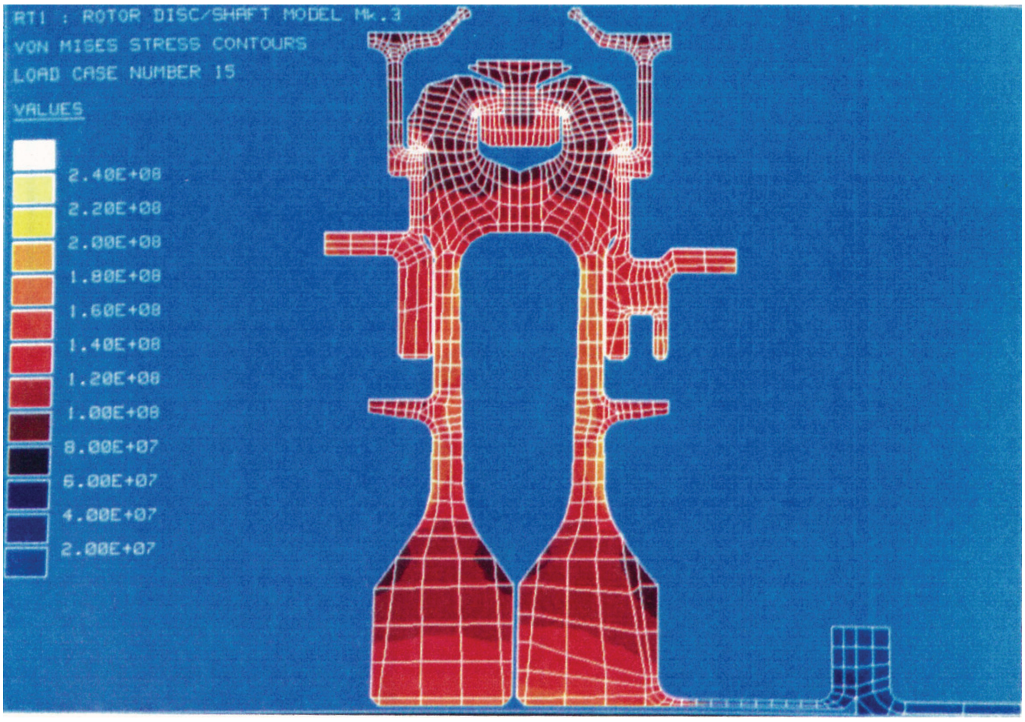

Figure 5.4: **Stress distribution through axi-symmetric disc/shaft model at 8,434 rpm, with no blade or gas loads**

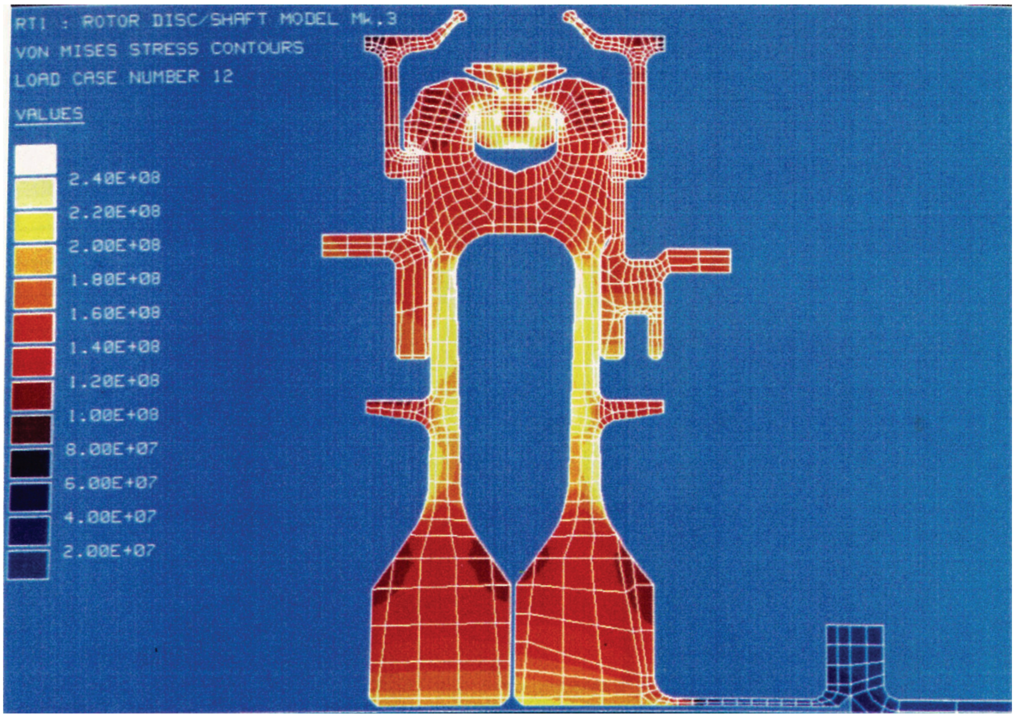

Figure 5.5: Stress distribution through axi-symmetric disc/shaft model at 8,434 rpm, with radially distributed load along blade-root fixing simulating blade load, but no axial gas load

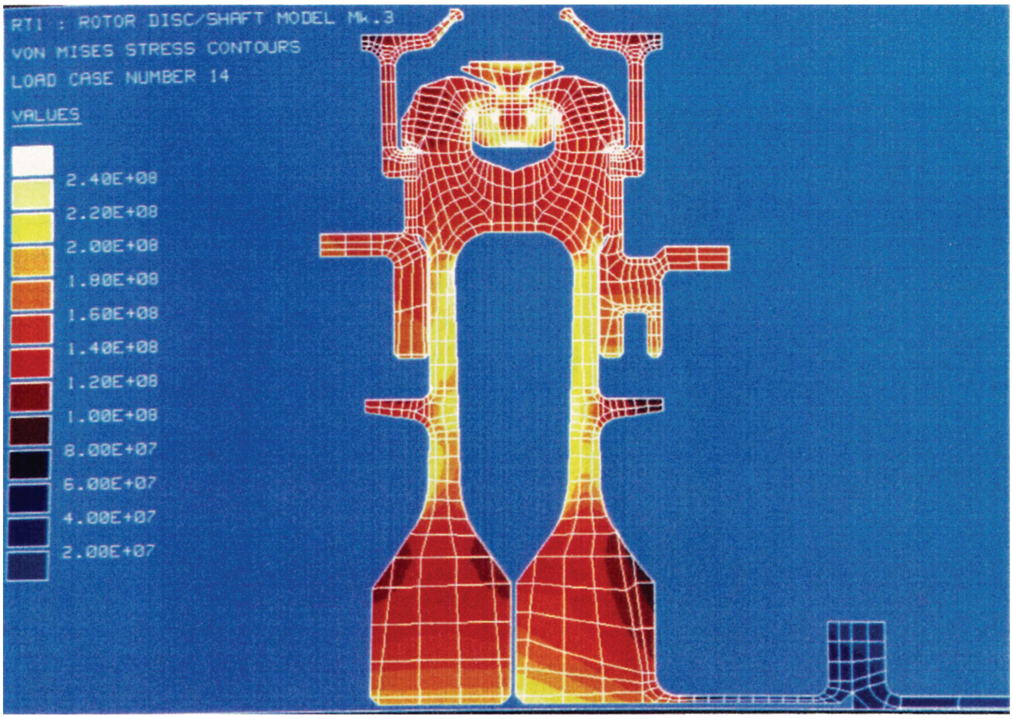

Figure 5.6: Stress distribution through axi-symmetric disc/shaft model at 8,434 rpm, with radially distributed load along blade-root fixing, simulating blade load and axial load simulating gas load

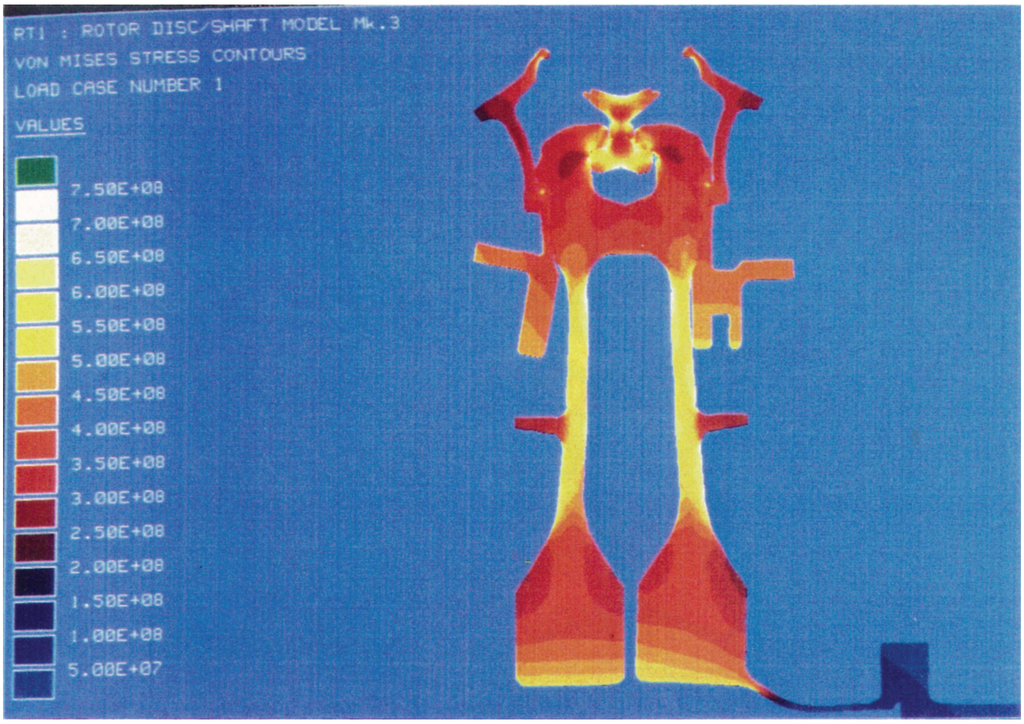

Figure 5.7: Stress distribution through, and deflected shape of, axi-symmetric disc/shaft model at 14,000 rpm, with radially distributed load along blade-root fixing simulating blade load, but no axial gas load

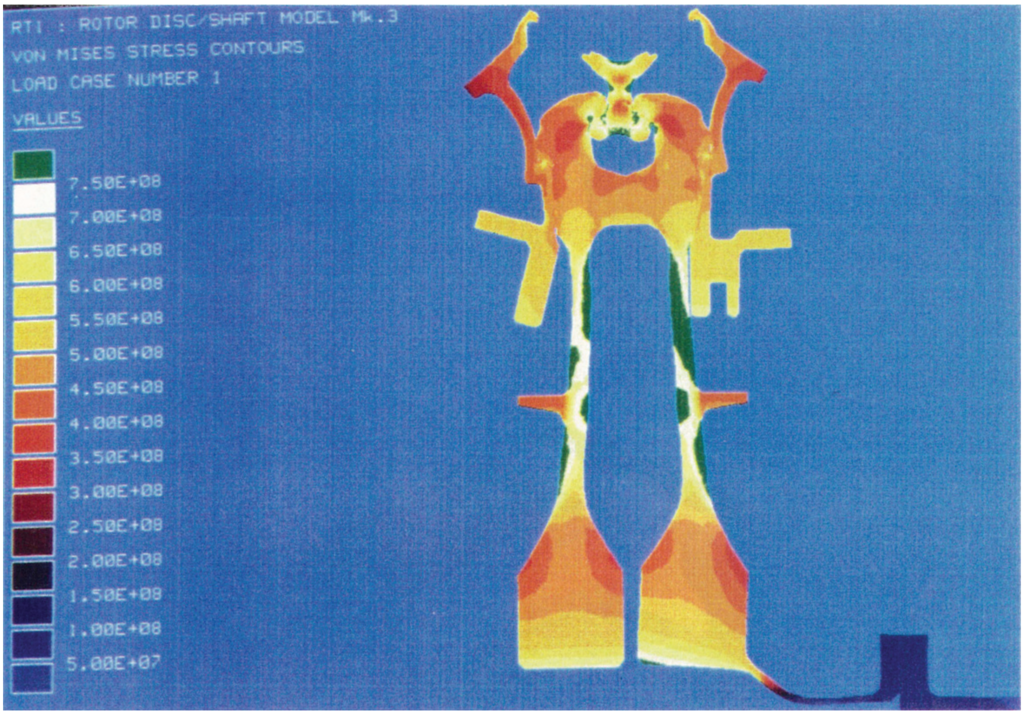

Figure 5.8: Stress distribution through, and deflected shape of, axi-symmetric disc/shaft model at 16,000 rpm, with radially distributed load along blade-root fixing simulating blade load, but no axial gas load

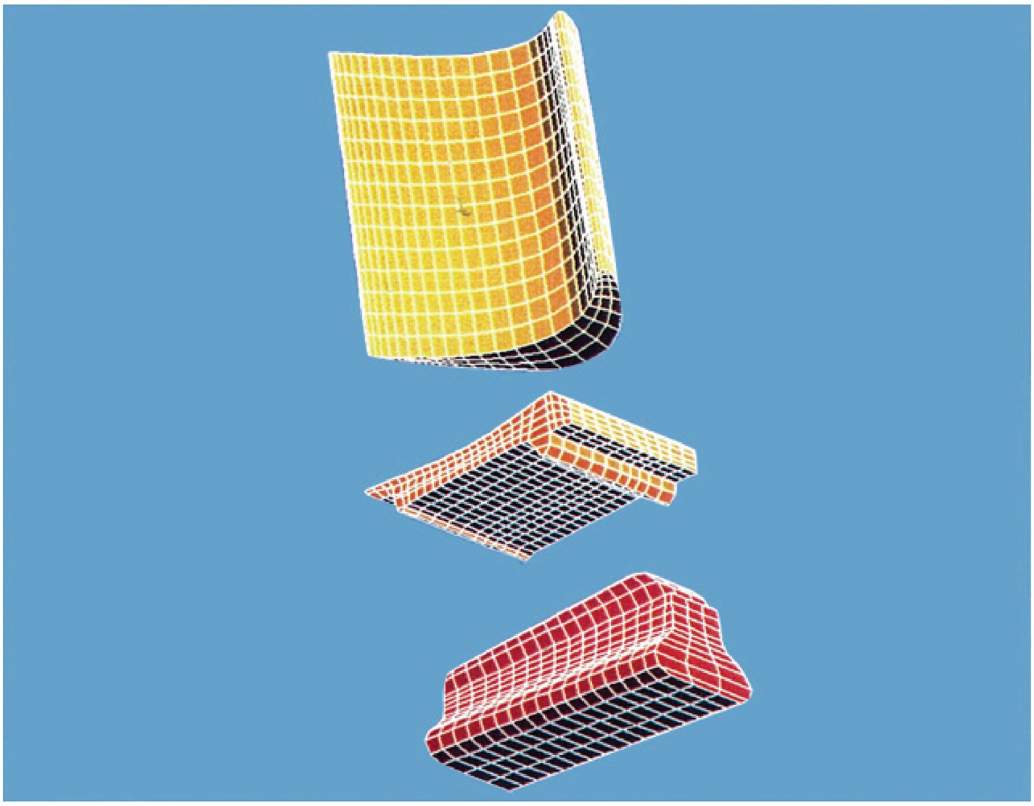

Figure 5.9: Three component models from which three-dimensional blade model was constructed

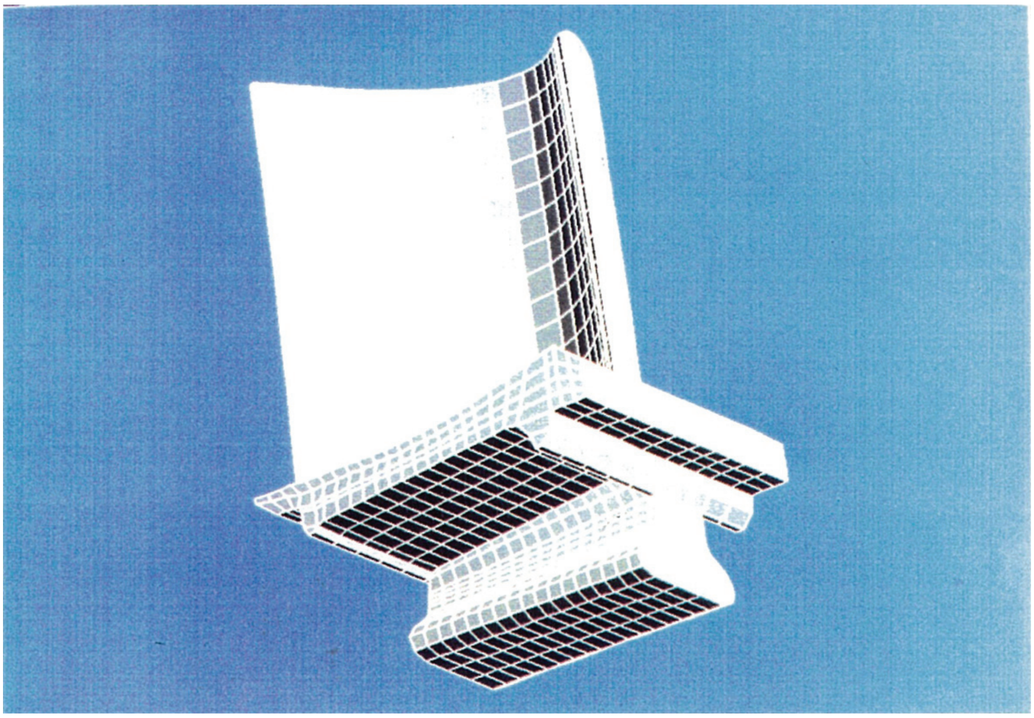

Figure 5.10: Solid model of final turbine blade finite-element model, using eight noded 'brick' elements

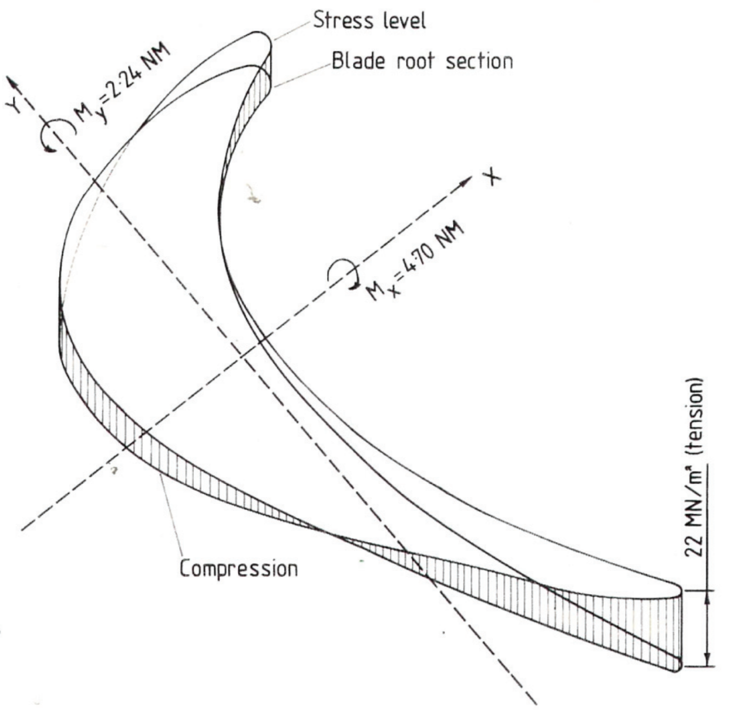

Figure 5.11: Direction of moments around blade root centroid set up consequent upon gas loads on blade aerofoil, and resulting direct stresses at blade root (produced by design condition gas loads)

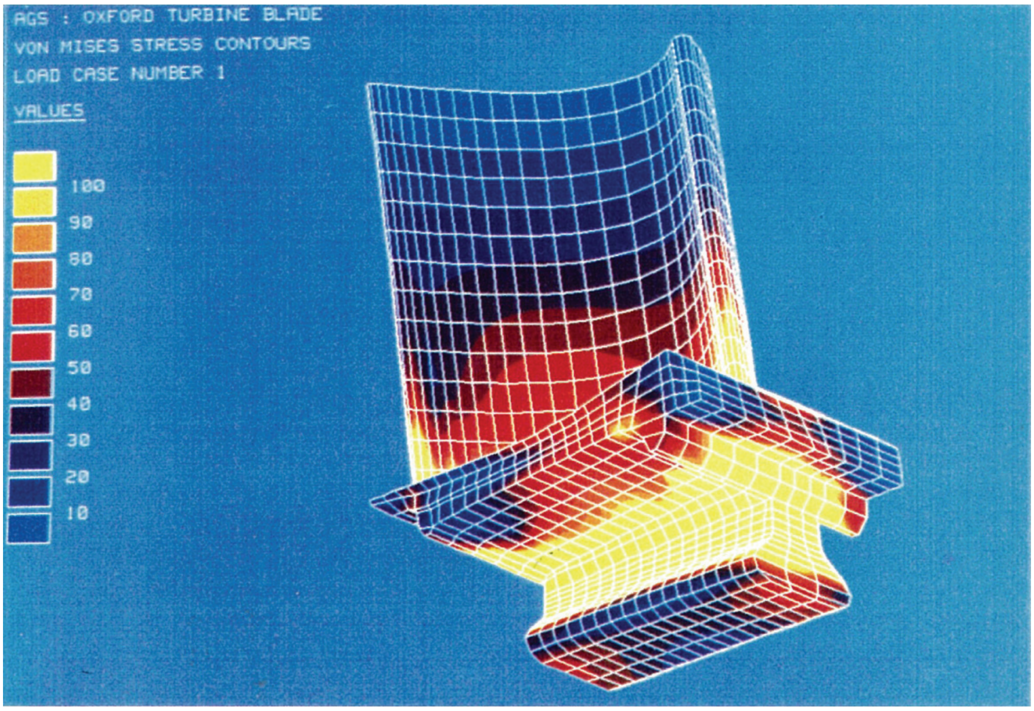

Figure 5.12: Stress distribution through blade due to rotation at 8,434 rpm; view of blade root, underside of platform and aerofoil

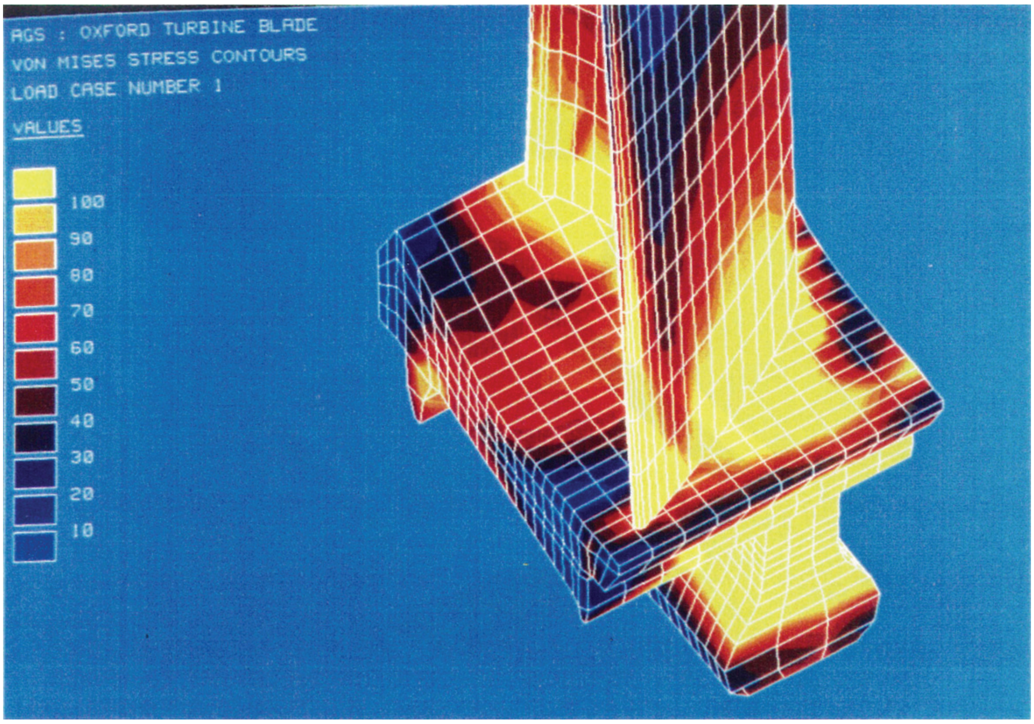

Figure 5.13: Stress distribution through blade due to rotation at 8,434 rpm; view of aerofoil, top side of platform and root

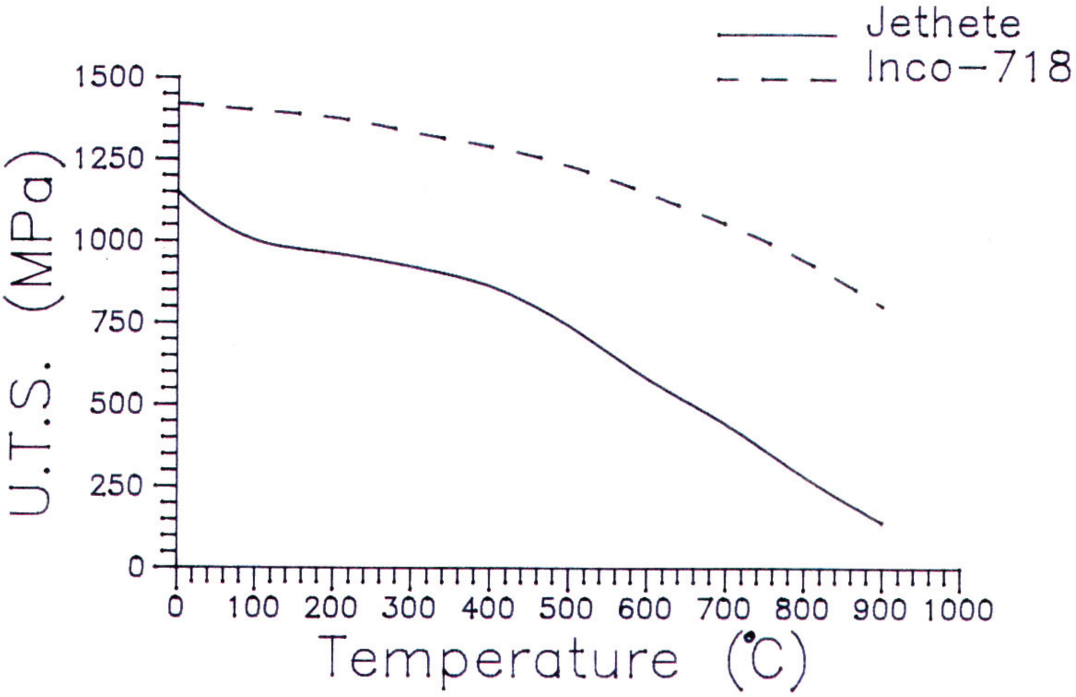

Figure 5.14: Effect of temperature on UTS of JETHETE (material from which turbine disc and un-instrumented blades were made) and INCO-718 (material from which instrumented blades were made)

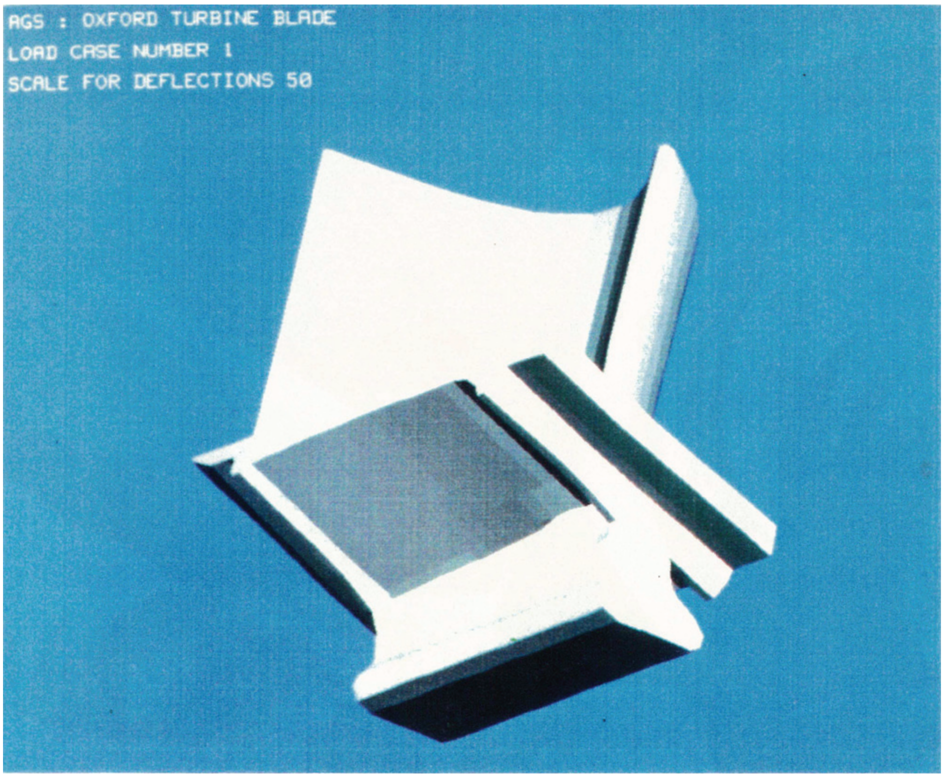

Figure 5.15: Blade-deflected shape due to rotation at 8,434 rpm

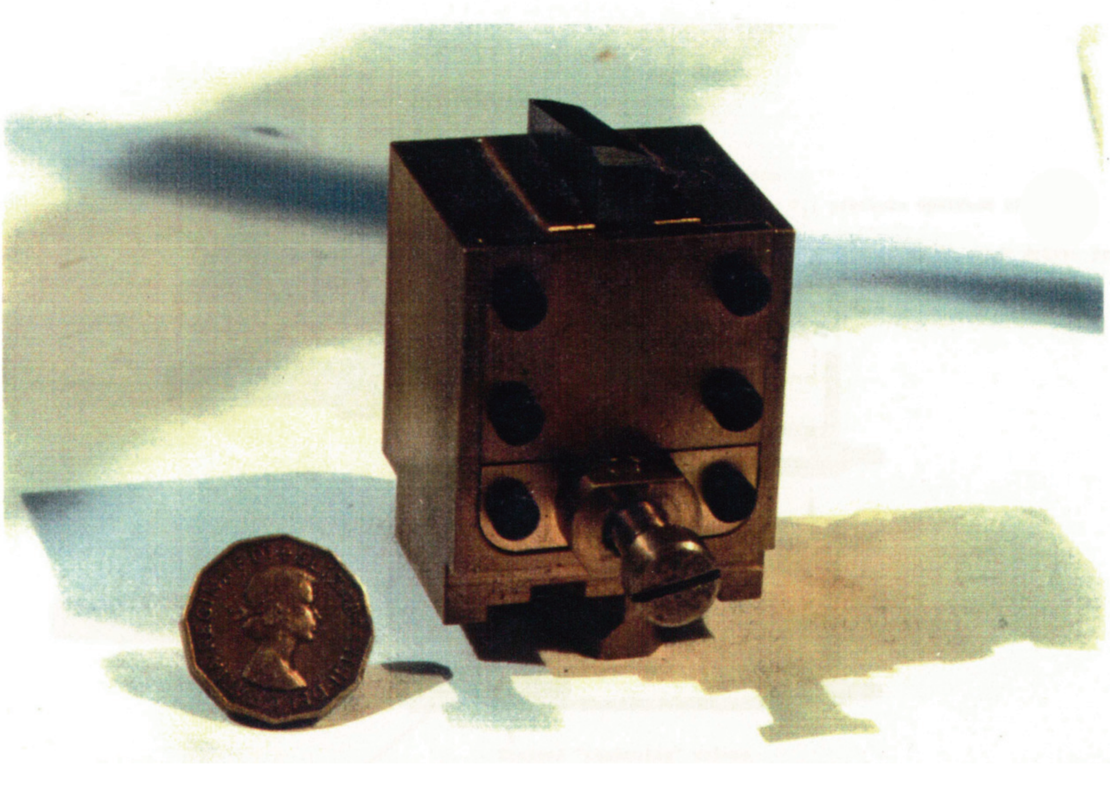

Figure 6.1: Disc-mounted cutter used to machine turbine blade overtip abradable seal concentric with turbine shaft

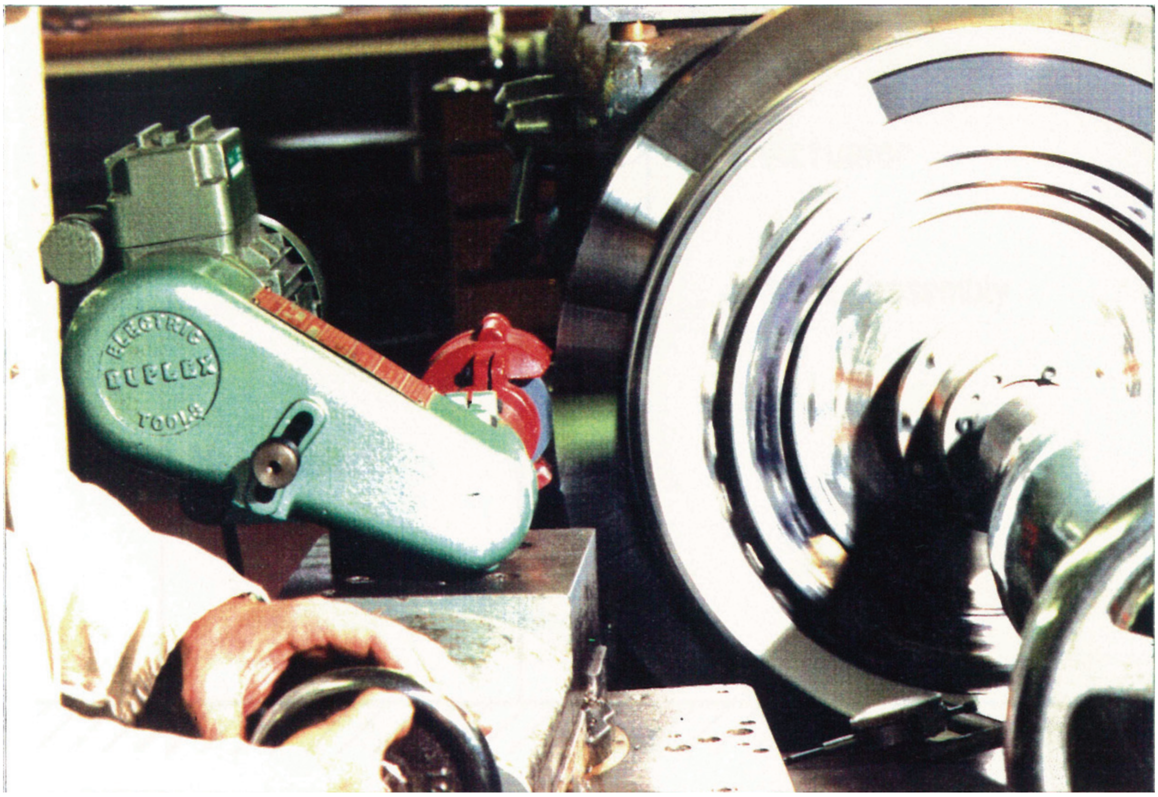

Figure 6.2: **Turbine blades ground to length while mounted on turbine disc (which was mounted on dummy shaft fitted in a lathe); rotational speed 60 rpm with grinding machine mounted on lathe headstock**

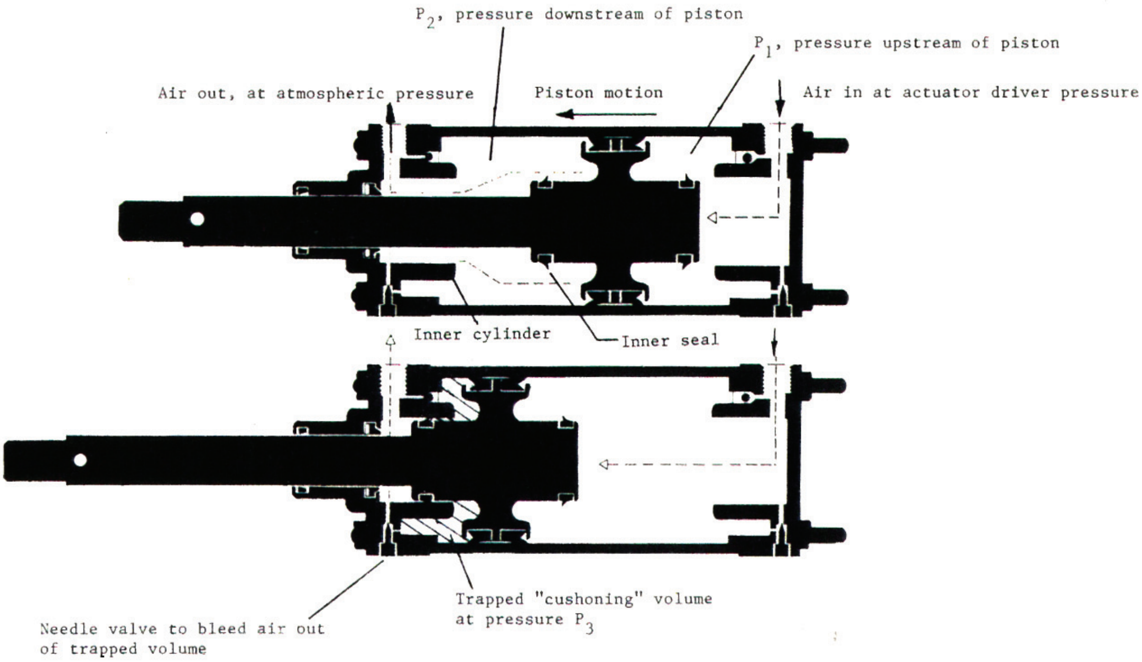

Figure 6.3: **Sectional view of actuator used to open the AGV**

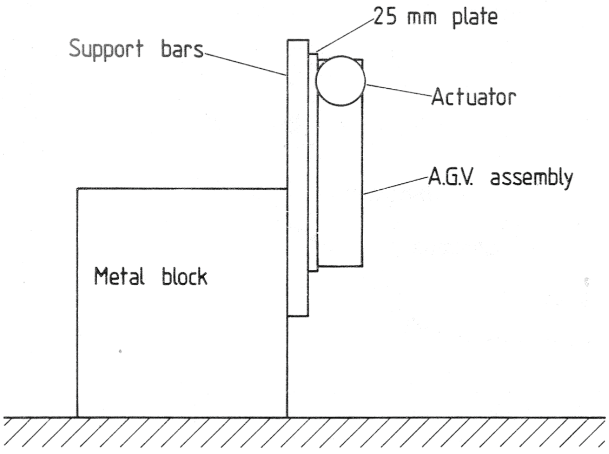

Figure 6.4: **Schematic view of AGV mounted on large metal block, with blanking plate between AGV and block to facilitate pressurising AGV front face during commissioning trials**

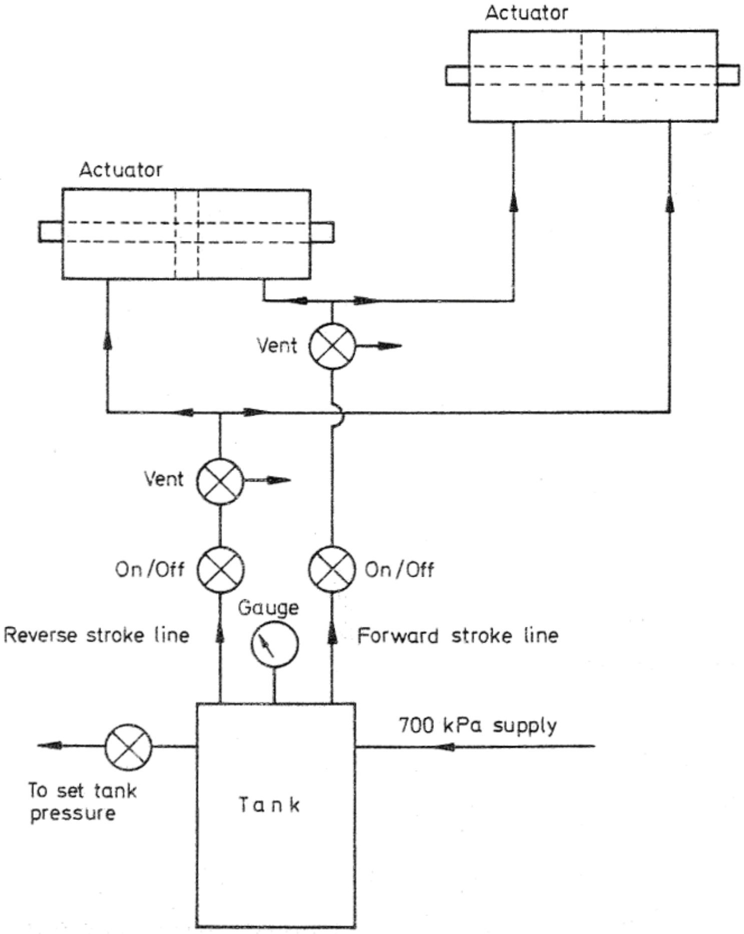

Figure 6.5: **AGV actuators air supply, developed while commissioning AGV and transferred to ILPT during assembly of turbine module**

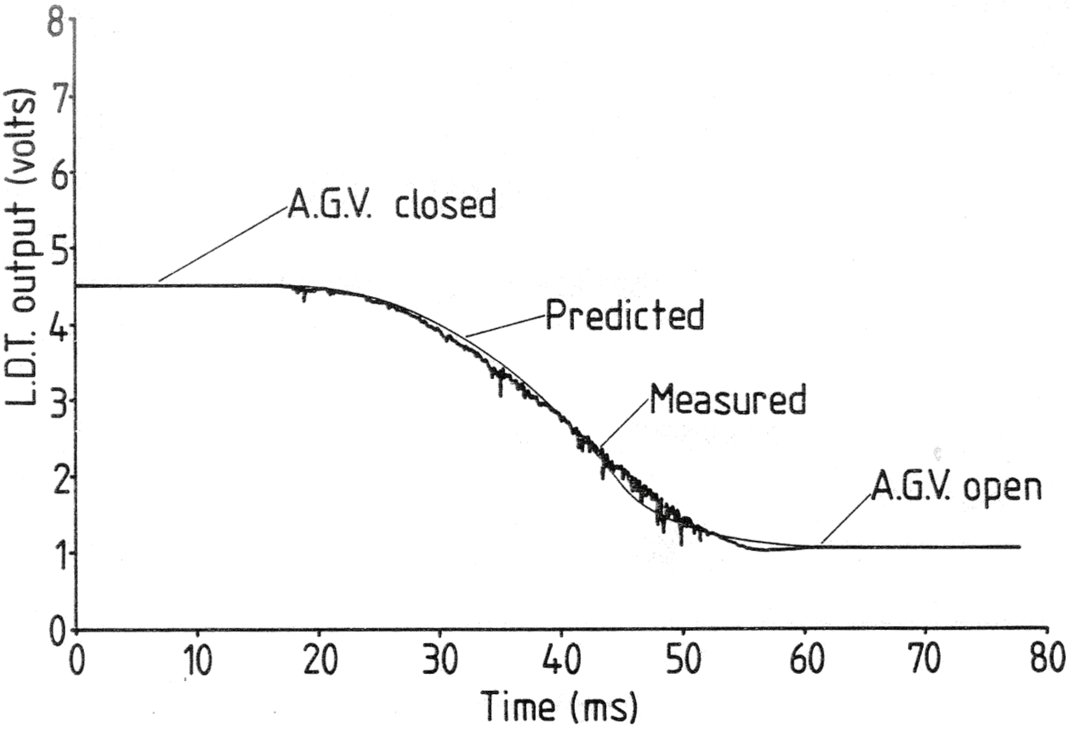

Figure 6.6: **Opening characteristics of AGV with no pressure on AGV front face, and 2.7×10^5 N/m² across actuators and 25 mm of actuator cushioning (maximum 35 mm)**

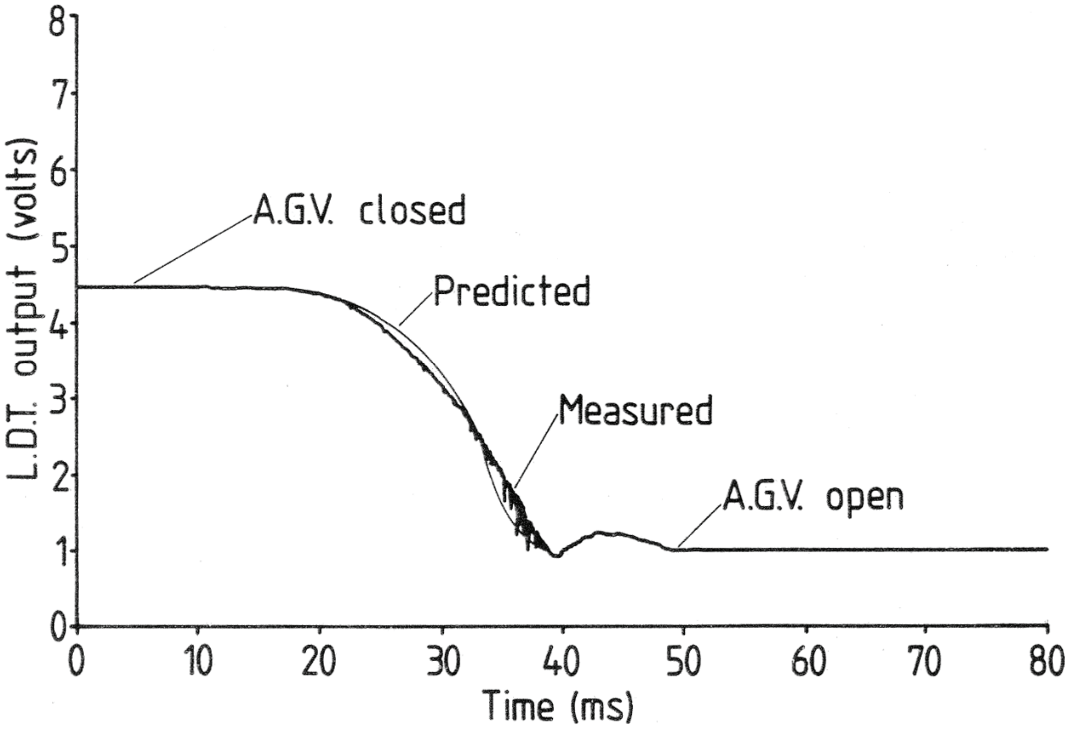

Figure 6.7: **Opening characteristics of AGV with 3.7×10^5 N/m² on AGV front face and 2.7×10^5 N/m² across actuators, with 35 mm cushioning (maximum 35 mm)**

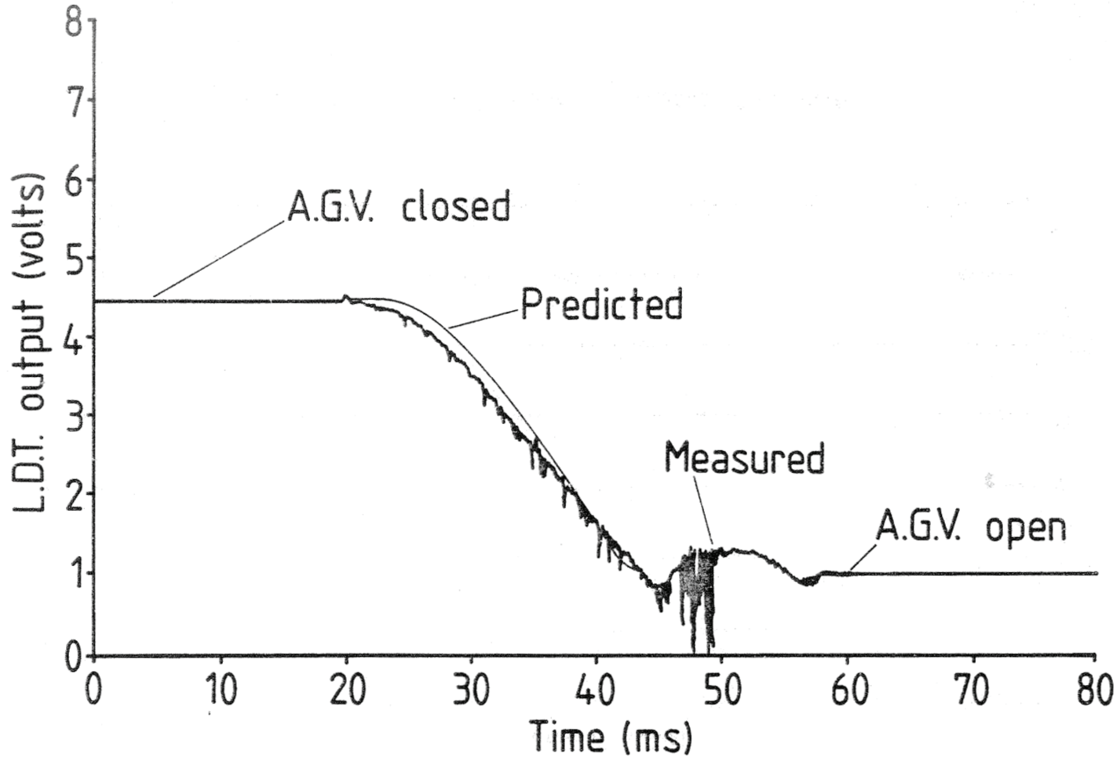

Figure 6.8: Opening characteristics of AGV with 8.02 x10^5 N/m² across the AGV, and 5.1 x 10^5 N/m² across actuators, with 35 mm cushioning (maximum 35 mm)

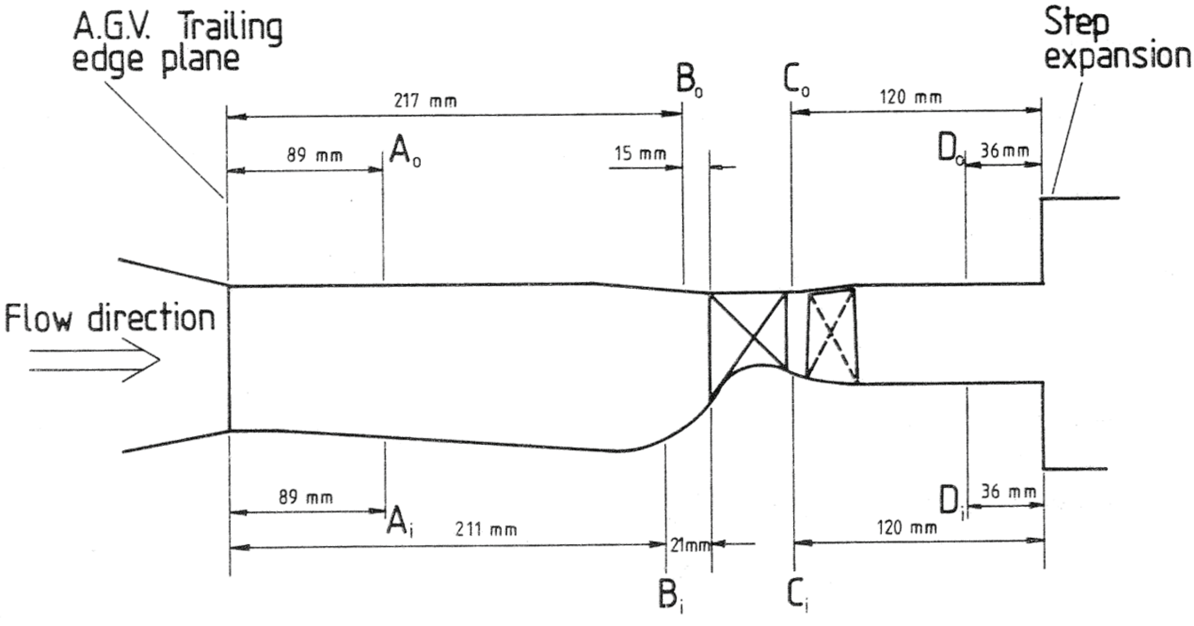

Figure 6.9: Side elevation of turbine module inlet duct and working section, with axial location of pressure measurement planes A, B, C, and D

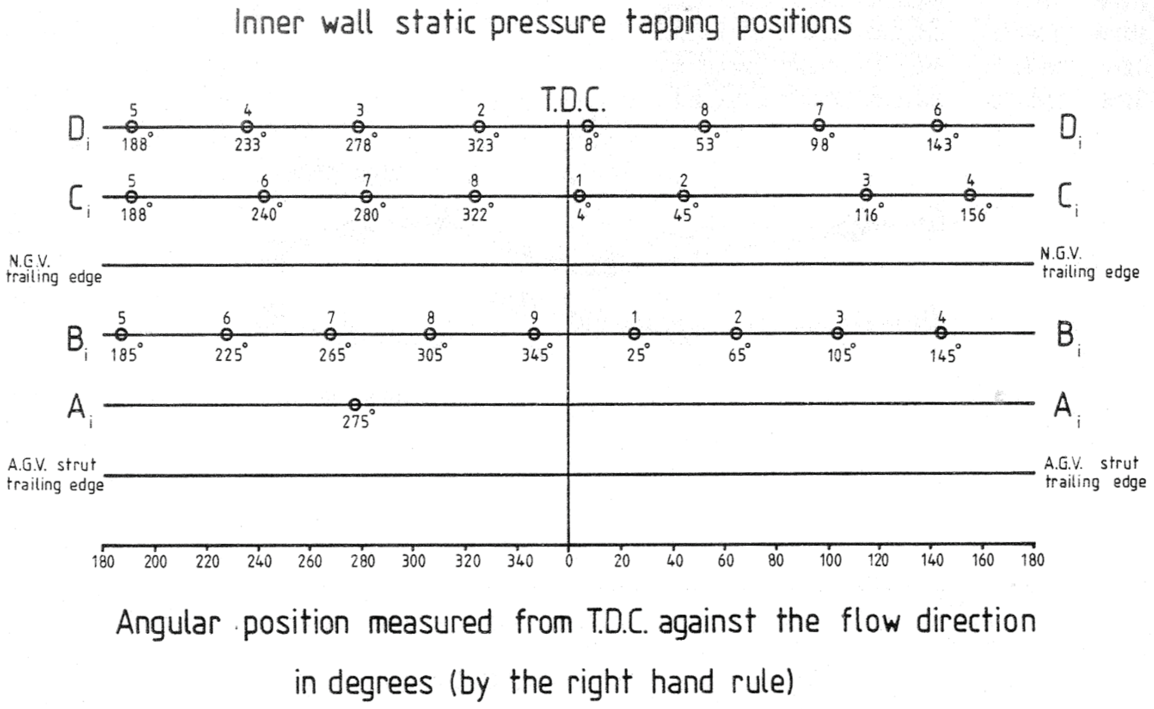

Figure 6.10: Angular position of inner annulus static pressure tappings measured from top dead centre (against flow direction)

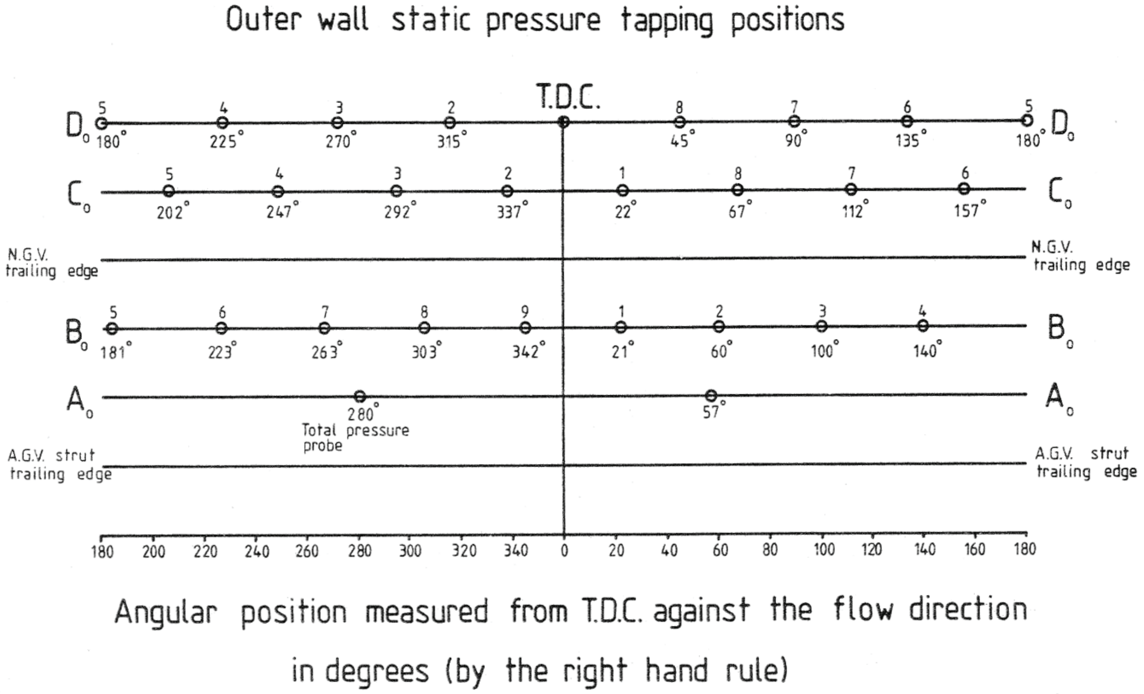

Figure 6.11: Angular position of outer annulus static pressure tappings measured from top dead centre (against flow direction)

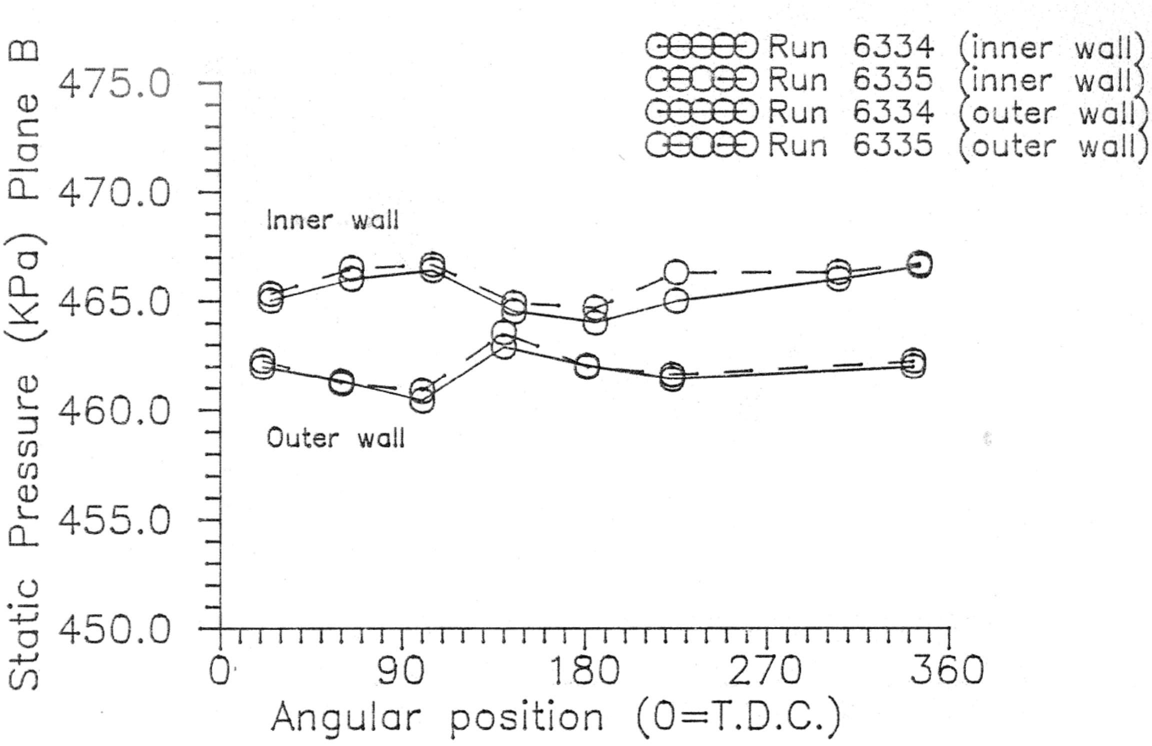

Figure 6.12: Plane B inner and outer annulus measured static pressures

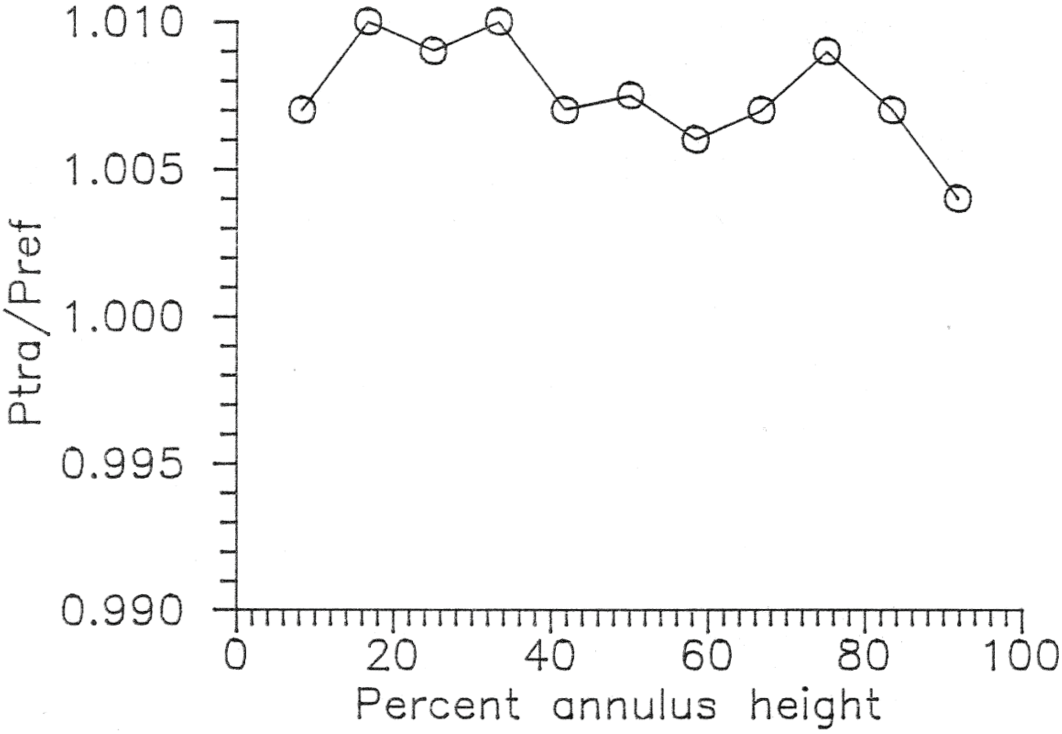

Figure 6.13: Radial traverse of vane inlet total pressure measured at Plane B non-dimensionalised with respect to total pressure measured in Plane A

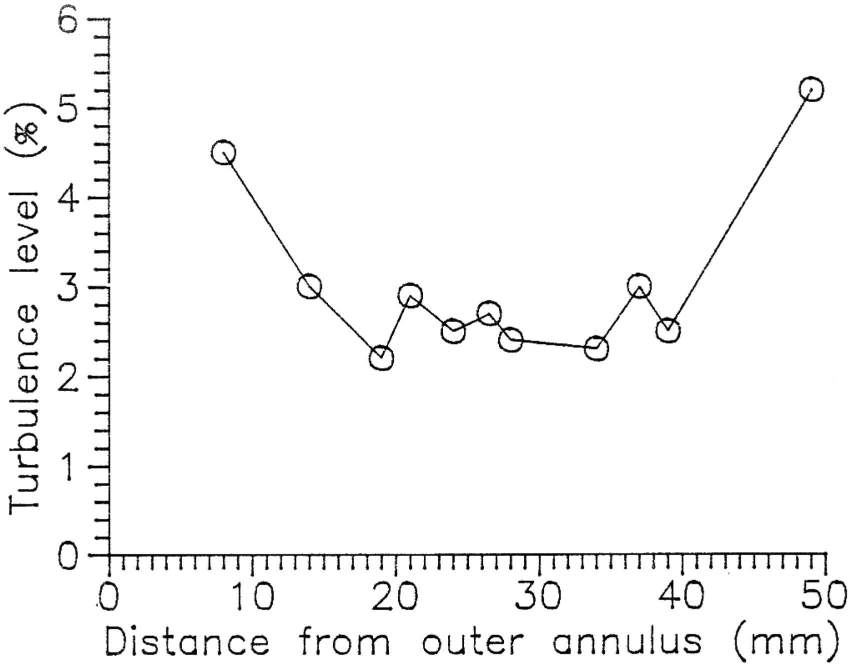

Figure 6.14: Radial traverse of vane inlet turbulence measured by IZSAK (1988) at Plane B with hot wire anemometer

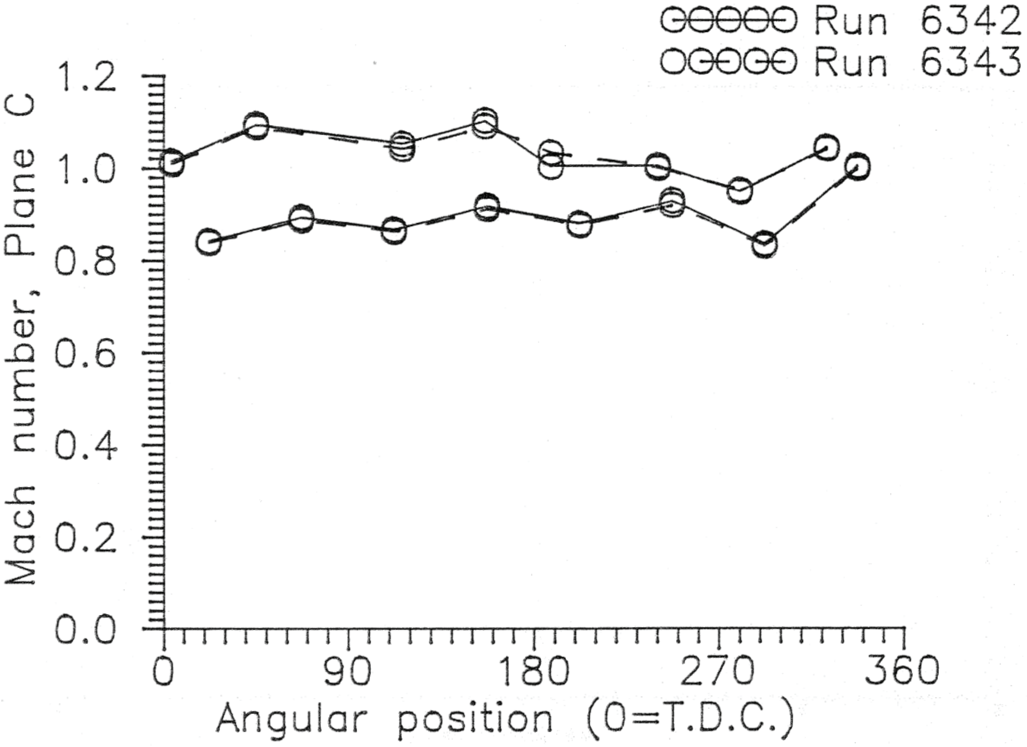

Figure 6.15: Vane exit inner and outer annulus Mach number distributions, calculated using measured static pressures at Plane C and total pressure at Plane A

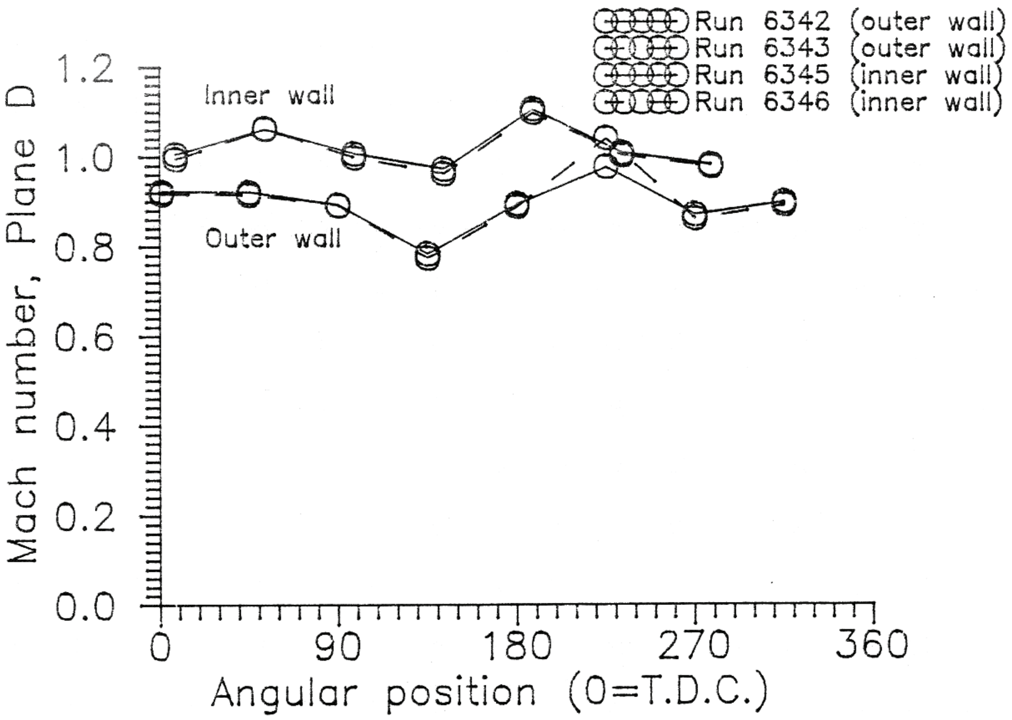

Figure 6.16: Blade exit inner and outer annulus Mach number distributions, calculated using measured static pressures at Plane D and total pressure measured at Plane A (no rotor during stage 2 commissioning)

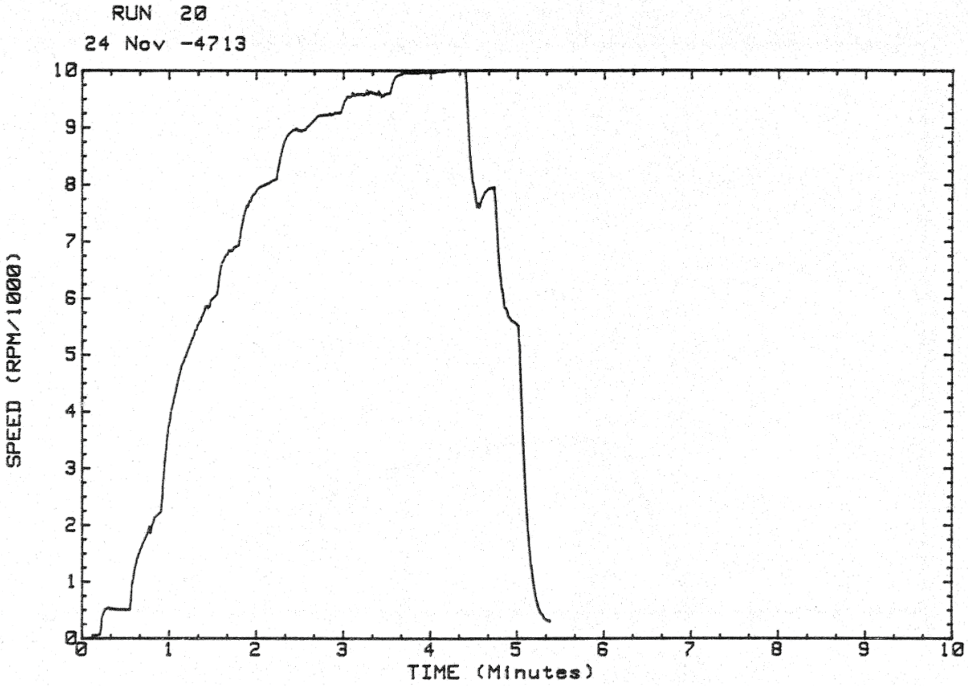

Figure 6.17: Turbine speed/time history during Stage I (shaft only) commissioning Run 20, during which shaft spun to overspeed condition using air motor

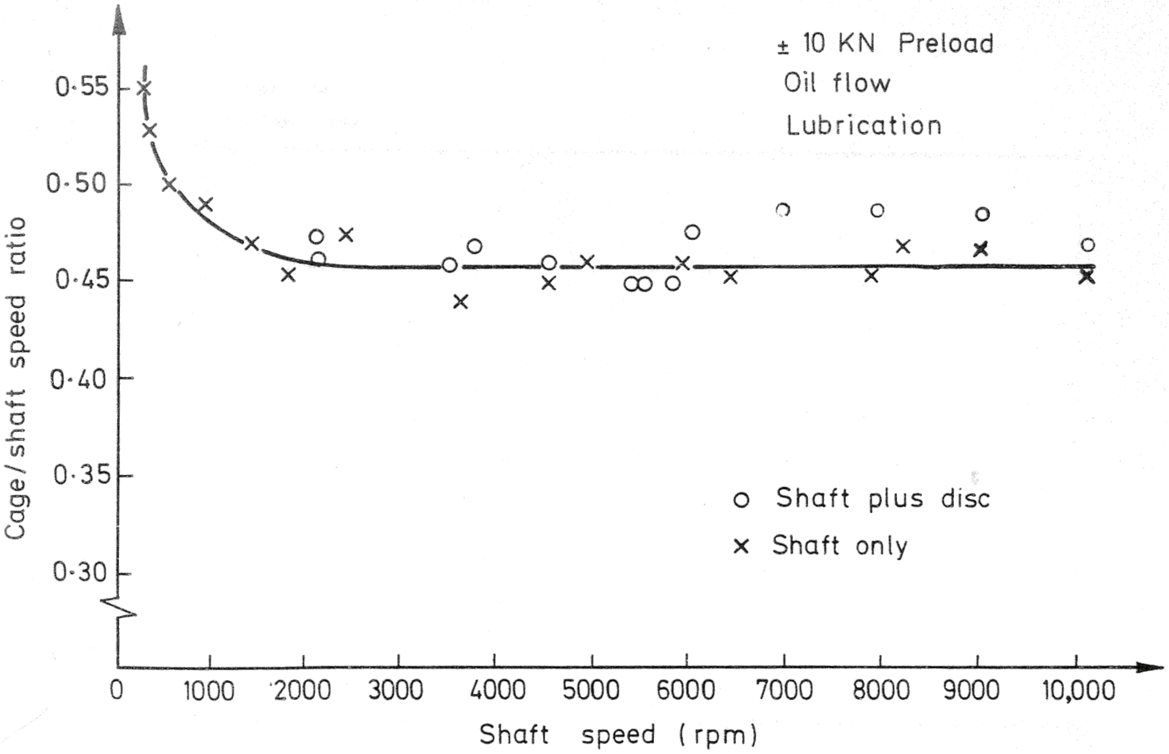

Figure 6.18: Measured cage/shaft speed ratio for single bearing during Stage I and II commissioning trials

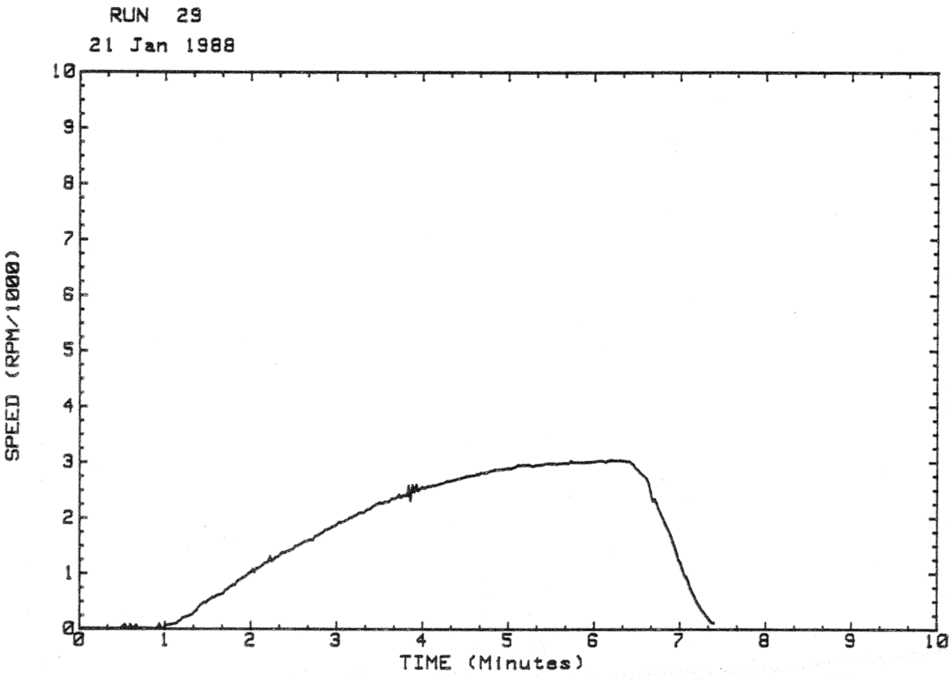

Figure 6.19: Turbine speed/time history during Stage II (shaft and bladed disc) commissioning Run 29

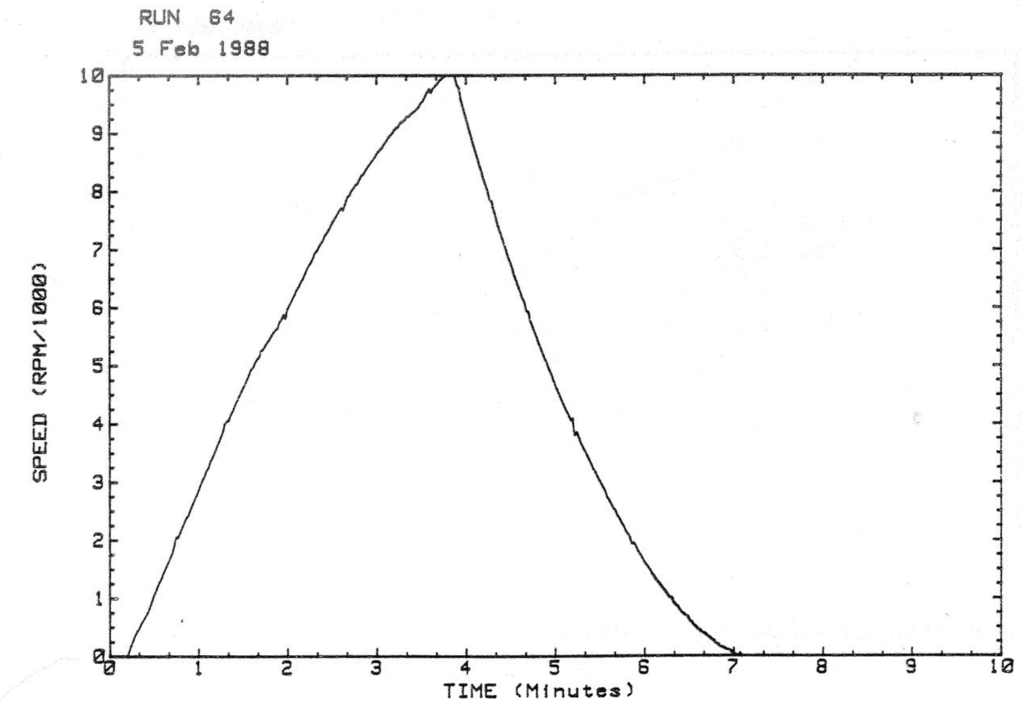

Figure 6.20: Turbine speed/time history during Stage II (shaft and bladed disc) commissioning Run 64, during which full rotating assembly was spun to overspeed condition using air motor

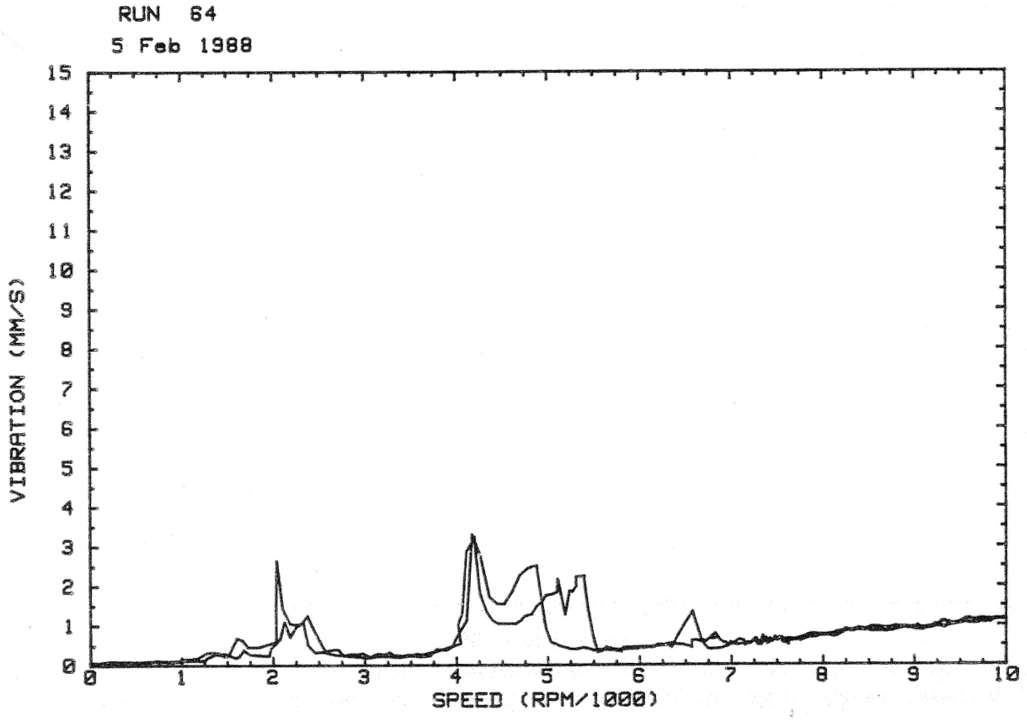

Figure 6.21: Turbine vibration/speed history during commissioning Run 64

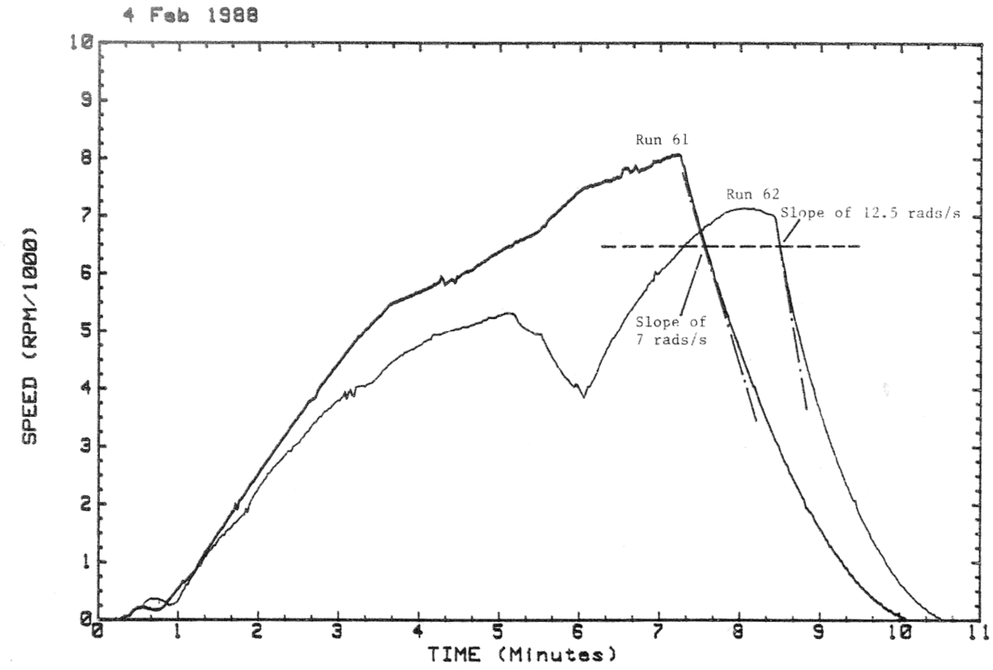

Figure 6.22: Turbine speed/time histories for two Stage II commissioning runs: Run 61 (pressure of 500 N/m² in working section) and Run 62 (pressure of 50 x 10³ N/m² in working section)

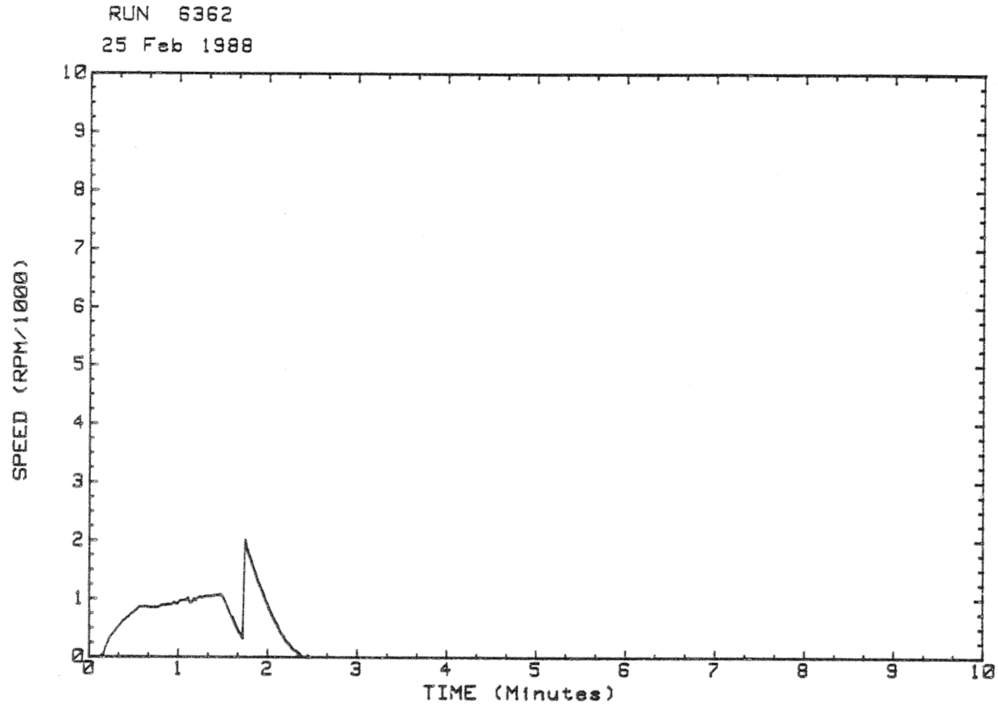

Figure 6.23: First Stage III commissioning trial: Run 6362, with fully bladed turbine disc and flow through the working section (initial turbine speed 500 rpm and Reynolds number of 25% of design value)

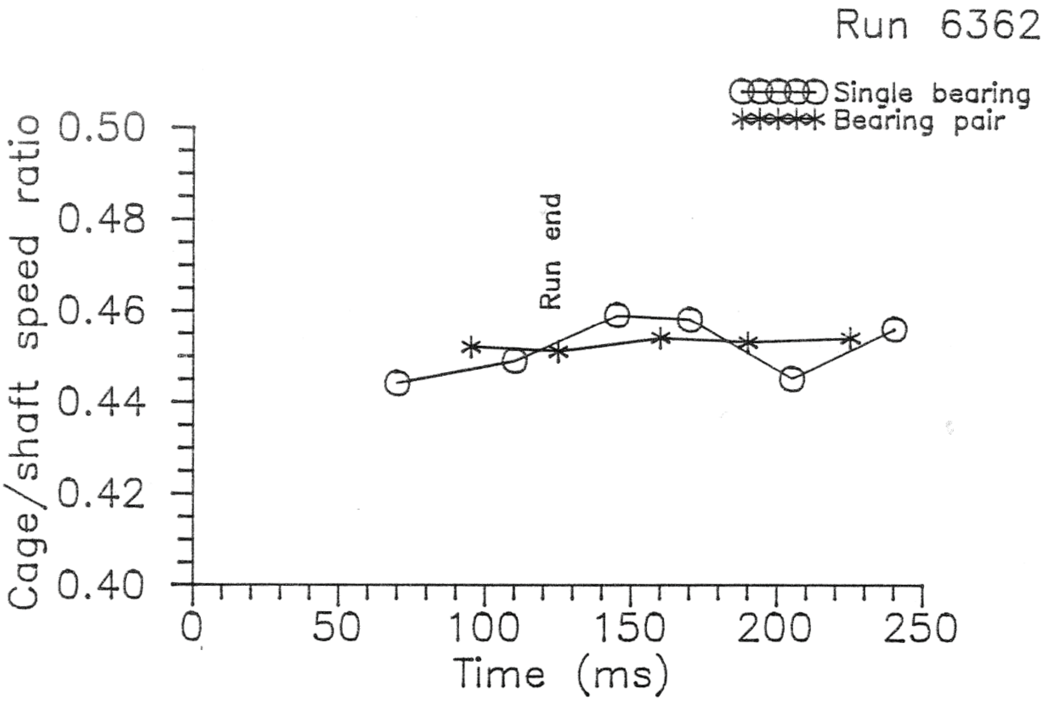

Figure 6.24: Bearing cage/shaft speed ratio for Run 6362

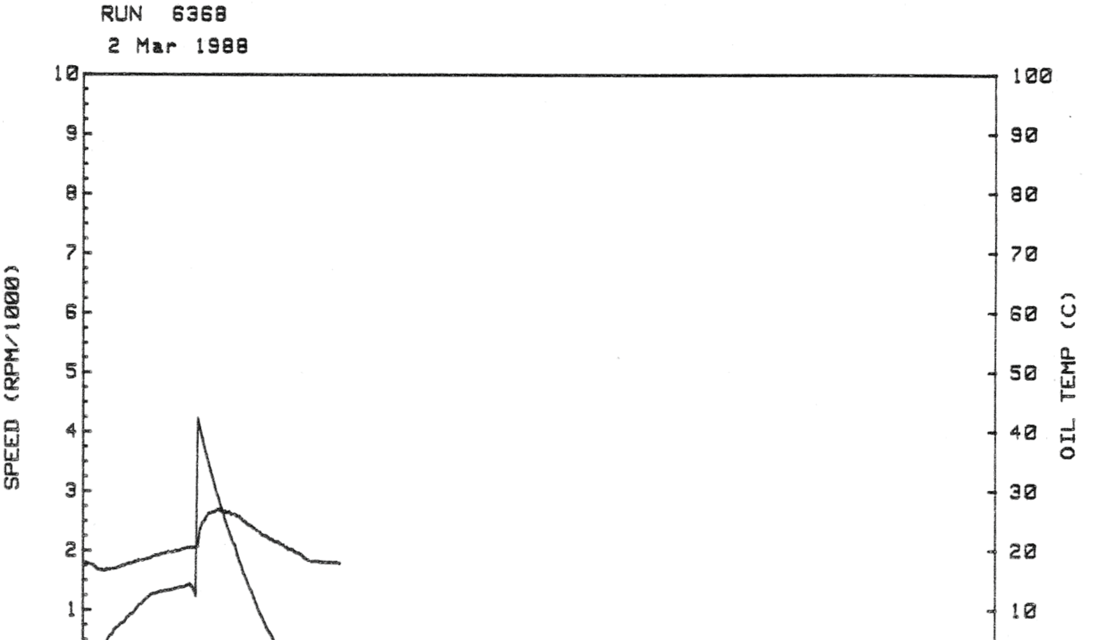

Figure 6.25: Stage III commissioning Run 6368: first run with 50% design-value Reynolds number flow through working section

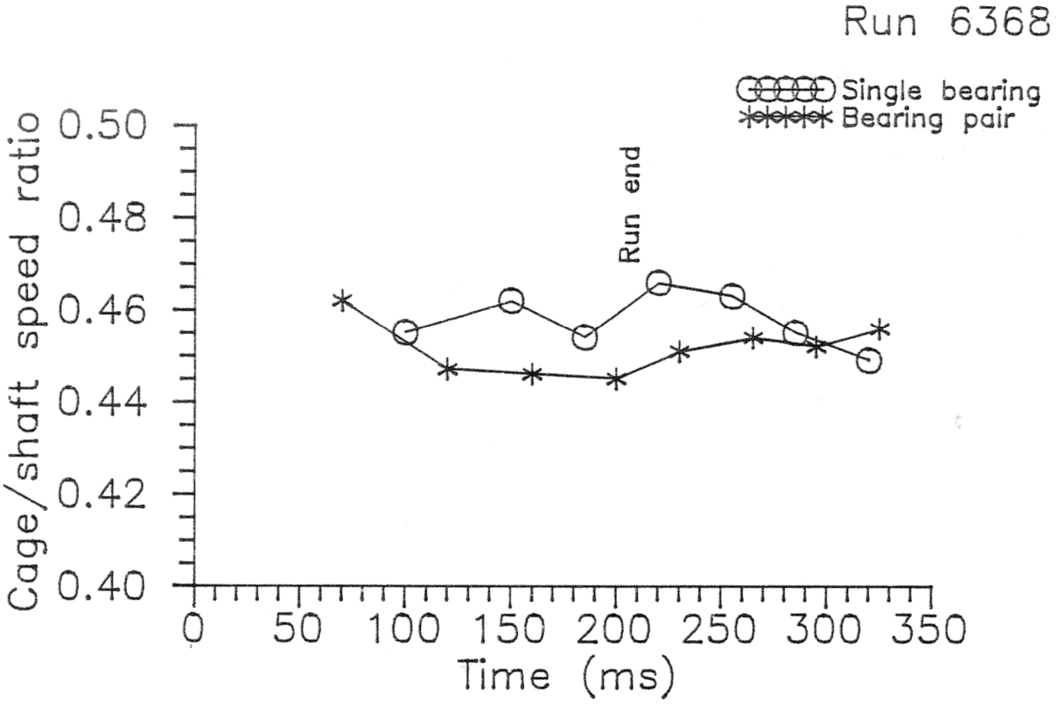

Figure 6.26: Bearing cage/shaft speed ratio for Run 6368

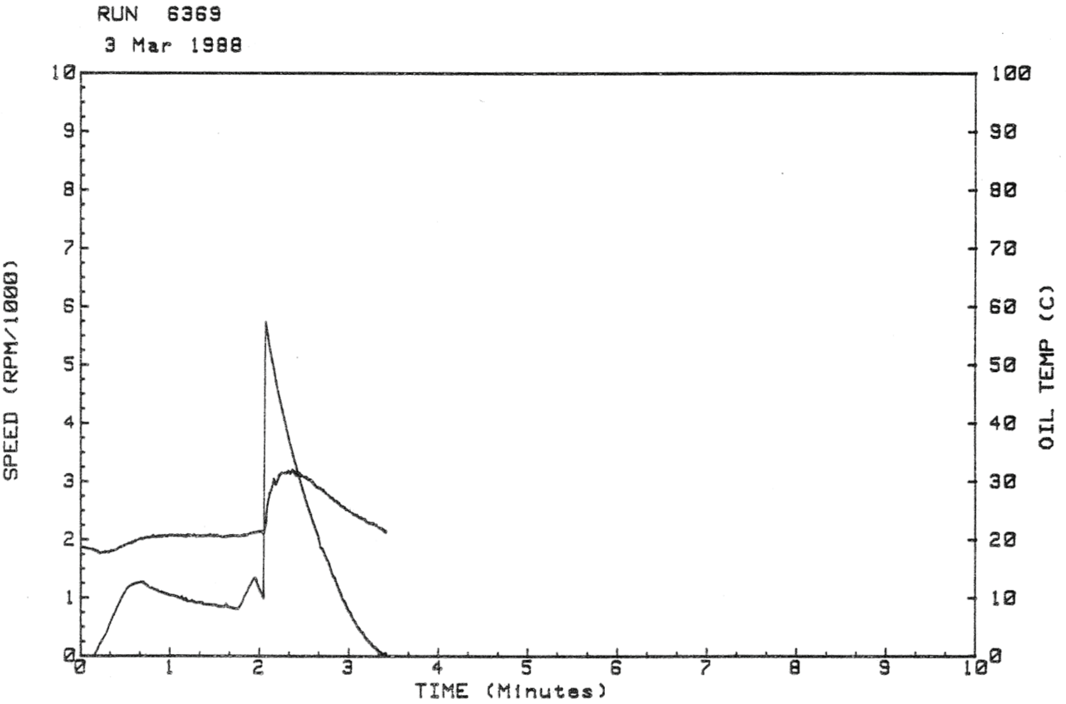

Figure 6.27: Stage III commissioning Run 6369: first run with design-value Reynolds number flow through working section

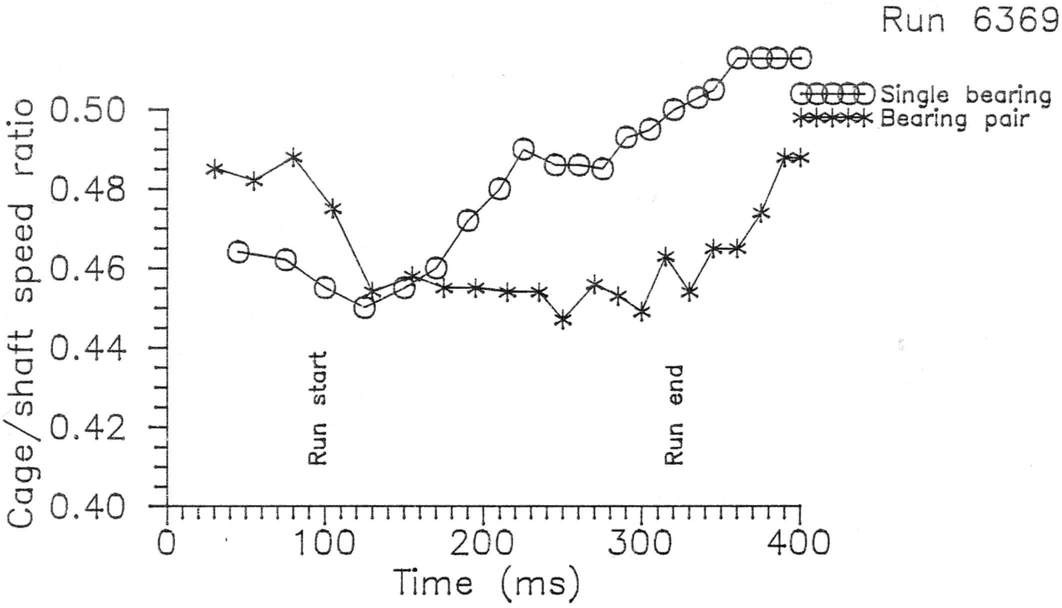

Figure 6.28: Bearing cage/shaft speed ratio for Run 6369

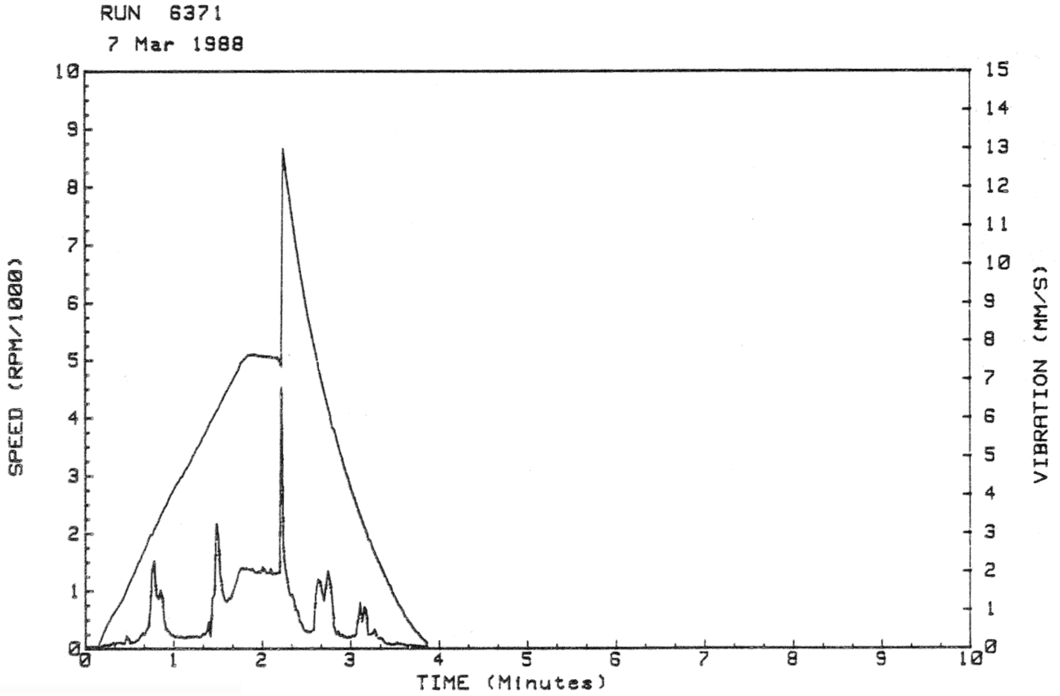

Figure 6.29: Stage III commissioning Run 6371: first run with design-value Reynolds number flow through working section with turbine design speed achieved during ILPT operation

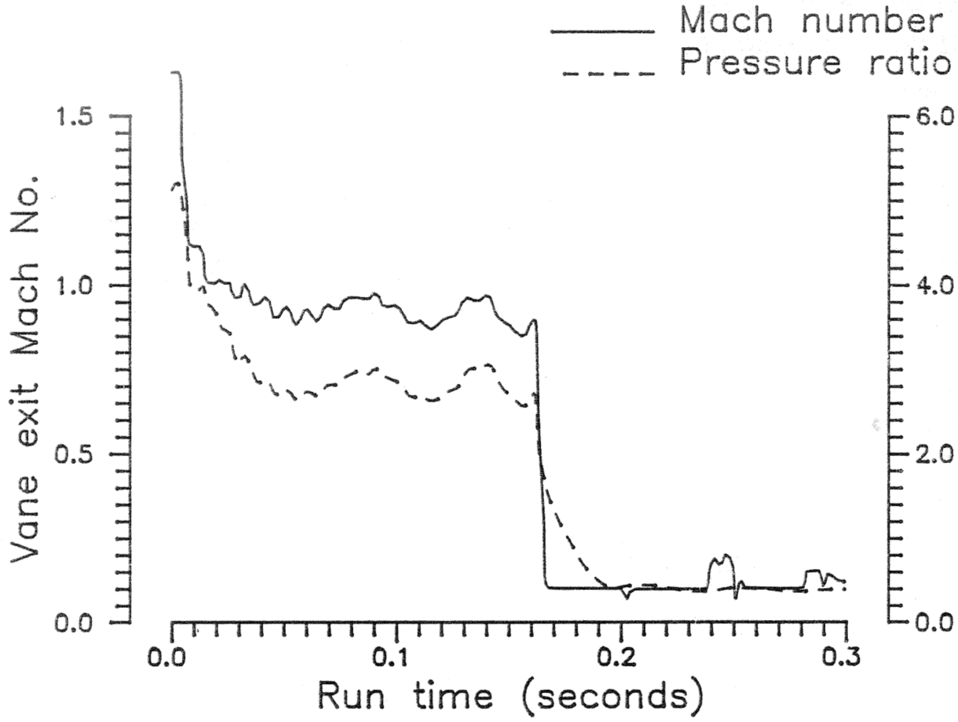

Figure 7.1: Vane exit Mach number and stage pressure ratio variation during Run 6384 (calculated using program 'ROTOR')

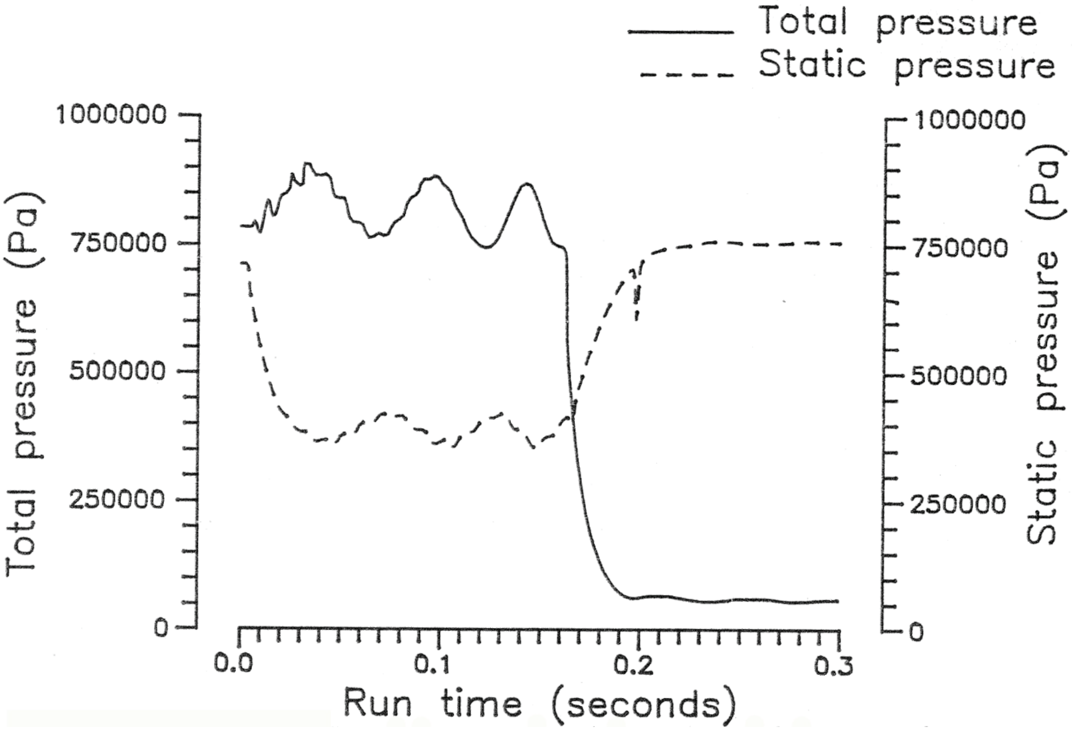

Figure 7.2: Total and vane exit inner annulus static pressure (in vane exit plane) measured during Run 6384

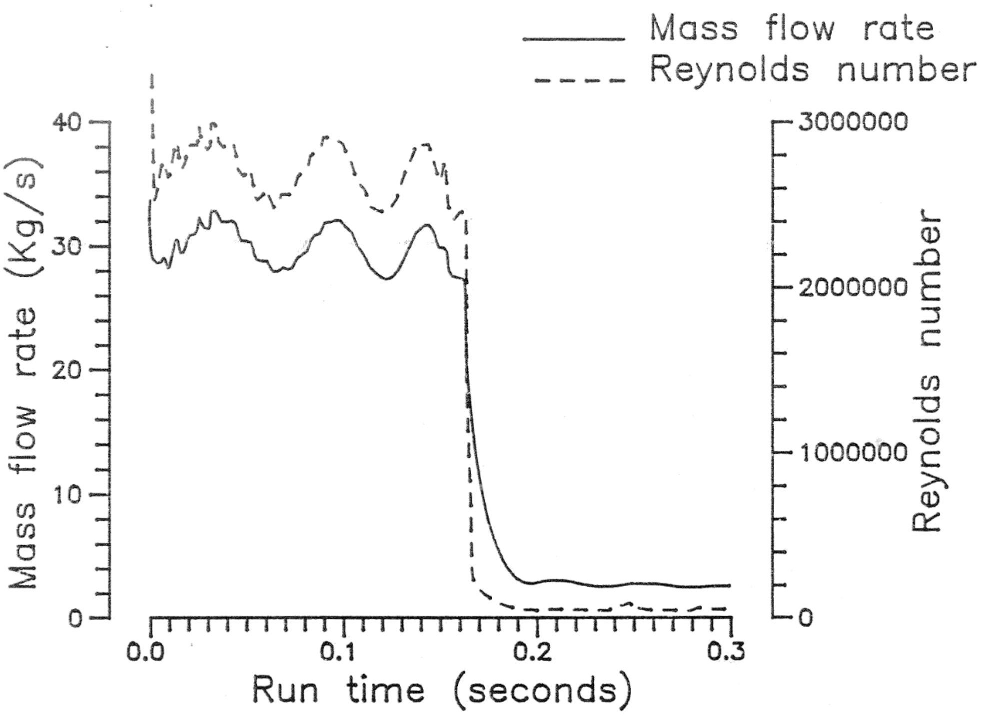

Figure 7.3: **Mass flow rate and Reynolds number variation during Run 6384 (calculated using program 'ROTOR')**

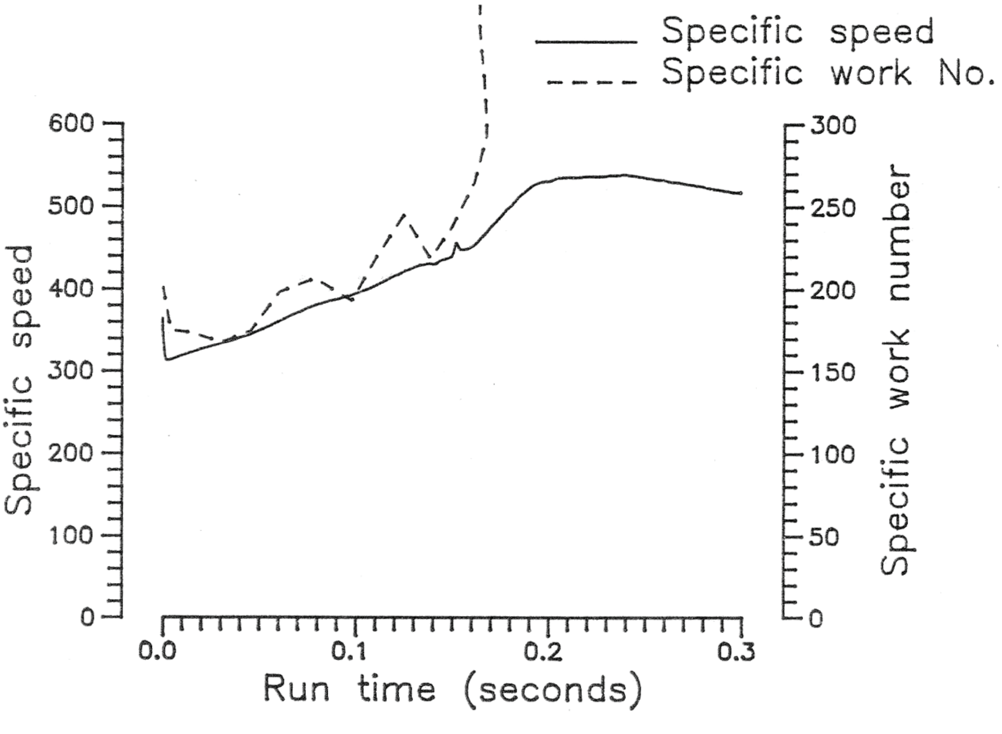

Figure 7.4: **Turbine specific speed and specific work number variation during Run 6384 (calculated using program 'ROTOR')**

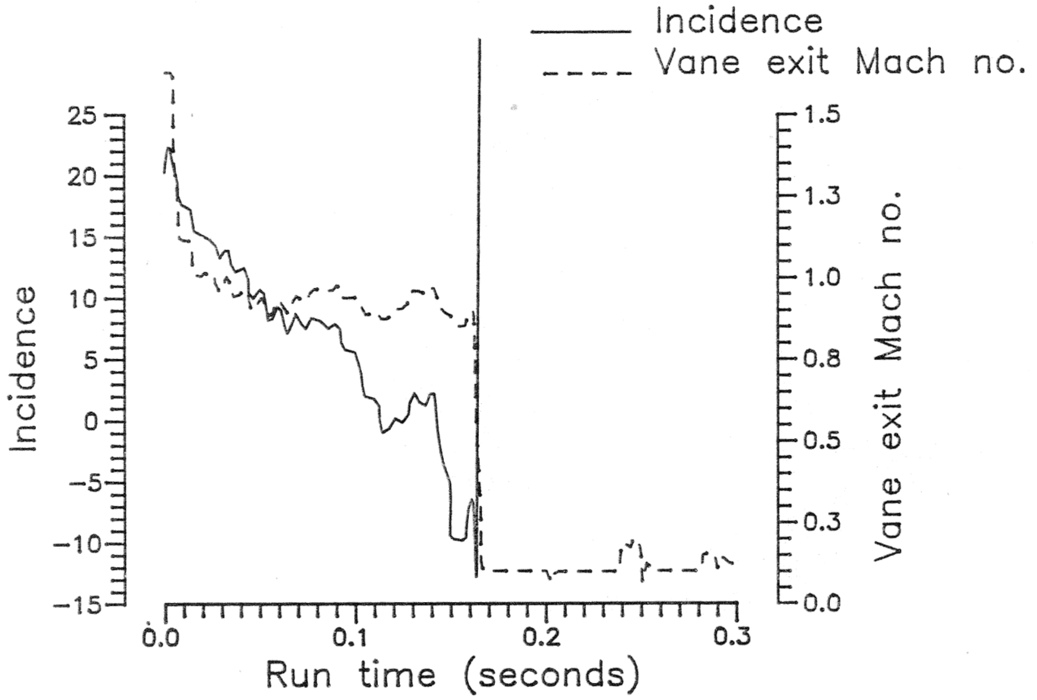

Figure 7.5: Blade mid-height incidence angle and vane exit Mach number variation during Run 6384 (calculated using program 'ROTOR')

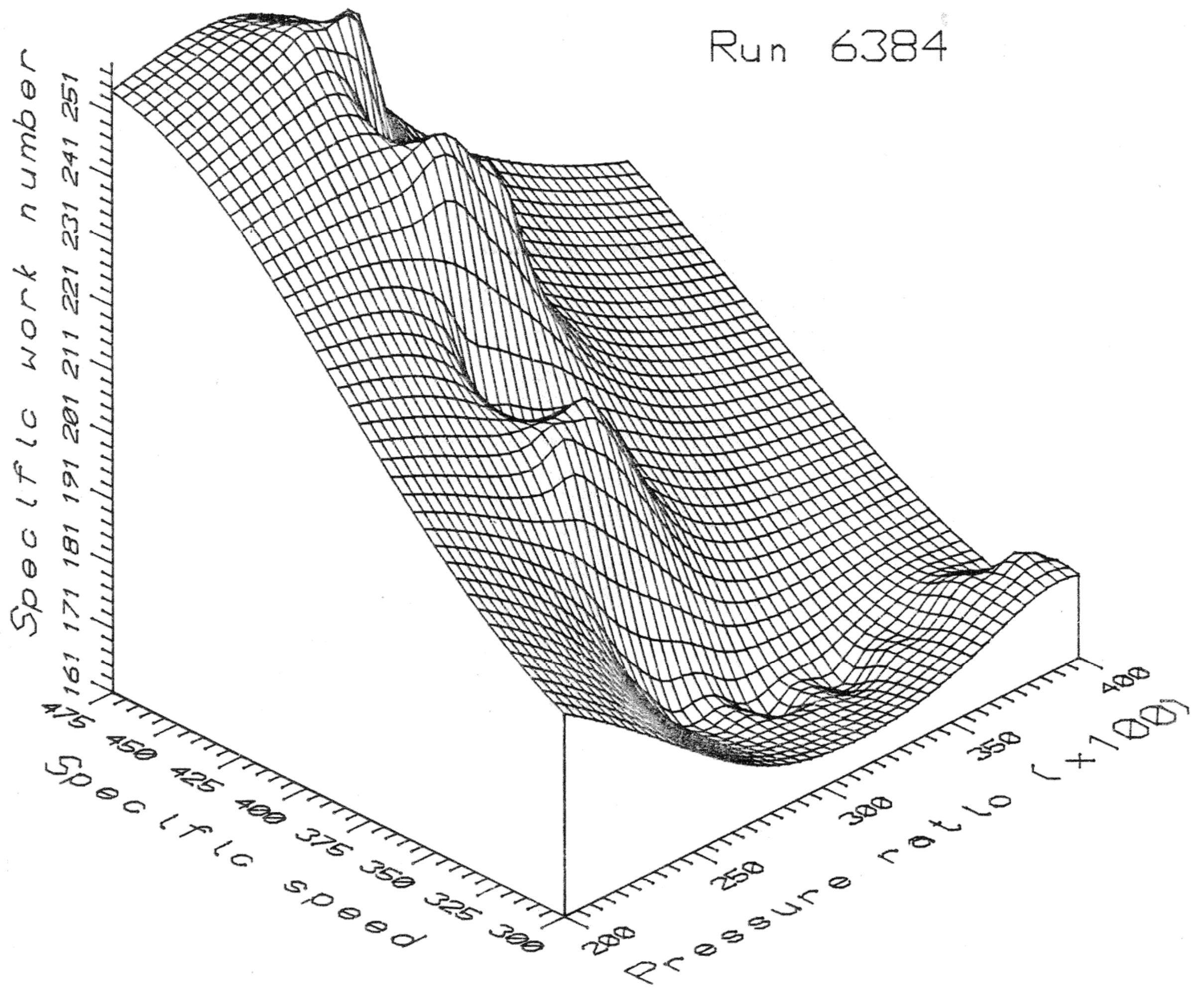

Figure 7.6a: Turbine performance map

Overlay for Figure 7.6a

The actual path of the B22 turbine over its performance map during ILPT Run 6384 is drawn, to illustrate the range of conditions covered by the turbine during ILPT operation. The hypodermic tube fill time may clearly be seen as the initial peak in pressure ratio of 4.0, dopping down to the design value of 2.8, with piston osscilations result in it verying between approximately 2.5 and 3.0. The actual trajectory of the turbine is a helix, due to the combined effect of piston ossilations in both pressure ratio and specific work number. This may be seen as "mountains" and "valleys" in the in the performance map, the trajectory progressing up the first mountain (at time step 57.5 ms), over the peak, into the valley and up the following peak. The sparsity of data used to create the surface in Fig.7.1 is reflected in the lack of surface detail away from the turbine's path, where the surface was interpolated from relatively distant data.

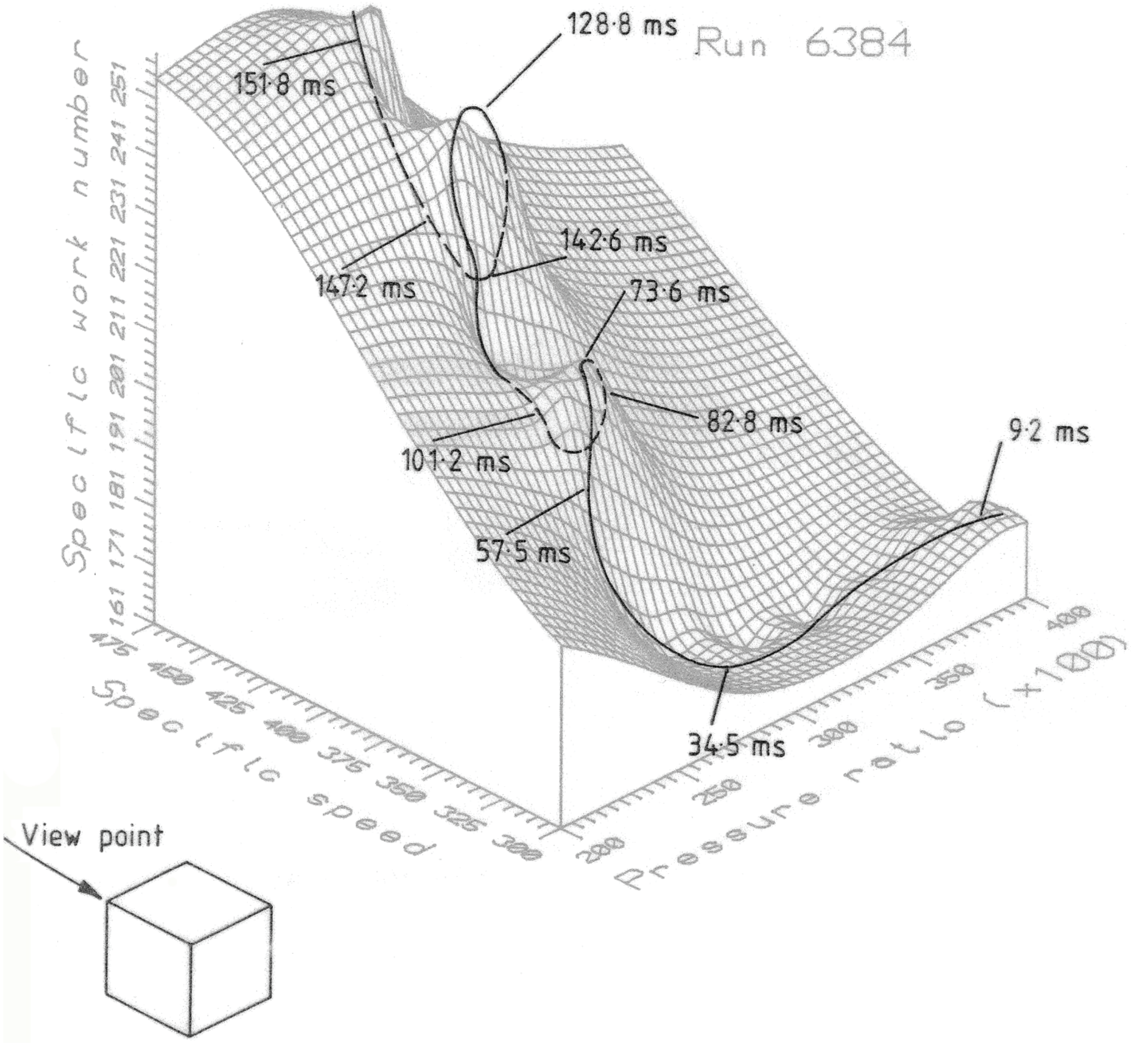

Figure 7.6a: Turbine performance map, with actual path traced by turbine during Run 6384 overlaid

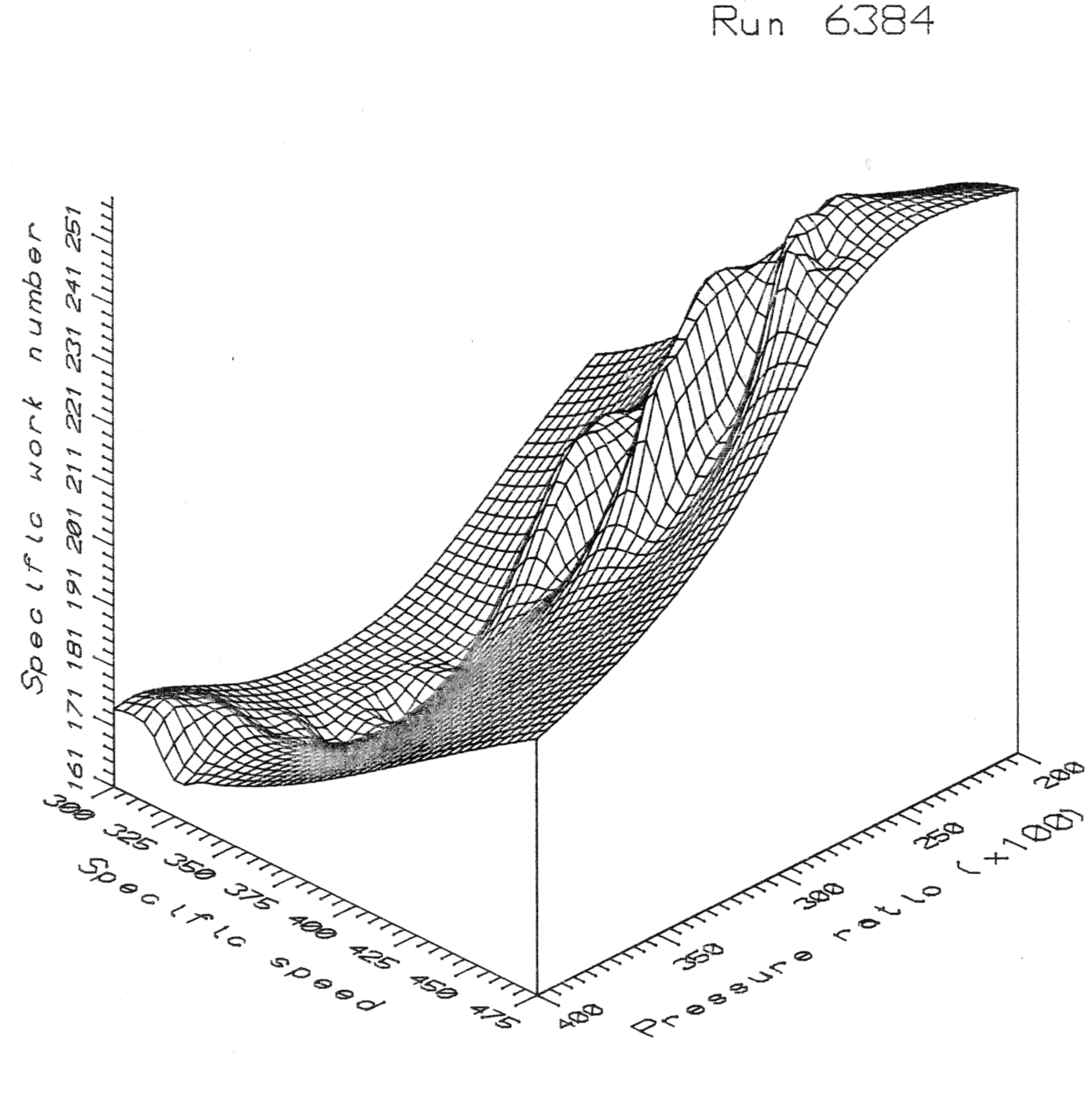

Figure 7.6b: Turbine performance map

Overlay for Figure 7.6b

The actual path of the B22 turbine over its performance map during the ILPT Run 6384, drawn from a view point rotated 180° from Fig.7.6a. The dashed sections of the path are those that fall behind a “mountain” in the performance map, and therefore are not visible from the observer’s view point.

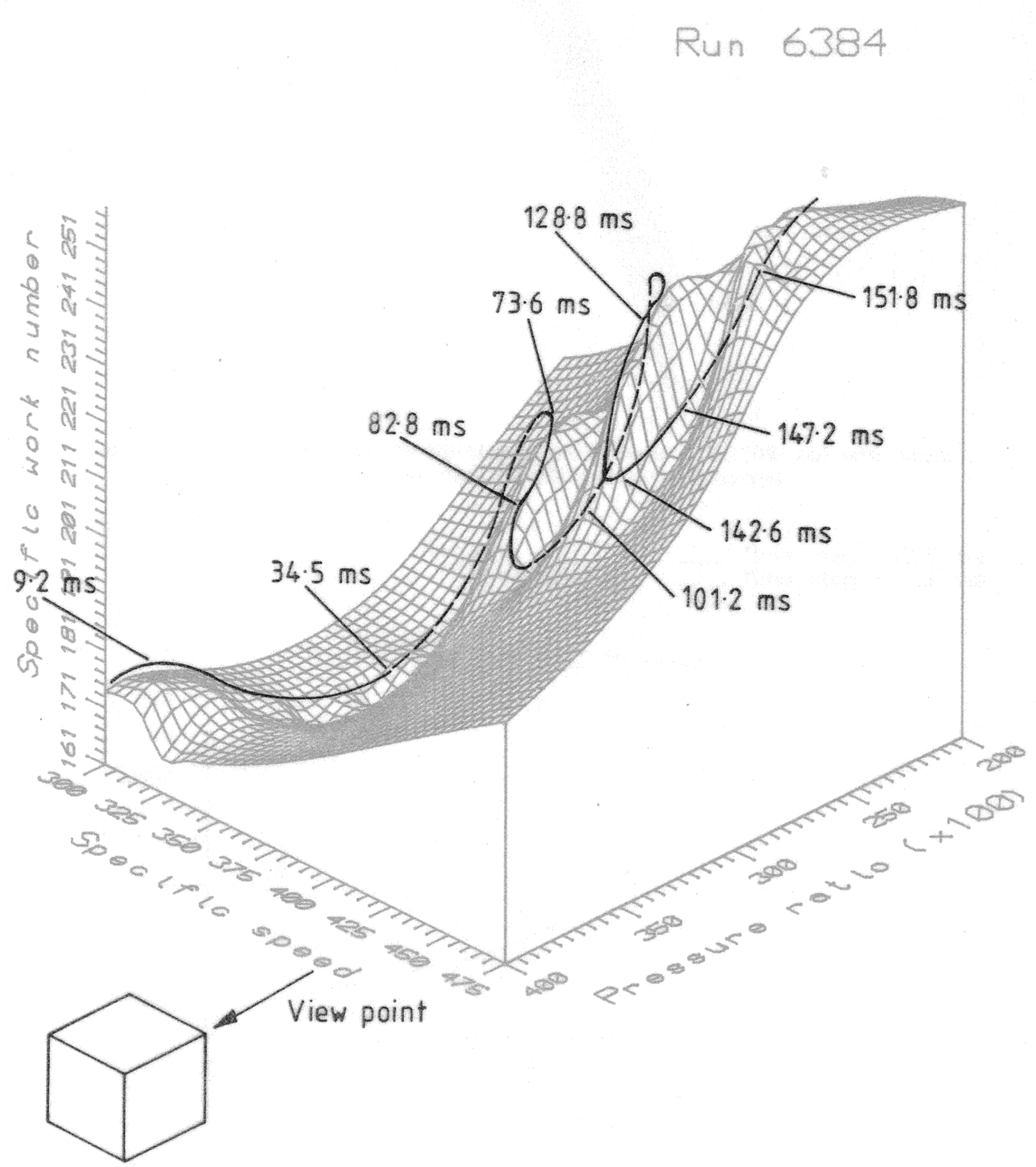

Figure 7.6b: Turbine performance map, with actual path traced by turbine during Run 6384 overlaid

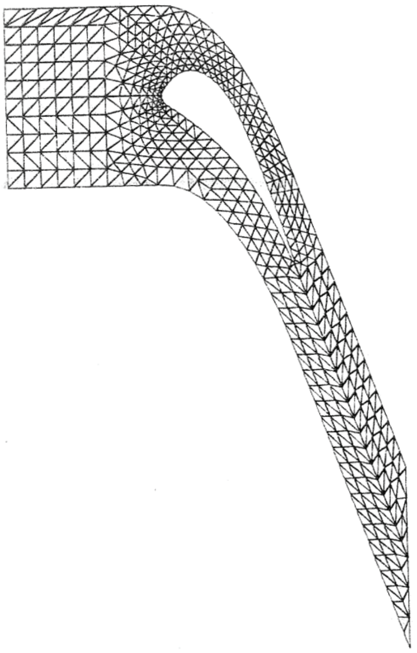

Figure 7.7: **Typical grid used by FINSUP to predict vane 10%, 50%, and 90% height Mach number (and blade-to-blade passage) distributions**

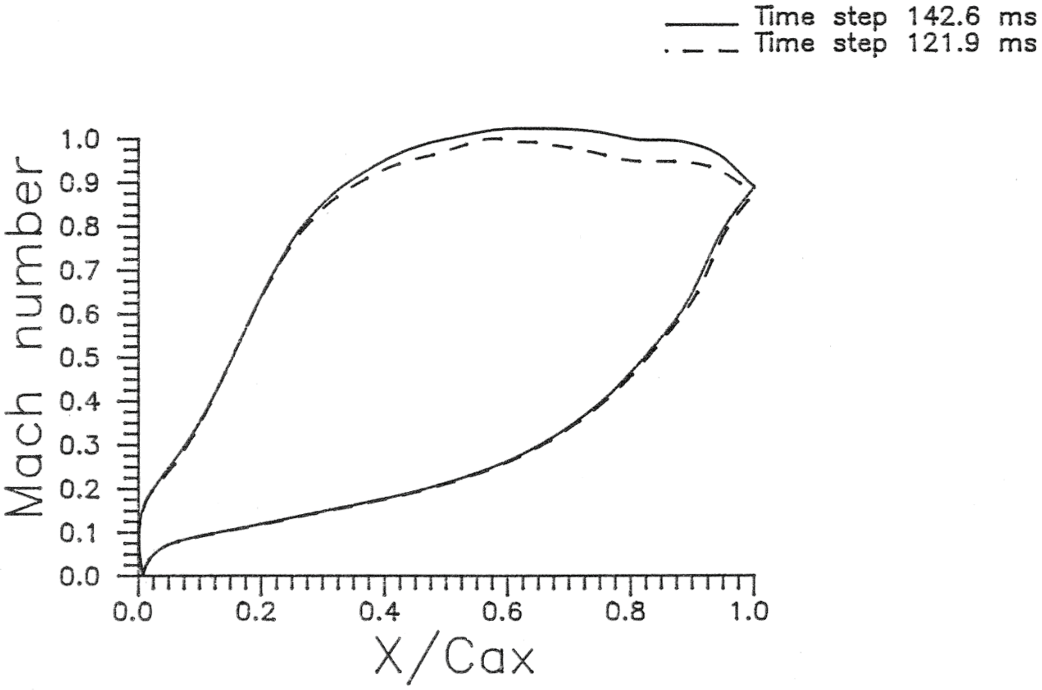

Figure 7.8: **Mach number distributions at 50% vane height using input data calculated by 'ROTOR' for time steps 121.9 ms and 142.6 ms, Run 6384, a trough and peak in piston oscillations**

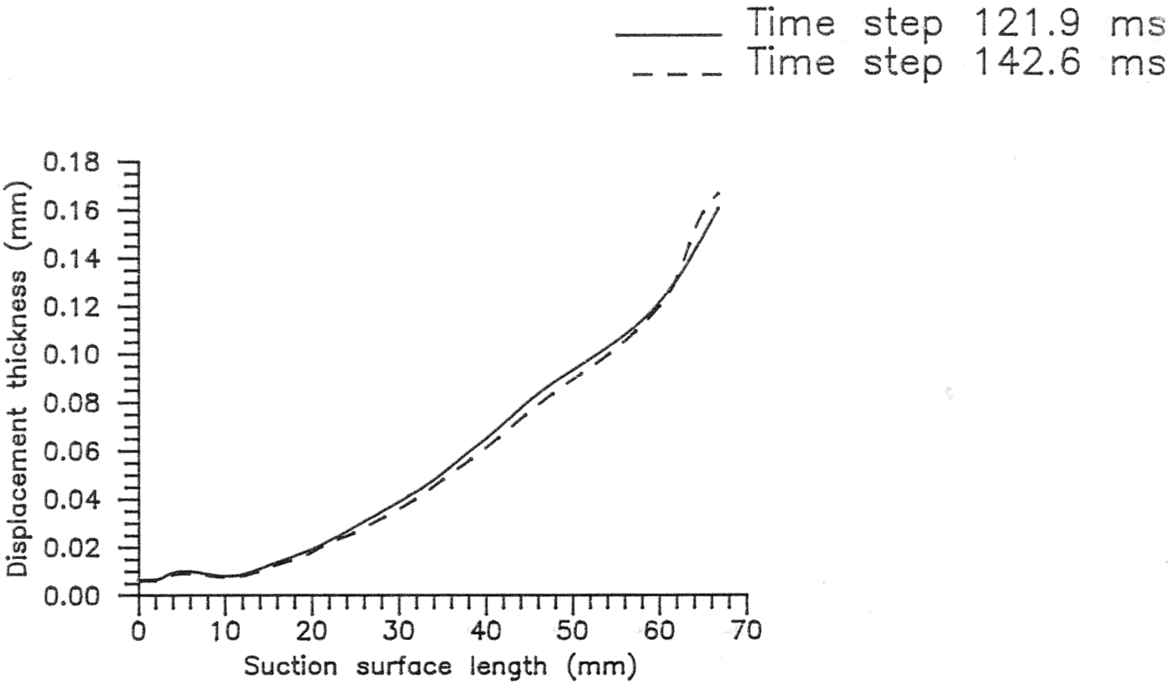

Figure 7.9: Boundary-layer displacement thickness on vane mid-height section suction surface for Run 6384; time steps 121.9 ms and 142.6 ms illustrating effect of piston oscillations on boundary-layer displacement thickness

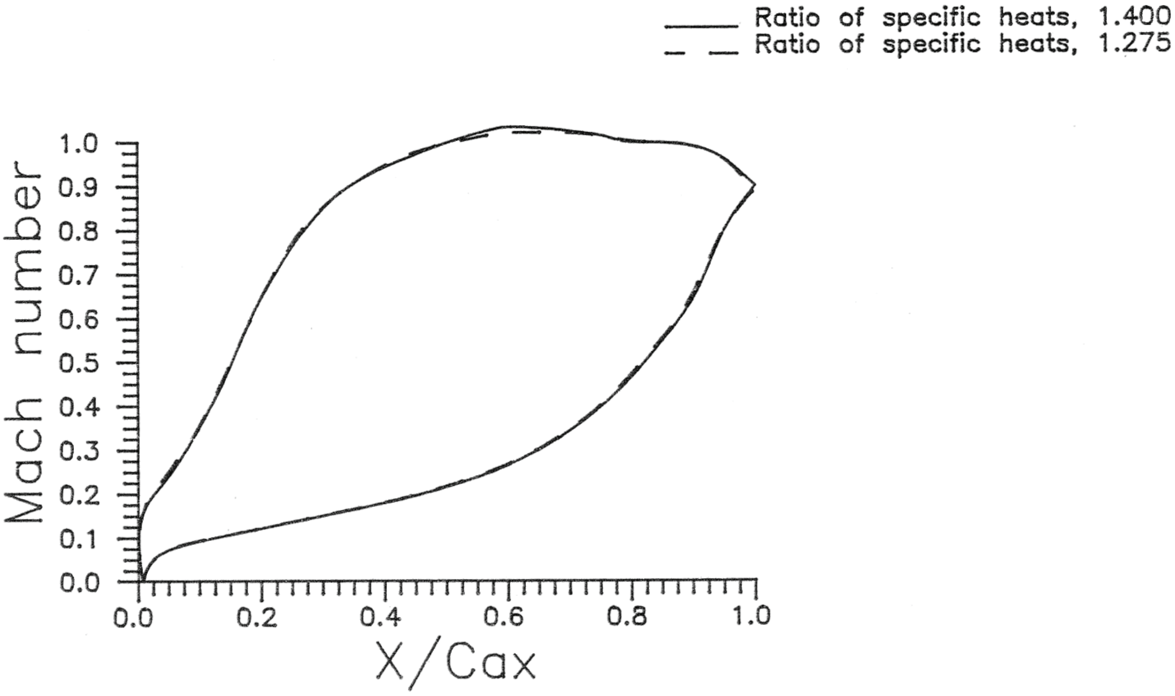

Figure 7.10: Vane mid-height Mach number distributions at turbine design conditions, with ratio of specific heats (γ) of 1.4 and 1.275

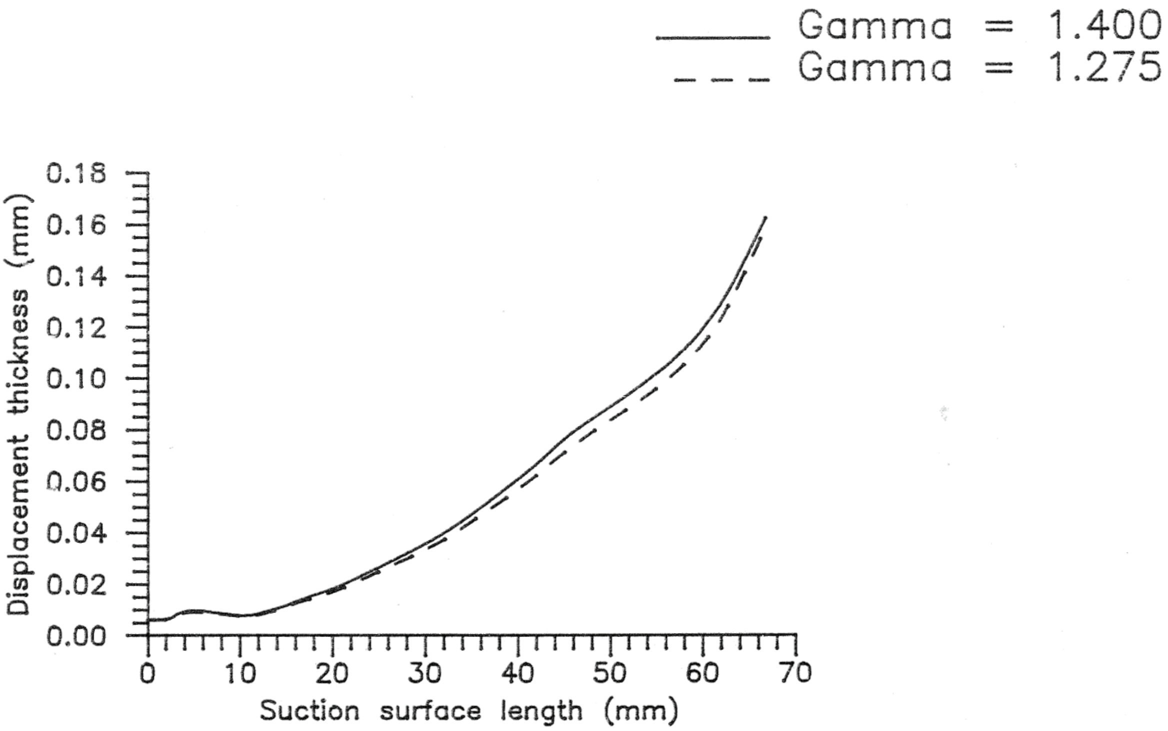

Figure 7.11: Boundary-layer displacement thickness on vane mid-height section suction surface at turbine design conditions with γ of 1.4 and 1.275

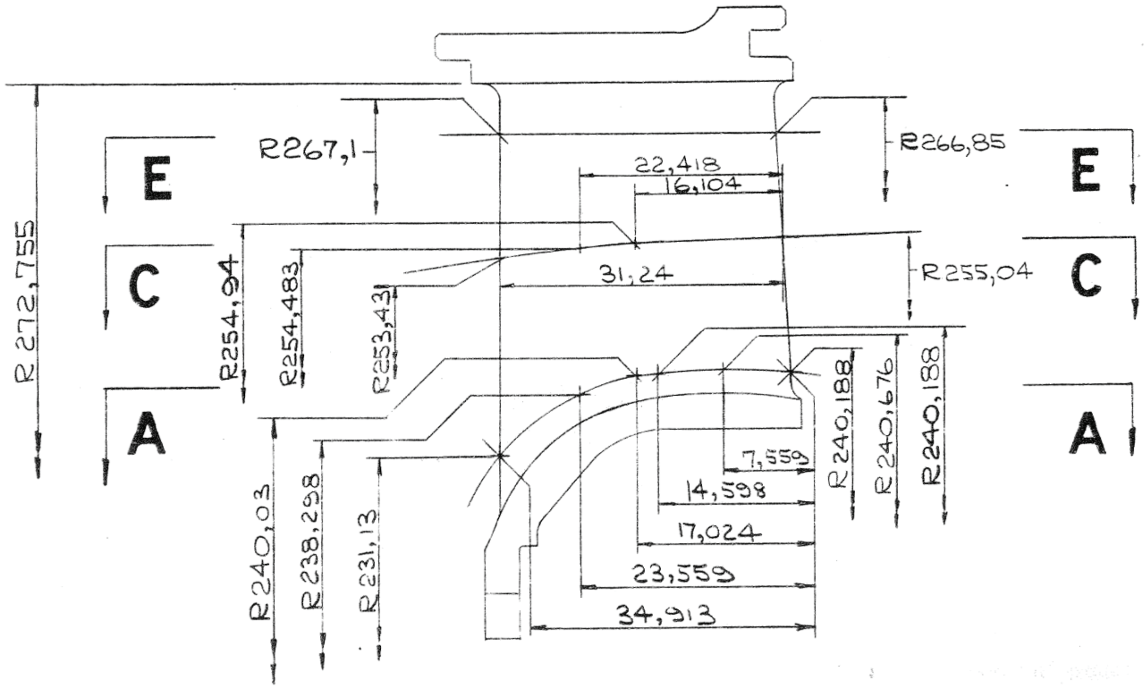

Figure 7.12: Three vane stream sections instrumented with static pressure tappings

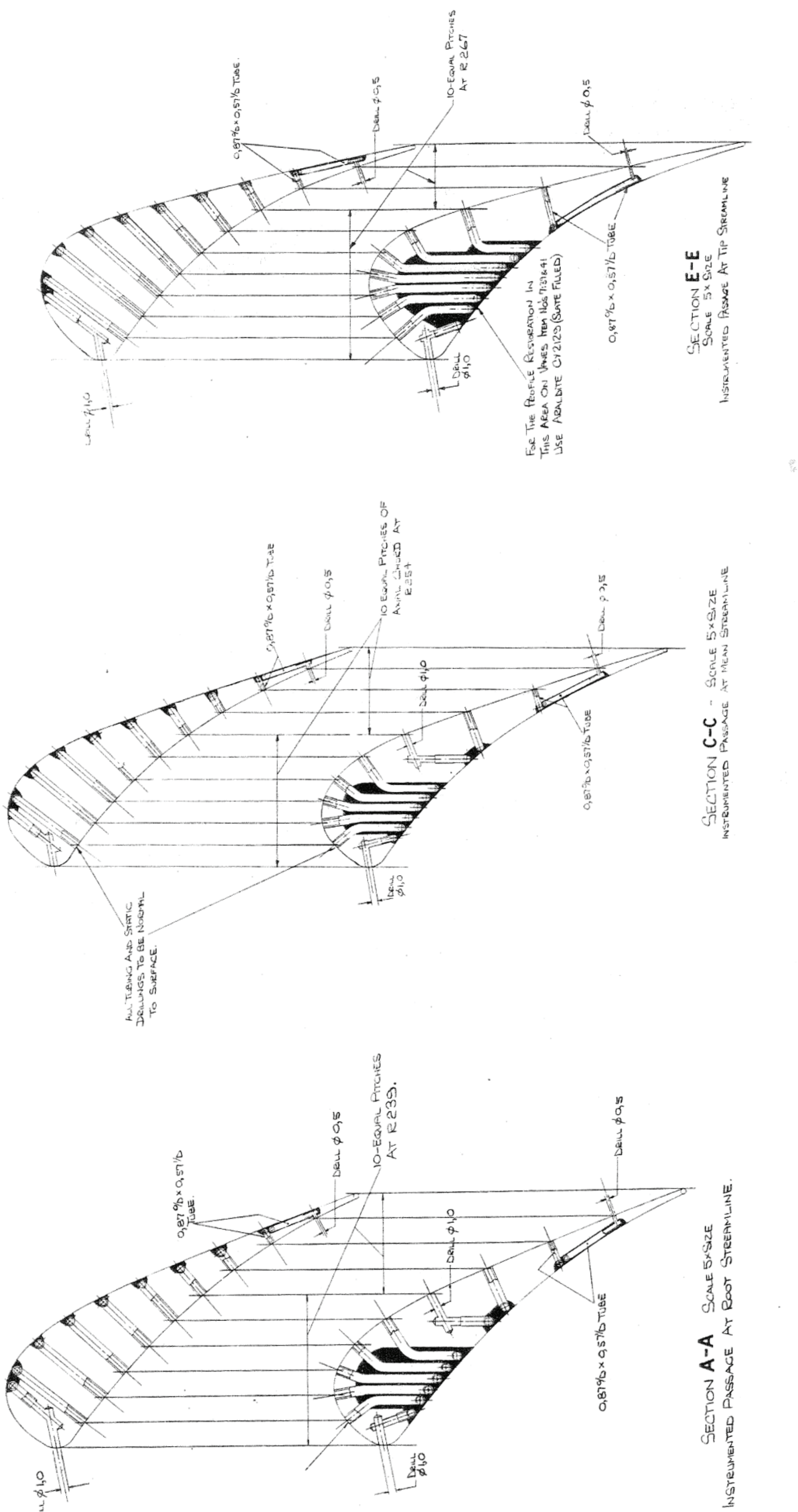

Figure 7.13: Three instrumented stream sections, illustrating location of static pressure tappings

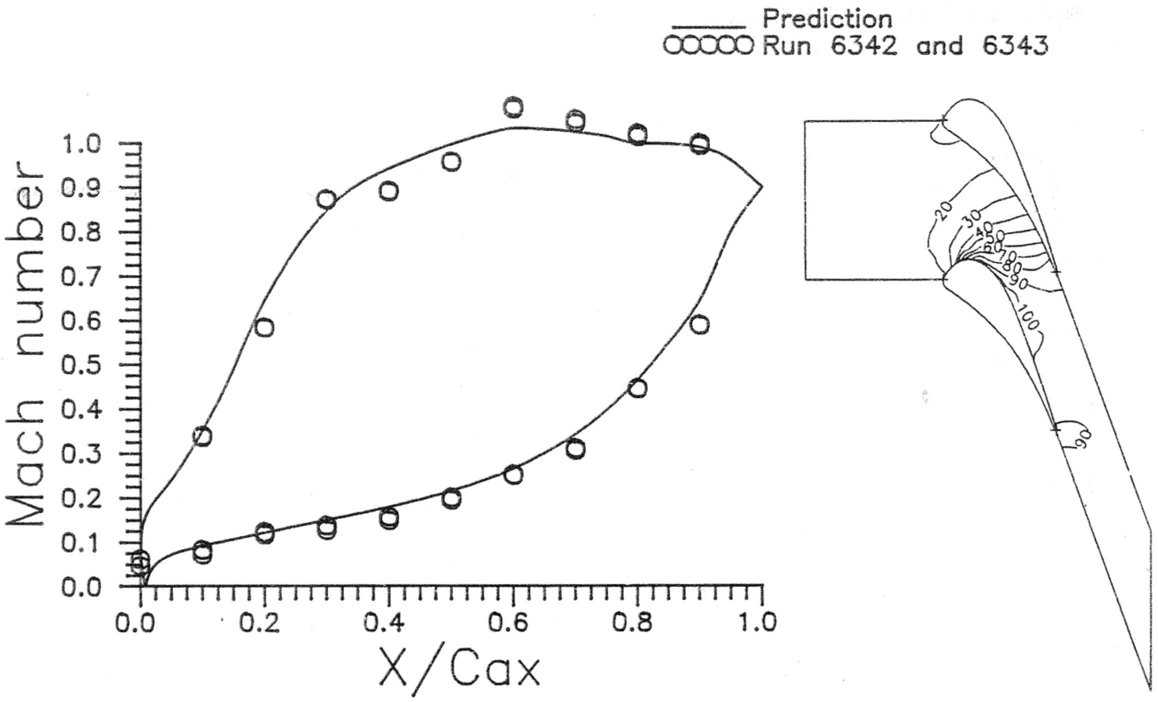

Figure 7.14: Vane mid-height Mach number distributions for Runs 6342 and 6343 and comparison with FINSUP prediction of Mach number distribution around mid-height section and across mid-height blade-to-blade passage

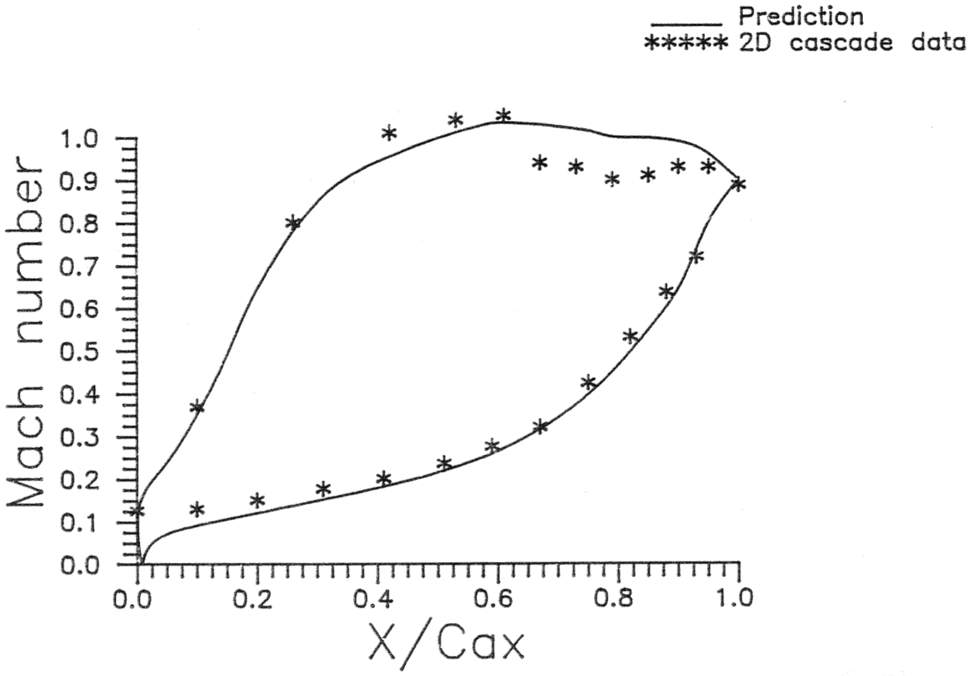

Figure 7.15: Two-dimensional cascade data (Nicholson, 1981), and comparison with FINSUP vane mid-height prediction

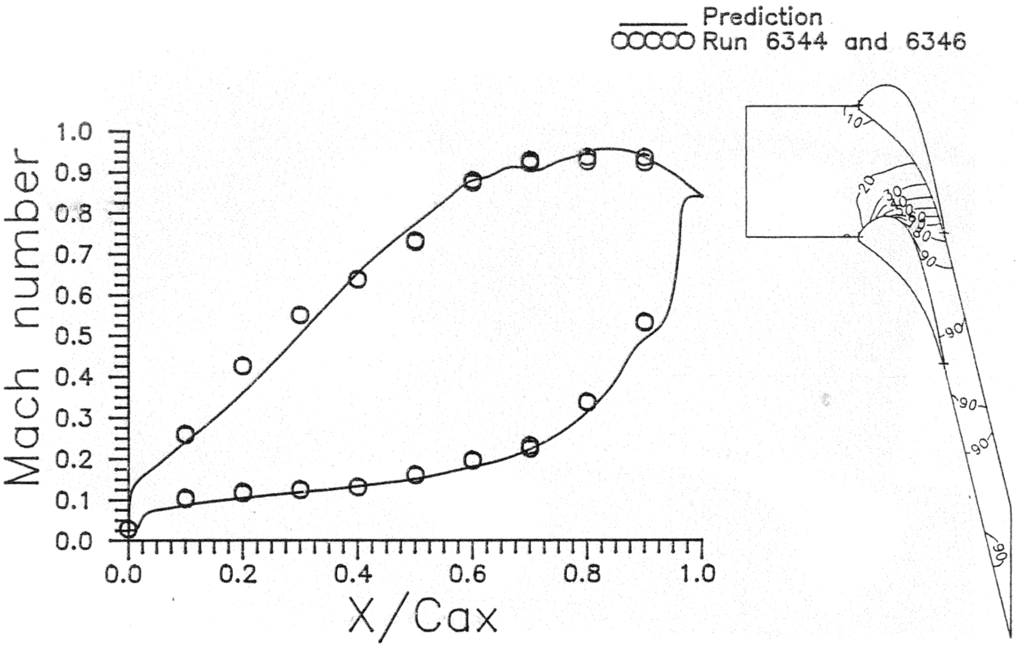

Figure 7.16: Vane tip Mach number distributions for Runs 6344 and 6346, and comparison with FINSUP prediction of Mach number distribution around tip section and across tip blade-to-blade passage

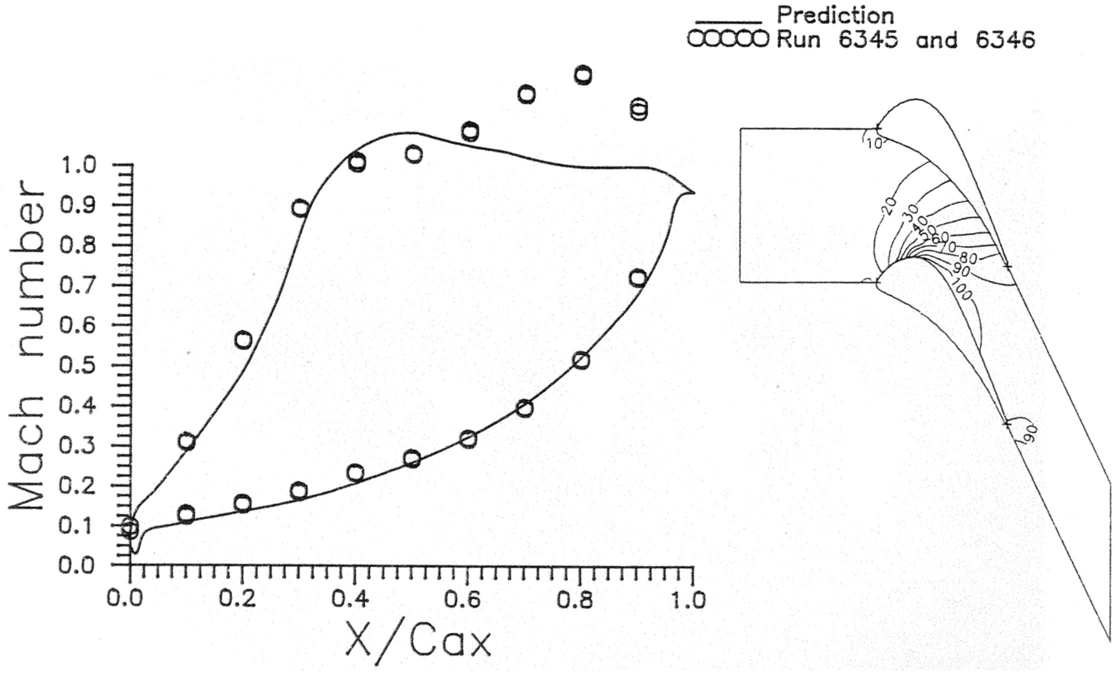

Figure 7.17: Vane hub Mach number distributions for Runs 6345 and 6346, and comparison with FINSUP prediction of Mach number distribution around hub section and across hub blade-to-blade passage

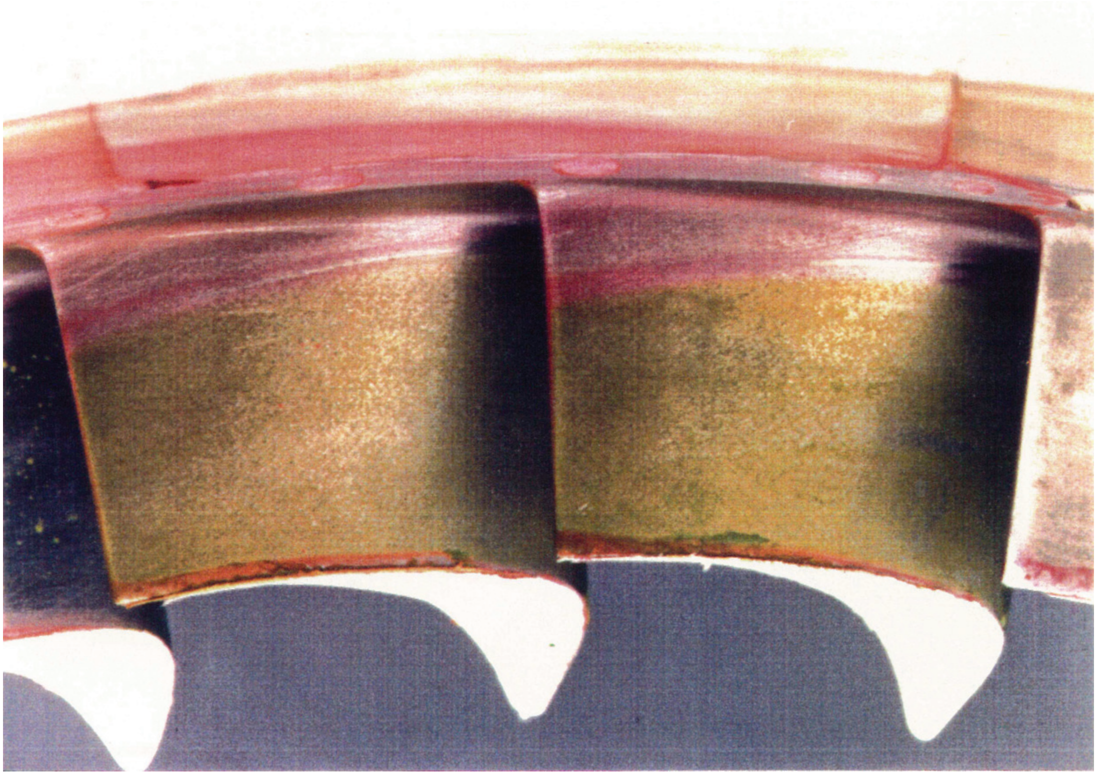

Figure 7.18: Two-colour flow visualisation of vane suction surface

Figure 7.19: Two-colour flow visualisation of vane and outer annulus

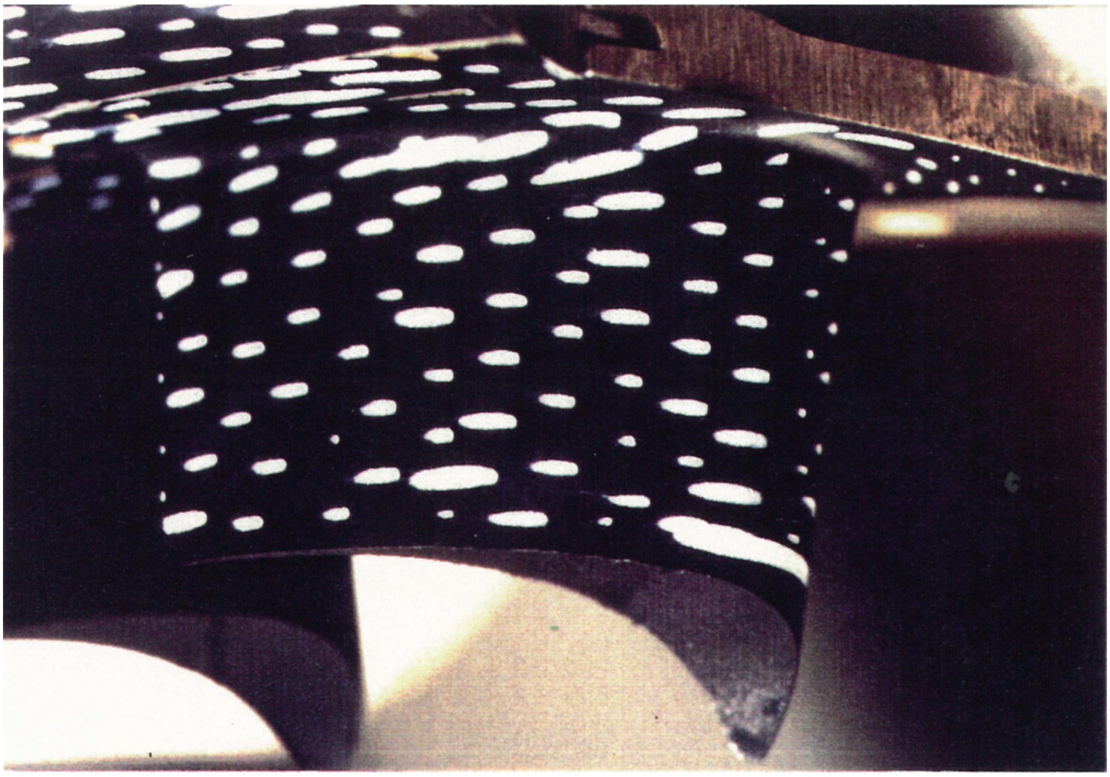

Figure 7.20: Oil dot flow visualisation of vane suction surface and outer annulus

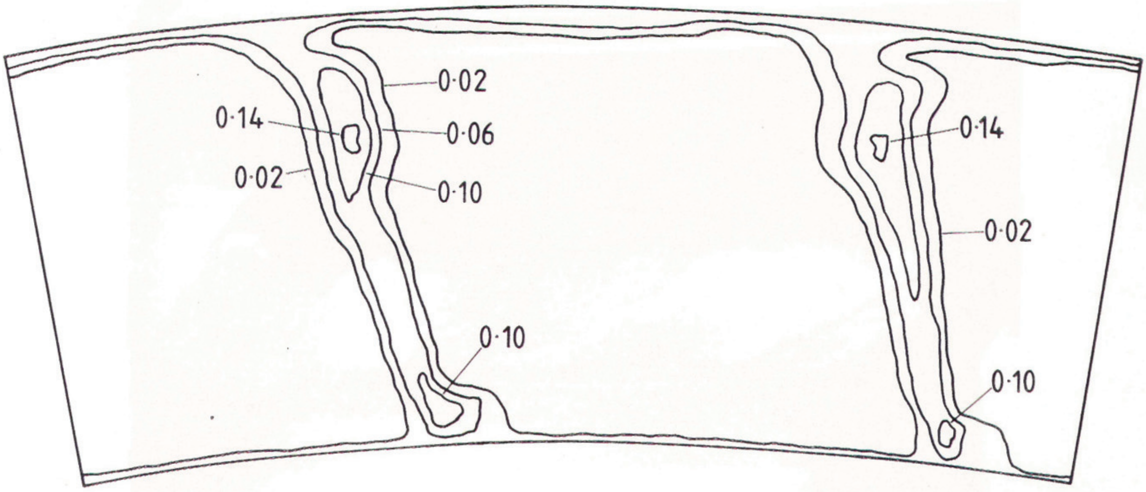

Figure 7.21: Area traverse of total pressure 10% vane axial chord downstream of vane trailing edge (adapted from Oliver, 1989)

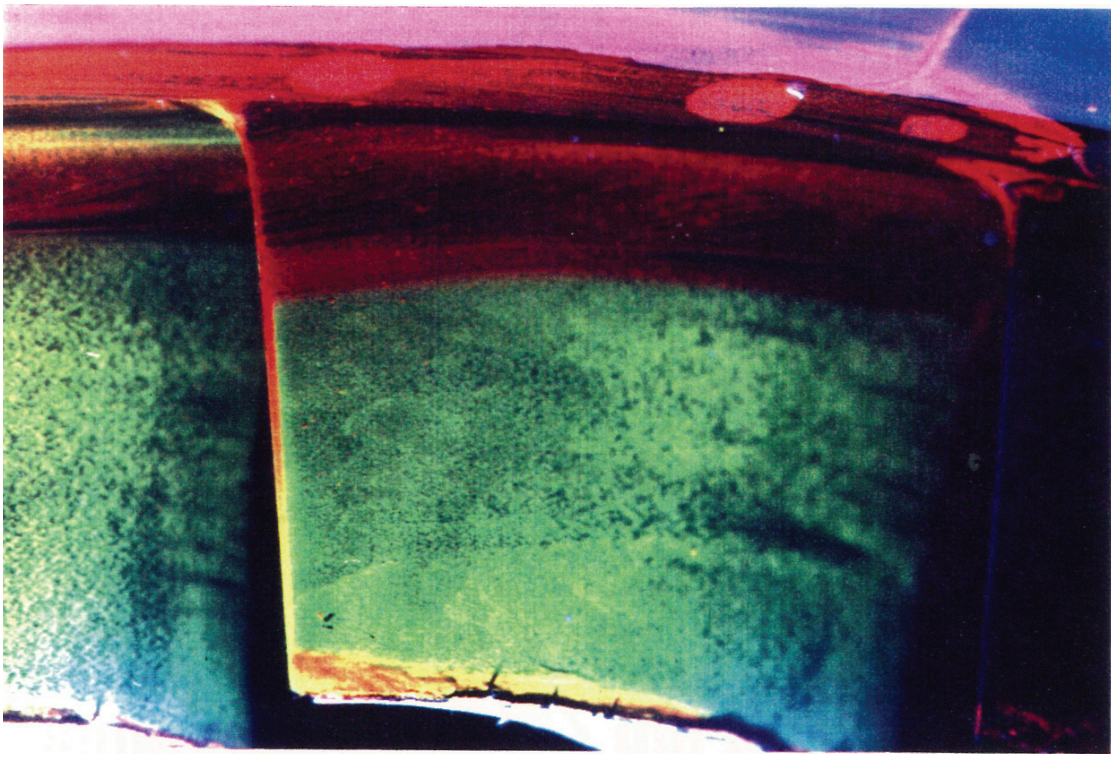

Figure 7.22: Two-colour flow visualisation of vane trailing-edge region, enhanced by illuminating vane with ultraviolet light

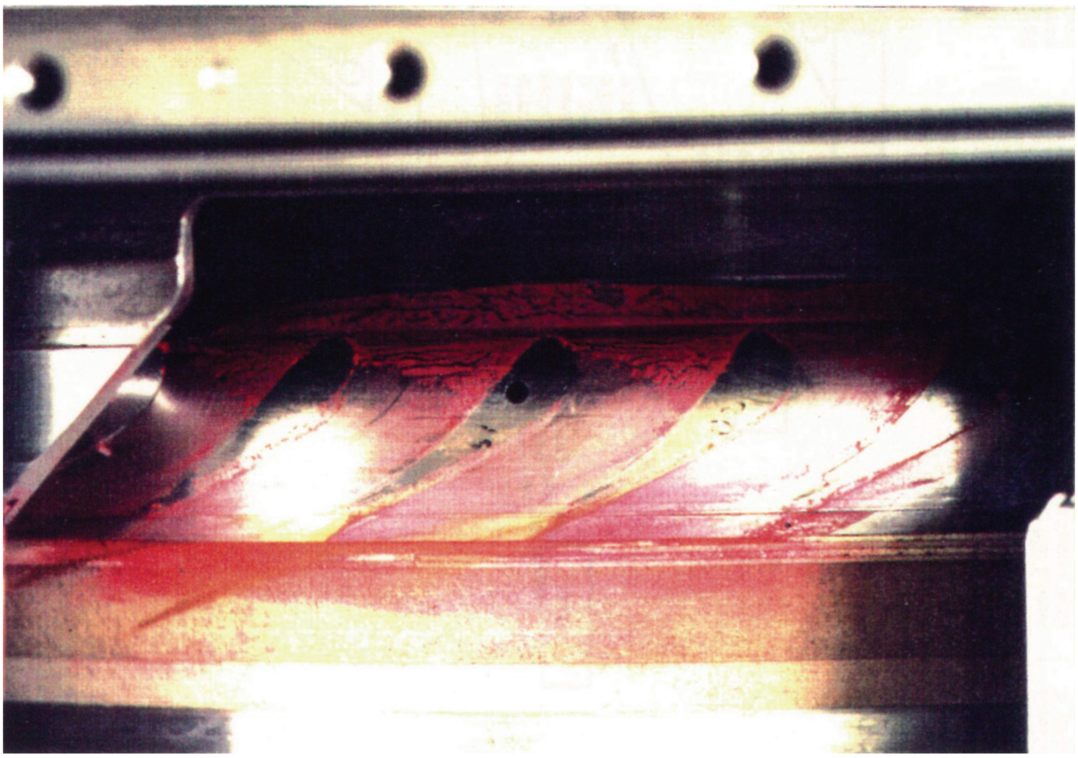

Figure 7.23: Two-colour flow visualisation of vane inner annulus

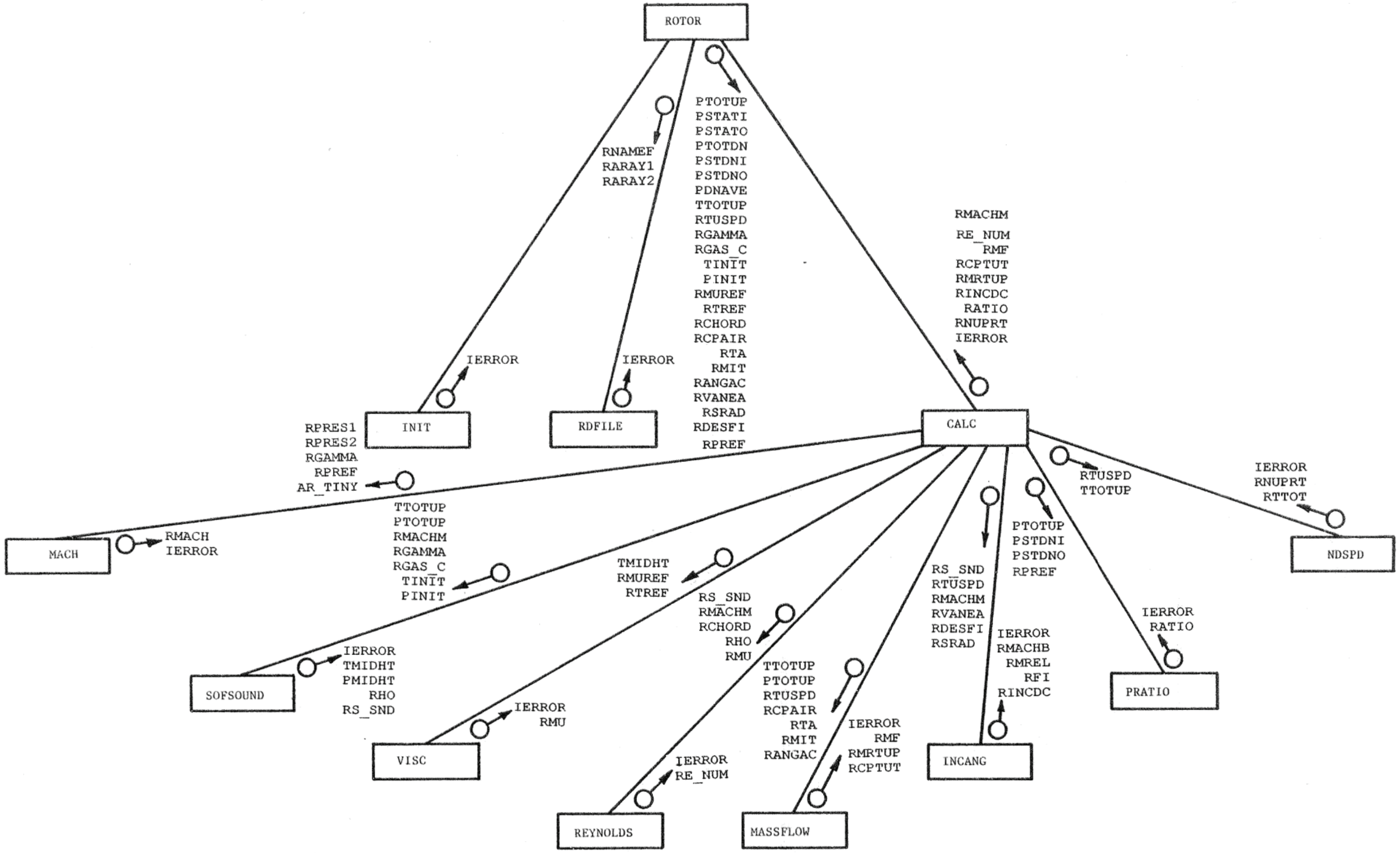

AR_TINY	! Very small number used instead of zero
RGAMMA	! Ratio of specific heats for air
RGAS_C	! Gas constant
TINIT	! Initial ILPT tube temperature
PINIT	! Initial ILPT tube pressure
RMUREF	! Referance viscosity for Sutherlands Law
RTREF	! Referance temperature for Sutherlands Law
RCHORD	! Nozzle Guide Vane chord
RCPAIR	! Specific heat capacity of air
RTA	! Nozzle Guide Vane throat area
RMIT	! Moment of inertia of the turbine disc
RANGAC	! Turbine disc angular acceleration
RVANEA	! Nozzle Guide Vane exit angle
RSRAD	! Radius of blade mid-height section
RDESFI	! Blade design condition inlet gas angle
RPREF	! National pressure tranducer ref pressure
PTOTUP	! Inlet total pressure
PSTATI	! Vane exit inner wall static pressure
PSTATO	! Vane exit outer wall static pressure
PTOTDN	! Downstream total pressure
PSTDNI	! Downstream inner wall static pressure
PSTDNO	! Downstream outer wall static pressure
PDNAVE	! Downstream average static pressure
TTOTUP	! Inlet total temperature
RTUSPD	! Turbine speed
RMACHM	! Vane exit, mid-height, Mach number
RE_NUM	! Reynolds number
RMF	! Mass flow rate
RCPTUT	! Cp delta T upon T
RMRTUP	! M root T upon P
RINCDC	! Blade incidence angle
RATIO	! Turbine pressure ratio
RNUPRT	! Turbine specific speed, N upon root T
IERROR	! Error flag
RMACHB	! Blade Mach number at radius RSRAD
RMREL	! Blade relative inlet Mach number, at radius RSRAD
RFI	! Blade relative inlet gas angle
RPRES1	! Total pressure
RPRES2	! Static pressure
RMACH	! Calculated Mach Number
RTTOT	! Square root of upstream total temperature
RNAMEF	! Name of file to be read
RARAY1	! Name of first variable in file (time)
RARAY2	! Name of second variable in file (pressure, temperature or speed)
RMU	! The vane exit, mid-height, viscosity
TMIDHT	! Vane exit, mid-height, static temperature
PMIDHT	! Vane exit, mid-height, static pressure
RHO	! Vane exit, mid-height, density
RS_SND	! Vane exit, mid-height, speed of sound

Figure A.1: Structure of 'ROTOR' program used to calculate time-varying non-dimensional and quasi non-dimensional groups from TOPSY measured data

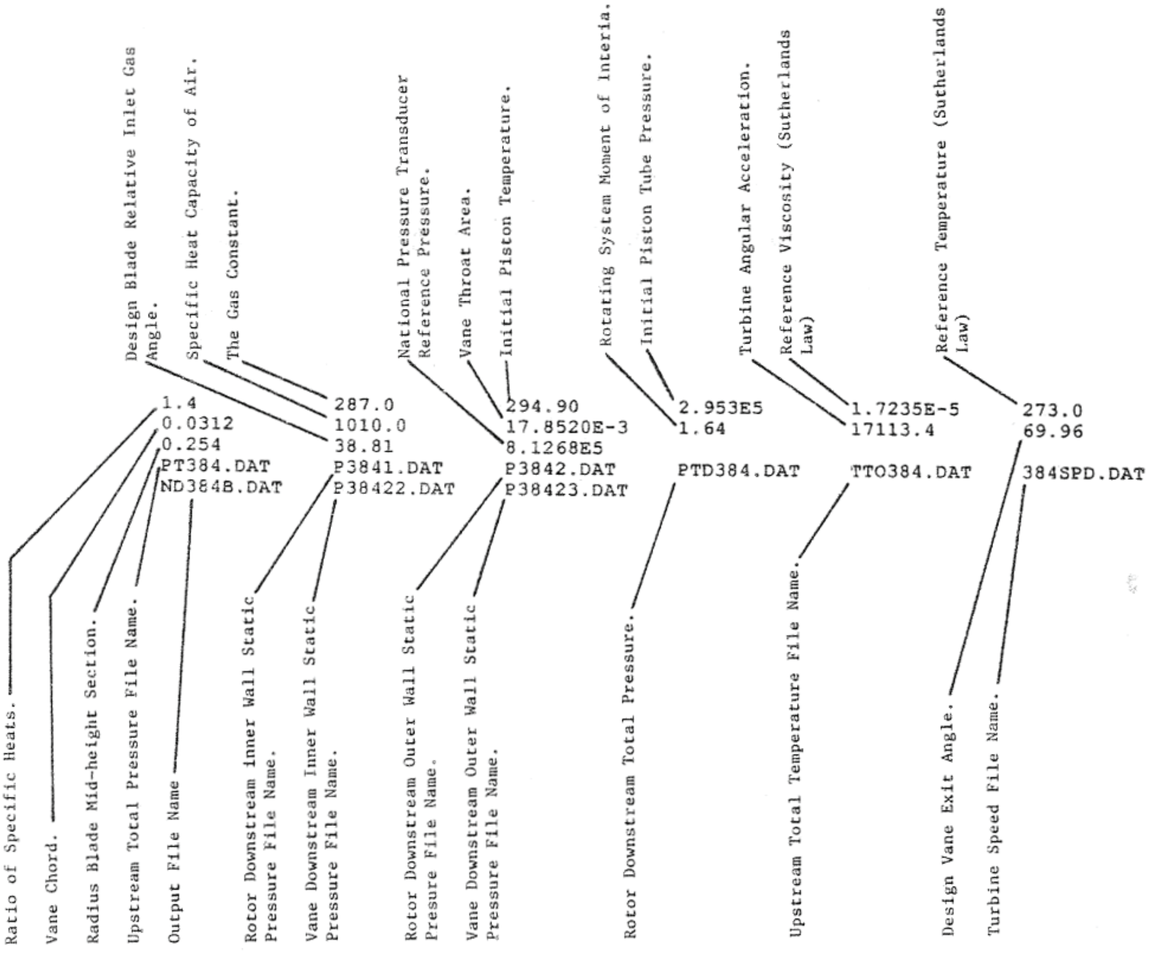

```
1.4          287.0         294.90
0.0312       1010.0        17.8520E-3     2.953E5      1.7235E-5     273.0
0.254        38.81         8.1268E5       1.64         17113.4       69.96
PT384.DAT    P3841.DAT     P3842.DAT      PTD384.DAT   TTO384.DAT    384SPD.DAT
ND384B.DAT   P38422.DAT    P38423.DAT
```

Figure A.2: Input data file used by 'ROTOR'